Université de Liège

Faculté de Sciences Appliquées

Département d'Aérospatiale et Mécanique

Groupe Turbomachines et Propulsion

# Contribution to

# Throughflow Modelling

# for Axial Flow Turbomachines

Thèse de doctorat

présentée en vue de l'obtention du grade de

Docteur en Sciences Appliquées

par

**Jean-François SIMON**

Ingénieur Civil Electro-Mécanicien (Aérospatiale)

Mars 2007

*"No one believes the CFD results except the one who performed the calculation, and everyone believes the experimental results except the one who performed the experiment"*

from P.J. Roache

# Acknowledgments

# Contents

# List of Figures

# List of Tables

# List of symbols

## Roman symbols

| | |
|---|---|
| $a$ | speed of sound |
| $b$ | blockage factor |
| $C_p$ | specific heat at constant pressure |
| $C_v$ | specific heat at constant volume |
| $E$ | total energy |
| $e$ | internal energy |
| $F$ | axial advective flux vector |
| $f_b$ | inviscid blade force |
| $f_v$ | viscous blade force |
| $G$ | radial advective flux vector |
| $H$ | total enthalpy |
| | normal flux vector |
| | gate function |
| $h$ | enthalpy |
| $I$ | rothalpy |
| $i$ | incidence |
| $k$ | thermal conductivity |
| | kinetic energy of the fluctuations |
| $k_t$ | eddy thermal conductivity |
| $M$ | Mach number |
| $N$ | blade count |
| $Pr$ | Prandtl number |
| $p$ | pressure |
| $q$ | heat flux |
| $q_m$ | mass flow |
| $R$ | gas constant |
| $r$ | radial coordinate |
| $Re$ | Reynolds number |
| $S$ | source term |
| $s$ | entropy (relative to the inlet conditions) |

| | |
|---|---|
| $T$ | temperature |
| $t$ | time |
| $U$ | conservative variables vector |
| | peripheral velocity |
| $V$ | absolute velocity |
| $W$ | relative velocity |
| $x$ | axial coordinate |

# Greek symbols

| | |
|---|---|
| $\alpha$ | absolute blade-to-blade flow angle |
| $\beta$ | relative blade-to-blade flow angle |
| $\gamma$ | specific heat ratio |
| $\delta$ | deviation |
| $\eta$ | isentropic efficiency |
| $\theta$ | circumferential coordinate |
| $\lambda$ | lean angle |
| $\mu$ | molecular dynamic viscosity |
| $\mu_t$ | turbulent dynamic viscosity |
| $\nu$ | CFL number |
| $\pi$ | pressure ratio |
| $\Sigma$ | contour of a control volume |
| $\rho$ | density |
| $\tau$ | viscous stress tensor |
| $\phi$ | limiter |
| $\Omega$ | angular velocity |
| | area of a control volume |
| $\varpi$ | loss coefficient |

# Operators

| | |
|---|---|
| $\overline{\phantom{x}}$ | averaging operator |
| $\sim$ | Favre averaging operator |
| $\overline{\phantom{x}}^t$ | time-averaging operator |
| $\overline{\phantom{x}}^e$ | Reynolds ensemble-averaging operator |
| $\overline{\phantom{x}}^a$ | passage-to-passage averaging operator |
| $\overline{\phantom{x}}^c$ | circumferential-averaging operator |

# Subscripts

| | |
|---|---|
| $i$ | inviscid |

| | |
|---|---|
| $m$ | meridional direction |
| $p$ | relative to pressure side |
| $s$ | relative to suction side |
| $R$ | relative to the rotors |
| $r$ | radial component |
| $rel$ | relative to the rotating frame |
| $S$ | relative to the stators |
| $v$ | viscous |
| $x$ | axial component |
| $\theta$ | circumferential component |

# Superscripts

| | |
|---|---|
| $'$ | unsteady non-deterministic fluctuation |
| $''$ | unsteady deterministic fluctuation |
| $'''$ | aperiodic fluctuation |
| $''''$ | circumferential fluctuation |
| $0$ | total quantity |

# Abbreviations

| | |
|---|---|
| CFL | Courant-Friedrich-Lewy |
| RANS | Reynolds-Averaged Navier-Stokes |
| SLC | Streamline curvature |
| TF | Throughflow |

# Introduction

The meridional theory for turbomachinery has a relatively long history. According to Cumpsty (1989), the idea of the radial equilibrium was already widespread in the early 1940's. In the late 1940's and the early 1950's, the simple radial equilibrium theory, neglecting the streamlines curvature, coupled with prescribed free or forced vortex circumferential velocity distributions were in use. Starting from the end of the 1960's, the throughflow methods began to replace these simple radial equilibrium calculations. The throughflow methods used at that time consisted of the streamline curvature (SLC) method and the stream function method. This age represents the beginning of the use of the Computational Fluid Dynamics (CFD) in the turbomachinery design.

Due to both the advent of the CFD and the increasing power of the computer 3-D Navier-Stokes computational codes for turbomachines started to appear. The place of the throughflow progressively moved from the nearly sole design tool at the beginning to one of the numerous tools used in a modern design tool chain for turbomachines nowadays. It is however still the backbone of the modern compressor and turbine design process (Horlock and Denton, 2005) and remains the most important tool for the designer (Denton and Dawes, 1999). It is mainly used at the preliminary design stage for specifying the target aerodynamic performances to be achieved by the blading. It also gives a first insight of the global component functioning. Every major modification occurring later during the blade design process will be reevaluated on the throughflow model basis.

The throughflows are exploited for different purposes. They can be used either in the design mode, where the total temperature or angular momentum and the total pressure are prescribed and the flow angles are sought, either in the analysis mode, where a known machine geometry is analysed to predict its performance. Another very important exploitation of the throughflow models lies in the interpretation of the experimental data. Indeed, often, only a few aerodynamic quantities are known from tests and only at a limited number of locations. For example, only the stagnation pressures and temperatures at blade leading and trailing edges and the static pressures at annulus endwalls are known. The throughflow is then used to recompute the aerodynamic flow field inside the whole machine from these experimental data. Finally, the throughflow model is also used for coupling single blade row calculations in order to compute the flow field inside a multistage machine (see Attia (2005) for a recent application). The throughflow gives the boundary conditions to the 3-D single

row calculations and the single row calculations give the flow angles and loss coefficients to the throughflow.

The main drawback of the throughflow models is that they heavily rely on empirical inputs, such as 2-D profile losses correlations or the aerodynamic blockage. The empirical calibrations included in a throughflow model allow them to accurately predict the flow field inside a whole machine and to provide credible designs, but this is only possible if the design parameters of that machine are close to the design parameters of the reference machine that has been used to calibrate the throughflow model. As explained by Adamczyk (1999), the 3-D calculations based on the aerodynamic inputs from calibrated throughflow have provided credible designs. However, continuing quoting Adamczyk, reliance on the throughflow model to set the main aerodynamic design parameters such as the aerodynamic matching of stages greatly impedes the utility of using of the 3-D CFD tools in the design process.

When Adamczyk made the previous remark, its goal was to promote the use of elaborated 3-D multistage solutions in place of the actual design tool chain based on both 3-D single row and throughflow simulations. In the present work, starting from the same statement on the dependence of the turbomachine design to the empiricism included in the throughflow models, a different direction is followed. It consists in the achievement of a less empiricism dependent throughflow model. This is the main goal of this work and it is done through two axis. The first one is oriented toward "classical throughflow" method and is based on a more complete set of equations compared to the classical streamline curvature throughflow, namely the Navier-Stokes throughflow equations. The second axis is oriented toward the obtention of a high order throughflow model set of equations. It is obtained with the same spirit and on the basis of the average passage set of equations of Adamczyk (1984).

## Navier-Stokes throughflow

The most widespread throughflow method is certainly the streamline curvature method. It is based on the normal equilibrium and gets its name from the inclusion of the flow curvature effect in the meridional plane. In 1980, Spuur has proposed another approach to compute the meridional flow field based on the Euler equations. This approach has only started to retain attention at in the 1990's. Recent works using this approach can be found in Baralon (2000) and Sturmayr (2004).

The methods based on the Euler equations present some interesting features and remove some of the drawbacks of the streamline curvature approach. A shock capturing property is built in the Euler equations and the mass-flow is a result of the computation, allowing to capture the choke mass flow. Furthermore, the generally adopted time-marching techniques to solve these equations bring a natural unsteady capability of the developed solvers.

A drawback of the throughflow model based on the SLC method as well as of the Euler

throughflow model is the treatment of the annulus endwalls which is inherently inviscid with a slip condition along the walls. This is probably the major concern with throughflow models. A common practice is to introduce an aerodynamic blockage which corrects the mass flow in order to obtain the right level of velocity in the core flow. This blockage factor is equivalent to the displacement thickness of the annulus endwalls boundary layers. This is a very sensitive quantity relying on empiricism. Indeed, if the aerodynamic blockage level is mispredicted, the compressor will be mismatched: some stages will not work at their design condition for the overall compressor design point. This can lead to reduce both the efficiency and the stall margin. Another solution is to include the effect of the viscous flow on the annulus endwall in an inviscid computation is to perform a separate boundary layer calculation. However, it is now recognised that the use of the boundary layer theory for computing the endwall flows inside a compressor is inappropriate (Cumpsty (1989) or Horlock and Denton (2005)).

In the present work, a third solution is brought with a throughflow model directly based on the Navier-Stokes equations. It is able to resolve the viscous flow on the annulus endwalls and the flow blockage is directly computed. Furthermore, this method is able to capture 2-D recirculations. The development of this model is one of the main contributions of this work.

## High order throughflow

Another step toward a less empiricism dependent throughflow is the use of the proposed high order throughflow method. This model is based on the Adamczyk's cascade of averaging procedure.

Different methods exist for obtaining an unsteady flow field at a lower cost than a 3-D unsteady simulation over full annulus including all blade passages. These are the domain scaling, the phase-lagged or the harmonic methods. The result of these methods is an unsteady flow field. Another approach is to try to obtain a mean (steady) representation of the unsteady flow. The result of this method is a steady flow field which contains the averaged effect of the unsteadiness. This is the average-passage model devised by Adamczyk (1984).

Adamczyk addresses the 3-D unsteady and turbulent flow field through several averaging operations. The first one is the well known Reynolds-averaging which eliminates the effect of the turbulence leaving a deterministic unsteady flow. The second one is a time-averaging removing the remaining effect of the unsteadiness which is due to the rotation of the rotor blades with respect to the stator ones. The last average is the aperiodic one which eliminates the aperiodicity of the flow due to the blade indexing (relative circumferential position of blade rows placed on the same shaft). The resulting flow field is steady and periodic but contains the mean effects of the turbulence, the unsteadiness and the aperiodicity. The equations associated to this flow show different unknown terms bringing the aforementioned effects. These terms are the Reynolds stresses, the deterministic stresses, the passage-to-

passage stresses and the blade forces. These equations, which have been rigorously obtained, are the average-passage equations of Adamczyk and describe the steady flow field inside a blade row embedded in a multistage configuration.

In this work, a subsequent step is performed by circumferentially averaging the average-passage equations in order to obtain an axisymmetric representation of the flow. These equations are also rigorously obtained and contain now the effect of the non-axisymmetry of the flow through circumferential stresses and blade forces. This set of equations represents the ultimate throughflow model which is obtained with no other assumptions that the ones prevailing to the establishment of the Navier-Stokes equations. They however present several unknown terms which have to be modelled or closed. The second main goal of this work is to study this high order throughflow model.

## Outline

This work is organised in five chapters. The first three chapters are dedicated to the "classical" throughflow based on the Euler/Navier-Stokes equations while the two last chapters address the high order throughflow model.

In the first chapter, the set of equations describing the Navier-Stokes throughflow model are derived. The different aspects linked to the modelling are addressed such as the inviscid blade force and the shock capturing properties or the viscous blade forces through the empirical profile losses. The radial mixing modelling as well as the endwall flow modelling used in this work are next presented. Finally, the impact of the 3-D blade effects such as the lean or the sweep inside a throughflow model is discussed.

The second chapter is dedicated to the numerical methods used to solve the equations obtained and described in the first chapter. The finite-volume method coupled to a time-marching procedure has been used. The standard algorithms used in this work are briefly described and the particularities of the numerics linked to the throughflow modelling, such as the treatment of the source terms, are highlighted. Finally, three verification testcases for which a well known solution exists are presented. They show the good behaviour of the numerical model.

The third chapter presents the results of the application of the model on three compressor testcases. Each of the three testcases highlights a different part of the physics included in the model. The first testcase is a single row transonic compressor which allows to discuss the shock capturing properties of the solver. The second testcase is a low speed 3.5 stage axial compressor which allows to highlight the effect of the radial mixing and the improvement brought by the Navier-Stokes model. The third testcase is a high subsonic compressor stage with a large boundary layer existing at the inlet plane of the test section, allowing to further study the viscous endwall flows modelling.

The fourth chapter presents the high order throughflow model and the derivation of its associated equations. With the help of two 2-D testcases, namely the development of a boundary layer over a flat plate and the spreading of a wake, the main properties of the equations are highlighted. A first attempt to evaluate the relative importance of the different unknowns brought by the averaging process is performed.

The last chapter presents the application of the high order model to two turbomachine testcases. These testcases reside in numerical simulations from which the different terms needed for the closure of the equations are extracted. The first one is a steady simulation of the a low speed compressor stage . The second one is an unsteady simulation of a transonic turbine stage. These testcases allow to further study the high order throughflow model and to show the improvements compared to a classical throughflow.

Finally, the conclusions of this work are drawn and directions for future research are given.

# Chapter 1

# Throughflow model

Most of the available throughflow codes are based on a radial (normal) equilibrium equation and a space-marching procedure. The most widespread method is certainly the so-called streamline curvature method. The advent of the CFD coupled to the increasing computer power allow the use of "more complete" sets of equations for throughflow analysis, such as the Euler or the Navier-Stokes equations. These methods do not exhibit a certain number of the SLC method shortcomings.

Indeed, with a throughflow model that directly solves the Euler/Navier-Stokes equations, the flow field inside a compressor or a turbine can be computed whatever the flow regime is. Shocks can also be captured and choked mass flow predicted naturally. Furthermore, these throughflows benefit from the well known CFD techniques for solving the Euler/Navier-Stokes equations and if the equations are solved by time-marching techniques, the unsteady capability is naturally included in the method. Also as it shares the same numerics as 3-D calculation codes, the coupling of both tools is made easier. The integration of both tools is indeed a desired feature in the design tool chain of a turbomachine. Finally, if the Navier-Stokes equations are used, the viscous flow developing on the annulus endwalls is captured and 2-D recirculations can be predicted.

The following brief literature survey allows to highlight the potential of the Euler and Navier-Stokes approaches for throughflow problems. A detailed review somewhat more oriented toward the numerical methods involved in the Euler throughflow is presented by Sturmayr (2004).

**Euler throughflow**

It seems that the first throughflow code based on the Euler equations is due to Spurr (1980). He used a time-marching technique to solve the Euler throughflow equations. He combined

a throughflow model and a blade-to-blade solver to build a Quasi-3D method. The solution obtained with the Quasi-3D method agrees well with a 3-D Euler solution for a transonic nozzle testcase.

An unsteady compressible Euler throughflow program was presented by Escuret and Garnier (1994) to study compressor instabilities. First, it was used in conjunction with a 1-D downstream volume and a throttle valve equation to simulate the onset of surge. Secondly, the Euler throughflow was coupled with a 3-D unsteady Euler solver in the blade free regions to simulate the rotating stall inception.

The 3-D numerical codes for solving the Euler/Navier-Stokes equations are far more widespread than the Euler throughflow solvers. A procedure to transform a 3-D computational code into a basic Euler throughflow was presented by Yao and Hirsch (1995). They also gave a detailed study of the impact of the chordwise distribution of the flow angle and blockage inside the blade rows.

In the same spirit as Yao and Hirsch (1995), Koiro *et al.* (1999) built an Euler solver on the basis of the turbomachinery oriented 3-D code ADPAC which is developed by the NASA (see for example Hall *et al.* (1995)). The purpose of their work is the unification of the 2-D design and the 3-D analysis tools. It is noteworthy that they used empirical correlations for the loss coefficient and the deviation angle. This is seldom done in the Euler throughflow frame, the general rule being to "manually" impose a certain level of loss and deviation.

Another domain where the Euler throughflow has a strong potential was illustrated by Dawes (1992). He presented the possibility offered by an Euler throughflow to be coupled with full 3-D viscous simulations for multistage configurations. In this perspective, only one blade row was solved in 3-D while the other blade rows were modelled axisymmetrically. This procedure brings the multistage environment (by the throughflow) when analysing or designing a single blade row.

Damle *et al.* (1997) illustrated the potential of the Euler models to design transonic and supersonic turbomachines. They successfully applied an Euler throughflow to the design of a supersonic fan stage as well as to the design of a transonic turbine stage. However, as remarked by Sturmayr (2004), it is not sure that the authors were aware of the different behaviours of the Euler throughflow with respect to the chosen way to represent the blade, especially the shock capturing properties. The design obtained by the author must therefore be analysed with care.

Another domain of interest for the Euler throughflows lies in the analysis or the preliminary design of a whole engine. Generally, at this level, the performances are obtained by 0-D models based on performance maps for the different components and thus heavily relied on empiricism. Improvements in the complete design of an engine would be brought by the use of more detailed models with less empiricism for the different components. Nowadays, 3-D models are far too expensive to be used at this stage but, at a lower level of fidelity,

1-D and 2-D simulation codes present an attractive trade-off. For example, a 1-D model for compressor and turbine was developed by Adam and Léonard (2005). It is a fast program that allows to construct a whole performance map of a multistage compressor in a few seconds only, on the basis of the annulus geometry and the blade angles at midspan. Stewart (1995) developed an axisymmetric model to simulate the whole flow in the gas path of a turbofan engine. This is not a full standalone analysis code as it requires some source terms computed by other computational codes. For example, it requires the flow angles computed by a SLC code for the compressor and turbine parts of the engine. From this point of view, the Euler throughflow of Stewart (1995) is more a vector for the different models of the engine components than a real simulation tool. Another example of a complete engine model based on the Euler equations is given by Abzalilov *et al.* (2005) with an application to unsteady flows. Very few details on the model are however provided in their publication.

Liu *et al.* (2000) applied a finite-volume throughflow model to a steam turbine with reverse flow conditions occurring both inside and downstream of a rotor. They succeeded in capturing some recirculation zones. However, as they used an Euler solver plus friction forces modelling the losses generated inside the blade row, these recirculations should be analysed with care. The results compared to experimental data are nevertheless very encouraging.

Baralon *et al.* (1997) particularly worked on the loss modelling. Profile losses and deviation angles together with endwall skin friction are introduced in the model. Their magnitudes are however not determined with a physical models such as empirical correlations but are rather specified "manually" to match the experimental results. It is one of the few Euler solvers that incorporates a spanwise mixing model (based on the turbulent diffusion model of Gallimore (1986)). From the same authors (Baralon *et al.*, 1998) the nature of the shocks captured by the Euler solver is investigated and a new way for computing the blade blockage factor with an approach similar to the one of Sayari and Bölcs (1995) is presented. The results of the application of their throughflow model to the computation of a whole speedline of a three-stage transonic fan are impressive.

Sturmayr and Hirsch (1999a) studied the shock capturing properties of the Euler throughflow equations and compared two formulations for the application of the blade force, an analysis one (specifying the camberline) and a design one (specifying the $rV_\theta$ distribution). Their study was performed on the NASA Rotor 67 transonic compressor. They found for this testcase that the design mode was in better agreement with 3-D Navier-Stokes solutions circumferentially averaged. They also built an hybrid mode which has the prediction capability of the analysis mode but the shock capturing properties of the design mode.

**Navier-Stokes throughflow**

One of the major concerns with throughflow models is the endwall flows modelling. The throughflow model presented above are based on the Euler equations. They contain some entropy generation terms, via a friction force coefficient, that allow the generation of the

(profile) losses across the blade rows. Concerning the annulus endwalls, they are generally modelled very crudely (if they are) in the frame of the Euler throughflow.

In the streamline curvature methods, the endwall flows are generally addressed by a separate boundary layer computation or by the introduction of an additional aerodynamic blockage. Cumpsty (1989) clearly explains the reasons why such methods should not be expected to be satisfactory. Among them, the fact that the boundary layer calculations are based on theories developed for the external aerodynamics and for well behaved flow is probably the more severe restriction regarding the strong conditions imposed to the flow inside a blade row.

From this observation, it seems natural to bring more physics into the model by using a more evolved model, i.e a throughflow model directly based on the Navier-Stokes equations. This is one of the main contributions of this work. To the knowledge of the author, the only other published Navier-Stokes throughflow solver is the one of Fay *et al.* (1999). They solved the parabolised Navier-Stokes equations by a pressure correction method (Patankar and Spalding, 1972). However, the sole application shown by these authors is a single stator row.

Another contribution to the viscous throughflow that is worth to be mentioned, although not based directly on the Navier-Stokes equations, is the viscous SLC throughflow of Howard and Gallimore (1993). They have modified an inviscid streamline curvature model containing a turbulent diffusion spanwise mixing model to introduce a non-slip condition at the endwalls together with the shear stresses along these endwalls.

The present chapter is divided as follows. First, the throughflow equations are derived by averaging the 3-D Navier-Stokes equations. The obtained equations show additional terms compared to the 3-D equations. Among them, the inviscid blade force and the viscous blade forces are of great importance. The modelling of theses terms is next described. Afterwards, the radial mixing and the annulus endwall flow modelling is addressed. Finally, the impact of some 3-D blade effects in a throughflow environment is discussed. These 3-D effects are the sweep, the lean and the localised blade twist.

## 1.1   Throughflow model equations

A rigorous approach for obtaining the throughflow equations is to circumferentially average the 3-D Navier-Stokes equations (recalled in the appendix B). This operation is performed inside the blade passage from the pressure side $\theta_p$ of a blade to the suction side $\theta_s$ of the following blade (figure 1.1).

Before performing the circumferential averaging each variable $f$ is split into a mean axisym-

metric value

$$\overline{f} = \frac{1}{\theta_s - \theta_p} \int_{\theta_p}^{\theta_s} f \, d\theta \tag{1.1}$$

and a circumferential fluctuation

$$f' = f - \overline{f} \tag{1.2}$$

When applied to the Navier-Stokes equations, the averaging process removes the circumferential coordinate but brings additional terms, the inviscid blade force, the viscous blade force and some terms due to the departure of the flow from an axisymmetric reference flow. These last contributions are similar to the Reynolds stresses but represent the transfer of energy and momentum between the 3-D and the axisymmetric flow fields. These terms, called circumferential stresses, are not negligible (see for example in Jennions and Stow (1986)) and impact the flow deflection, the losses, the secondary flows, etc. Some methods exist for extracting the circumferential stresses from blade-to-blade calculations and for reintroducing them in throughflow computations (Jennions and Stow, 1985a,b). However, as often in the throughflow models, those terms will not be simulated here but their effects will be rather included via profile losses and deviation. The study of the impact of the circumferential stresses on the flow field is the subject of chapters 4 and 5.

Mathematically, the blade forces originate from the fact that the averaging operator and the derivation operator do not commute inside the blade passage. This is due to the presence of the blade walls. The Leibniz's integral rule is therefore used. It gives a formula for the
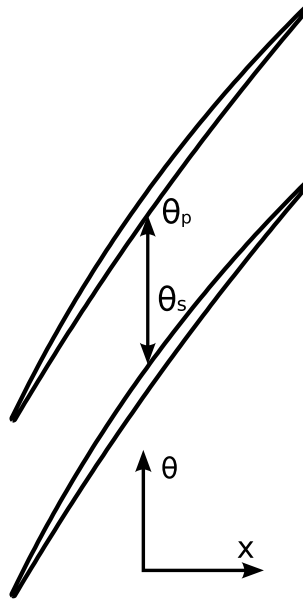


Figure 1.1: Circumferential averaging

differentiation of a definite integral whose limits are functions of the differential variable. For the axial derivative, it gives:

$$\overline{\frac{\partial f}{\partial x}} = \frac{1}{\theta_s - \theta_p} \int_{\theta_p}^{\theta_s} \frac{\partial f}{\partial x} \, d\theta = \frac{1}{\theta_s - \theta_p} \frac{\partial}{\partial x} \int_{\theta_p}^{\theta_s} f \, d\theta - \frac{1}{\theta_s - \theta_p} \left( f_s \frac{\partial \theta_s}{\partial x} - f_p \frac{\partial \theta_p}{\partial x} \right) \tag{1.3}$$

which can be rewritten more compactly:

$$\overline{\frac{\partial f}{\partial x}} = \frac{1}{b} \frac{\partial b \overline{f}}{\partial x} - \frac{1}{\theta_s - \theta_p} \left[ f \frac{\partial \theta}{\partial x} \right]_p^s \tag{1.4}$$

where $b$ is the blockage factor. It results from the tangential blade thickness and is defined as:

$$b = 1 - \frac{\psi}{2\pi/N} = \frac{(\theta_s - \theta_p)}{2\pi/N} \tag{1.5}$$

where $\psi$ is the circumferential thickness of the blades and $N$ the number of blades. The blockage factor $b$ is lower than 1 inside the blade row and equal to 1 outside of the blade row.

Finally, the 3-D Navier-Stokes equations circumferentially averaged are written as follows:

$$\frac{\partial U}{\partial t} + \frac{\partial b \, (F - F_v)}{\partial x} + \frac{\partial b \, (G - G_v)}{\partial r} = b \, (S + S_v) + (S_b + S_{bv}) \tag{1.6}$$

with

$$U = \begin{bmatrix} b\rho & b\rho V_x & b\rho V_r & b\rho V_\theta & b\rho E \end{bmatrix}^T$$

$$F = \begin{bmatrix} \rho V_x \\ \rho V_x V_x + p \\ \rho V_x V_r \\ \rho V_x V_\theta \\ \rho V_x H \end{bmatrix} \qquad G = \begin{bmatrix} \rho V_r \\ \rho V_r V_x \\ \rho V_r V_r + p \\ \rho V_r V_\theta \\ \rho V_r H \end{bmatrix} \qquad S = \frac{1}{r} \begin{bmatrix} -\rho V_r \\ -\rho V_r V_x \\ \rho V_\theta V_\theta - \rho V_r V_r \\ -2\rho V_r V_\theta \\ -\rho V_r H \end{bmatrix}$$

$$F_v = \begin{bmatrix} 0 \\ \tau_{xx} \\ \tau_{xr} \\ \tau_{x\theta} \\ \tau_{xj} V_j - q_x \end{bmatrix} \qquad G_v = \begin{bmatrix} 0 \\ \tau_{xr} \\ \tau_{rr} \\ \tau_{r\theta} \\ \tau_{rj} V_j - q_r \end{bmatrix} \qquad S_v = \frac{1}{r} \begin{bmatrix} 0 \\ \tau_{xr} \\ \tau_{rr} - \tau_{\theta\theta} \\ 2\tau_{r\theta} \\ \tau_{rj} V_j - q_r \end{bmatrix}$$

$$S_b = \frac{N}{2\pi b} \begin{bmatrix} 0 \\ -\left[p\dfrac{\partial\theta}{\partial x}\right]_s^p \\ -\left[p\dfrac{\partial\theta}{\partial r}\right]_s^{\not{p}} \\ \left[\dfrac{p}{r}\right]_s^p \\ \left[\dfrac{p}{r}\right]_s^p \Omega r \end{bmatrix} \qquad S_{bv} = \frac{N}{2\pi b} \begin{bmatrix} 0 \\ \left[\tau_{xj}\dfrac{\partial\theta}{\partial j}\right]_s^p \\ \left[\tau_{rj}\dfrac{\partial\theta}{\partial j}\right]_s^{\not{p}} \\ \left[\tau_{\theta j}\dfrac{\partial\theta}{\partial j}\right]_s^{\not{p}} \\ \left[\tau_{\theta j}\dfrac{\partial\theta}{\partial j}\right]_s^p \Omega r - \left[q_j\dfrac{\partial\theta}{\partial j}\right]_s^p \end{bmatrix}$$

where $\dfrac{\partial\theta}{\partial j}$ is equal to, respectively for j equal $1, 2, 3$, $\dfrac{\partial\theta}{\partial x}$, $\dfrac{\partial\theta}{\partial r}$ and $-1$.

The system of equations (1.6) is presented in the convenient vector form. $U$ is the vector of conservative variables, $F$ and $G$ are the advective flux vectors, $F_v$ and $G_v$, the viscous flux vectors. The source terms $S$ and $S_v$ are due to the expression of the system in cylindrical coordinates. The system of equations is closed by the state equation. For thermally perfect gases:

$$p = \rho R T \tag{1.7}$$

where $R$ is the gas constant. The total energy $E$ and the total enthalpy $H$ are defined as follows

$$E = e + \frac{1}{2}V_i V_i = C_v T + \frac{1}{2}V_i V_i \tag{1.8}$$

$$H = h + \frac{1}{2}V_i V_i = C_p T + \frac{1}{2}V_i V_i \tag{1.9}$$

where $C_v$ and $C_p$ are respectively the specific heat coefficient at constant volume and pressure. They are related to each other by the adiabatic exponent $\gamma$:

$$\gamma = \frac{C_p}{C_v} \tag{1.10}$$

The shear stresses and the heat fluxes appearing in $F_v$, $H_v$ and $S_v$ are calculated as

$$\tau_{xx} = \frac{2}{3}(\mu_t + \mu)\left(2\frac{\partial V_x}{\partial x} - \frac{\partial V_r}{\partial r} - \frac{V_r}{r}\right) \qquad \tau_{rr} = \frac{2}{3}(\mu_t + \mu)\left(2\frac{\partial V_r}{\partial r} - \frac{\partial V_x}{\partial x} - \frac{V_r}{r}\right)$$

$$\tau_{\theta\theta} = \frac{2}{3}(\mu_t + \mu)\left(2\frac{V_r}{r} - \frac{\partial V_x}{\partial x} - \frac{\partial V_r}{\partial r}\right) \qquad \tau_{xr} = (\mu_t + \mu)\left(\frac{\partial V_r}{\partial x} + \frac{\partial V_x}{\partial r}\right)$$

$$\tau_{x\theta} = (\mu_t + \mu)\frac{\partial V_\theta}{\partial x} \qquad\qquad\qquad \tau_{r\theta} = (\mu_t + \mu)\left(\frac{\partial V_\theta}{\partial r} - \frac{V_\theta}{r}\right)$$

$$q_x = -(k + k_t)\frac{\partial T}{\partial x} \qquad\qquad\qquad q_r = -(k + k_t)\frac{\partial T}{\partial r}$$

The molecular dynamic viscosity $\mu$ is computed from the Sutherland formula. The eddy viscosity $\mu_t$ is obtained by a mixing-length approximation. The usual simplifications that come with such a model and non-hypersonic flows (Wilcox, 1993) have already been performed on the energy balance (equation 1.6).

The thermal conductivity $k$ is linked to the molecular viscosity by the Prandtl number, which is assumed to be equal to 0.72. Similarly a turbulent Prandtl number equal to 0.9 is used to obtain the eddy thermal conductivity $k_t$.

The two last terms of the equation (1.6), together with the blockage factor, represent the action of the blade rows on the flow. The source term $S_b$ corresponds to the inviscid part of the blade force. It is due to the pressure field acting on the blade surfaces. The source term $S_{bv}$ is due to the shear stresses and the heat fluxes acting along the blade surfaces. In the present model, the blade walls are supposed to be adiabatic, meaning that $S_{bv}$ is reduced to the contribution of the shear stresses. In the following, this term will be referred to as the viscous blade force. The modelling of these blade forces is the topic of the two following sections.

## 1.2    Inviscid blade forces

The source term $S_b$ in equation (1.6) is written in function of quantities relative to the blade pressure and suction sides. In an axisymmetric model, these quantities are unknown and the blade force must therefore be modelled with the available information. This information differs with the kind of **problems** that is treated:

- the first class of problem is the analysis one. From the known geometry of a given machine, its performances are sought,

- the second class of problem is the design one. In that case, the geometry of a machine is sought from prescribed performances.

On the other hand, the throughflow model can be divided in two classes of **methods**:

- the first class is the analysis method where the blade camberline is directly specified to the throughflow model,

- the second class of method is the design one where the circumferential velocity is prescribed.

The design method can be used to solve an analysis problem as well as an analysis method can be used to solve a design problem. For example a design problem can be solved by an analysis method coupled to an optimisation technique. In this work, the focus will be put on the analysis problem but both the analysis and the design methods will be used to solve it.

In order to model the inviscid blade force, the latter is split into the blade blockage contribution $S_{b1}$ and the blade flow deflection contribution $S_{b2}$.

## 1.2.1 Blade blockage contribution

This contribution is due to blade circumferential thickness. It brings the effect of the contraction of the flow path inside the blade passage together with the blade blockage factor. It is similar to the cross section variation in the 1-D Euler nozzle equations.

$$
S_{b1} = \begin{bmatrix} 0 \\ \dfrac{p}{b}\dfrac{\partial b}{\partial x} \\ \dfrac{p}{b}\dfrac{\partial b}{\partial r} \\ 0 \\ 0 \end{bmatrix} \tag{1.11}
$$

## 1.2.2 Blade flow deflection contribution

The second part of the inviscid blade force is responsible for the flow deflection of the flow across the blade row. The following information is used to compute the three components of the blade force.

The blade force is intended to deflect the flow without generating losses, as it is the role of the viscous blade force to produce them. Furthermore, in the reference frame of the blade of interest, the blade force should not work. However, a force that does not work and that has a component aligned with the flow direction will generate entropy as it will be shown in the following section. Therefore an orthogonality condition of the blade force to the flow has to be imposed:

$$
\vec{f_b}\left(\vec{V} - \vec{\Omega}r\right) = 0 \tag{1.12}
$$

The second information that is prescribed is an information on the radial component of the blade force. It is obtained from the stacking line of the blade sections. The radial blade force is important when the blade stacking line is inclined with respect to the radial

direction. Such a geometrical configuration is called bow or compound lean and is used, for example, to enhance the flow developing along the endwalls. To introduce the radial blade force, a relation between the radial and the circumferential components of the blade force is prescribed:

$$\frac{f_{br}}{f_{b\theta}} = -\tan\lambda \tag{1.13}$$

where $\lambda$ is the angle between the normal to the blade camber surface and the $\theta$ axis direction (see figure 1.2). A study of the effect of the blade lean in the frame of a throughflow computation will be presented later in section 1.7.
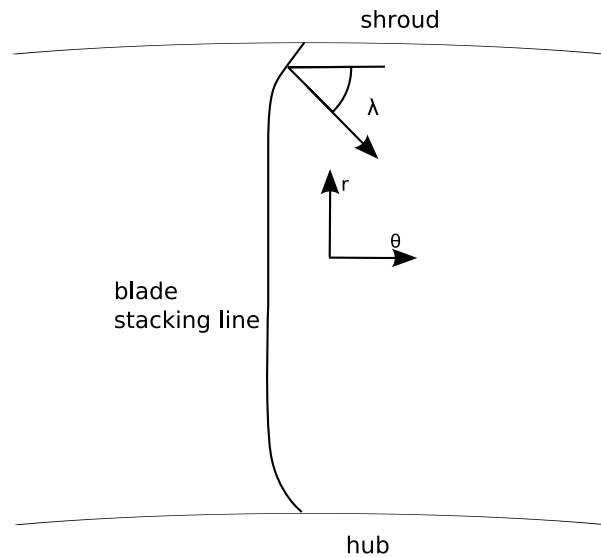


Figure 1.2: Definition of the lean angle: camber surface inclination (axial view)

Finally, an information is needed on the modulus of the blade force (or one of its component) as the previous relations give only its direction. This information is obtained either by an analysis method either by a design method. Three main options are available: analysis formulation, design formulation and analysis formulation from the circumferential momentum.

**Analysis formulation**

In the analysis approach the flow is required to follow a mean path which is given by the camber surface (plus a deviation angle taken from empirical relations). To achieve this condition, an iterative procedure is used. The modulus of the blade force is modified at each iteration by a quantity proportional to the difference between the actual flow condition and

the slip condition along the mean flow path:

$$\frac{\partial f_b}{\partial \tau} = -C \left( V_x n_x + V_r n_r + (V_\theta - \Omega r) n_\theta \right) \tag{1.14}$$

where $n_x$, $n_r$ and $n_\theta$ are the components of the vector normal to the mean flow path. $\tau$ is the pseudo time materializing the convergence process.

This equation has been given by Baralon *et al.* (1997) but for the circumferential component of the force instead of the modulus of the force. As it will be shown later, imposing the modulus of the blade force provides more robustness to the convergence process. The equation (1.14) is integrated in time together with the five conservative equations. At convergence of the whole process, the flow slips on the mean flow path. The constant $C$ allows to adjust the rate of response of the blade force to a violation of the slip condition. In practice, the condition of orthogonality of the blade force to the flow (equation 1.12) is replaced by a condition of orthogonality of the blade force to the mean flow path. At convergence the two surfaces coincide and the second method has proved to be more robust due to the non fluctuating direction of the blade force during the convergence.

### Design formulation

Another way of imposing the presence of the blades is to specify the circumferential velocity $V_\theta^{target}$ (or $rV_\theta^{target}$), i.e. a design method:

$$\frac{\partial f_b}{\partial \tau} = C \left( V_\theta^{target} - V_\theta \right) \tag{1.15}$$

This option has been used by Sturmayr and Hirsch (1999a). In the same way as the equation (1.14), the modulus of the force is modified when the actual velocity $V_\theta$ differs from the imposed value $V_\theta^{target}$. At convergence, $V_\theta = V_\theta^{target}$. The $V_\theta^{target}$ is computed as follows. From the known flow angle at the trailing edge, the circumferential velocity can be computed with the help of the actual axial velocity:

$$V_{\theta te} = V_{x te} \tan \alpha_{te} \tag{1.16}$$

The velocity at the leading edge $V_{\theta le}$ is given by the upstream flow. The circumferential velocity inside the blade passage is obtained by interpolation between $V_{\theta te}$ and $V_{\theta le}$.

### Analysis formulation from circumferential momentum

A last option, which follows again an analysis approach, is to compute the blade force from the circumferential momentum which is therefore not solved anymore in the bladed regions.

This approach has been used by Dawes (1992). This technique is also widely used in the SLC throughflow models (see for example Üçer and Shreeve (1992)). The flow angle is imposed in the bladed region and the steady circumferential momentum balance allows to calculate the circumferential blade force as:

$$r\ f_{b\theta} =\ q_m \left( \frac{\partial r V_\theta}{\partial m} \right) \tag{1.17}$$

The radial and axial components of the blade forces are found from the relations (1.13) and (1.12).

The question is to determine which is the best method for the applications studied in this work. The methods 1 and 3 are pure analysis methods and necessitate no other information than the blade geometry. On the other hand, the method 2 necessitates additional information about how the circumferential velocity evolves inside the blade passage in the streamwise direction. Sturmayr and Hirsch (1999a) have found for a transonic rotor compressor that a power law fits well the data provided from a 3-D calculation. However, the exponent of the power law they used differs with the operating point. This clearly shows the lack of generality of the method. Furthermore, it is not expected that these results are valid for other machines such as subsonic compressors or transonic turbines. Other power law exponents or laws of evolution of the circumferential velocity must be sought. The method 2 is therefore not retained.

It will be shown in chapter 2, devoted to the numerical aspects, that it is preferable from a robustness point of view to work with the magnitude of the blade force instead of its circumferential component. For this reason, the method 1 will be used and will be referred to as the analysis method in the following.

A final remark on the difference between the methods listed above is the different shock capturing properties of the analysis and the design methods. This will be the topic of the next section.

In addition to the three components of the force appearing in the momentum equations, the work done by the blades on the flow in a rotor is added to the energy equation. The second contribution of the inviscid blade force therefore takes the following form:

$$S_{b2} = \begin{bmatrix} 0 \\ f_{bx} \\ f_{br} \\ f_{b\theta} \\ f_{b\theta}\,\Omega r \end{bmatrix} \tag{1.18}$$

In the following, two aspects of the inviscid blade forces are presented. First, the shock capturing properties are reviewed. They differ in function of the formulation used to impose the presence of the blade. Secondly, the leading edge flow singularity is studied.

### 1.2.3 Shock capturing properties

One advantage of the finite volume throughflow over the streamline curvature method that is often pointed out is its ability to capture shocks and to predict the chocking mass flow. It is a well known fact that the analysis mode can capture shock waves while the design mode can not (at least for subsonic meridional Mach number). However, it seems that to the exception of Baralon *et al.* (1998) for the analysis mode and of Sturmayr and Hirsch (1999a) for both modes, the properties of the captured shock have not been carefully studied.

Indeed the design method (equation 1.15) and the analysis method (equation 1.14) exhibit distinct shock capturing properties. These different shock capturing properties can be explained by analysing the corresponding Rankine Hugoniot equations relative to the set of equations.

Let us consider a simplified case where the radial velocity and all variations in the radial direction have been neglected, i.e. some kind of meridional view of a linear cascade blade-to-blade flow. Furthermore, the blades are supposed to have no thickness and to be free of loss. This has no consequence on the generality of the demonstration.

The Rankine-Hugoniot equations for such a flow are written:

$$[\rho V_x] = 0 \tag{1.19}$$
$$\rho V_x [V_x] + [p] = f_{bx} \, \Delta x \tag{1.20}$$
$$\rho V_x [V_\theta] = f_{b\theta} \, \Delta x \tag{1.21}$$
$$\rho V_x [h^0] = \Omega r f_{b\theta} \, \Delta x \tag{1.22}$$

with $[W_\theta] = [V_\theta]$.

**Design method**

In the design method, a smooth distribution of $W_\theta$ is imposed:

$$[W_\theta] = 0 \tag{1.23}$$

The equation (1.21) therefore gives $f_{b\theta} = 0$ and the equation (1.12) gives in turn $f_{bx} = 0$. Finally, the Rankine-Hugoniot relations are:

$$[\rho V_x] = 0 \tag{1.24}$$
$$\rho V_x [V_x] + [p] = 0 \tag{1.25}$$
$$[h^0] = 0 \tag{1.26}$$

A design method is thus able to capture shock for an axial Mach number (a meridional Mach number if the radial direction is not neglected) superior to one. This corresponds to the Rankine-Hugoniot equations that would be obtained for a simple channel flow. In practice, an axial Mach number superior to one is hardly met in conventional compressors. Furthermore, the physical meaning of such a captured shock is dubious for a rotating blade, as the total enthalpy is conserved and not the rothalpy.

**Analysis method**

In the analysis method, a smooth distribution of the flow angle $\beta$ is prescribed:

$$[W_\theta] = [V_x] \tan \beta \tag{1.27}$$

The equations (1.21) and (1.12) thus give:

$$f_{b\theta} = \frac{\rho V_x [V_x] \tan \beta}{\Delta x} \tag{1.28}$$

$$f_{bx} = \frac{-\rho V_x [V_x] \tan^2 \beta}{\Delta x} \tag{1.29}$$

Injecting

$$W = \frac{V_x}{\cos \beta} \tag{1.30}$$

in the system of equations (1.19) to (1.22), one finally obtains:

$$[\rho W] = 0$$
$$\rho W [W] + [p] = 0$$
$$\left[h^0\right] - \Omega r [V_\theta] = [I] = 0$$

This corresponds to the Rankine-Hugoniot relations for a normal shock in the blade-to-blade plane. Thus, the analysis approach captures shocks for a relative Mach number superior to one. The intensity of the captured shock is equal to the intensity of a normal shock in the blade-to-plane plane for the same upstream Mach number.

The difference of the shock capturing properties for both methods is illustrated on the figures 1.3 (a) and (b). These results have been obtained on a transonic rotor. Details on the computations are given in section 3.1. The two computations have been run with exactly the same boundary conditions. The only difference lies in the way the presence of the blade is specified, either by an analysis or a design formulation. As expected, the analysis formulation captures a shock and the design one not. The loss captured by the analysis

(a) analysis formulation       (b) design formulation
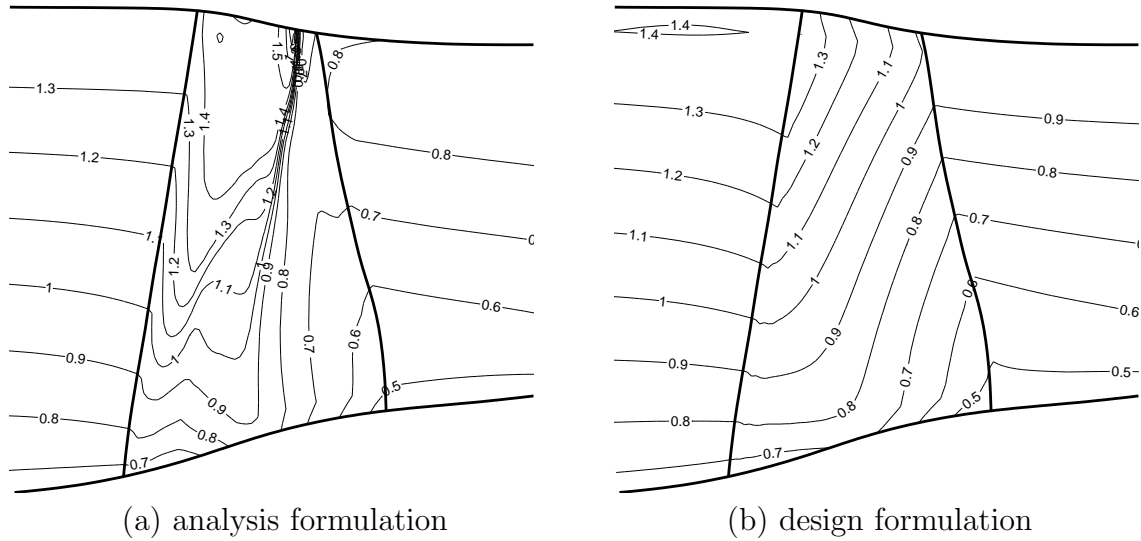
Figure 1.3: Relative Mach number isovalues: a shock is captured with the analysis formulation

method can complete or replace a shock loss model. For the design computation, a shock loss model is mandatory.

On the figure 1.3 (a), one can see that the orientation of the captured shock is not constrained to the radial direction. Its orientation is function of the geometry through the blockage and the camber distribution. It is also function of the boundary conditions.

The physical meaning of such a discontinuity in the meridional plane is questionable. The circumferential average of the real 3-D solution would not exhibit such a discontinuity unless the shock is orthogonal to the machine axis. Such an axisymmetric shock is seldom met in practice. A normal shock in the 3-D solution would then appear as smeared in the meridional plane over the distance $\Delta x$ (see figure 1.4). The shock captured by the throughflow analysis mode must therefore not be viewed as representative of the 3-D pitch averaged solution but rather as a way to model the shock losses. Further considerations on the shock capturing properties will be given in section 3.1 dedicated to the analysis of the NASA Rotor 67.

## 1.2.4 Leading edge discontinuity

By its axisymmetric nature, the throughflow model cannot predict the prerotation of the flow ahead of a blade row. If a blade row model that imposes the flow angle is used (an analysis method), a discontinuity occurs at the leading edge if the flow is not aligned with the leading edge blade camber angle. The problem can be easily illustrated by considering a single stationary blade row subject to an incoming flow for which the circumferential angle

(a) normal shock　　　　(b) axisymmetric shock
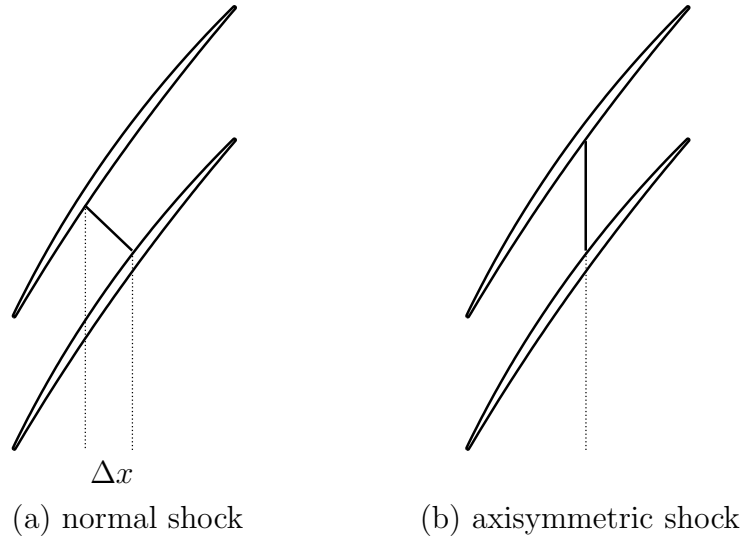
Figure 1.4: Shock orientation in the blade-to-blade plane
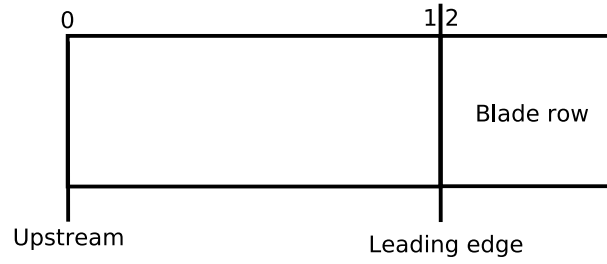


Figure 1.5: Leading edge discontinuity

is $\alpha_0$. If the radial velocity is neglected as well as the variations in the radial direction, the circumferential component of the momentum balance outside of the blade row reduces to the convection of the circumferential velocity:

$$\frac{\partial \rho V_x V_\theta}{\partial x} = 0 \tag{1.31}$$

Applying this equation to the control volume represented on the figure 1.5 (from the upstream station (station 0) to the leading edge (station 1)), the following relation for the flow angle at the station 1 is obtained:

$$\tan \alpha_1 = \frac{\rho_0 V_{x0}^2}{\rho_1 V_{x1}^2} \tan \alpha_0 \tag{1.32}$$

Thus, the flow angle just upstream of the leading edge, at station 1, is provided by the upstream flow angle $\alpha_0$. On the other hand, just downstream of the leading edge, at station 2, the flow angle is forced to be equal to the blade camber angle $\alpha_b$ by the blade row model,

i.e.:

$$\tan \alpha_2 = \tan \alpha_b \tag{1.33}$$

This results in a discontinuity at the leading edge which can lead to an unacceptable loss generation. Despite its importance, this phenomenon has received very few attention, and at the exception of Baralon *et al.* (1998), it seems that this problem has not been addressed at all. Baralon *et al.* (1998) have attributed the discontinuity problem to the sudden application of a source term in the bladed region. From the previous discussion, it is clear that this sudden application of a source term is due to the axisymmetry assumption. The methodology proposed by Baralon *et al.* (1998) for subsonic flows is adopted here. It consists in modifying the blade surface angle in the leading edge region so that it adapts to the incident flow. This modification of the mean blade camber is only performed on the first percents of the chord and the real geometry is still used to compute the parameters necessary to feed the empirical correlations. For example, the computation of the off-design losses by empirical correlations is still performed with the real incidence calculated from the original blade angles.

An illustration of the effect of the leading edge discontinuity on the loss generation is presented on figure 1.6. It compares the axial evolution of the entropy on a streamwise grid line for two computations made on a compressor stage, one with the leading edge adaptation and the other without. Both computations were run with an Euler model without entropy generation terms so that the solution for both calculations should give an isentropic evolution through the blade rows. The level of incidence on the blade profile is approximately 3 degrees for both the rotor and the stator. The computed isentropic efficiency is equal to 0.999 for the leading edge adaptation case and equal to 0.953 for the case without adaptation. This illustrates the high level of error even for the case of a relatively low level of incidence.
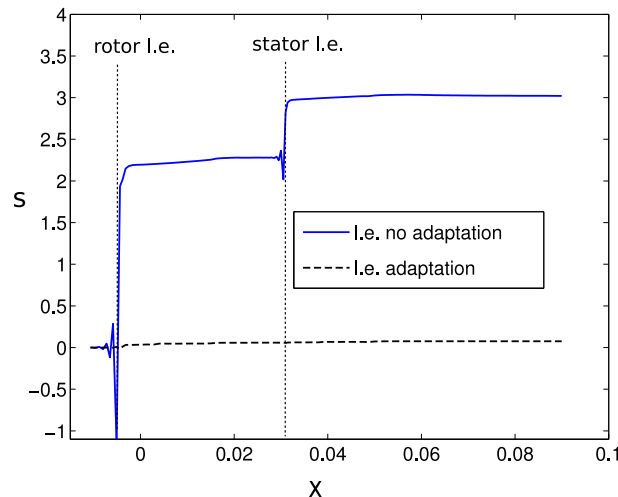


Figure 1.6: Leading edge adaptation

An objection that can be raised against this leading edge adaptation technique is that it locally modifies the aerodynamic blade loading distribution compared to the strict mean

camber surface imposition. However the assumption that the flow follows the mean camber surface in the region of the leading edge is also very questionable. The flow in that region is highly non-axisymmetric. The leading edge adaptation is felt here as an improvement toward a more physical behaviour of the blade row model. Furthermore, this modification does not modify the global blade loading.

Another cure to the leading edge discontinuity is to avoid imposing the blade angle in the forward part of the blade, over the $x_1$ first percents but rather to specify the circumferential velocity in that region, i.e. to use a design method (equation 1.15) in the forward part of the blade. The circumferential velocity at the leading edge $V_{\theta le}$ is given by the circumferential velocity just upstream of the leading edge. The circumferential velocity at the location $x_1$ is given by the actual axial velocity at this location and the blade angle. The circumferential velocity between the leading edge and the $x_1$ location is linearly interpolated. The performance of this method is similar to the previous method. However, no shock can be captured in the portion of the blade where the design method is used.

## 1.3 2-D profile losses and viscous blade forces

The circumferential averaging performed in the blade passage has thrown away the material presence of the blades which do not appear anymore as wall boundary conditions in the throughflow calculation. Their effects is however brought back by distributions of forces. As the deflection of the flow has been modelled by an inviscid blade force distribution, the loss generation inside the blade passage is modelled by a distribution of viscous forces. This loss generation is due to the shear stresses acting on the blade walls as well as the circumferential stresses. In the present throughflow model, this contribution is neglected but its effect is nevertheless included in the empirical relations together with the effect of the wall shear stresses. In chapters 4 and 5, throughflow computations including the circumferential stresses will be proposed.

### 1.3.1 Distributed loss model

The losses are introduced in the Euler/Navier-Stokes equations by the distributed loss model (see for example Horlock (1971), Bosman and Marsh (1974) or Hirsch (1988)). The purpose of this model is to prescribe consistently some losses in an inviscid computation. This is achieved by introducing a distribution of friction forces per unit volume $\vec{f_v}$ in the momentum equation. These forces are aligned with the flow but point in the opposite direction. Furthermore, these forces do not contribute to the relative energy equation (expressed in the reference frame of the blade under consideration). It results that the work performed by this force is only meant to produce entropy. The equation of the entropy change is given by

the following expression:

$$\rho T \frac{ds}{dt} = -\vec{W} \, \vec{f_v} \tag{1.34}$$

where $W$ is the velocity in the reference frame under consideration. Reverting this equation, a relation can be obtained which provides the modulus of the force related to a prescribed entropy gradient $\partial_m s$ along a streamline:

$$f_v = \rho T \frac{W_m \partial_m s}{W} \tag{1.35}$$

The entropy gradient $\partial_m s$ is computed from the entropy increase along a streamline across the blade row $\Delta s_m$ and the length of the streamline $l_m$ (calculated from inlet to outlet of the blade row) :

$$\partial_m s = \frac{\Delta s_m}{l_m} \tag{1.36}$$

Strictly speaking, the relation (1.35) is only valid for the Euler equations as the underlying hypothesis of the distributed loss model is the absence of shear stresses (and its modelling by the distributed friction forces). In the region of high gradients captured by the Navier-Stokes equations, near the annulus endwalls, this relation is not correct and does not introduce the exact intended entropy rise $\Delta s_m$. Nevertheless, it is still used as a coarse approximation in that region. Indeed, the regions where this approximation is the most questionable is also the region where the relative contribution of $\Delta s_m$ to the global entropy production is the lowest.

Finally, with the addition of the work done by the friction forces in a rotor, the source term $S_{bv}$ takes the following form:

$$S_{bv} = \begin{bmatrix} 0 \\ f_{vx} \\ f_{vr} \\ f_{v\theta} \\ f_{v\theta} \, \Omega r \end{bmatrix} \tag{1.37}$$

## 1.3.2   2-D profile losses

The so-called 2-D losses are briefly discussed in this section. They are thought to be generated by an hypothetical 2-D flow in the blade-to-blade plane. The 3-D losses, resulting from the interaction of the blades and the annulus endwall will be addressed later in this chapter. The focus is put here on the loss generation inside compressors blades only. The losses comprise the profile loss measured by a loss coefficient $\varpi$ and the deviation angle $\delta$, even

though, strictly speaking, the latter is not a loss generating phenomenon. The deviation is equal to the difference between the flow angle and the blade angle at the outlet of the blade row $\beta_2'$. This is a particularly important phenomenon to be modelled, not only because it determines the work done by the compressor but also because it acts as a blockage term. A bad estimation of it leads to the wrong mass flow. This is easily shown by considering an inviscid flow in an axial rotor (no radial shift) and considering a fixed outlet static pressure. In the relative frame of reference, the following relation holds:

$$\frac{p_{2rel}^0}{p_2} = \left(1 + \frac{\gamma - 1}{2} M_{2x}^2 \left(1 + \tan^2\left(\beta_2' + \delta\right)\right)\right)^{\frac{\gamma}{\gamma - 1}} \tag{1.38}$$

As the ratio $p_{2rel}^0/p_2$ is fixed, an increase in $\delta$ will in general results in a decrease of the axial Mach number and from there a decrease of the mass flow.

In the present work, the profile losses and the deviation angles are computed by empirical correlations. These correlations are generally expressed in the form of a design or reference value plus an off-design contribution. This off-design contribution is generally computed in function of the difference between the actual incidence $i$ and a reference incidence $i_{\text{ref}}$, the latter being also obtained through empirical correlations. For example, a quadratic law for the evolution of the off-design contribution with the incidence is often used for the profile loss coefficient:

$$\varpi = \varpi_{\text{ref}} + C\left(i - i_{\text{ref}}\right)^2 \tag{1.39}$$

The reference values are function of the geometry of the blade, the Reynolds number, the inlet Mach number, etc.

In the present work, the Carter rule's (Carter, 1950) is used for the on-design part of the deviation angle and the correlation of Creveling (1968) for the off-design part. The well-known correlation of Koch and Smith (1976) is used for the on-design part of the loss coefficient and the correlation of Creveling (1968) is added for the off-design part. The reference incidence is taken from the NASA-SP 36. The choice of these correlations is inspired from the review of Çetin *et al.* (1987). The modification of the reference incidence that they proposed has not been implemented here because it results in a too high reference incidence leading to a too high loss coefficient. This has also been observed by Boyer and O'Brien (2002).

These well known correlations work quite well for classical families of blade profiles such as C4 or NACA-65 families. They have been found to be quite reliable for subsonic compressors studied in the present work. However, the geometry of modern compressors or turbines generally do not belong anymore to a standard family of profiles. They are made of custom-tailored blade profiles. In that case, the above correlations will certainly fail. The performances of these modern profiles, in terms of loss coefficients and deviation angles, are generally available to the manufacturers but this information remains proprietary.

On the other hand, recent works in the field of the blade-to-blade correlations may help to overcome the lack of information for modern profiles. König *et al.* (1996) have proposed improvements of existing profile loss correlations based on a large database of modern blade profiles. They also proposed to base the calculation of the deviation on a singularity method. Another interesting method to obtain correlations for an arbitrary family of profile is the method proposed by Pfitzinger and Reiss (1997). They computed the loss coefficient and the deviation angle with a blade-to-blade code for several values of the geometrical and aerodynamic parameters such as the stagger or the incidence. The resulting database is next used to feed the throughflow computation instead of the empirical correlations. These two methods have however not been implemented here.

## 1.4 Radial mixing

Radial mixing or spanwise mixing can be emphasised from the analysis of the measurements obtained from a multistage compressor. The losses extracted from the total pressure and temperature with the help of an (inviscid) throughflow model may exhibit a strange behaviour: the losses close to the endwall may seem unreasonably low while the midspan losses may seem unreasonably high. This is due to the phenomenon of radial mixing that redistributes radially the losses and the energy inside a turbomachine

According to Cumpsty (1989), this spreading phenomenon is responsible for the emphasis put on minimising the profile loss, even though this is not a great part of the total losses. The spanwise mixing also explains why the loss pattern does not accentuate as one progress through a compressor and why some sort of repeating pattern is observed: some process redistributes the flow properties across the span. The figure 1.7 illustrates this by comparing the results of two computations including or not a radial mixing model with the experimental results. The comparison is performed on a 3-stage compressor.

Two explanations were first proposed for explaining the phenomenon of radial mixing. Adkins and Smith (1982) attribute the mixing to a convective effect due to spanwise velocity while Gallimore and Cumpsty (1986) propose an explanation based on the turbulent diffusion. Both approaches succeed in predicting the radial mixing in several compressors. A debate arose from that observation that two different models were able to catch the radial mixing phenomenon. It was finally recognised that both effects contribute to the radial mixing (Wennerstrom, 1991). Since then, several variants appeared, some including only the turbulent diffusion effect (Üçer and Shreeve, 1992), some including both effects (De Ruyck *et al.* (1989) for the compressor field and Lewis (1993) for the turbine field).

On the subject of which model is the more adequate, Denton and Dawes (1999) made the following remark: "Any theoretical modelling of mixing is so oversimplified that it is preferable and simpler to include an empirical rate of exchange of mass, enthalpy, angular
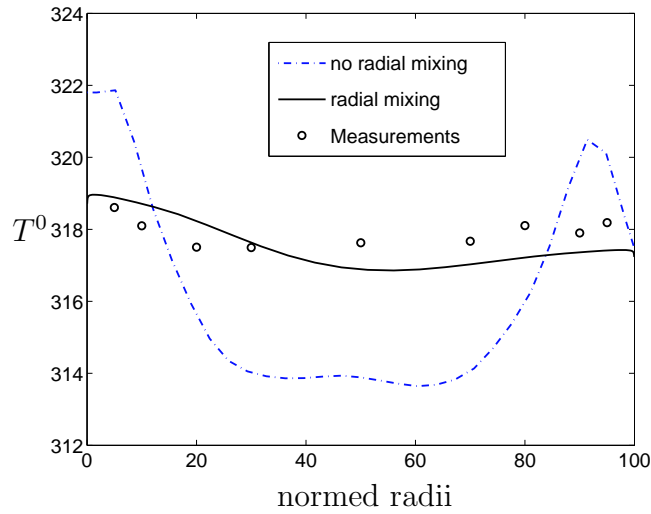
Figure 1.7: Radial distribution of total temperature at the outlet of a three-stage compressor: comparison of computations with and without a radial mixing model

momentum an entropy between streamlines.". We agree with this observation and this is why we chose the model of Gallimore and Cumpsty (1986). This model finally results in specifying a certain level of mixing which is constant over the span and through the compressor. Furthermore, it has been shown by Gallimore (1986) that the resulting flow field is relatively independent of the exact level of the mixing. A variation of an order of two or three in the level of mixing didn't deteriorate significantly the quality of the solution he obtained. This is also the reason why Gallimore and Cumpsty (1986) chose to ignore the spanwise variation of the mixing coefficient.

The radial mixing is introduced in the present throughflow model by the shear stresses and the heat fluxes appearing in the Navier-Stokes throughflow. The details of the implementation is presented in section 1.5.1. For an inviscid model including a spanwise mixing computation, the shear stresses and the heat fluxes are added to the Euler equations. The boundary conditions however stay the inviscid ones, i.e slip at wall, no shear stresses and no heat fluxes through the endwalls. As explained above, the model of Gallimore is based on the assumption that the level of mixing, and from there the level of the turbulent viscosity, is constant over the span. The level of mixing that must be specified according to the Gallimore relation is sometimes very high and leads to turbulent viscosity of the order of 1000 times the kinematic viscosity. In such a case, if all of the components of the viscous stresses are kept, large and unphysical losses are generated close to the blade edges or even inside the blade rows due to the streamwise gradients of the mean flow quantities. When such a problem occurs, only the radial derivatives are kept.

The radial mixing, as presented above, may seem to be an extra physical phenomenon that must be included in the model on the top of the fluid mechanics equations. Historically, it has been introduced in the inviscid SLC throughflow methods to allow mixing between

streamlines. This is needed because of the assumptions made for deriving the SLC model. In particular, the assumptions of an inviscid, axisymmetric and steady flow remove the physics generating the radial mixing.

In chapter 4, a throughflow model based on the averaged unsteady 3-D Navier-Stokes equations will presented. The equations of that model exhibit some stresses, analogous to the Reynolds stresses but that bring the effect of the non-axisymmetry of the flow and of its unsteadiness. This more elaborated model do not necessitate the inclusion of a radial mixing model. With that kind of model in mind, one can view the radial mixing model of Gallimore and Cumpsty (1986) as a way of closing the stresses (both the circumferential and the deterministic ones) by a Boussinesq hypothesis.

## 1.5 Endwall flow losses

The flow developing along the annulus endwalls represents certainly the more complex part of the flow inside a compressor and it is also the less well understood part. Several specific phenomena take place in that region such as the tip leakage flow or the passage vortex. This region is also responsible for the generation of several secondary flow phenomena illustrated on figure 1.8.
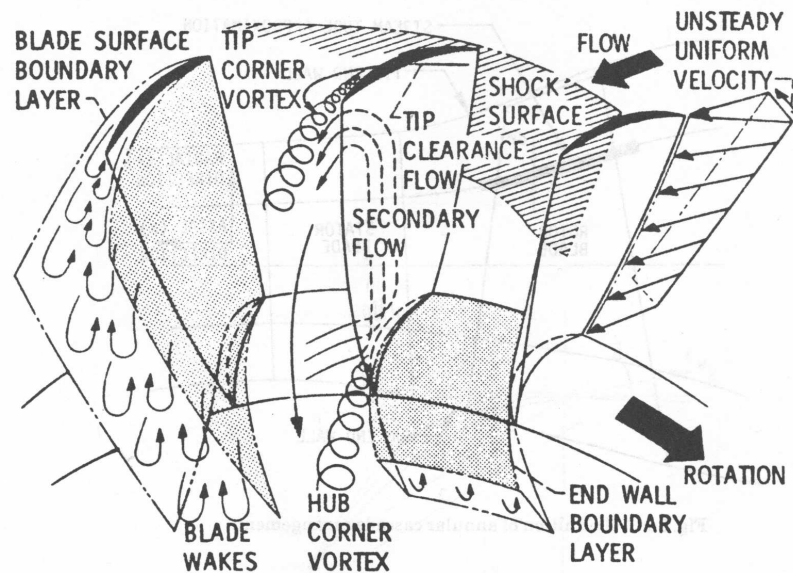


Figure 1.8: Three-dimensional losses pattern

The most widespread method to account for the endwall flows in a throughflow approach is to use a separate boundary layer calculation, coupled or not to a secondary flow model,

while the core flow is computed by the inviscid streamline curvature method (see for example De Ruyck *et al.* (1989), Dunham (1995) or Horlock and Perkins (1974) for a review on the boundary layer methods).

That kind of method presents several deficiencies. Cumpsty (1989) clearly exposes why such methods should not be expected to work well for the annulus endwalls of a compressor. Among others, the fact that the boundary layer theory has been devised for the external aerodynamics for which the flow is well behaved is probably one of the most important points. Another reason is that there is not always a clear separation between the boundary layer and the core flow.

In the present contribution, the endwall losses are somewhat arbitrary divided into two parts. The first part is the 2-D endwall losses resulting from the development of the flow on the hub and the shroud. These losses are similar to the losses due to a flow developing in a channel and they are captured by the Navier-Stokes equations. The second part of the endwall losses is the so-called 3-D loss resulting from the interaction of the blades with the endwalls. This part is not captured by an axisymmetric model and must therefore be modelled.

### 1.5.1 Two-dimensional hub-to-tip endwall losses

For the viscous terms present in the Navier-Stokes equations, the main modelling task consists in choosing a turbulence model. The algebraic model of Baldwin and Lomax (1978) has been selected here for its rapidity and its robustness. It is a two layer model:

$$\mu_t = \begin{cases} \mu_{tin} & \text{if} \quad y \leq y_{lim} \\ \mu_{tout} & \text{if} \quad y \geq y_{lim} \end{cases} \tag{1.40}$$

The switch between the inner and outer layers is made when the distance from the wall $y$ is equal $y_{lim}$, which is the lowest value of $y$ for which $\mu_{tout}$ is greater than $\mu_{tin}$.

**Inner layer**

The inner layer is computed from the Prandtl mixing length hypothesis:

$$\mu_{tin} = \rho l^2 \left| \vec{\Omega} \right| \tag{1.41}$$

For an axisymmetric flow, the modulus of the vorticity is given by:

$$\left| \vec{\Omega} \right| = \sqrt{\left( \frac{\partial V_x}{\partial r} - \frac{\partial V_r}{\partial x} \right)^2 + \frac{\partial V_\theta}{\partial x}^2 + \left( \frac{\partial V_\theta}{\partial r} + \frac{V_\theta}{r} \right)^2} \tag{1.42}$$

The mixing length $l$ is supposed to grow linearly with the distance from the wall $y$, proportionally to the von Karman constant $\kappa$ and weighted by the Van Driest damping function:

$$l = \kappa y \left( 1 - e^{\frac{y^+}{A^+}} \right) \qquad (1.43)$$

**Outer layer**

The outer viscosity is given by the following relation:

$$\mu_{tout} = \rho \, \alpha \, C_{cp} \, F_{wake} \, F_{Kleb}(y) \qquad (1.44)$$

where

$$F_{wake} = \min \left( y_{max} F_{max}, \, C_{wk} \, y_{max} \, \frac{V_{max}^2}{F_{max}} \right) \qquad (1.45)$$

The distance $y_{max}$ is the distance for which the momentum of the vorticity (weighted by the Van Driest damping function)

$$F(y) = y \left| \vec{\Omega} \right| \left( 1 - e^{\frac{y^+}{A^+}} \right) \qquad (1.46)$$

is maximum. In practice, the profile is scanned in the direction normal to the wall, and the previous function is computed at each node. The maximum value is obtained by a quadratic fit as recommended by Baldwin and Lomax (1978). The quantity $V_{max}$ is equal to the maximum of the velocity in the profile for the cases treated in this work, which correspond to channel flows. The intermittency factor $F_{Kleb}$ is given by:

$$F_{Kleb}(y) = \left[ 1 + 5.5 \left( \frac{y \, C_{Kleb}}{y_{max}} \right)^6 \right]^{-1} \qquad (1.47)$$

The constants appearing in the Baldwin-Lomax model are given in the table 1.1.

| $A^+$ | $C_{cp}$ | $C_{Kleb}$ | $C_{wk}$ | $\kappa$ | $\alpha$ |
|-------|----------|------------|----------|----------|----------|
| 26 | 1.6 | 0.3 | 0.25 | 0.41 | 0.00168 |

Table 1.1: Baldwin-Lomax model constants

The Baldwin-Lomax model has been used as it is for the throughflow computations based on 3-D simulation that will be presented in chapter 5. It has also been used as it is for the

Navier-Stokes computation without radial mixing model. However, when a radial mixing model is introduced, the turbulent viscosity computed by the Baldwin-Lomax model close to the endwall has to be connected to the value of the viscosity computed from the radial mixing model in the core flow region. Indeed, it is not possible to use the Gallimore viscosity close to the endwalls in the Navier-Stokes computations. Such a high viscosity associated with the large gradients of the variables would lead to very high viscous shear stresses and would result in a non physical solution, provided that the calculation did converge. The solution adopted here is to use the inner layer of the Baldwin-Lomax and to let the viscosity grow until it reaches the value prescribed by the relation of Gallimore.

## 1.5.2 Three-dimensional endwall losses

### 1.5.2.1 Empirical correlations of Roberts

Two-dimensional correlations are used to estimate the profile losses and the deviation angle over the full span. Additional modelling is required to introduce the effects of the three-dimensional flows, such as the tip clearance flow or the passage vortex. These phenomena arise from the interaction between the blades and the annulus walls and cannot be captured under the axisymmetry assumption.

In the present model the experimental correlations from Roberts *et al.* (1986, 1988) have been implemented to introduce these 3-D effects. They provide the additional deviation and loss coefficient that must be added to the 2-D distributions. The figure 1.9 gives the 3-D correlations shape for a rotor. One can observe the classical evolution of the deviation with an overturning at the hub and an overturning followed by an underturning at the tip. The loss coefficient also presents the classical shape at both endwalls.

In the case of Navier-Stokes computations, one can wonder whether the empirical correlations of Roberts take into account the endwall losses which are already captured by the axisymmetric Navier-Stokes model. From Roberts *et al.* (1988) it seems that the measurements used by Roberts to generate the correlations were generally not performed close to the endwalls (the first measurement point is at about 5 % of the blade height). Therefore this correlation cannot incorporate entirely the losses along the endwalls. Furthermore the shear stresses and the heat fluxes resulting from the development of the flow along the endwalls and captured by the viscous model dominate the loss production near the annulus wall.

This is illustrated on the figure 1.10 representing the loss coefficient for a rotor of a single stage compressor. The dotted line represents the losses predicted by the 2-D and 3-D correlations implemented in an inviscid model. The dash-dotted line represents the losses captured by the viscous model alone. The full line represents the losses due to the combination of the abovementioned correlations and the captured viscous stresses. These considerations led us to superimpose the 3-D losses predicted by the correlation of Roberts *et al.* (1986, 1988) to

(b) loss coefficient       (b) deviation
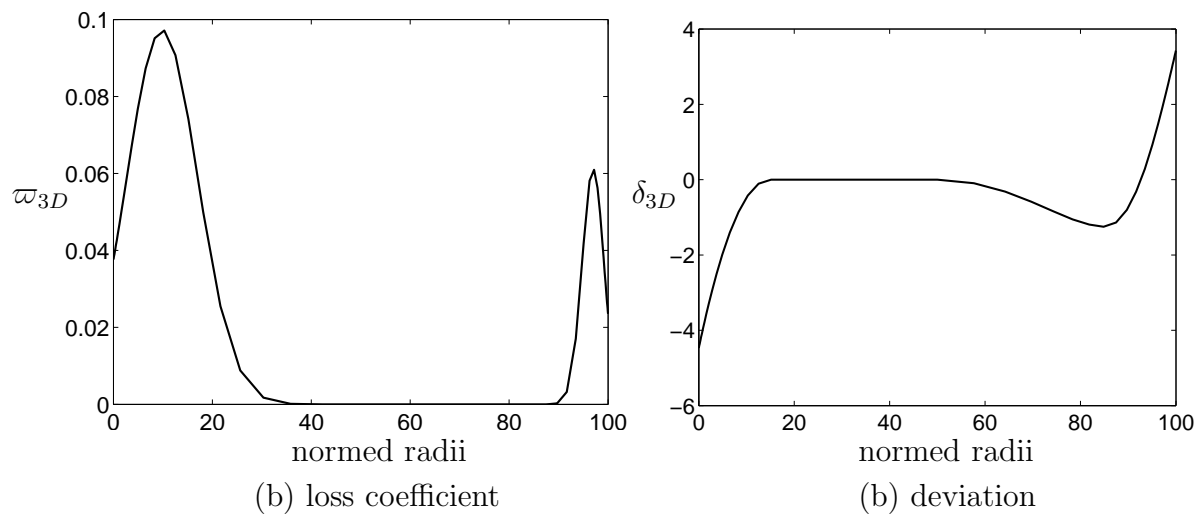
Figure 1.9: Three-dimensional correlations of Roberts

the losses captured by the Navier-Stokes model. However, it is acknowledged that a better way of specifying the 3-D losses is welcome.
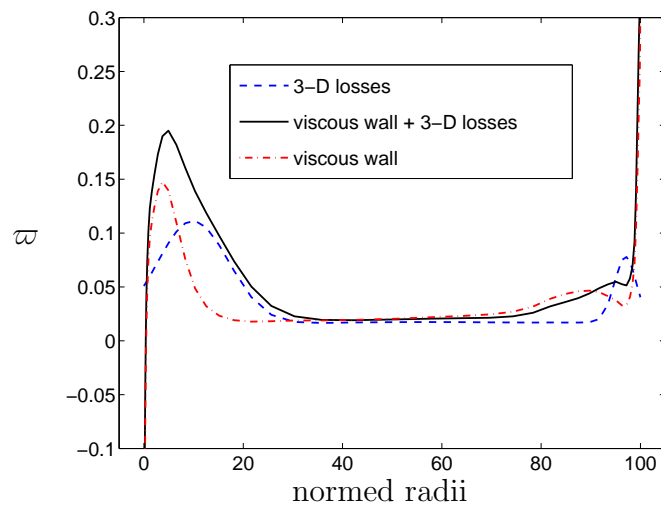


Figure 1.10: Comparison of the imposed losses and the computed ones

In a rotating blade row, due the high energy transferred to the flow by the blades, large temperature gradients occur, giving large heat fluxes toward the core flow. This cooling effect can lead to the diminution of the entropy along a streamline and explains the negative loss coefficient on the figure 1.10.

### 1.5.2.2 Blade force modification

The previous method lacks of generality due to the empiricism embedded in the correlations. An improved method for capturing the 3-D flows is proposed here. It is inspired from the work of Gallimore (1997). In the frame of its viscous SLC method, Gallimore has proposed to modify the blade force (its circumferential component more exactly) in the endwall regions. The modification he proposed for the blade force is based on experimental observations of the blade wall static pressure field, noteworthy the observations of Dring (1993). These results show that the circumferential component of the blade force varies smoothly across the span and does not exhibit rapid changes as one approaches the endwalls contrary to the circumferential momentum change across the blade row (see figure 1.11 from Dring (1993)). This is an illustration of the well known fact that the pressure field does not vary much across a boundary layer in the direction orthogonal to the wall.
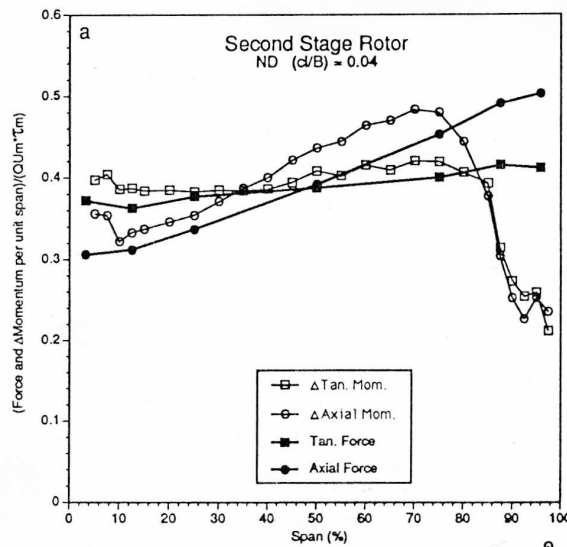


Figure 1.11: Radial distributions of the measured blade force and momentum change across a rotor (axial and circumferential (tangential)) from Dring (1993)

From that observation it seems possible to extrapolate some information across the span to compute the blade force in the endwall regions. A simple model for the evolution of the circumferential blade force in the endwall region has been developed here. For a rotor row, the following model is applied:

- for the hub flow, the circumferential component of the blade force is kept constant over a given portion of the span starting from the hub,

- for the tip flow, the blade force is set to zero in the gap. The blade force is also kept constant from a given spanwise position to the tip gap. It was found that this last

modification is necessary in order to obtain the correct level of underturning in the tip region. It is in agreement with the experimental observations of Gallimore (1997) and Dring (1993).

This is a rather simple model and more elaborated predictions of the evolution of the blade force inside the boundary layer can be devised (see the model of Gallimore (1997) for example). The purpose here is to evaluate the benefit that such a method could bring on the 3-D losses prediction (loss and deviation).

In the regions where the inviscid blade force is modified, the flow does not follow anymore the camber surface. In order to avoid the generation of numerical losses, it is important that the blade force stays orthogonal to the flow (see section 1.2). For this reason, it is not possible to work directly on the modulus of the blade force. To avoid imposing a constrain on the modulus of the force, the modification is performed on its circumferential component. The other components are computed so that the resulting blade force remains orthogonal to the flow field.

The modification of the blade force is tested hereafter on a rotor representative of a modern highly loaded low pressure compressor. It is the first rotor of a three-stage compressor developed by Techspace Aero. The flow path is shown on the figure 1.12 together with the mesh used in the present study. Results of 3-D Navier-Stokes simulations on that rotor are also available from Techspace Aero. The comparison of the throughflow results obtained together with the 3-D Navier-Stokes solution is given hereafter. More information on the study can be found in Nicks (2006).
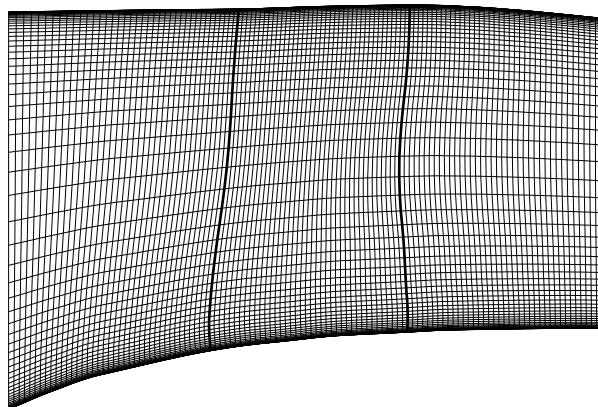


Figure 1.12: Mesh for the Techspace Aero rotor

The modification of the blade force has been performed over about 15 % of the span. This extent has been chosen more or less arbitrarily in order to influence the flow field over the correct fraction of the span. This extent could be determined automatically with a criterion based on the boundary layer thickness for example. The figures 1.13 and 1.14

present the results obtained in terms of deviation and loss coefficient. For both quantities, two calculations are presented: one with the blade force modification (TF NS 3-D) and the other without (TF NS 2-D). These two calculations are compared with the 3-D Navier-Stokes solution which represents the reference solution.

The figure 1.13 (a) shows the deviation at the hub. Thanks to the constant blade force through the boundary layer, the overturning is predicted in both location and magnitude. At the tip, the underturning is also predicted but with less precision. It is globally under-estimated except very close to the tip gap. A way to improve the situation would be to decrease the blade force in that region instead of keeping it constant. This is in agreement with the experimental results of Storer and Cumpsty (1991). The improvement brought by the modification of the blade force compared to the 2-D solution is clearly demonstrated.



(a) deviation at hub                     (b) deviation at tip
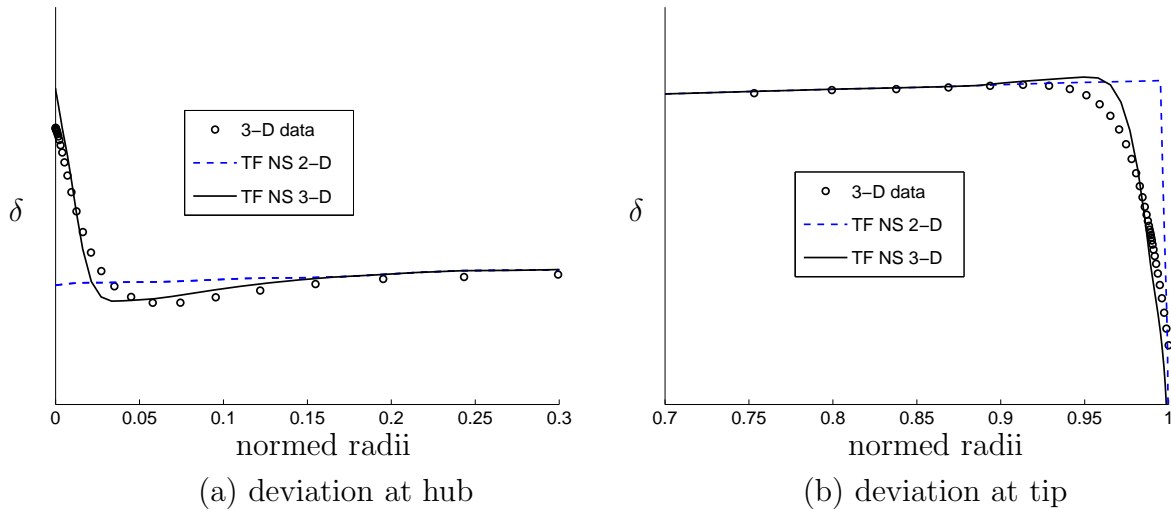
Figure 1.13: Impact on the deviation of the blade force modifications in the endwall regions

Concerning the loss coefficient, the blade force modification has only a very slight effect on the flow development at the hub (figure 1.14 (a)). Indeed the proposed modification of the inviscid blade force does not model the loss generated by the interaction of the blade and the annulus endwall. For the tip region (figure 1.14 (b)), the situation is different, removing the blade force in the tip gap induces some friction forces at the tip of the blade. The resulting loss coefficient is more similar to the one obtained by the 3-D Navier-Stokes simulation but with a lower intensity: some flow features such as the loss generated by the tip vortex flow is not modelled in the throughflow.

In conclusion, the 3-D deviation is relatively well predicted by the blade force modification model. This is not the case for the 3-D losses as the mechanisms that generate those losses is not modelled (at the exception of some parts for the tip region). A way to model these losses is to rely on the characteristics of the captured 3-D deviation. Indeed, as it is (at least partly) the same phenomena that are responsible for the generation of the 3-D losses and the 3-D deviation, it should be possible to determine the 3-D loss coefficient from the
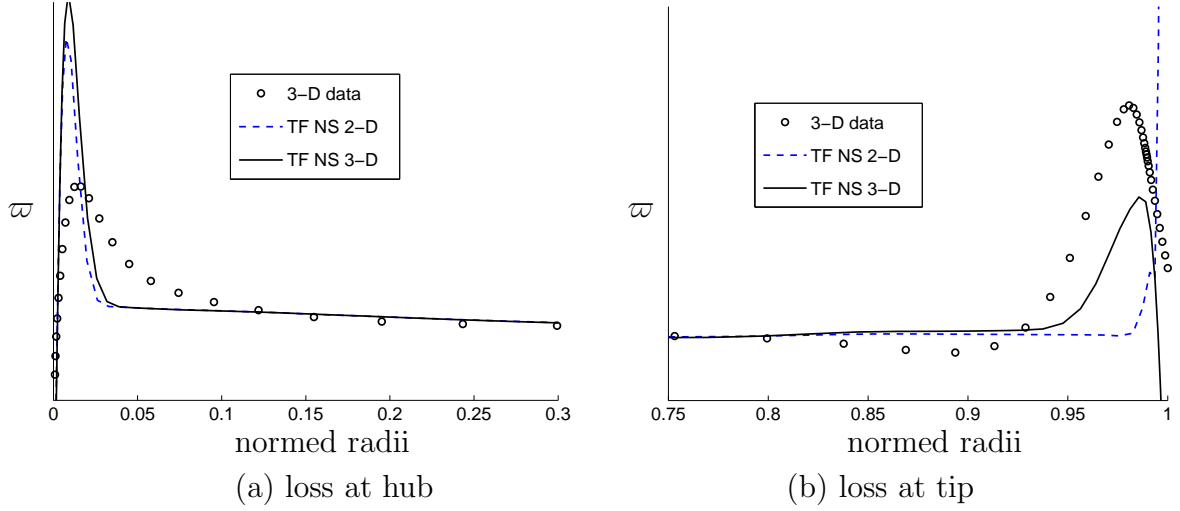
Figure 1.14: Impact on the loss coefficient of the blade force modifications in the endwall regions

captured 3-D deviation. For example, the maximum underturning at the tip is probably well correlated with the maximum loss coefficient in the same region. This is also true for the spanwise extent of the 3-D deviation and losses effects. A starting point to obtained such a 3-D loss correlation would be to use the 3-D correlations of Roberts *et al.* (1986, 1988). This however has not been done in the present work and thus the blade force modification has not been used in calculations presented in chapter 3. The model used for calculating the 3-D losses is the empirical model of Roberts presented in the section 1.5.2.1.

## 1.6 Final set of equations

With all the terms of the equation (1.6) modelled and made explicit, the final form of the set of equations that defines the present throughflow model is:

$$\frac{\partial U}{\partial t} + \frac{\partial b\left(F - F_v\right)}{\partial x} + \frac{\partial b\left(G - G_v\right)}{\partial r} = b\left(S + S_v\right) + b\left(S_{b1} + S_{b2} + S_{bv}\right) \tag{1.48}$$

with

$$U = \begin{bmatrix} b\rho & b\rho V_x & b\rho V_r & b\rho V_\theta & b\rho E \end{bmatrix}^T$$

$$F = \begin{bmatrix} \rho V_x \\ \rho V_x V_x + p \\ \rho V_x V_r \\ \rho V_x V_\theta \\ \rho V_x H \end{bmatrix} \qquad G = \begin{bmatrix} \rho V_r \\ \rho V_r V_x \\ \rho V_r V_r + p \\ \rho V_r V_\theta \\ \rho V_r H \end{bmatrix} \qquad S = \frac{1}{r} \begin{bmatrix} -\rho V_r \\ -\rho V_r V_x \\ \rho V_\theta V_\theta - \rho V_r V_r \\ -2\rho V_r V_\theta \\ -\rho V_r H \end{bmatrix}$$

$$
F_v = \begin{bmatrix} 0 \\ \tau_{xx} \\ \tau_{xr} \\ \tau_{x\theta} \\ \tau_{xj} V_j - q_x \end{bmatrix} \qquad
G_v = \begin{bmatrix} 0 \\ \tau_{xr} \\ \tau_{rr} \\ \tau_{r\theta} \\ \tau_{rj} V_j - q_r \end{bmatrix} \qquad
S_v = \frac{1}{r} \begin{bmatrix} 0 \\ \tau_{xr} \\ \tau_{rr} - \tau_{\theta\theta} \\ 2\tau_{r\theta} \\ \tau_{rj} V_j - q_r \end{bmatrix}
$$

$$
S_{b1} = \begin{bmatrix} 0 \\ \dfrac{p}{b}\dfrac{\partial b}{\partial x} \\ \dfrac{p}{b}\dfrac{\partial b}{\partial r} \\ 0 \\ 0 \end{bmatrix} \qquad
S_{b2} = \begin{bmatrix} 0 \\ f_{bx} \\ f_{br} \\ f_{b\theta} \\ f_{b\theta}\,\Omega r \end{bmatrix} \qquad
S_{bv} = \begin{bmatrix} 0 \\ f_{vx} \\ f_{vr} \\ f_{v\theta} \\ f_{v\theta}\,\Omega r \end{bmatrix}
$$

## 1.7   3-D blade effects

The use of 3-D blade design in turbomachines is recognised as a way to improve their performances. There is no doubt that 3-D (multistage) viscous calculations can handle such 3-D effects. This is more questionable for the throughflow models. Some effects cannot be captured by them and only be modelled very crudely but others can be quite accurately represented. As the throughflow is a preliminary design tool that will provide a first guess of geometry, it is important to know which effect it can handle and which it can not. According to Gallimore *et al.* (2002), simple models are incorporated into throughflow methods in the industry to adapt throughflow model to 3-D blade shapes.

In the following, some of these so-called 3-D effects are discussed as well as their modelisation inside a throughflow model based on the Euler/Navier-Stokes equations. These so-called 3-D effects are the sweep, the localised blade twist and the lean. The term lean will be used here for the displacement of the stacking axis away from the radial direction. This feature is often found in the literature as bow (compound lean) and dihedral. Some interesting discussions on the effect of the bow can be found in Weingold *et al.* (1997) while the effects of dihedral and sweep are discussed in Sasaki and Breugelmans (1998) or Roy *et al.* (2002). Denton and Xu (1999) presented an insightful contribution on the exploitation of three-dimensional flow effects in turbomachinery design. The following discussion of the different 3-D phenomena is greatly inspired from this reference.

### 1.7.1   Sweep

The sweep is defined as the inclination of the leading or trailing edge with respect to the incident flow (see figure 1.15). For subsonic flow, it can be used to reduce the leading edge

loading. An important effect of the sweep is the reduction of the shock losses for transonic compressors or fans. Indeed, the shock losses are proportional to the component of the Mach number normal to the shock front. For a swept blade, the shock is also swept in the meridional plane. As a result, for a given incident Mach number, the component normal to the shock front will be lowered if the shock is swept with the same consequence for the shock losses. Wadia *et al.* (1997) have reported efficiency improvements with forward sweep for several transonic compressor.
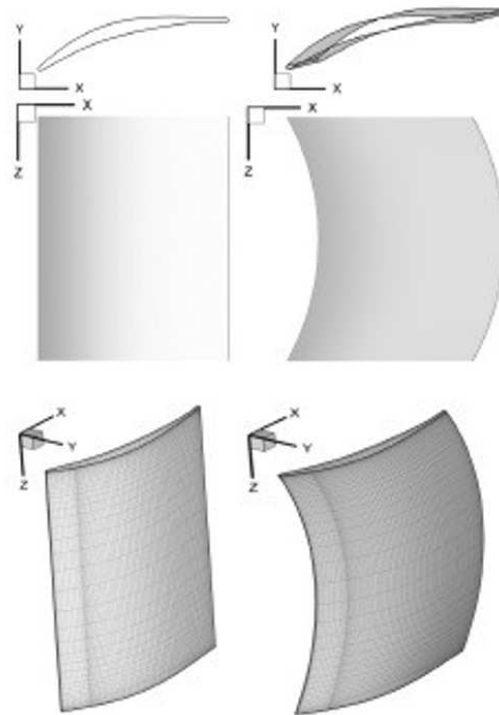


Figure 1.15: Swept blade from Rábai *et al.* (2007)

The SLC throughflow or Euler/Navier-Stokes throughflows based on a design formulation for the blade force have no shock capturing property and rely on shock loss correlations. It is not expected that such models are able to predict the shock orientation and the loss reduction associated with the sweep. On the other hand, Euler/Navier-Stokes throughflows based on the analysis formulation have shock capturing properties. The orientation of the shock is free and imposed by the boundary conditions and the blade geometry only, i.e the camber distribution as well as the blockage distribution. The figure 1.3 (a) illustrates the free orientation of the capture shock. The reduction of the shock loss brought by the sweep can therefore be theoretically considered as a result of the orientation of the captured front shock. However it is true that the shock loss captured by the throughflow is not necessary the correct one, i.e. the one that would be obtained with a 3-D code.

## 1.7.2 Localized blade twist

The localized blade twist, also known as end-bends, consists in twisting the blade in the region of the endwalls over a radial distance which is short in comparison to the blade chord. The purpose is to reduce the high incidences in the endwalls regions by aligning the blade with the flow. These high incidences are provoked by the lower axial velocity close to the endwall in conjunction with the change of reference frame between rotor and stator and the secondary flow effects from the upstream row. By aligning the leading edge to the flow, the suction surface deceleration is reduced and the blade suction boundary layer is less susceptible to separate.

With the Navier-Stokes throughflow solver, the high incidence can be predicted in the endwalls regions. This is shown on the figure 1.16 which compares the incidence relative to a stator placed behind a rotor and computed by both Navier-Stokes and "classical" Euler computations. The Navier-Stokes computation succeeds in predicting the high incidence due to the change in the reference frame combined to the lower axial velocity close to the endwall.
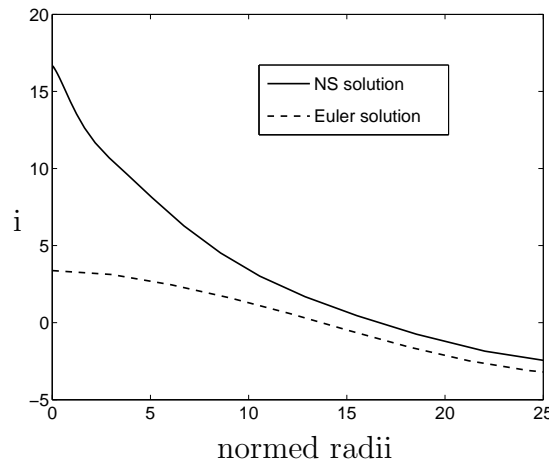


Figure 1.16: Comparison of the incidence on a stator row for Navier-Stokes and Euler computations

However, to be useful, this information on the incidence must be complemented by a model or an empirical relation giving the losses in the endwall region in function of the incidence. Indeed, the 2-D blade-to-blade empirical relations, that have been described in a previous section, are not valid in the endwall regions where the flow is far from being two-dimensional. As presented above, in the present contribution, the 3-D empirical correlations of Roberts *et al.* (1988) are used in the endwall regions. They bring the effect of the interaction of the blades and the endwalls. To the knowledge of the author, it is the sole 3-D empirical correlation for compressors available in the open literature. However these 3-D correlations do not take into account the incidence on the blade profile. This means that they will not feel the reduction of incidence associated with the localised blade twist. Unless a specific

correlation giving the losses in the endwall regions in function of the incidence or the loading is developed, the phenomenon could not be taken into account. Nevertheless, the information on the incidence that is given by the Navier-Stokes throughflow is a valuable information in the strategy of reducing the incidence in the endwall region, as its increase close to the endwall is predicted.

### 1.7.3 Lean

Leaning a blade is one of the most powerful 3-D effects. It consists in giving to the blade a non-radial stacking axis. The figure 1.2 representing the leaning of the stacking axis of a blade in a plane orthogonal to the rotation axis illustrates the definition used for the lean angle. An illustration of the blade lean is given on the figure 1.17.
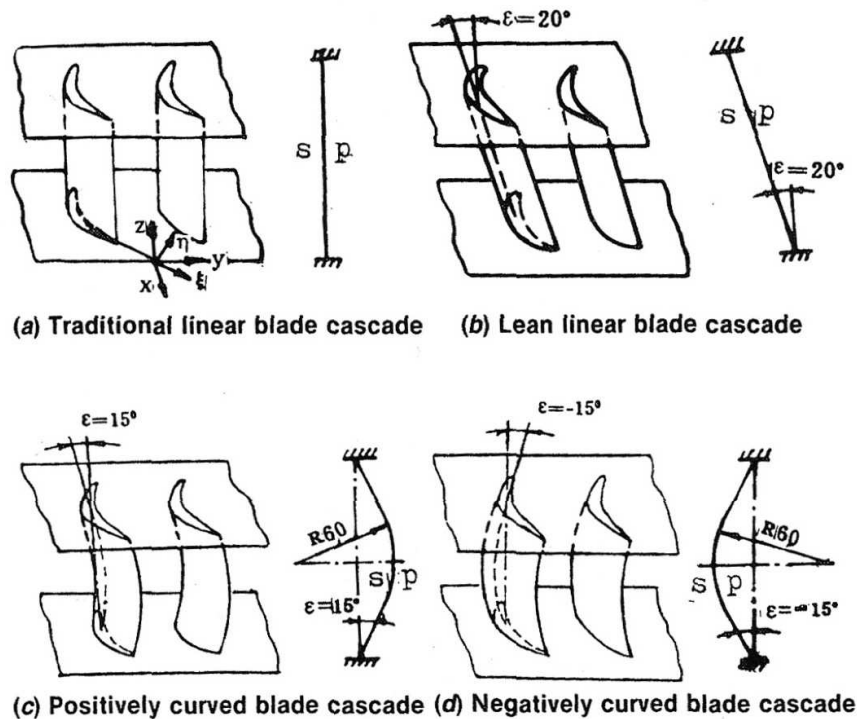


Figure 1.17: Leaned blade from Han *et al.* (1994)

According to Denton and Xu (1999), one of the most common application of 3-D flows is the use of blade lean to change the spanwise variation of the stage reaction. In low hub-to-tip ratio machines, the root reaction can be dangerously low. In that case, the use of the lean can help by increasing the pressure on the hub. This effect can be easily explained from the radial equilibrium written in the following form:

$$\frac{\partial p}{\partial r} = \frac{\rho V_\theta^2}{r} + \frac{\rho V_m^2}{R_c} - f_{br} \tag{1.49}$$

The first term on the right hand side is the centrifugal term, the second is the streamline curvature effect and the last the radial component of the blade force. The radial blade force is given by the lean angle and the circumferential component of the blade force (relation 1.13). It has an impact on both the radial pressure gradient and the streamline curvature. For high aspect ratio blades, the streamline curvature term will dominate and will extend outside of the blade row as shown on the figure 1.18 for a downward radial blade force. Outside of the blade row, the effect of the streamline curvature is to increase the pressure on the hub and decrease it on the shroud. This effect is axisymmetric and fully captured by a throughflow computation. It is illustrated on the figure 1.19 representing the pressure and the axial velocity downstream of a turbine stator for several values of the lean angle. The stator is prismatic and deflect the flow from 0° to 40°. The aspect ratio of the blade is equal to 2.
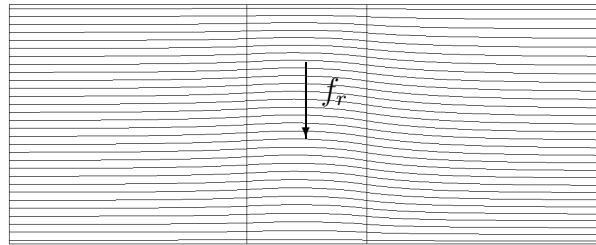


Figure 1.18: Effect of a downward radial blade force on the streamlines



(a) static pressure                           (b) axial velocity
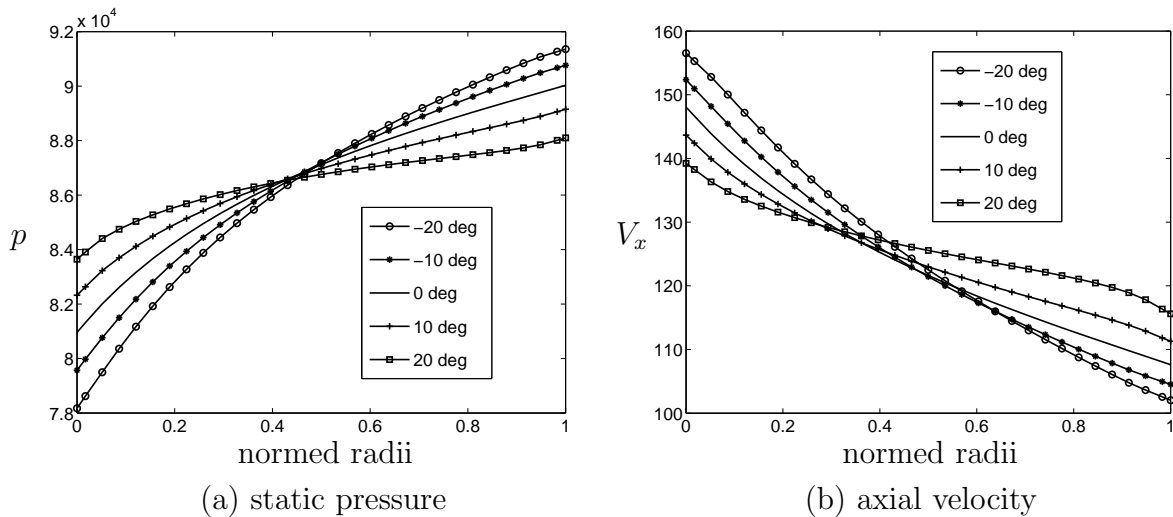
Figure 1.19: Static pressure and axial velocity at the outlet of a turbine stator for different lean angles

Conventionally, in 3-D computations or in experimental tests, the lean angle is said to be positive if the pressure side forms an acute angle with the endwall. In a throughflow model, the distinction of the pressure side and the suction side does not exist and is somewhat replaced by the sign of the circumferential blade force. In the present throughflow model,

the conventional sign for the lean angle is given by the relation (1.13). As an example, for a turbine stator, the circumferential component of the blade force is positive and the relation (1.13) gives a force toward the hub for a positive lean angle. In a compressor stator, the force is oriented in the opposite direction for the same sign of the lean angle.

Another feature of the lean that is looked for by the designer is its ability to control the endwall losses. In a compressor stator, the lean is used to reduce or suppress the corner separation thanks to the unloading of the endwall sections. At a throughflow level, unless a specific model linking this decrease in the loading and the loss generated by the corner separation, it is not expected that this effect could be included.

One of the effects induced by the lean on the losses is given by the mass flow redistribution over the span. This effect can be captured by a throughflow model. To illustrate this, let us consider a turbine stator for which a bi-parabolic distribution of the lean angle is prescribed. Negative lean angle are found at the shroud and positive angle at the hub. This distribution of lean increases the pressure close to the endwalls and diverts the fluid toward the midspan sections. Let's also suppose that the entropy increase across the blade row follows a bi-parabolic distribution. This distribution is shown on the figure 1.20 (a). It gives higher losses close the endwall mimicking the effect of the annulus boundary layer.

The result in term of the flux of entropy ($\rho V_x s$) is shown on the figure 1.20 (b) for a station located inside the blade row and for several values of the lean angle. A zoom is performed close to the hub region. Due to the lower velocity in the endwall regions, the loss flux is lower when leaning of the stacking axis is applied. On the other hand, the losses increase for the midspan sections. Finally, a global reduction of the losses is obtained by the lean process. This explanation for the loss reduction due to lean is maybe an oversimplification of the reality (see Denton and Xu (1999) for several possible explanations for the loss reduction due to lean) but it is a way to introduce the impact of the lean on the losses in a throughflow model in the preliminary design of a turbomachine.



(b) entropy increase　　　　(b) entropy flux
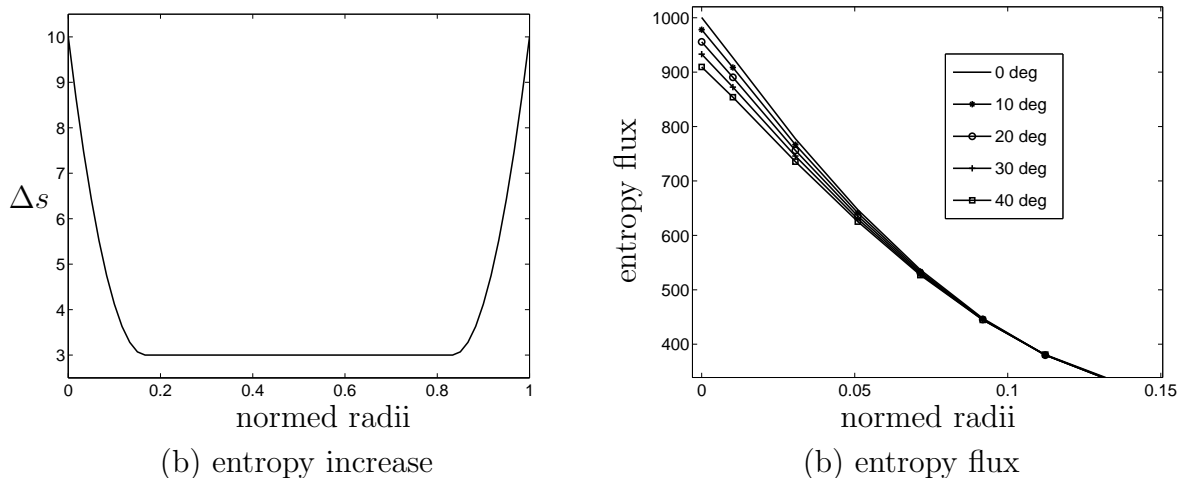
Figure 1.20: Prescribed entropy increase across the blade row

# Chapter 2

# Numerical methods

This chapter is devoted to the numerical resolution of the equations governing the throughflow model presented in the previous chapter. This throughflow model is either based on the Euler or the Navier-Stokes equations. Efficient and accurate techniques to solve these sets of equations are available in the literature and will be used in this work. The purpose here is not to develop new algorithms but rather to choose among the available techniques the most appropriate for a throughflow model. For the sake of completeness, the adopted techniques are briefly presented and emphasis is put on the particularities encountered in the frame of a throughflow model.

## 2.1  Finite volume technique

The set of equations (1.48) defining the throughflow model can be rewritten in the following compact form:

$$\frac{\partial U}{\partial t} + \frac{\partial F}{\partial x} + \frac{\partial G}{\partial r} = S \tag{2.1}$$

where $F$ represents the global axial flux, $G$ the global radial flux and S the sum of the source terms. This set of equations is solved by the well known finite volume technique. This technique is based on the integral form of the equations (2.1) which is the original form under which the fluid flow equations can be derived. This formulation is conservative and allows to capture discontinuities such as the shock waves encountered in transonic and supersonic flows. The computational domain is divided into control volumes to which the conservation principles are applied. For a (two-dimensional) control volume of area $\Omega$ and of contour $\Sigma$, the integral form of the equations (2.1) is written as:

$$\frac{\partial}{\partial t} \int_\Omega U \, d\Omega + \int_\Omega \left( \frac{\partial F}{\partial x} + \frac{\partial G}{\partial r} \right) d\Omega = \int_\Omega S \, d\Omega \tag{2.2}$$

The application of the Green Gauss theorem allows to rewrite the system of equations as follows:

$$\int_\Omega \frac{\partial U}{\partial t} \, d\Omega = \int_\Sigma (F n_x + G n_r) \, d\Sigma + \int_\Omega S \, d\Omega \tag{2.3}$$

where $n_x$ and $n_r$ are the axial and radial components of the inward normal to the contour $\Sigma$. By defining the normal flux $H = F n_x + G n_r$, the following expression is obtained:

$$\int_\Omega \frac{\partial U}{\partial t} \, d\Omega = \int_\Sigma H \, d\Sigma + \int_\Omega S \, d\Omega \tag{2.4}$$

Several possibilities exist for the choice of the control volume type and the location of the unknowns. In the present work, the control volumes coincide with the mesh cells and the unknowns are located at the centroid of the control volumes. This is the so-called cell-centred method.

The contour $\Sigma$ is equal to the sum of $N_j$ segments constituting the edge of the surface. The right-hand side of equation (2.4) is then discretized as follows:

$$\frac{\partial U}{\partial t} = \frac{1}{\Omega} \sum_{j=1}^{N_j} \int_{\Sigma_j} H \, d\Sigma + S \tag{2.5}$$

where $U$ and the source term $S$ represent now averaged values over the cell. This last equation can also been rewritten in the usual residual form:

$$\frac{\partial U}{\partial t} = R(U) \tag{2.6}$$

The time derivative is kept although the sought solution of the equations is the steady one. Indeed the mathematical nature of the steady state Euler equations changes with the flow regime. The equations are hybrid for subsonic flows and hyperbolic for supersonic ones. This means that if the steady form of the equations is to be solved, different algorithms should be used following the flow regime. The problem is even more pronounced for transonic flows where both regimes coexist. A way to overcome this difficulty is to solve the unsteady form of the equations, which is always hyperbolic with respect to the time. The steady state solution is then viewed as the asymptotic solution of the unsteady equations with constant boundary conditions with respect to the time.

The equations (2.5) are written in the convenient semi-discretized form. The equations are discretized in space but stay continuous in time. This method is called the method of lines.

It leads to a system of ordinary differential equations in time over the N control volumes. The accuracy of the steady state solution depends only on the technique used to discretize the right hand side of the equation (2.5), i.e. the discretization of the normal flux and of the source terms.

In the following the different aspects of both space and time discretizations are described. Before that, the discretization of the computational domain itself is addressed.

## 2.2 Flow domain and blade discretization

The 2-D discretization of a compressor or turbine flow path (without technological effects) does not necessitate any particular treatment. The simplicity of the geometry allows to use structured mono-block meshes. The sole constraint is that the leading edge and the trailing edge traces must be mesh-lines. An example of the mesh used is given on the figure 2.1.
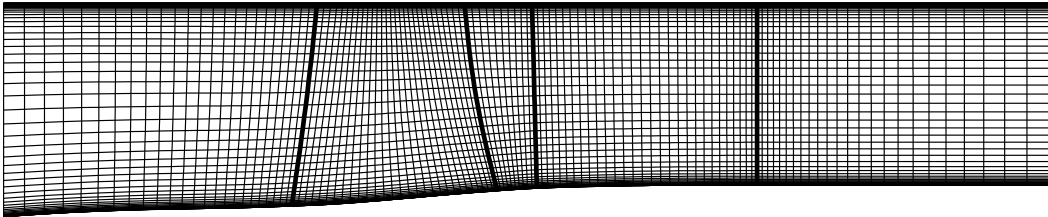


Figure 2.1: Navier-Stokes mesh of a 1-stage compressor

A discretization of the blade itself is also necessary. Indeed, even though the walls of the blade do not appear anymore as solid boundaries in a throughflow model, several parameters of the blade geometry are needed. For example, the blade camber angle at each cell centre, or the blade blockage at the middle of each cell edge. Often, the geometry is given by a series of $N_s$ 2-D sections defined from the hub to the shroud and each section is defined by a series of $N_p$ points. In order to obtain the geometry at the desired location (cell centre or middle of cell edge), an interpolation procedure is necessary. The problem of obtaining the blade geometry parameters at these locations is similar to the problem consisting in obtaining the distribution of the calculation points on the blade surface for a 3-D calculation code.

A 2-D finite volume type interpolation procedure is used to interpolate the required information. A mesh is constructed from the $N_s \times N_p$ data points. The derivative $\vec{\nabla} f_d$ of a given quantity $f$ is simply obtained at the centre of each cell $d$ of the constructed mesh by applying the Green-Gauss theorem. For each point $i$ where the quantity $f$ is needed, the closest point $d$ from the data mesh is sought. The value at the point $i$ is then obtained from the Taylor

expansion around the point $d$ limited to the first order:

$$f_i = f_d + (\vec{x}_i - \vec{x}_d)^T \, \vec{\nabla} f_d \tag{2.7}$$

where $\vec{x}_d$ and $\vec{x}_i$ are the vectors locating respectively the points $i$ and $d$.

## 2.3 Spatial discretization

The application of the Green-Gauss theorem to the Navier-Stokes equations (equation 2.4) enables to reduce the order of the system by one. The difficulty relies now on the evaluation of the normal flux $H$ at the cell interface which must be done for each cell edge of the mesh. The normal flux is split into two contributions: the inviscid flux $H_i$ and the viscous flux $H_v$. The global accuracy of the method can be evaluated by analysing the accuracy of the finite volume discretization of the inviscid and viscous terms, i.e.:

$$\frac{1}{\Omega} \int_\Sigma (H_i + H_v) \; d\Sigma \tag{2.8}$$

For an inviscid problem, the finite volume discretization of the advective term must be evaluated with a first order accuracy at least in order to be consistent. For a viscous problem, the diffusive fluxes must be evaluated with a first order accuracy in order to be consistent and the advective fluxes with a second order accuracy in order to preserve the accuracy of the viscous terms. Discussions on the accuracy of the finite volume method are available in Delanaye (1996) and Jasak (1996). According to Delanaye (1996), the two ingredients that provide the spatial accuracy of a scheme are:

- the order of the reconstruction process. The reconstruction is the process that permits to compute the value of the unknowns on the cell edges. This procedure is necessary to compute the fluxes at this location,

- the numerical integration of the fluxes through each edge of the control volume by a Gauss quadrature rule.

Delanaye (1996) has shown that for unstructured meshes, a third order accurate reconstruction is mandatory as well as using two Gauss points for the flux integration in order to compute the advective flux consistently in the frame of a viscous computation. However, for regular meshes, some error cancellations occur and a second order accurate discretization of the advective fluxes can be achieved with a linear reconstruction and one Gauss point for the flux integration. Furthermore, for a regular mesh (low skewness, locally aligned cells),

mono-dimensional reconstruction in each direction of the mesh are thought to be sufficiently accurate. As the meshes necessary to study throughflow problems are very regular, the 1-D reconstruction approach (with obviously one Gauss point for the flux integration) has been retained. The validity of this approach will be demonstrated in section 2.9.2.

## 2.4   Inviscid flux

The most straightforward method for discretizing a spatial derivative operator on a given set of grid points is based on a symmetric choice of the neighbours of the point itself, i.e. a central scheme. Applying this scheme to the Euler equations comes down to ignoring their hyperbolic character and violates the forbidden signals rule. Furthermore, additional artificial dissipation must be added to the central scheme to avoid the decoupling of odd-even points (fourth order dissipation term) and to avoid oscillations around discontinuities such as shock waves (second order dissipation).

On the other hand, upwind methods try to incorporate the main physical properties of the equations into the discretization, allowing to follow the physical directions of propagation typical of the hyperbolic problems. The part of the information taken from both sides of an egde is adjusted accordingly to the flow properties. For example, for a supersonic flow, only the upstream information is taken into account.

The first upwind methods developed were first order accurate only (on regular meshes), leading to a poor representation of the simulated phenomena. They were based on a constant evolution of the unknowns inside a given cell. Higher order representations can be obtained by adding information on how the unknowns vary inside a cell. This operation is performed by the reconstruction process, which enables to compute the value of the unknowns at the cell interface. There are several ways to do this. For unstructured meshes, multidimensional reconstructions are needed (see Coirier (1994) or Delanaye (1996)). As stated above, for the high quality meshes used in this work, mono-dimensional reconstruction together with one Gauss point for the evaluation of the integral of the flux are sufficient to provide high order accuracy.

A drawback of the extension of the upwind scheme to higher order is that it is necessary to introduce some artificial dissipation to avoid oscillations in the region of shock waves in the same way as a second order artificial dissipation is needed in central methods. This is generally done by introducing limiters such as in the TVD (Total Variation Diminishing) method. As pointed by Hirsch (1994), an upwind TVD scheme can be seen as a rational way to derive an appropriate level of dissipation.

In the following the reconstruction method, which is based on the MUSCL method proposed by Van Leer (1974, 1977), is described and next the limiting device is introduced. Before

that, the computation of the flux itself is presented.

## 2.4.1  Flux computation

In an upwind method the normal flux $H_i$ (the inviscid part of $H$) is computed from a left state $(U^L)$ and a right state $(U^R)$ which are interpolated, respectively, from the left and from the right of the corresponding cell:

$$H_i = H_i \left( U^L, U^R \right) \tag{2.9}$$

By splitting the flux vector $H_i$ into two contributions, $H_i^+$ corresponding to the information propagating from the left to the right and $H_i^-$ corresponding to the information propagating from the right to the left, $H_i$ is discretized as follows:

$$H_i \left( U^L, U^R \right) = H_i^+ \left( U^L \right) + H_i^- \left( U^R \right) \tag{2.10}$$

which represents an upwind discretization. For a supersonic flow from the left to the right, the flux vector reduces to:

$$H_i \left( U^L, U^R \right) = H_i^+ \left( U^L \right) = H_i \left( U^L \right) \tag{2.11}$$

This means that only the upstream information is used and that this information is propagated in the downstream direction only. The criterion for splitting the fluxes is based on the sign of the propagation speed of the information. Methods that are based on this criterion are called flux vector splitting. The flux vector splitting implemented in this work is the one of Van Leer (1982). The expression of the axisymmetric fluxes of Van Leer is given in the appendix A.1. It is mainly used here for the Euler computations. For shear flows, the Van Leer scheme is inaccurate as it does not resolve correctly the contact discontinuities. This is due to the numerical dissipation in the momentum flux transverse to direction of the main flow (see for example Manna (1992) for a detailed analysis).

For the Navier-Stokes computation, another way to compute the advective fluxes is used. They are obtained by searching the local solution of the Euler equations at the interface between two cells. The problem which consists in the evaluation of the variables at the interface of two cells with different constant states $U^L$ and $U^R$ is known as the Riemann problem. The exact solution to that problem can be obtained by the interaction of the waves originating from the difference between the two states $U^L$ and $U^R$ at the cell interface. This is the approach followed by Godunov (1959). Due to its non-linearity, this problem must be solved iteratively and is so computationally costly. The computational cost can be reduced by solving an approximation of the local Riemann problem. The most popular approximate
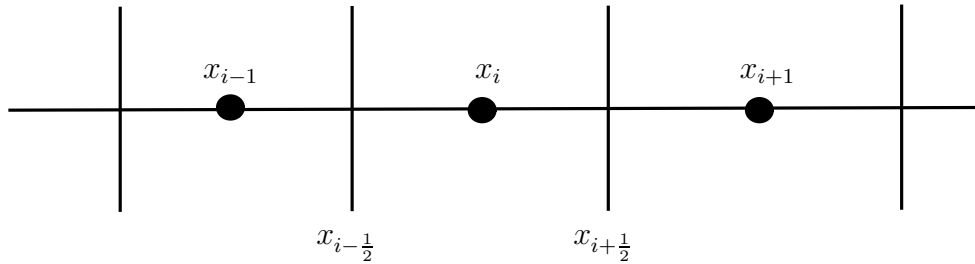
Figure 2.2: MUSCL stencil

Riemann solver is probably the method of Roe (1981) where the fluxes are computed as follows:

$$H_i = \frac{1}{2}\left(H_i\left(U^L\right) + H_i\left(U^R\right)\right) - \frac{1}{2}\sum_{j=1}^{5}\left|\lambda^j\right|r^j\delta W^j$$

where $\lambda^j$ are the eigenvalues of the jacobian matrix A, $r^j$, the right eigenvectors of the matrix A and $\delta W^j$, the strength of the waves. The complete expression of the axisymmetric Roe's fluxes is given in the appendix A.2.

## 2.4.2 MUSCL Reconstruction

The reconstruction process allows to determine the left and right states on the cell faces that are needed for the evaluation of the advective fluxes. A first solution is to take for these left and right states, the solution at the points located respectively on the left and on the right of the face. This so-called constant reconstruction is normally inconsistent. However, on a regular mesh, some error cancellation occurs and the scheme based on the constant reconstruction may be considered as first order accurate. To obtain a higher precision the solution must be interpolated (reconstructed) on the cell interfaces.

The interpolation method used in this work is the MUSCL (Monotonic Upstream Scheme for Conservation Laws) reconstruction developed by Van Leer (1974, 1977). It is based on third order mono-dimensional Taylor expansions in both directions of the mesh. It relies on a three points stencil. The central point for the discretization is located on the left (resp. right) of the face for the evaluation of left (resp. right) state. This is the point $x_i$ on the figure 2.2 for the evaluation of the left (right) state of the $i + \frac{1}{2}$ $(i - \frac{1}{2})$ face.

By computing the first and the second derivatives and reintroducing the corresponding results in the Taylor expansion, the reconstruction for $u_{i+\frac{1}{2}}^L$ and $u_{i-\frac{1}{2}}^R$ leads to the following

expressions (see for example Demeulenaere (1997)):

$$u_{i+\frac{1}{2}}^L = u_i + \frac{\Delta x_i}{4\overline{\Delta x}} \left[ (u_i - u_{i-1}) \left( \frac{1 + \frac{\epsilon}{2} - \eta \frac{\Delta x_i}{\overline{\Delta x}}}{1 - \frac{\epsilon}{2}} \right) + (u_{i+1} - u_i) \left( \frac{1 - \frac{\epsilon}{2} + \eta \frac{\Delta x_i}{\overline{\Delta x}}}{1 + \frac{\epsilon}{2}} \right) \right] \quad (2.12)$$

$$u_{i-\frac{1}{2}}^R = u_i - \frac{\Delta x_i}{4\overline{\Delta x}} \left[ (u_i - u_{i-1}) \left( \frac{1 + \frac{\epsilon}{2} + \eta \frac{\Delta x_i}{\overline{\Delta x}}}{1 - \frac{\epsilon}{2}} \right) + (u_{i+1} - u_i) \left( \frac{1 - \frac{\epsilon}{2} - \eta \frac{\Delta x_i}{\overline{\Delta x}}}{1 + \frac{\epsilon}{2}} \right) \right] \quad (2.13)$$

where

$$u_i = \frac{1}{\Delta x_i} \int_{x_i - \frac{\Delta x_i}{2}}^{x_i + \frac{\Delta x_i}{2}} u(x) \, dx$$

$$\overline{\Delta x} = \frac{1}{2} \left( \Delta x_{i+\frac{1}{2}} + \Delta x_{i-\frac{1}{2}} \right) = \frac{1}{2} \left( \frac{\Delta x_i + \Delta x_{i+1}}{2} + \frac{\Delta x_i + \Delta x_{i-1}}{2} \right)$$

$$\epsilon = \frac{\Delta x_{i+\frac{1}{2}} - \Delta x_{i-\frac{1}{2}}}{\overline{\Delta x}}$$

$$\Delta x_i = x_{i+\frac{1}{2}} - x_{i-\frac{1}{2}}$$

The variable $u_i$ represents the average value of the primitive variables over the cell $i$. The factor $\epsilon$ is representative of the mesh stretching level. The parameter $\eta$ qualifies the reconstruction: when $\eta$ equals $1/3$, the reconstruction is third order accurate, i.e. it can exactly approximate a parabolic function, and is called quadratic. For all other values of $\eta$ the reconstruction is second order accurate, i.e. it can exactly approximate a linear function, and is said to be linear.

For the particular case of a uniform mesh, the classical MUSCL formula are obtained:

$$u_{i+\frac{1}{2}}^L = u_i + \frac{1}{4} \left[ (1 - \eta) (u_i - u_{i-1}) + (1 + \eta) (u_{i+1} - u_i) \right] \quad (2.14)$$

$$u_{i-\frac{1}{2}}^R = u_i + \frac{1}{4} \left[ (1 - \eta) (u_{i+1} - u_i) + (1 + \eta) (u_i - u_{i-1}) \right] \quad (2.15)$$

### 2.4.3  TVD Scheme

High order schemes are prone to oscillate in the vicinity of steep gradients or discontinuities such as shock waves. These oscillations are not physical and can prevent the solution to converge or at least perturb the convergence process. In the latter case, the accuracy of the solution is generally spoiled by the oscillations. A cure to this problem has been brought by the TVD schemes. They allow to obtain a smooth solution in the vicinity of the discontinuity

and high order solution in the smooth regions of the flow. The development of those schemes is based on the property of monotonicity, which is briefly recalled hereafter together with the concept of TVD. These concepts can be illustrated with the one-dimensional scalar conservative law:

$$\frac{\partial u}{\partial t} + \frac{\partial f(u)}{\partial x} = 0 \tag{2.16}$$

A numerical scheme, with a $2l + 1$ points stencil, applied to the previous equation, written in the form of:

$$u_i^{n+1} = F\left(u_{i-l}^n, \ldots, u_i^n, \ldots, u_{i+l}^n\right) \tag{2.17}$$

is said to be monotone if the function $F$ is a monotone increasing function of all of its arguments:

$$\frac{\partial F}{\partial u_k}\left(u_{i-l}^n, \ldots, u_i^n, \ldots, u_{i+l}^n\right) \geq 0 \qquad \forall i - l \leq k \leq i + l \tag{2.18}$$

The scheme is said to be TVD if the total variation, defined by:

$$TV\left(u^n\right) = \sum \left|u_{i+1}^n - u_i^n\right| \tag{2.19}$$

decreases with the iterations:

$$TV\left(u^{n+1}\right) \leq TV\left(u^n\right) \tag{2.20}$$

A TVD scheme preserves the monotonicity, i.e. it does not allow new extrema to be created. This concept of TVD is sufficient to avoid the apparition of spurious oscillation in the vicinity of the discontinuities. Although these concepts are only 1-D their applications in several dimensions works well.

The Godunov theorem (Godunov, 1959) states that there is no linear scheme which is monotone and second order accurate. However, a non linear scheme can be TVD and still remains high order accurate. The TVD condition can be fulfilled if, in the reconstruction procedure for the left and right states, the amplitudes of the gradients are limited to certain bounds (Harten *et al.*, 1983). In the MUSCL reconstruction, these constraints on the gradients are introduced by non linear functions called limiters. They are designed to act in the vicinity of a discontinuity, where they reduce the accuracy of the reconstruction, and to not to perturb the solution in the smooth regions.

For example, in the case of a regular uniform mesh (equations 2.14 and 2.15), the limiters $\phi$ modify the difference $(u_{i+1} - u_i)$ and $(u_i - u_{i-1})$ when their ratio moves away from unity.

The reconstruction is then rewritten as follows:

$$u^L_{i+\frac{1}{2}} = u_i + \frac{1}{4}\left[(1-\eta)(u_i - u_{i-1})\,\phi\left(\frac{u_{i+1} - u_i}{u_i - u_{i-1}}\right) + (1+\eta)(u_{i+1} - u_i)\,\phi\left(\frac{u_i - u_{i-1}}{u_{i+1} - u_i}\right)\right]$$
$$(2.21)$$

$$u^R_{i-\frac{1}{2}} = u_i + \frac{1}{4}\left[(1-\eta)(u_{i+1} - u_i)\,\phi\left(\frac{u_i - u_{i-1}}{u_{i+1} - u_i}\right) + (1+\eta)(u_i - u_{i-1})\,\phi\left(\frac{u_{i+1} - u_i}{u_i - u_{i-1}}\right)\right]$$
$$(2.22)$$

In the case of non uniform meshes, it is the gradients that are modified.

The limiters must fulfill a certain numbers of criteria. For a detailed review of these criteria and of the different limiters developed in the 80's, see Yee (1989). In the present work, the *minmod* limiter, developed by Chakravaty and Osher (1983) is used and applied to the primitive variables.

# 2.5   Viscous flux

The calculation of the viscous fluxes requires the evaluation of the primitive variables and their first derivatives at the middle of the edge of the considered cell. A consistent viscous flux discretization requires that both the primitive variables and their first derivatives are evaluated with a second order accuracy. However, as for the calculation of the inviscid fluxes, some error cancellation occurs on regular meshes such as those used in the present work and a first order accurate evaluation of the first derivative at the Gauss quadrature point is accurate enough.

The primitive variables at the middle of an edge of a cell are obtained by taking the mean of the left and the right values $U^L$ and $U^R$ obtained by the MUSCL reconstruction. The derivatives are obtained by the diamond path scheme (Coirier, 1994) which is described hereafter. This scheme leads to a first order accurate evaluation of the first derivative.

An approximation of the first derivative at the middle of a cell edge $e$ can be obtained by applying the Green-Gauss theorem to the so-called diamond path. This path consists in a four-sided polygon obtained by joining two vertices of an edge and the centroids of the cells sharing this edge (the dotted-line on the figure 2.3).

In order to compute this derivative, the value at cell vertices must be known. They are

obtained by a linear interpolation. The solution at the vertex 0 is evaluated by:

$$q_0 = \frac{\sum_{i=1}^{N} w_i \, qi}{\sum_{i=1}^{4} w_i} \tag{2.23}$$

where $q_i$ denotes the value at the centres of the cells surrounding the vertex 0 and $w_i$ represents the weight associated with each cell and is defined as follows:

$$w_i = 1/d_i + \Delta w_i \tag{2.24}$$

where $d_i$ is the distance between the point 0 and the point $i$. The perturbations $\Delta w_i$ are obtained by solving a minimisation problem subject to the constraint that the interpolation must be exact for a linear function. This is obtained by the method of the Lagrangian multipliers. For more details, see Coirier (1994) or Geuzaine (1999).

Finally, the weight functions are given by:

$$w_i = 1/d_i + \lambda_x \, (x_0 - x_i) + \lambda_y \, (y_0 - y_i) \tag{2.25}$$

with the Lagrangian multipliers

$$\lambda_x = \frac{I_{xx}R_y - I_{yy}R_x}{I_{xx}I_{yy} - I_{xy}^2}$$

$$\lambda_y = \frac{I_{xy}R_x - I_{xx}R_y}{I_{xx}I_{yy} - I_{xy}^2}$$
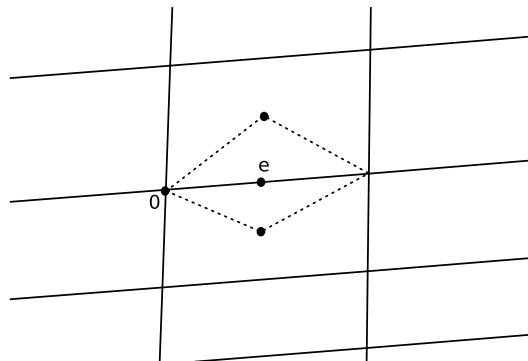


Figure 2.3: Diamond path scheme

where

$$R_x = \sum_{i=1}^{N} (x_i - x_0)$$

$$R_y = \sum_{i=1}^{N} (y_i - y_0)$$

$$I_{xx} = \sum_{i=1}^{N} (x_i - x_0)^2$$

$$I_{yy} = \sum_{i=1}^{N} (y_i - y_0)^2$$

$$I_{xy} = \sum_{i=1}^{N} (x_i - x_0)(y_i - y_0)$$

Beside the accuracy of the discretization, the performance of a viscous scheme can be measured by its compactness and its positivity. The positivity property is a concept associated with the maximum principle that must satisfy a Laplacian operator. Locally, it simply states that the value at a point is bounded by the values at the neighbouring points. That means that no local extrema are permitted. This is similar to the monotonicity principle for the discretization of the inviscid terms. A (large) non-positivity can lead to a less robust or even unstable scheme.

Vaassen (2005) has extensively studied the performance of several viscous discretizations and found that the diamond path is quite competitive in terms of compactness and positivity. It is however not consistent on general meshes. But, as pointed by Vaassen (2005), the inconsistency is not detrimental to the accuracy of the final solution. Furthermore, on the regular meshes that are used in the present work, due to some error cancellation phenomena, the diamond path is (nearly) consistent.

## 2.6   Source terms

The advective schemes used in this work have been developed in the frame of the homogeneous form of Euler equations. Rigorously, these schemes should be modified to weigh the presence of the source terms (and even the presence of the viscous terms) or alternatively, the source terms should be upwinded. Roe (1987) has proposed such a method for the Roe's flux splitting (see Bermudez and Vazquez (1994) and Müller and Jenny (1999) for extension and generalisation).

In the frame of the throughflow model equations (system 1.48), such modifications have

not been found necessary. To the exception of the source term originating from the flow deflection contribution of the inviscid blade force ($S_{b2}$), the source terms are weak and vary smoothly so that no particular treatment is necessary.

Concerning the $S_{b2}$ term, there is a particular circumstance where it may be necessary to use a special discretization. This is for the leading edge discontinuity, already discussed in section 1.2.4. If the flow has to be turned instantaneously at the leading edge without generating losses, some modifications of the flux balance must be undertaken. This approach has been followed by Nigmatullin and Ivanov (1994) and by Baralon (2000). They are able to deal with a discontinuity in the flow angle at the leading edge without generating entropy. In the present work, the solution of modifying the flow path over the first part of the blade row and not to try to resolve a discontinuity in the flow angle at the leading edge has been followed. This solution sounds more physical, at least for subsonic flow. In conclusion, the source terms are discretized in a centred way and no modification of the flux splitting is performed.

In the following, some of the characteristics of both contributions of the inviscid blade force, i.e. the deflection of the flow and the blockage are analysed. First, the way to compute the blade force itself is analysed and next a study of the mesh resolution is performed for the throughflow problem. Finally, some remarks are made concerning the discretization of the blade blockage source term.

## 2.6.1 Flow deflection contribution

**Blade force computation**

In the equations (1.14) and (1.15), the expression allowing to compute the flow deflection contribution of the inviscid blade force has been written in function of the modulus of the blade force and not in function of its circumferential component. The latter is the most natural way to obtain it and is in fact the sole alternative when the circumferential component of the momentum equation is not solved in the blade passage. This natural form however leads to convergence problems if the blade flow angle is high as it can be seen from the following example that neglects the radial component of the blade force. In that case, the axial component of the blade force is directly obtained by the following relation in function of the flow angle $\alpha$:

$$f_{bx} = -\tan\alpha\, f_{b\theta} = -\frac{V_\theta}{V_x} f_{b\theta} \tag{2.26}$$

During the convergence process or close to the annulus endwalls for a Navier-Stokes computation, when low or zero axial velocity occurs, this formulation leads to slow convergence or divergence of the resolution process. The formulation based on the modulus of the blade

force does not exhibit this drawback. This formulation has been taken from Sturmayr (2004). In the present work, it is applied to both analysis and design formulations.

The advantage in working with the blade angle instead of the flow angle when computing the blade force with the analysis mode is also highlighted by the equation (2.26). The blade angle does not vary during the convergence process and does not necessitate the flow variables to be computed. This avoids the singularity at $V_x = 0$.

The modulus of the blade force is computed by the pseudo-time dependent equations (1.14) and (1.15). They are integrated in time within the Runge-Kutta procedure together with the five conservation equations (see section 2.7).

## Mesh resolution

In the frame of the capture of the leading edge discontinuity, Nigmatullin and Ivanov (1994) and Baralon (2000) have analytically solved the flux balance at the leading edge. Their goal was to modify the flux balance in this region to instantaneously turn the flow at the leading edge without generating any numerical losses.

The underlying idea of the work done by Nigmatullin and Ivanov (1994) and Baralon (2000) is borrowed here and somewhat extended to be valid inside the blade passage. The purpose is to *a priori* evaluate the discretization error, in term of entropy generation, due to the deflection of the flow inside the blade passage. Indeed, as we will see, at the exception of the trivial case of a constant blade angle, some non-physical entropy, i.e. numerical loss, is generated by the inviscid phenomenon of flow deflection by a blade force. The question that has to be answered is what is the mesh resolution necessary to avoid spoiling the solution with numerical losses.

For this purpose, let us consider again the simple testcase used in the section 1.2.3 and which consists in a meridional view of a linear blade-to-blade cascade (no radial direction). The blockage effect, as well as the viscous blade forces, are neglected. Furthermore, a stator blade is considered here. The conservation laws applied to the control volume of the figure 2.4 located inside a blade row are written as follows:

$$\rho_2 V_{x2} = \rho_1 V_{x1} \tag{2.27}$$

$$\rho_2 V_{x2}^2 + p_2 = \rho_1 V_{x1}^2 + p_1 + f_{bx}\Delta x \tag{2.28}$$

$$\rho V_{x2} V_{\theta 2} = \rho V_{x1} V_{\theta 1} + f_{b\theta}\Delta x \tag{2.29}$$

$$\rho_2 V_{x2} h_2^0 = \rho_1 V_{x1} h_1^0 \tag{2.30}$$

The orthogonality condition of the blade force with respect to the camber surface is added to the previous equations:

$$f_{bx} = -f_{b\theta} \tan \alpha_s \tag{2.31}$$

where $\alpha_s$ is the blade angle at the centre of the cell under consideration.
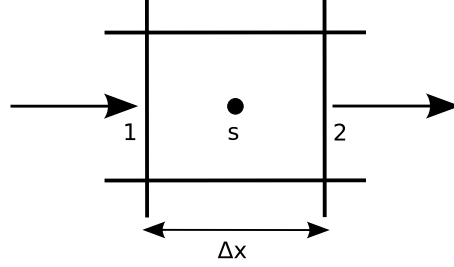


Figure 2.4: Control volume

If the blade angles $\alpha_1$, $\alpha_2$ and $\alpha_s$ are different, the previous system of equations does not provide an isentropic solution. The generation of entropy and the total pressure erosion are given by the following relations:

$$\Delta s_{21} = -R \ln \frac{p_2^0}{p_1^0} \tag{2.32}$$

$$\frac{p_2^0}{p_1^0} = \frac{p_2}{p_1} \left( \frac{1 + \dfrac{\gamma - 1}{2} M_1^2 \dfrac{M_2^2}{M_1^2}}{1 + \dfrac{\gamma - 1}{2} M_1^2} \right)^{\frac{\gamma}{\gamma - 1}} \tag{2.33}$$

where

$$\frac{p_2}{p_1} = \frac{\rho_2}{\rho_1} \left( 1 + \frac{\gamma - 1}{2} M_{1x}^2 \left[ \left( 1 + \tan^2 \alpha_1 \right) - \left( \frac{\rho_2}{\rho_1} \right)^2 \left( 1 + \tan^2 \alpha_2 \right) \right] \right) \tag{2.34}$$

$$\frac{M_2}{M_1} = \sqrt{\frac{p_1}{p_2} \frac{\rho_1}{\rho_2} \frac{1 + \tan^2 \alpha_2}{1 + \tan^2 \alpha_1}} \tag{2.35}$$

$$\frac{\rho_1}{\rho_2} = \frac{-b \pm \sqrt{b^2 - 4ac}}{2a} \tag{2.36}$$

$$a = -M_{1x}^2 \left( 1 + \tan \alpha_s \tan \alpha_2 - \frac{\gamma - 1}{2\gamma} \left( 1 + \tan^2 \alpha_2 \right) \right) \tag{2.37}$$

$$b = M_{1x}^2 + \frac{1}{\gamma} + M_{1x}^2 \tan \alpha_s \tan \alpha_1 \tag{2.38}$$

$$c = -\frac{1}{\gamma} - \frac{\gamma - 1}{2\gamma} M_{1x}^2 \left( 1 + \tan^2 \alpha_1 \right) \tag{2.39}$$

In order to solve the previous set of equations, some assumptions have to be made on the evolution of the flow angle inside the studied cell. The blade angle is supposed to vary linearly. The flow angles at the different locations are finally coupled by the following relations:

$$\alpha_s = \alpha_1 + \frac{d\alpha}{dx}\frac{\Delta x}{2} \tag{2.40}$$

$$\alpha_2 = \alpha_1 + \frac{d\alpha}{dx}\Delta x \tag{2.41}$$

For a given Mach number and for a given value of $\frac{d\alpha}{dx}$ representative of the blade geometry, the generation of losses can be computed for a set of values of the mesh resolution $\Delta x$. Another more meaningful way of presenting the results obtained from the previous established flux balance is to compute the loss generated in function of the number of points $n_p$ used to discretize a given variation of the flow angle $\Delta \alpha$. In other words, it comes back to evaluate the number of points necessary to discretize correctly the blade row for a given blade camber angle. This is a very valuable information in order to generate an appropriate mesh.

The figures 2.5 and 2.6 represent such information in terms of the loss pressure ratio and of the entropy increase. This is for the particular case of a Mach number $M_1$ equal to 0.8 and for an increase of the blade angle of 1° . Several values of the $\alpha_1$ blade angle are plotted. As expected the error diminishes with the number of points used to discretize the blade. An important information is given by the great influence of the blade angle at which the flow deflection is performed. For high values of $\alpha_1$, dense meshes must be used. Another observation not shown here is that the error level increases with the Mach number.

On the figure 2.7 (a) and (b), some results obtained on the VEGA2 transonic turbine stage are shown. The evolution of the VEGA2 nozzle blade angle with the axial direction is shown on the figure 2.7 (a) for the midspan section. The blade angle reaches 72° at the trailing edge. Two Euler computations (with no added losses by friction forces) have been run on this turbine nozzle. The first computation has been performed with an equally spaced distribution of points in the axial direction, the second with a clustering of grid points near the trailing edge. The results are given on the figure 2.7 (b) for the midspan position. It represents the entropy evolution inside the blade row in function of the blade angle of the nozzle. This clearly illustrates the error arising from the discretization of the source terms and the necessity of using a denser mesh at high blade angle.

The following rule has been extracted from the experience gained on the different axial turbomachines studied in this work. As long as the blade flow angle (blade angle plus a deviation) does not exceed 60° - 65° either in the absolute or in the relative reference frame, a uniform mesh in the blade row with about 30 to 40 cells (depending on the Mach number) in the axial direction is sufficient. Otherwise denser meshes must be used in the region where the blade angles are high.
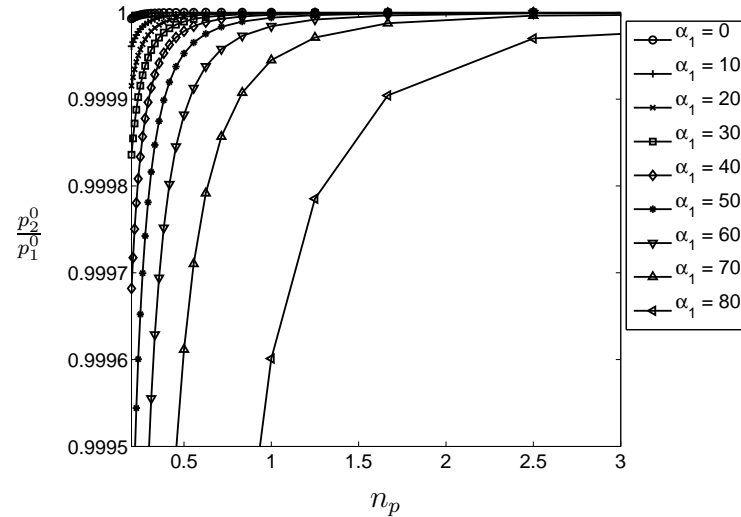
Figure 2.5: Discretization error due to the flow deflection contribution of the inviscid blade force: total pressure ratio given for a Mach number $M_1 = 0.8$ and a variation of the blade angle $\Delta\alpha = 1$.
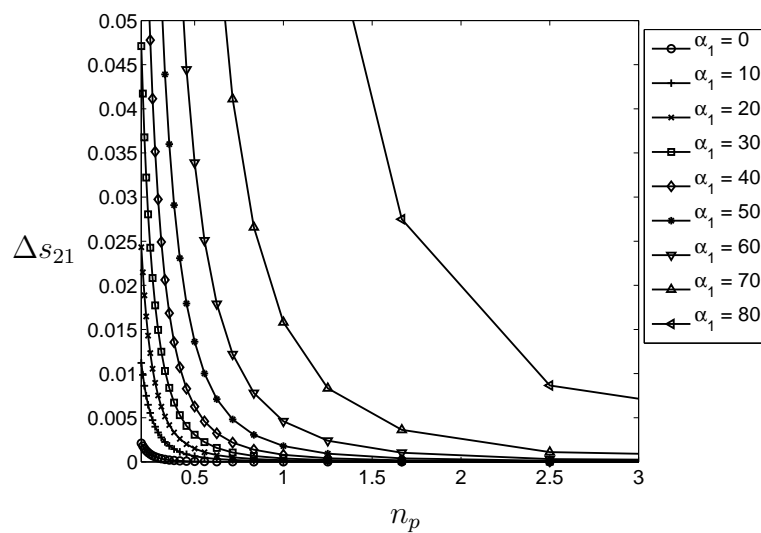


Figure 2.6: Discretization error due to the flow deflection contribution of the inviscid blade force: entropy increase given for a Mach number $M_1 = 0.8$ and a variation of the blade angle $\Delta\alpha = 1$.

(a) skeleton angle
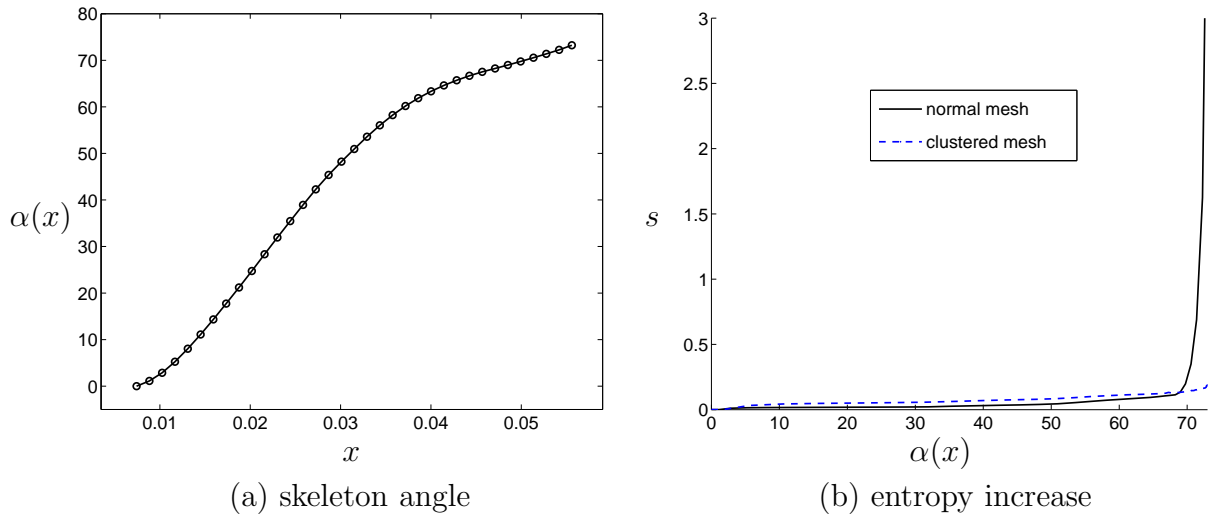
(b) entropy increase

Figure 2.7: VEGA2 nozzle angle distribution at midspan (a) and entropy increase in function of the nozzle angle at midspan (b)

## 2.6.2   Blade blockage contribution

Concerning the blockage contribution of the inviscid blade force (formula 1.11), the gradient of the blockage factor $\vec{\nabla}b$ needs to be computed at each cell-centre. At the beginning of this work a finite-difference method based on 1-D cubic spline interpolation was used to compute this gradient but large numerical losses were observed. The reason for the generation of those losses was not that the finite difference method was not accurate enough. The reason was that the $p\vec{\nabla}b$ term is a term that actually balances or compensates the term $\vec{\nabla}bp$ found in the inviscid flux. If the gradient of the blockage is not discretized in the same way as the pressure term, i.e. by a finite volume approach, numerical errors occur. The gradient of the blockage is therefore obtained by the Green-Gauss theorem, from the value of the blockage at the middle of each cell-edge:

$$\vec{\nabla}b = \int_\Sigma b\,\vec{n}\,d\Sigma \tag{2.42}$$

## 2.7   Time discretization

As stated in the introduction of this chapter, the throughflow set of equations is solved under its unsteady form despite the fact that the steady solution only is of interest. This method avoids the difficulties linked to the mathematical behaviour change of the equations with the flow regime. Steady boundary conditions are imposed and an initial guess of the solution must be provided to start the time-marching procedure. This initial guess is viewed as a

perturbation of the steady state solution of the equations which is obtained after a certain number of pseudo-time iterations.

As we are not interested in the physical meaning of the transient solution during the convergence process, the sole criterion for choosing the time integration method is the speed at which the algorithm converges to the steady state solution. From this point of view, the implicit methods are very interesting, they are very stable and they allow to reach steady states in short times. An illustration of the benefit of such a method in the frame of a solver that shares the same technology as the one used here (MUSCL type reconstruction) is available in Léonard *et al.* (1997) for a blade to blade (analysis and design) computation code. The implicit method allows a speed up of 5 to 10. In the frame of the finite volume Euler throughflow solver, it seems that the only implicit time integration is due to Nigmatullin and Ivanov (1994). However, they did not show the improvement brought by the implicit method over an explicit one, nor details on the implicit scheme.

In the present work, the focus has been put on the physical modelling of the throughflow problem rather than on the numerical methods used to solve it. This is the reason why an explicit Runge-Kutta time integration method has been used. It is straightforward to implement but less efficient than an implicit method.

The Runge-Kutta method is a multistage time integration algorithm. It was introduced in the field of the computation of the Euler equations by Jameson *et al.* (1981). By applying the Runge-Kutta discretization to the semi-discretized equation (2.6), the following general expression (in the low-memory usage formulation) is obtained:

$$U^0 = U^n$$
$$U^1 = U^0 + \alpha^1 \Delta t R \left( U^0 \right)$$
$$\dots$$
$$U^{m-1} = U^0 + \alpha^{m-1} \Delta t R \left( U^{m-2} \right)$$
$$U^m = U^0 + \alpha^m \Delta t R \left( U^{m-1} \right)$$
$$U^{n+1} = U^m$$

where $m$ is the number of stages of the algorithm and $\alpha_m$ are the coefficients defining the different Runge-Kutta schemes.

The explicit methods suffer from stability limits that disallow the use of large time steps. The stability condition for an hyperbolic system writes down:

$$\left| \lambda_{max} \frac{\Delta t}{\Delta x} \right| \leq \nu_{max} \tag{2.43}$$

where $\nu_{max}$ is the maximum allowable Courant-Frederich-Levy (CFL) number which depends on the chosen Runge-Kutta scheme. $\lambda_{max}$ is the largest eigenvalue of the spatial discretization

operator $R(U)$. The relation (2.43) simply states that the temporal integration will be stable inasmuch as that the distance covered during the time $\Delta t$ by a disturbance propagating at the speed $\lambda_{max}$ is lower than distance between two points (times the maximum allowable CFL number for the chosen integration scheme).

Essers (2003) analysed different Runge-Kutta schemes and gave the following criteria for evaluating their performances:

- the first one is the stability region of the scheme (weighted by the number of stages of the algorithm) and the maximum allowable CFL. This criterion maximises the dissipation by the boundaries of the computational domain,

- the second one is a criterion based on the transient dissipation capability of the scheme inside the computational domain.

Based on these two criteria, two schemes are interesting, a fourth order, the RK41A which favours the dissipation by the boundaries and a third order, the RK31B, which has very good transient damping properties. The associated coefficients for these two schemes are given in the table 2.1.

|  | $\alpha_1$ | $\alpha_2$ | $\alpha_3$ | $\alpha_4$ | $\nu_{max}$ |
|---|---|---|---|---|---|
| 4-stage (RK41A) | 1/4 | 5/14 | 14/25 | 1 | 2.58 |
| 3-stage (RK31B) | 8/17 | 17/20 | 1 | − | 1.53 |

Table 2.1: Runge Kutta schemes parameters

A very efficient way to accelerate explicit schemes is the multigrid method (Brandt, 1977). In the frame of an Euler throughflow model, Sturmayr (2004); Sturmayr and Hirsch (1999b) have shown the improvement brought by the multigrid acceleration. The multigrid provides an acceleration up to a factor 14 for a subsonic testcase. If shocks are to be captured however the benefit is less important and the multigrid even deteriorates the convergence rate for choked operating points. This technique has not been implemented here.

Another well known acceleration technique is the residual smoothing. It has been used here under its implicit form (Jameson and Baker (1983)). The idea is to replace the residual at the cell $i$ by the average of the neighbour residuals. It introduces a certain degree of implicitness in the discretization and thus allows to use larger CFL number while staying in the stability region of the Runge-Kutta scheme. For a linear problem without dissipation, one can find (Jameson and Baker, 1983) that the stability can be obtained for any CFL number $\nu$ provided that the smoothing parameter $\epsilon$ satisfies:

$$\epsilon \geq \frac{1}{4}\left(\frac{\nu^2}{\nu^*} - 1\right) \tag{2.44}$$

where $\nu^*$ is the CFL number of the non smoothed scheme. This relation gives the value of $\epsilon$ to use for the desired CFL number $\nu$. For non-linear problems, the relation (2.44) does not hold anymore and the smoothing parameter must be found experimentally.

With the residual smoothing acceleration, a limitation arises in the choice of the largest CFL number. The number of iterations to achieve the convergence is a monotone function of the smoothing parameter (Kroll and Jain, 1987) and a limit exists from which it is not anymore computationally efficient to increase the CFL. Furthermore, as the smoothing parameter increases, the damping property of the spatial operator deteriorates (Enander, 1997). Practically, the minimum value of $\epsilon$ is sought for increasing values of the CFL until the computational time deteriorates. The combination of the value giving the best performances are given in the table 2.2 for 3 cases: a simple channel, an Euler throughflow and a Navier-Stokes throughflow computations. In the same time, the best Runge-Kutta scheme for each case is also tabulated.

|  | RK scheme | CFL | $\epsilon$ |
|---|---|---|---|
| Simple channel | RK41A | 12 | 4 |
| Euler throughflow | RK31B | 9 | 3.5 |
| NS throughflow | RK41A | 7 | 3 |

Table 2.2: Performance of the Runge-Kutta schemes with an implicit residual smoothing

The time-dependent equation allowing to obtain the modulus of the blade force (equation 1.14) is integrated in time together with the five conservation equations inside the Runge-Kutta procedure. A relaxation coefficient is however introduced for this equation in order to obtain the quickest convergence. For subsonic computations, a coefficient between 0.2 to 0.5 has been found to give the better convergence rate as well as a coefficient between 1.0 to 2.0 for the transonic computations. Applying the residual averaging to this additional equation has not been found to be efficient. Including the blade force equation in the time integration scheme gives more robustness and improves the convergence rate. The curve on the figure 2.8 gives the decrease of the residual during the convergence process and it can be seen that the residuals of the different equations decrease with the same rate.

## 2.7.1 Initialisation

In order to initialise the time-marching procedure, it is necessary to provide a first estimation of the solution. If the compressor to be analysed is composed of several blade rows, a uniform solution will not, in general, be sufficiently accurate and will lead to the divergence of the time integration. A very simple procedure has been developed to initialise the computation from the knowledge of a given reference axial velocity. First, as the computed cases are mainly axial machine, the radial velocity is neglected everywhere. Next, the circumferential velocity is computed from the blade geometry and allows to compute the total temperature.
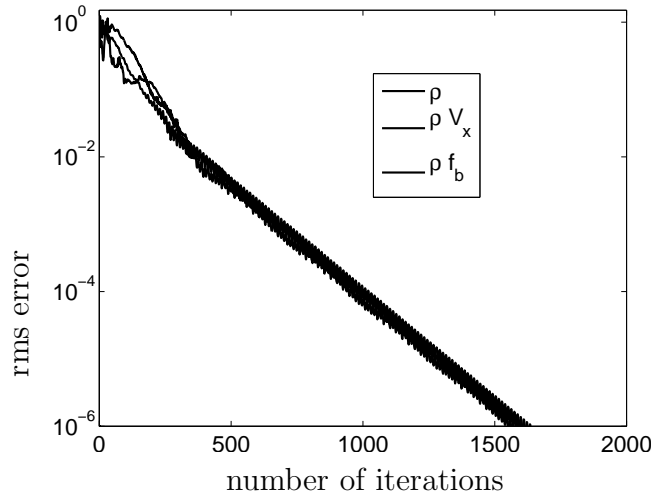
Figure 2.8: Convergence curves for the continuity, the axial momentum conservation and the blade force equations

The total pressure is then computed isentropically from the total temperature. From these variables, the static temperature and the static pressure can be evaluated which in turn gives the density.

In some cases, the blade forces computed from the pseudo time-dependent equation cannot update sufficiently quickly in the first iterations and the flow can not sustain the adverse pressure gradient. This leads to large backflows and to the divergence of the process. A straightforward solution is to lower the outlet static pressure and to use a first order spatial scheme for the first iterations.

## 2.8   Boundary conditions

In the cell-centred discretization adopted here, there are no nodes on the physical boundaries. This leads to a weak formulation of the boundary conditions. These conditions are therefore enforced by imposing the normal flux through each boundary segment. In the present work the method of Léonard *et al.* (1997) is used: additional nodes (but no unknowns to which a control volume would be associated) are placed on the boundaries (figure 2.9 for the wall boundary condition). They allow to explicitly impose the boundary conditions through the primitive variables. They are also used in the reconstruction process.

The number of boundary conditions to be imposed on each part of the domain limits is given by the mathematical nature of the equations and is different for the Euler and Navier-Stokes equations. In practice, only the wall boundary condition is different owing to the fact that on the other boundaries, at inlet and outlet of the domain, the nature of the flow is
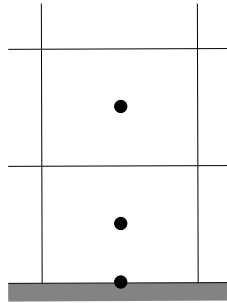
Figure 2.9: Additional node on the boundary (wall)

mainly inviscid. This is a generally admitted treatment of the boundary conditions in the turbomachine codes.

For the Euler equations, the number of physical boundary conditions $n_b$ that must be imposed is equal to the number of waves entering the domain while the number of numerical boundary conditions $n_n$ is equal to the number of waves leaving the computational domain. The sum of $n_b$ and $n_n$ is equal to number of equations.

The sign of the eigenvalues of the Jacobian matrix of the equations projected onto the boundary gives the number of physical boundary conditions that must be imposed. However this is only an information on the number of variables to be imposed and does not help in choosing which variable to impose. In the present work, the following classical set of boundary conditions generally encountered in the turbomachinery field is used.

**Inlet**

At subsonic inlet, the total pressure, the total temperature and the circumferential and radial flow angles are imposed as physical boundary conditions. The information that is taken from the interior of the domain is the mass flow.

No model has been devised here to treat flow conditions leading to the so-called "unique incidence" condition. According to Cumpsty (1989), this condition is the choking condition only for high inlet Mach numbers (higher than 1.5). Such applications are not addressed here. For a throughflow model accounting for the unique incidence condition, see Boure and Gillant (1985).

**Outlet**

At subsonic outlet, the static pressure is imposed. The density and the three components of the velocity are linearly extrapolated toward the outlet as numerical boundary conditions.

The distribution of the static pressure along the outlet boundary cannot be chosen arbitrarily. It must respect the momentum conservation law projected along the outlet boundary. Otherwise, although a converged solution can be obtained, this solution is meaningless. Therefore, from a given level of static pressure at a reference radius, a physical distribution of the pressure is computed thanks to the momentum equilibrium. This distribution is then imposed as a boundary condition. The following combination of the axial and radial components allows to compute the pressure increase between two nodes on the boundary:

$$\Delta p = \frac{\partial p}{\partial r}\Delta r + \frac{\partial p}{\partial x}\Delta x \tag{2.45}$$

The radial and axial pressure derivatives are computed by the conservation equations of the radial and axial momentum:

$$\frac{\partial p}{\partial r} = \frac{\rho V_\theta^2}{r} - \frac{\rho V_r^2}{r} - \frac{\partial \rho V_r^2}{\partial r} - \frac{\partial \rho V_r V_x}{\partial x} \tag{2.46}$$

$$\frac{\partial p}{\partial x} = -\frac{\partial \rho V_x^2}{\partial x} - \frac{\partial \rho V_r V_x}{\partial r} - \frac{\rho V_r V_x}{r} \tag{2.47}$$

If the boundary is orthogonal to the machine axis so that $\Delta x = 0$ and if the radial velocity is supposed to be negligible, the pressure gradient reduces to:

$$\frac{\partial p}{\partial r} = \frac{\rho V_\theta^2}{r} \tag{2.48}$$

This is the so-called simple radial equilibrium condition very often used for the axial turbomachine. Negligible differences have been observed in the present work between both formulations in term of accuracy. However, the general equilibrium seems to have a destabilising effect for transonic configurations and prevents the solution to converge if a relaxing procedure for the frequency at which the pressure distribution is updated is not set up.

**Euler wall**

Only one condition must be imposed at the wall for Euler computations, namely the impermeability condition:

$$\vec{V} \cdot \vec{n} = 0 \tag{2.49}$$

Note that this is also the boundary condition imposed for Euler computations with spanwise mixing model, i.e. with viscous shear stresses inside the domain.

If this condition is imposed in the normal flux along the boundary, the following flux at the

wall is obtained:

$$H_i = \begin{bmatrix} 0 \\ pn_x \\ pn_r \\ 0 \\ 0 \end{bmatrix} \tag{2.50}$$

The computation of the pressure (together with the primitive variables) is performed by the consistent boundary condition method of Deconinck and Struijs (1988) for the Van Leer flux and by the compatibility relations for the Roe scheme (Léonard *et al.*, 1997).

**Navier-Stokes wall**

The number and the nature of the boundary conditions to be imposed at the wall for the Navier-Stokes equations are well-known, namely the impermeability and the non-slip conditions. These conditions give here:

$$V_x = 0 \tag{2.51}$$
$$V_r = 0 \tag{2.52}$$
$$V_t = \Omega r \tag{2.53}$$

where $\Omega r$ is the peripheral velocity of the rotating hub. Furthermore a thermal boundary condition must be imposed, either an isothermal wall:

$$T = T_{wall} \tag{2.54}$$

or an adiabatic wall:

$$\frac{\partial T}{\partial \eta} = 0 \tag{2.55}$$

The gradients necessary to compute the shear stresses and the heat fluxes (in case of isothermal wall) are next computed at the node on the wall. This allows to compute the normal viscous flux. Finally, the pressure on the wall has to be computed in order to obtain the advective flux through the wall. The classical hypothesis for the high Reynolds flow is used. It gives:

$$\frac{\partial p}{\partial \eta} = 0 \tag{2.56}$$

# 2.9   Verification cases

Three verification cases are presented hereafter. Their purposes are to verify that the model performs correctly on simple testcases for which analytical or known solutions exist. The first one is the development of a boundary layer over a flat plate. The second one is a channel flow on skewed meshes and the last case is a free-vortex rotor.

## 2.9.1   Development of a boundary layer over a flat plate

The computational domain is presented on the figure 2.10. The flow regime is laminar over the first part of the plate and turbulent on the rear part. The turbulence model of Baldwin-Lomax is used and switched on for a Reynolds number of 200000. A slip condition is imposed in front of the flat plate and on the upper limit of the domain. A Reynolds number of $Re_L$ base on the distance along the wall of 2000000 was used with a free-stream Mach number of 0.2. More details on this testcase can be found in Yoder (1998). The computed skin friction coefficient $C_f$ is compared to the laminar law of Blasius ($C_f = 0.664\,Re_x^{-0.5}$) and to the turbulent law of Howatson ($C_f = 0.0576\,Re_x^{-0.2}$) on the figure 2.11. The agreement is good.
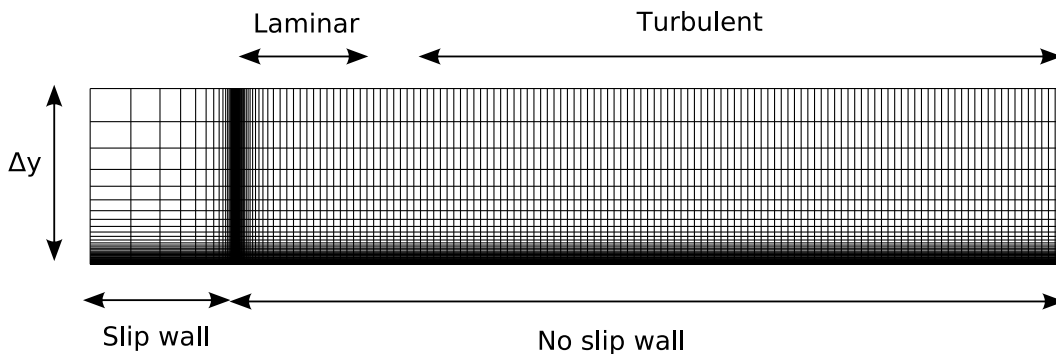


Figure 2.10: Flat plate definition and mesh

## 2.9.2   Channel flow on skewed meshes

The development of a boundary layer over a flat plate presented above is a classic validation testcase for computational codes. It is however often performed on meshes with very high quality which are not always representative of the quality of the actual meshes used for "real" cases. The purpose of the testcase proposed in this section is to test the algorithms,
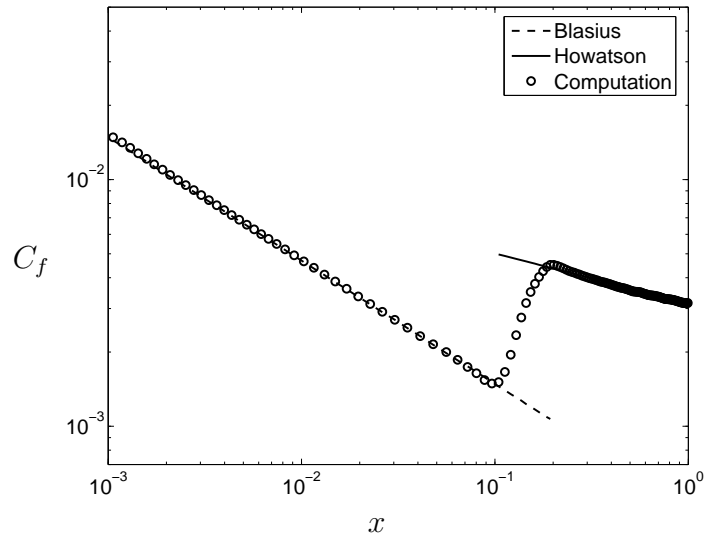
Figure 2.11: Flat plate skin friction coefficient

validated for the flat plate, on meshes which are representative of those used in practical throughflow problems.

The development of the flow inside a channel is studied. A solution is first obtained on a uniform mesh and serves as the reference solution. Next, a computation is performed on a skewed mesh whose quality is similar to the quality of the mesh encountered in a turbomachinery testcase. This is the skewed mesh 1. Finally a computation is performed on an exaggerated skewed mesh. This is the skewed mesh 2. The three meshes are shown on the figure 2.12.

The solutions obtained in terms of axial velocity, entropy and turbulent viscosity are presented on the figure 2.13. which represents radial distributions at the outlet of the channel. The figure 2.13 (a) gives a global overview of the solutions obtained. The three other figures are zooms close to the hub. The solution obtained on the skewed mesh 1 fits exactly the one obtained on the uniform mesh. For the skewed mesh 2, some slight discrepancies occur for the turbulent viscosity which is the less well predicted quantity (figure 2.13 (d)). However, as shown by the axial velocity and the entropy (figure 2.13 (b) and (c)), this has little effect on the flow field.

In conclusion, it has been shown that the implemented scheme correctly predicts the flow on a typical mesh used in this work. It is however true that those skewed meshes do not exhibit all types of errors encountered in real life testcases with, for example, the error due to the misalignment of the points used in the reconstruction process. However, other verification testcases including the curvature of the solid boundaries and which possess exact solutions are not known to the author.
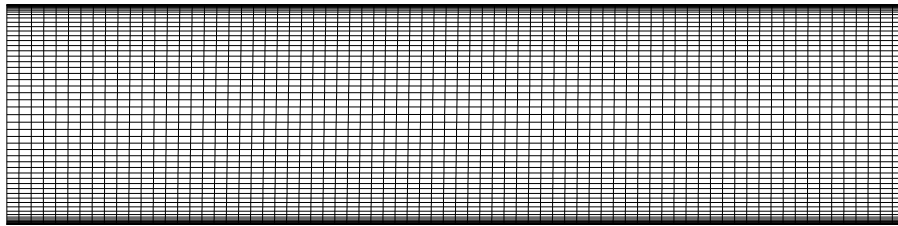
(a) uniform mesh
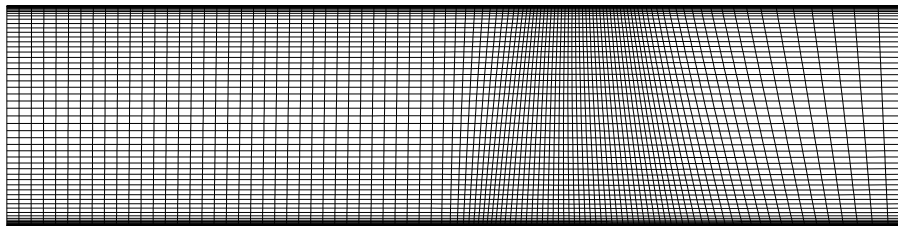


(b) skewed mesh 1
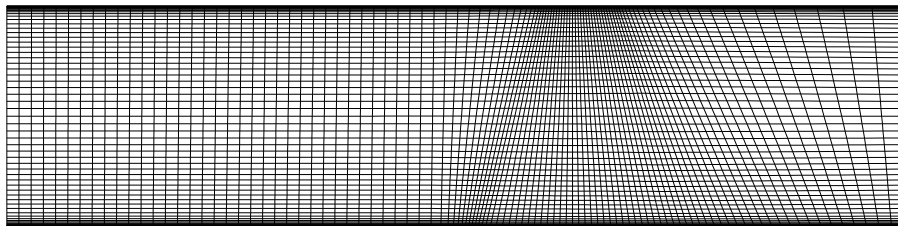


(c) skewed mesh 2

Figure 2.12: Channel flow meshes

(a) axial velocity

(b) axial velocity (zoom)

(c) entropy (zoom)

(d) turbulent viscosity (zoom)
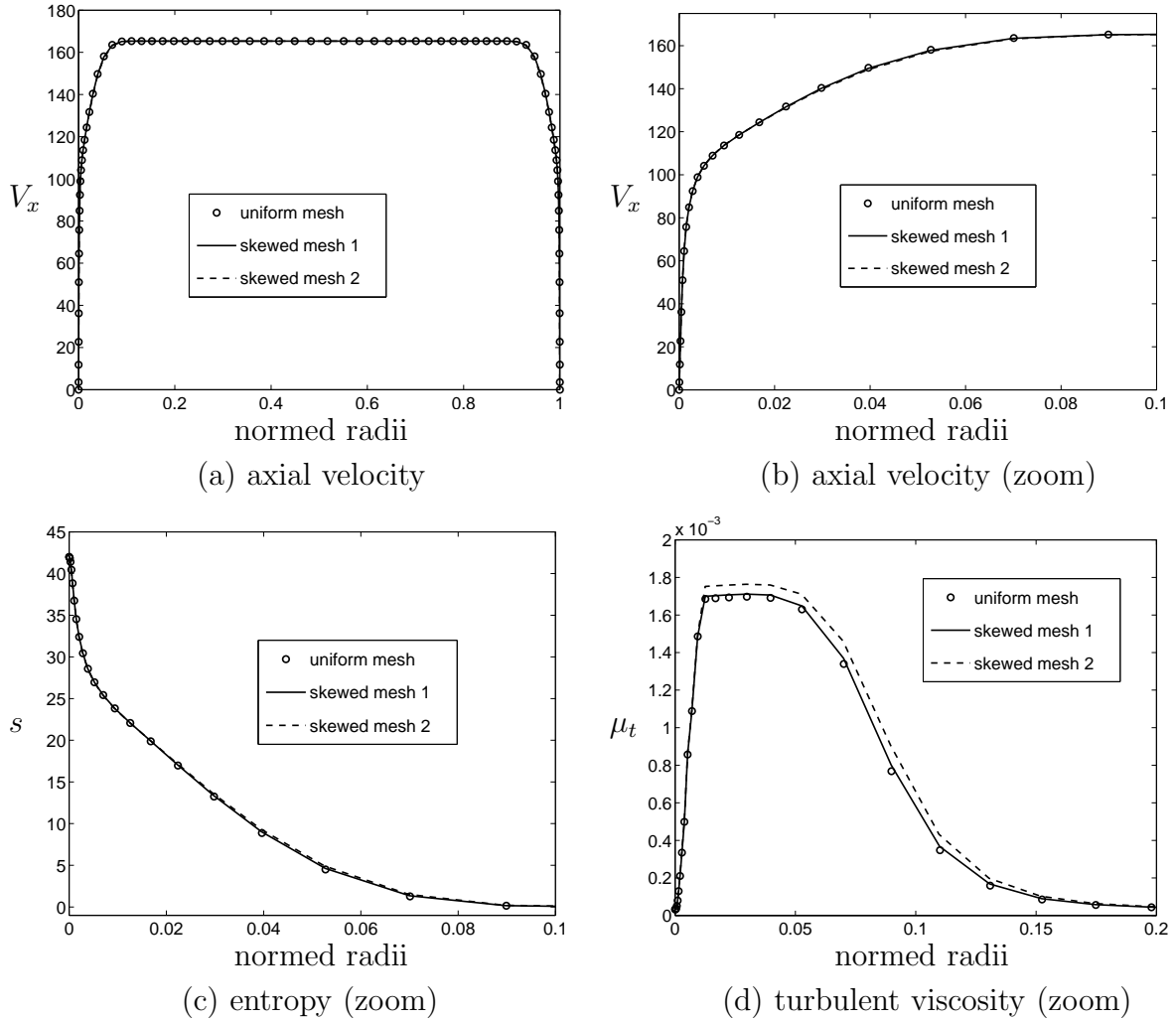
Figure 2.13: Radial distributions at the outlet of the channel. Comparison between the solution computed on skewed meshes and on the uniform mesh

### 2.9.3 Free vortex rotor

This verification case is a theoretical one for which it exists an analytical solution. It allows to check the advective flux implementation together with the blade force model (equation 1.14). It consists in a free vortex rotor, defined by the following radial distributions of the circumferential velocity:

$$V_{\theta 1} = \frac{k_1}{r_1} \qquad V_{\theta 2} = \frac{k_2}{r_2} \tag{2.57}$$

where $k_1$ and $k_2$ are constant.

The rotor is placed within an annular flow path and the flow is supposed to be inviscid. It

is further imposed that the flow is axial at inlet, i.e. $k_1 = 0$. Under those assumptions, an analytical solution exists over which the computed solution can be compared, enabling to check the inviscid part of the solver.

The figure 2.14 compares the results of the computation with the analytical results, in terms of Mach number, static pressure and flow angle. The agreement is perfect validating the model.



(a) Mach number

(b) static pressure

(c) flow angle
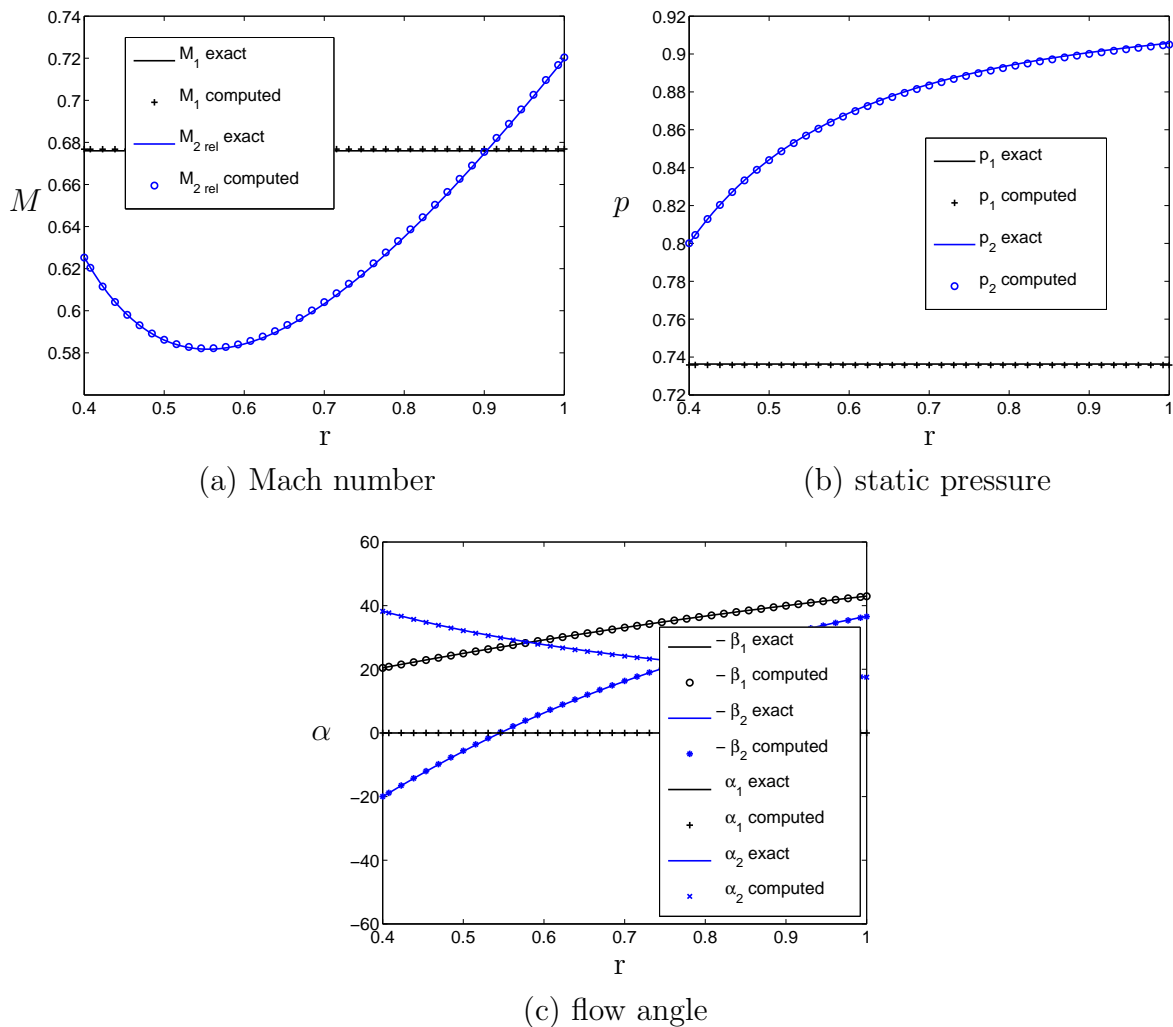
Figure 2.14: Comparison of the radial distributions computed by the throughflow with the analytical solution

# Chapter 3

# Results

This chapter is dedicated to the application of the developed throughflow model to three testcases available in the literature. Each testcase highlights a particular aspect of the physics included in the model. The first one is the Nasa Rotor 67. It is a transonic rotor which will allow to illustrate the shock capturing properties of the model. The second testcase is the PW3S1 compressor. It is a 3.5 stage low speed compressor on which the radial mixing and the viscous calculation will be tested. Finally, a one stage high subsonic compressor from Rolls-Royce will allow to further study the viscous model. The table 3 summarises the main parameters of these three compressors.

| | N stage | $q_m$ [kg/s] | $\pi$ | $\eta_{is}$ | $\Omega$ [RPM] |
|---|---|---|---|---|---|
| NASA 67 | 0.5 | 34.57 | 1.642 | 0.93 | 16043 |
| PW3S1 | 3.5 | 4.28 | 1.346 | 0.861 | 5455 |
| Rolls-Royce | 1 | 8.75 | 1.236 | 0.883 | 9262 |

Table 3.1: Global parameters of the testcases

A last testcase over which the Navier-Stokes throughflow has been applied is not presented in this chapter but in chapter 5. It is the low speed one stage CME2 compressor and it is used for the comparison of a classical throughflow with a high order throughflow.

## 3.1  Nasa Rotor 67

The NASA Rotor 67 is a low aspect ratio transonic axial flow fan. It is widely used in the literature to validate 3-D CFD codes. Its design tip relative Mach number is around 1.38. Experimental measurements on this compressor have been reported by Strazisar *et al.* (1989). The uncertainties on the measurements for the outlet station are given in table 3.2

| Flow angle | 1 deg |
|---|---|
| Temperature | 0.6 K |
| Total pressure | 1000 Pa |
| Static pressure | 700 Pa |

Table 3.2: Maximum uncertainties on the measurements for the outlet station of the NASA Rotor 67

An overview of the meridional flow path is given on the figure 3.1 together with the mesh used in the present study. The mesh is made of $128 \times 31$ grid points with $50 \times 31$ grid points inside the rotor. The model used to compute this compressor is an Euler model (with entropy generating blade force) as it is expected that the main feature of the flow field will be captured by it.
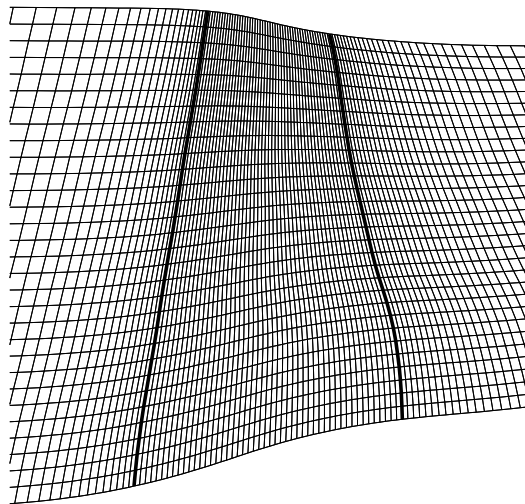


Figure 3.1: NASA Rotor 67 mesh

In the frame of the validation of Euler throughflow models, the rotor 67 has been computed by the following authors: Yao and Hirsch (1995), Sturmayr and Hirsch (1999a); Sturmayr (2004) and Baralon *et al.* (1997, 1998). Large discrepancies are found in the results produced by these authors. This illustrates the difficulty to model transonic compressor in throughflow models. The figure 3.2 shows the different solutions obtained by these authors in terms of the position of the captured shocks. In the case of Yao and Hirsch (1995), it is the static pressure which is given while for the two other authors, the location of the shock is given by the relative Mach number. The discrepancy between the obtained results mainly occurs because of the modelling choices made by the different authors.

Yao and Hirsch (1995) used the real geometry of the rotor for both camber angle and blockage factor. They extracted the deviation and the loss coefficient from the experimental data.

(a)                                    (b)                                    (c)
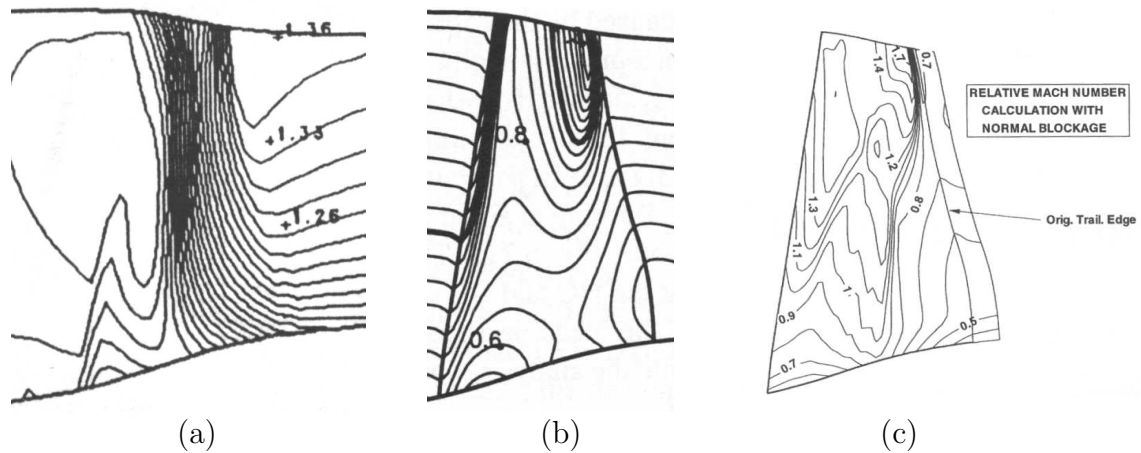
Figure 3.2: Comparison of the location of the shock for the peak efficiency operating point: (a) static pressure contours from Yao and Hirsch (1995), (b) relative Mach number contours from Sturmayr and Hirsch (1999a), (c) relative Mach number contours from Baralon *et al.* (1998)

The shock they captured is nearly radial and located at mid-chord. It extends to about 2/3 of the blade height. The results they present (which are not reproduced here) in terms of radial distributions of the computed quantities at the outlet of the rotor do not match very well the experimental data.

Sturmayr and Hirsch (1999a) computed the Nasa Rotor 67 with both design and analysis methods. The focus is put here on their analysis method which possesses a shock capturing mechanism. The authors didn't use the exact rotor geometry for the camber angle and the blockage factor. They rather replaced them by power laws distributions matching the main parameters of the blade geometry. For example, a streamwise parabolic distribution of the blockage factor is devised which respects the value of the maximum blockage and the location at which it occurs. The flow angle they imposed is equal to the camber angle plus a deviation which is taken from a reference solution. The reference solution is not the experimental data but a 3-D solution obtained from a Navier-Stokes simulation, their purpose being to compare the complete throughflow solution with the 3-D circumferentially averaged solution. Although the 3-D simulation does not match exactly the experimental data, it is considered here to be sufficiently close to be compared with the two other throughflow computations. On the figure 3.2 (b), it can be seen that a two shocks pattern is captured: after capturing a first shock close to the leading edge, the flow re-accelerates until a second shock is captured. This pattern has also been observed by the authors at other operating points. No radial distributions of the computed quantities are provided, making it difficult to judge the accuracy of the model.

Baralon *et al.* (1998) noted the poor quality of the solution obtained when the real geometry is used. They tried to remedy to that problem by introducing a normal blockage, in the

same way as Sayari and Bölcs (1995), in place of the circumferential blockage (see figure 3.3). With this method, the blockage is computed with respect to the streamwise direction in the blade-to-blade plane. This allows a great enhancement of the captured choking mass flow. Baralon *et al.* (1998) showed good results in terms of radial distributions of total pressure and temperature compared to the near-peak efficiency experimental data.
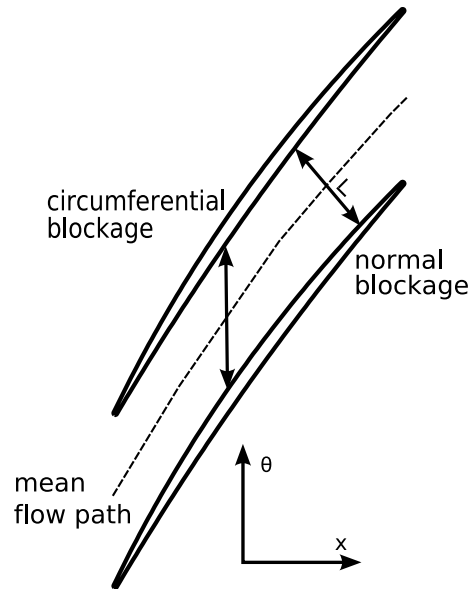


Figure 3.3: Circumferential and normal blockages

## 3.1.1 Analysis method

In the present work, it has also been observed that the use of the real blockage does not lead to correct and accurate solutions. For example, performing a computation with the outlet static pressure and the deviation angle extracted from the near peak efficiency experimental data leads to the obtention of a chocked solution. This is due to the circumferential blockage and is illustrated on the figure 3.4 (a) giving the relative Mach number contours. The captured shock is very close to the trailing edge at tip and extends over the whole span. The obtained choking mass flow is equal to 33.4 kg/s while the experimentally measured mass flow at choke is equal to 34.96 kg/s. This lower value of the chocking mass flow has also been observed by both Yao and Hirsch (1995) and Baralon *et al.* (1998) using the circumferential blockage.

To remedy to this deficiency of the model, the normal blockage proposed by Baralon *et al.* (1998) has been used but under a simplified form which consists in computing the normal blockage as follows:

$$b = b_{circ} \cos \beta_m \tag{3.1}$$

(a) circumferential blockage          (b) normal blockage
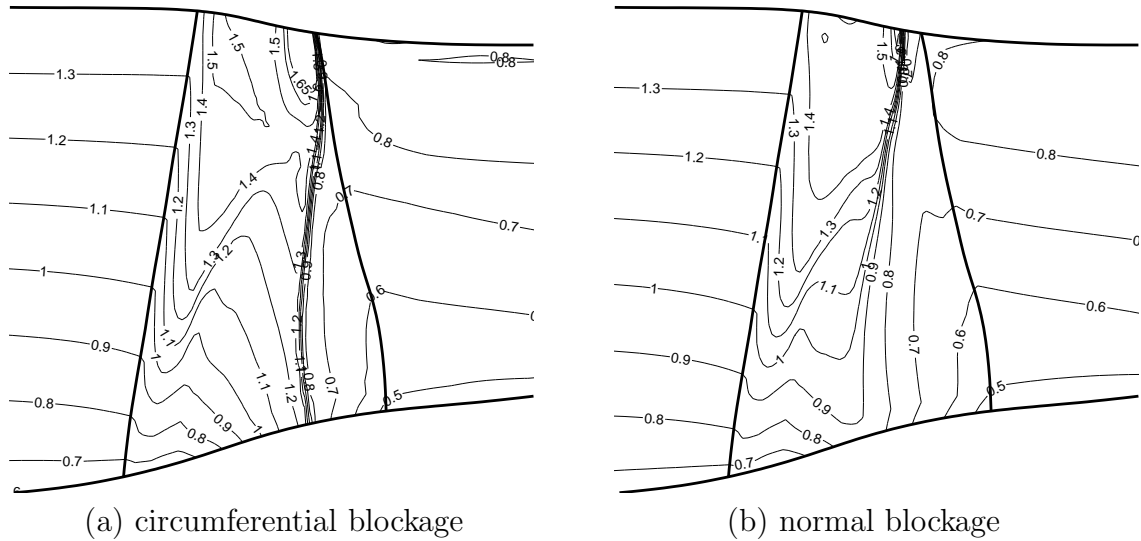
Figure 3.4: Contours of the relative Mach number with the circumferential and the normal blockages

where $b_{circ}$ is the circumferential blockage and $\beta_m$, the blade angle. With this form of blockage, the computed chocking mass flow is now equal to 35.1 kg/s which is very close to the experimental one. The Mach number contours obtained with the normal blockage for the peak efficiency operating point are presented on the figure 3.4 (b). The shock is no longer located at the trailing edge and its radial extent is reduced.

The figure 3.5 compares the results obtained by the throughflow model with the measurements. The deviation distribution has been extracted from the 3-D Navier-Stokes solution of Sturmayr and Hirsch (1999a) and slightly adapted to match the experimental distribution of total temperature. Similarly, a realistic but arbitrary distribution of losses has been imposed. However, no loss has been imposed on the last 30 % of the span as it was expected that the captured shock would give too much loss in that region. The overall agreement between the computation and the measurements is thought to be rather good. To help us to judge of the quality of the results, those of a 3-D Navier-Stokes simulation performed by Arnone (1994) are presented at the figure 3.6.

The main discrepancy between the solution and the measurements is found to be close to the tip section where the captured shock generates too much loss. On the figure 3.5 (a), the distribution of total pressure that would result of an isentropic evolution of the flow for the same temperature ratio is given. It helps in evaluating the level of loss generated by the shock. The main weakness of the followed approach is that the intensity of the shock, and therefore of the loss it generates, cannot be controlled as it is given by the upstream Mach number and the geometry. The computed isentropic efficiency is equal to 0.91, compared to the 0.93 measured experimentally. This measured isentropic efficiency is probably overestimated due to the lack of measurements in the boundary layer at the outlet of the rotor as can be seen from the radial distribution of measurement points on the figure 3.5.

(a) total pressure ratio

(b) total temperature ratio

(c) static pressure

(d) absolute flow angle
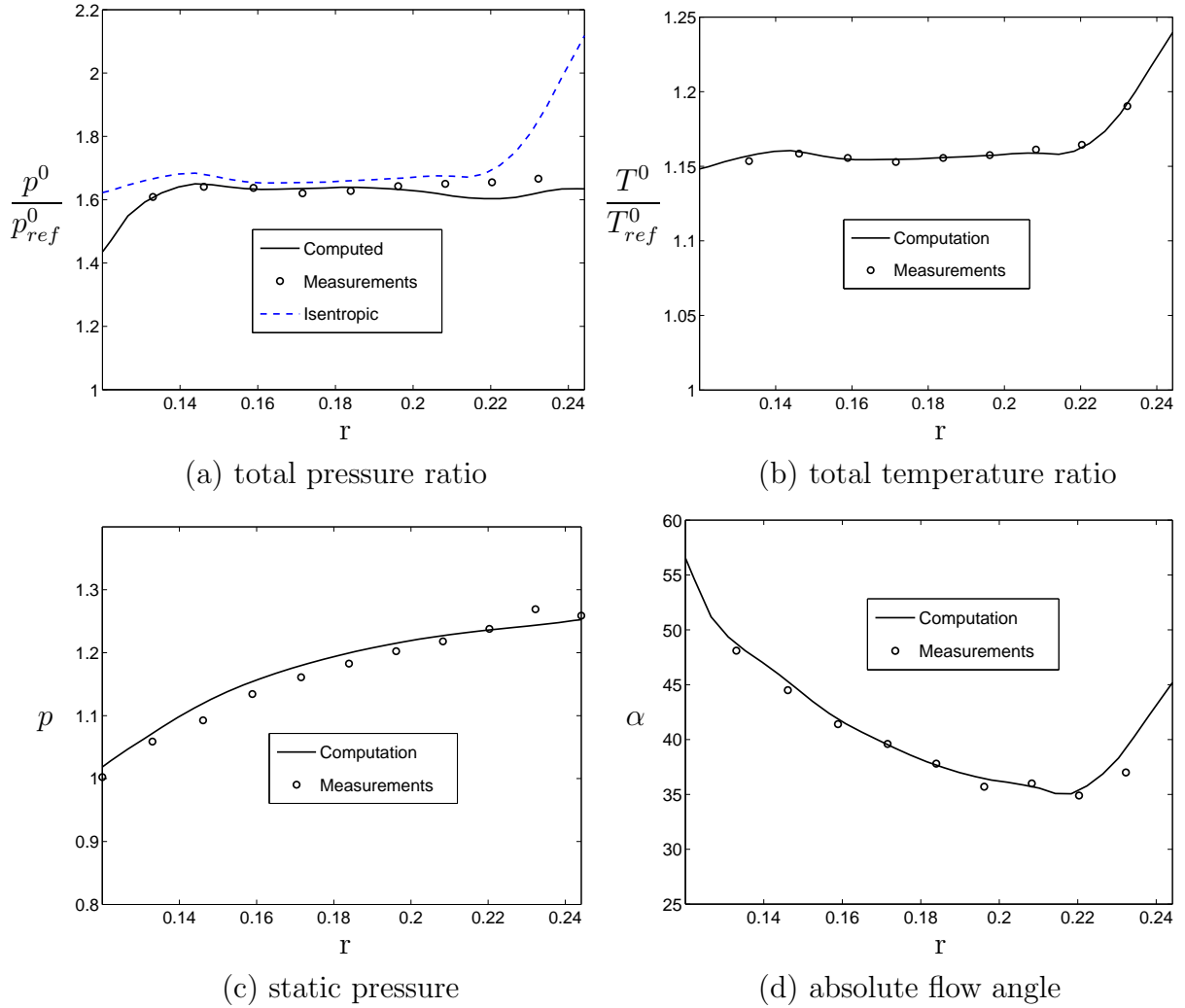
Figure 3.5: Comparison of the computed distributions of quantities at the outlet of the rotor with the measurements. The computation has been run with the normal blockage.

On the figures 3.5 (b) and (d), the agreement of both the total temperature and the absolute flow angle means that the correct velocity level has been computed. Indeed the Euler equation for turbomachines coupled to the balance of the energy show that the obtention of the correct total temperature implies that the circumferential velocity has been computed correctly. Besides, the agreement of the absolute flow angle means that the axial velocity is also correctly predicted. This can be summarised by the following relations valid along a streamline between the inlet and the outlet of the rotor:

$$C_p \Delta T^0 = \Delta\left(U V_\theta\right) = \Delta\left(U V_x \tan\beta + U^2\right) \tag{3.2}$$

where $U$ is the peripheral velocity which is more or less constant over a streamline.
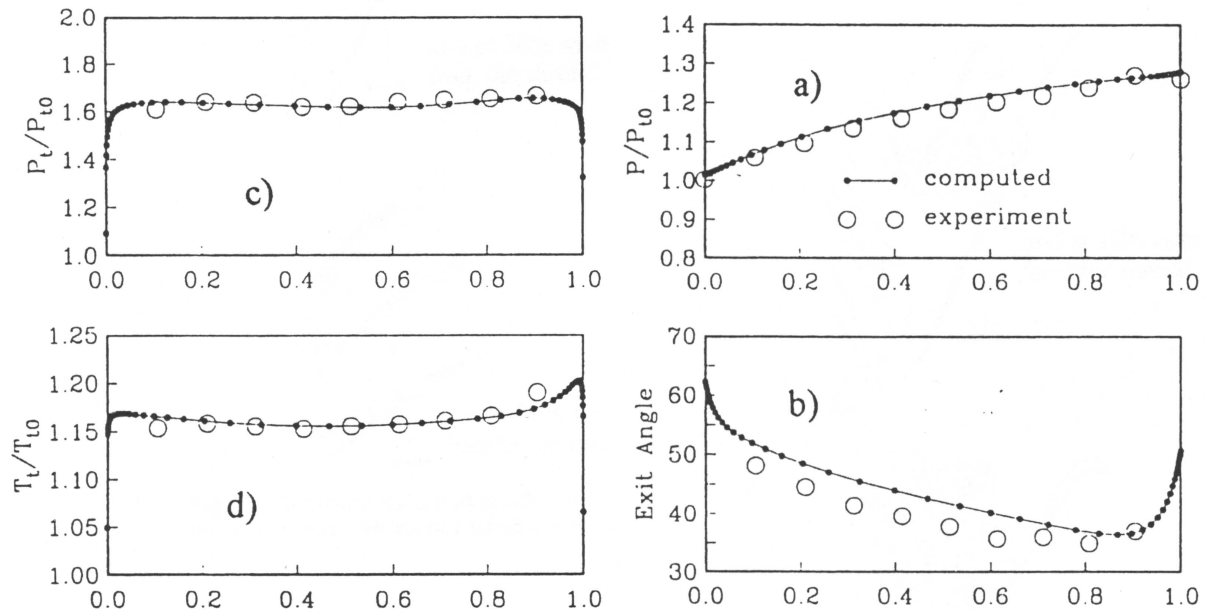
Figure 3.6: Results of a 3-D viscous computation of the NASA Rotor 67 (Arnone, 1994)

## 3.1.2   Design method

Another computation has been run on the Nasa Rotor 67 testcase using the design formulation for the blade force calculation. The flow angle is specified at the trailing edge. From this flow angle, the circumferential velocity can by computed with the help of the actual axial velocity. A linear evolution of this circumferential velocity between the leading edge value and the trailing edge value is used to compute $W_\theta$ inside the blade row. It is sure that a more elaborated distribution can be devised but it is sufficiently accurate for the discussion to be presented here.

The figure 3.7 shows the results obtained with the design formulation. To achieve the correct work done in the rotor, the relative flow angle at the trailing edge has been adjusted, via the deviation, to match the total temperature distribution. As no shock is captured, the losses in the tip region are underpredicted and the total pressure is overpredicted. It is necessary to add a specific relation giving the loss generated by the shock. The flow angle is also not correctly predicted in the tip region despite the fact that the total temperature is and, by there, the circumferential velocity increase through the rotor (figure 3.7 (b)). This is due to the fact that it is a diffusion process that has led to the work done and not a shock. The axial velocity is too high leading to a too low flow angle for the correct circumferential velocity.

(a) total pressure ratio

(b) total temperature ratio

(c) static pressure

(d) absolute flow angle
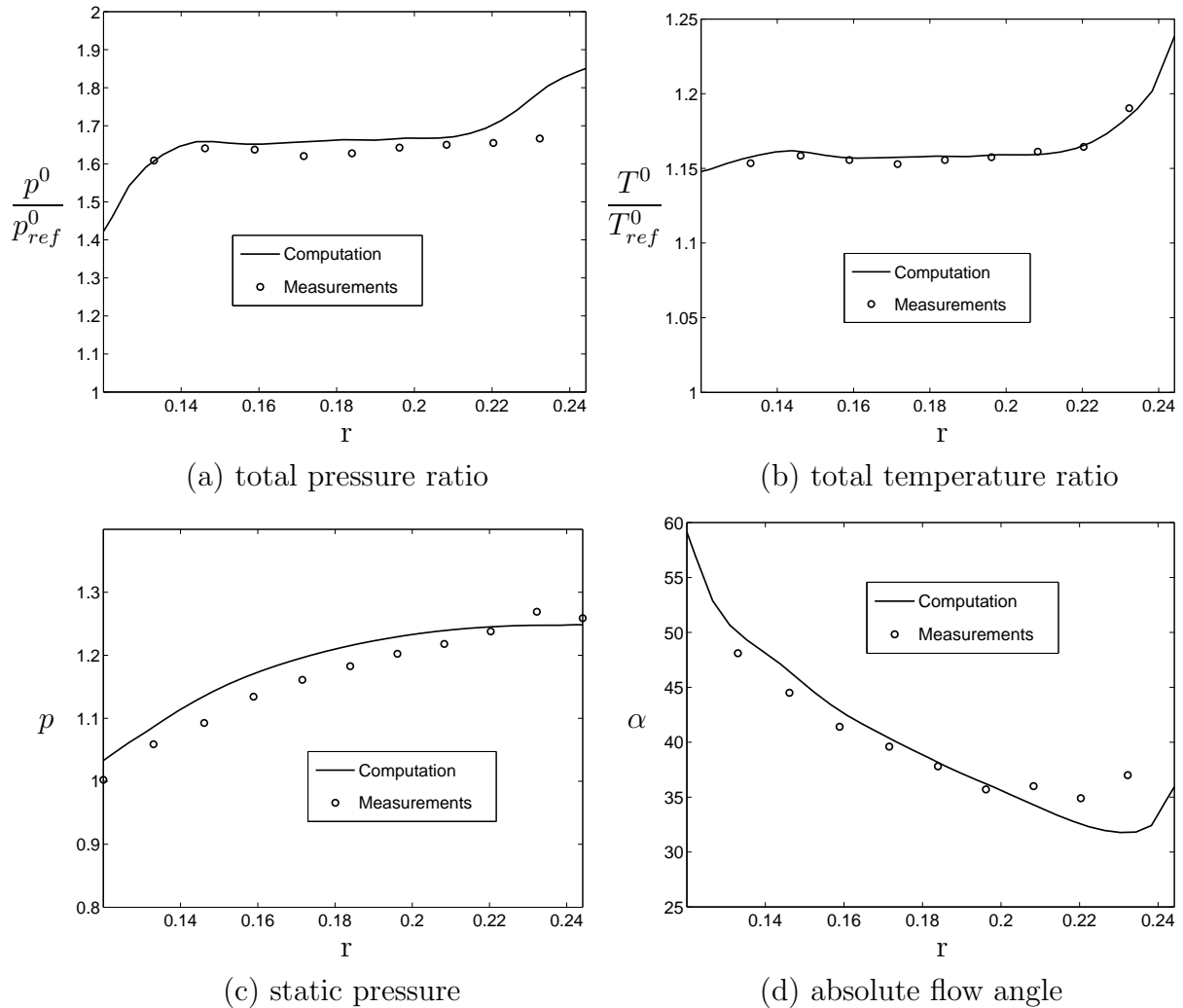
Figure 3.7: Comparison of the computed distributions of quantities at the outlet of the rotor with the measurements. Design formulation.

### 3.1.3   Conclusions

Concerning the analysis method, its main drawback is that it is not possible to control the intensity of the shock and from there the level of losses. This may, in general, lead to an overestimation of the losses. It seems that there is no obvious solution to this problem. A second drawback that must be acknowledged is that in the course of obtaining a solution for the present testcase, it has been found that the solution is extremely sensitive to the blockage and to the flow angle distributions. For example, a two shocks pattern can be obtained if the leading edge adaptation is performed on a too long portion of the chord. The influence of the blockage has also been demonstrated by the drastically different solutions obtained with the circumferential and the normal blockages.

On the other hand, for the design method, the obtained solution at the outlet of the blade row is not very sensitive to the blockage and to the swirl velocity distributions. The drawback of the design method is that because it has no built-in mechanism to generate shock, additional loss must be added, in the same way as for the classical SLC throughflow codes. Furthermore, it has also no built-in mechanism to predict choking mass flow.

It seems that the debate on which throughflow model is the most appropriate to compute transonic compressors is still open.

## 3.2   PW3S1 3.5-stage compressor

The PW3S1 and PW3S2 are both 3.5 stage compressors designed and tested by Burdsall *et al.* (1979) and Behlke *et al.* (1979). They have been noteworthy used by both Adkins and Smith (1982) and Gallimore (1986) to validate their respective spanwise mixing models. The difference between the two compressors lies in their aspect ratios. Only the lower aspect ratio configuration, called 3S1, has been considered here. A meridional overview of the compressor is shown on the figure 3.8. The inlet guide vane has been included in the simulation. The three stators are cantilevered and the averaged hub and shroud clearance is 1.4 % of the span. The annulus walls are cylindrical and considered as adiabatic.
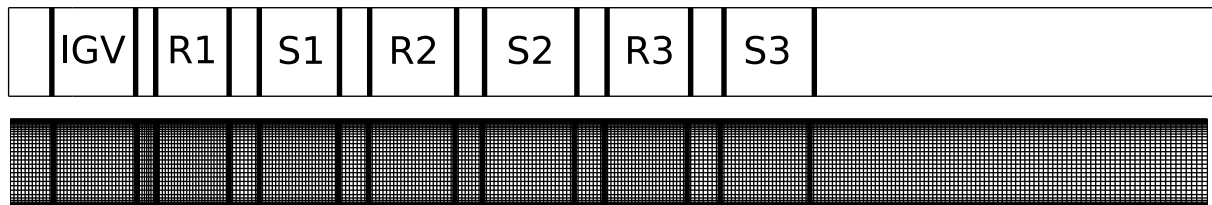


Figure 3.8: Overview of the PW3S1 computational domain and the corresponding Navier-Stokes mesh

The following correlations have been used for the loss and the deviation. The 2-D deviation is estimated by the Carter's rule (design) and the correlation of Creveling (1968) (off-design) while the profile losses are obtained from the Koch and Smith (1976) (design) and Creveling (1968) (off-design) correlations. Three-dimensional losses are added following Roberts *et al.* (1986, 1988).

Behlke *et al.* (1979) have reported experimental distributions of total pressure and total temperature at the inlet and outlet sections of the compressor. The outlet measurement plane is placed several chords downstream of the last stator. The uncertainty concerning the measurements is 0.1% of the full-scale reading for the pressure and 0.14 °C for the temperature. In order to estimate the improvement brought by the Navier-Stokes model

and to illustrate the effect of the spanwise mixing, three numerical simulations have been performed and will be compared to the measurements:

1. an Euler-based computation with 2-D and 3-D losses (Euler calculation 1),

2. the same Euler-based computation plus the spanwise mixing model (Euler calculation 2),

3. a full Navier-Stokes computation including the spanwise mixing model.

The level of turbulent viscosity required by the spanwise mixing model has been computed from the relation given by Gallimore and Cumpsty (1986) and is equal to approximately 900 times the kinematic viscosity. As shown by Gallimore (1986), the exact level of the turbulent viscosity for the radial mixing model is not very important.

The mesh used for the Euler computations is composed of $318 \times 30$ cells with approximately 25 cells axially in each blade row. The Navier-Stokes computation shares the same axial distribution of cells but 60 cells are distributed radially. The same back pressure has been specified at the hub for the 3 computations. Due to the geometry of the domain, high axial length to radial length ratio, the Runge-Kutta scheme RK31B has been chosen for its transient damping properties. It allows to reach the steady state, characterised by a drop of the residual of five orders, 20 % faster then the RK41A scheme. The value of the CFL is taken to 7 with a residual smoothing factor equal to 10. The computational time is, respectively for the 3 computations, 6, 9 and 13 minutes on a Pentium 4 at 3 GHz.

The large computation times are due to the low speed nature of this testcase, as the convergence of the algorithm is slowed down at low Mach numbers. This problem could be solved by locally preconditioning the set of equations. It is noticeable that the Navier-Stokes computation is only 1.5 times slower than the Euler computation with radial mixing model. The computational cost per node is approximately equal for both computations but the Navier-Stokes one has two times more nodes. However, the number of iterations required to reach the specified accuracy is lower for the Navier-Stokes computation due to a better damping of the oscillations inside the domain. On this subject, the spanwise mixing model has a beneficial effect on the convergence speed thanks to the high level of viscosity inside the domain.

The figure 3.9 (a) gives the radial distribution of total temperature and clearly illustrates the benefit of including a spanwise mixing model. Both the Navier-Stokes and the Euler computation 2 capture the correct redistribution of the energy along the span and thus avoid the accumulation of total temperature close to the endwalls. The difference in the mean level of total temperature at the outlet for the three computations is due to the different levels of captured losses. As the same outlet static pressure is applied for the three computations, the mean levels of total pressure at outlet are approximately equal (see table

3.3). The underprediction of losses by both Euler computations therefore is responsible for a lower level of total temperature when compared to the measurements or to the Navier-Stokes computation.



(a) total temperature  (b) total pressure
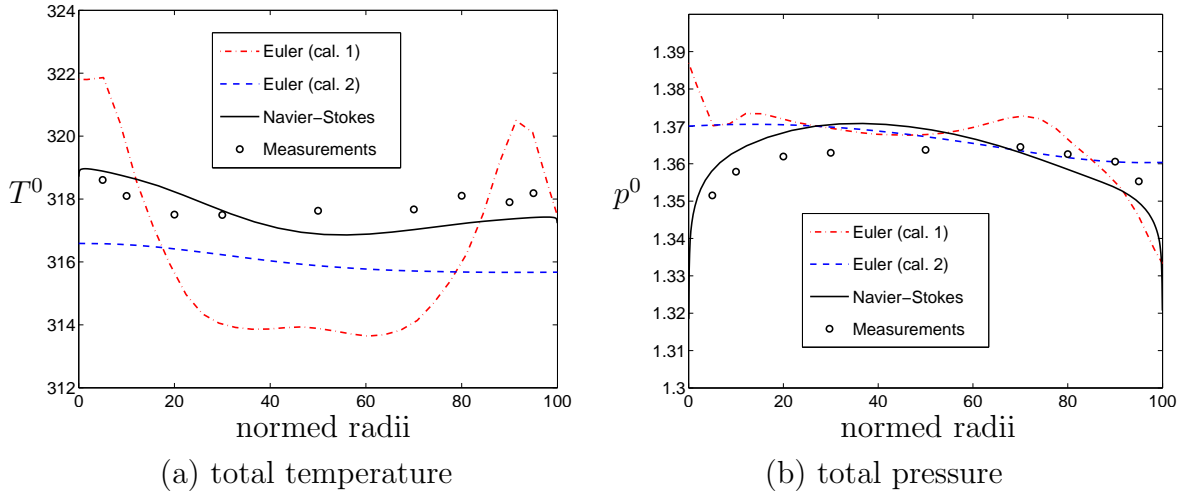
Figure 3.9: Radial distributions of total pressure and temperature at the outlet of the PW3S1 compressor

The Navier-Stokes model captures the high gradients near the endwalls. This results in a realistic total pressure distribution in these regions. The radical improvement of the predicted total pressure compared to the Euler model is shown on the figure 3.9 (b). This results in a good estimation of the isentropic efficiency (table 3.3). As the blockage of the boundary layer has also been well estimated, the computed mass flow agrees well with the measured one, as shown on the table 3.3. This is not the case for the Euler computations which underestimate both the losses and the flow blockage due to the endwalls, despite the fact that they include 3-D losses and deviation.

It is noteworthy that the difference between the computed global performances for the two Euler calculations is very weak despite the large difference in the radial distributions. This is due to the fact the spanwise mixing model contributes only weakly to the generation of losses and blockage. The lack of measurements close to the endwalls does not allow further comparisons between the Navier-Stokes solution and the measurements.

## 3.3 Rolls-Royce 1-stage compressor

This testcase is a single stage high subsonic compressor for which measurements have been reported by Ginder and Harris (1990). It is a close-coupled stage with moderate loading and high reaction. It has conventional blade profiles, DCA for the rotor and C4 mod 2 for the stator. Only the rotor is cantilevered with an average tip clearance of 0.25 % of the blade

|                | $q_m$ (kg/s) | $\pi$  | $\eta_{is}$ |
|----------------|--------------|--------|-------------|
| Measurements   | 4.28         | 1.346  | 0.861       |
| Euler (cal.1 ) | 4.44         | 1.349  | 0.925       |
| Euler (cal. 2) | 4.48         | 1.349  | 0.921       |
| Navier-Stokes  | 4.30         | 1.346  | 0.869       |

Table 3.3: Comparison of the computed global performances to the measured ones for the PW3S1 compressor

height. A particularity of this testcase is the thick annulus endwall boundary layer at inlet (10 to 20 % of the annulus height), from which the interest for testing the Navier-Stokes model.

The flow path is represented on the figure 3.10. The experimenters used spoiler rings on the hub and casing to generate a suitable inlet velocity profile. The location of the spoiler coincides with the inlet of the physical domain shown on the figure 3.10. However, no measurements are available just downstream of this spoiler to provide the inlet boundary conditions to the numerical simulation.

The first measurement plane that can provide the inlet conditions is close to the leading edge of the rotor, at the end of the convergent part of the flow path. The mesh starts at this location on the figure 3.10. The flow angle between the projection of the velocity in the meridional plane and the axial direction (the streamline slope) at the inlet of the domain had to be approximated as it was not provided in the data. It has been approximated by a linear variation from the wall angle at the hub and at the casing.

Contrary to 3-D simulations, for which it is important to avoid placing the inlet and the outlet planes too close to the blade leading and trailing edges, the short distance between the inlet plane and the leading edge of the rotor did not bring any problem. Indeed, as a throughflow model is axisymmetric, there is no incompatibility with the flow and the imposed axisymmetric boundary conditions. The sole problem at the throughflow level in terms of the positioning of the inlet and outlet planes could be due to the curvature of the streamlines set up by the blade and that cannot be handled by the boundary conditions.

The empirical correlations of Carter, Koch and Smith (1976) and Creveling (1968) for the profile losses and deviations, and the correlations of Roberts *et al.* (1986, 1988) for the 3-D effects are used. The correlation for the deviation has however been slightly modified. An additional two degrees deviation has been added to the Carter's rule. Such a modification of the Carter's rule is a common practice (Cumpsty, 1989). As it will be shown below, this allows to match both mass flow and work input for the nominal speedline of the compressor.

The Euler mesh has 105×35 cells and the Navier-Stokes one 113×60 cells. The computational time for a drop of the residual of 5 orders is, respectively for both computations, 1.5 and 2.5

minutes on a Pentium 4 at 3 GHz.

Radial distributions of different measured quantities are compared to the solution obtained with the Navier-Stokes and the Euler-based models including 3-D losses and spanwise mixing model. Both computations were performed with the same back pressure at the hub.

Before analysing the results, it is worth noting that, according to the experimenters (Ginder and Harris, 1990), the main weakness of this testcase is the uncertainty surrounding the rotor exit conditions. Moreover, the experimenters have scaled certain measured quantities, such as the total temperature at the rotor outlet (figure 3.12 (a)) to match the overall performance. Therefore, comparisons between different locations are made difficult. This can partly explain the discrepancies between calculations and measurements, particularly for the total temperature at the rotor outlet. No indication concerning the measurements accuracy is available.

The figures 3.11 (a) and (b) compare measurements at the stator exit with the predictions. The radical improvement on the total pressure distribution brought by the Navier-Stokes model with respect to the Euler one is due to the high losses near the endwalls captured by the Navier-Stokes model. This enables a low total pressure, together with a low axial velocity and a high level of energy input in the rotor (figure 3.12 (a)).

The figure 3.11 (a) shows that, at both endwalls, the temperature is overpredicted. For the tip section, it is due to an overprediction of the total temperature at the outlet of the rotor (figure 3.12 (a)). Concerning the hub section, it seems that a high mixing occurs between the rotor and stator exit measurement planes, respectively located at 5 % of the axial chord ahead of the leading edge of the stator and 30 % of the axial chord downstream the trailing edge of the stator. This high mixing may be of the unsteady type and is not present in the simulation.

Important differences in the total temperature (figure 3.12 (a)), and to a smaller extent in the absolute flow angle (figure 3.12 (b)), are observed between the results of the Navier-
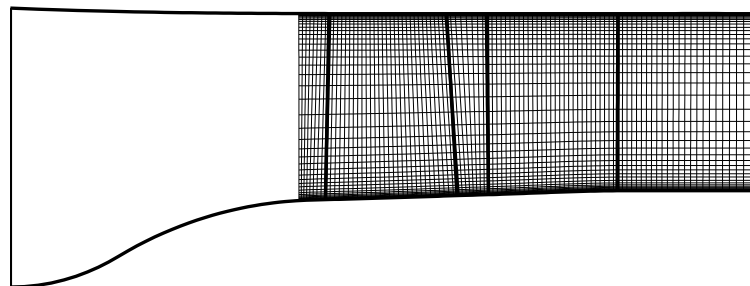


Figure 3.10: Overview of the Rolls-Royce compressor flow path and Navier-Stokes mesh

(a) total temperature ratio

(b) total pressure ratio
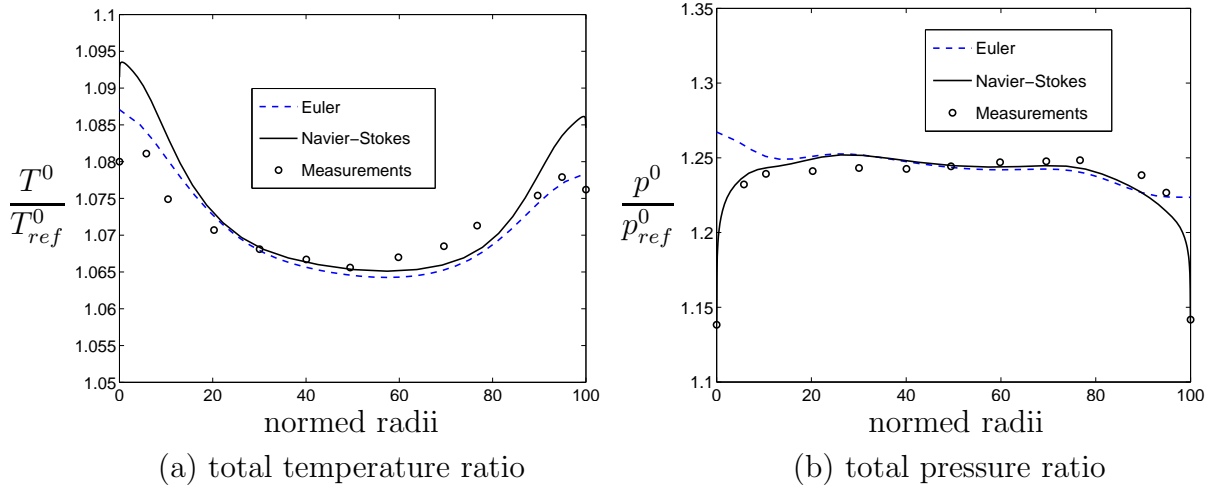
Figure 3.11: Radial distributions of total temperature and pressure at the outlet of the stator of the Rolls-Royce compressor



(a) total temperature ratio

(b) absolute flow angle
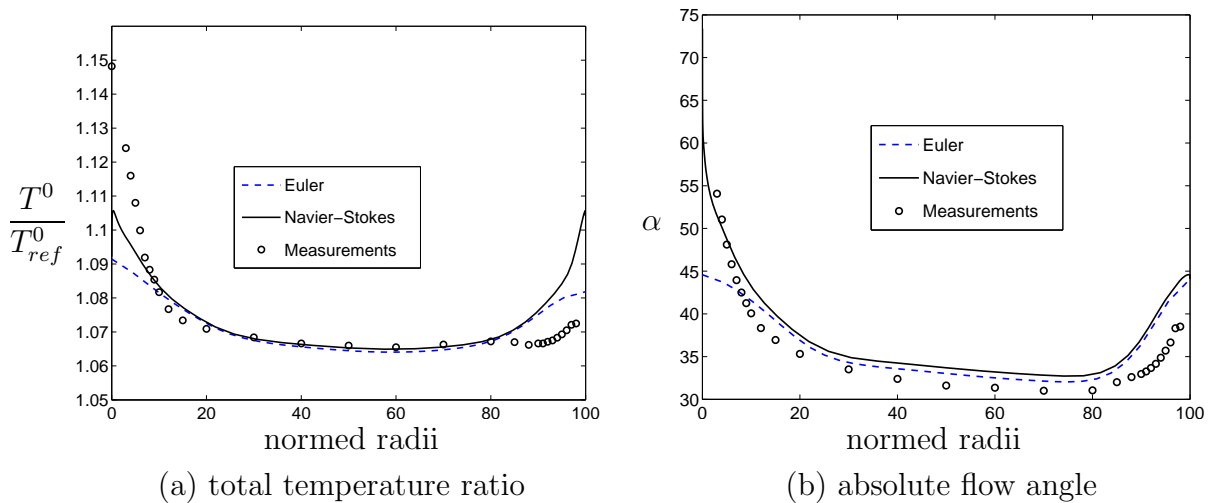
Figure 3.12: Radial distributions of temperature and absolute flow angle at the outlet of the rotor of the Rolls-Royce compressor

Stokes model and the measurements at the rotor exit. In the Navier-Stokes simulation, the principal characteristic of the flow near the annulus wall is the re-energetisation of the flow in the rotor due to the low axial velocity, somewhat balanced by the underturning (at the tip) or accentuated by the overturning (at the hub) as predicted by the 3-D empirical correlations.

At the tip, the high energy input predicted by the calculation is not present in the measurements, indicating that the underturning has been underestimated and/or that the velocity defect near the annulus endwalls is badly estimated. Indeed, in this rotor, for which the inlet flow is axial and the inlet total temperature is uniform, the total temperature and the absolute flow angle at the rotor exit (station 2) are linked by the following relation (from

the Euler equation and the energy balance):

$$\frac{T_2^0}{T_{in}^0} = 1 + \frac{1}{C_p T_{in}^0} \; \Omega r_2 \; \tan \alpha_2 \; V_{x2} = 1 + \frac{1}{C_p T_{in}^0} \; \Omega r_2 \; (\tan \beta_2 \; V_{x2} + \Omega r_2) \qquad (3.3)$$

Thus, the discrepancy can be attributed either to a bad prediction of $V_{x2}$, $\beta_2$ or of both quantities. It is not possible to choose between the explanations because no measurement of the velocity magnitude are available. However, the errors in total temperature and flow angle are well correlated, meaning that the discrepancy probably comes from the deviation modelling and that the velocity defect is rather well estimated. The same reasoning applies to the hub flow.

The table 3.4 compares the global performances computed by the Euler and the Navier-Stokes models with the measurements. For the correct mass flow, the Navier-Stokes computation slightly overpredicts the pressure ratio. This is due to the overprediction of the total temperature ratio as the isentropic efficiency has been correctly estimated. The Euler computation with 3-D losses and spanwise mixing model does not capture the flow blockage and overpredicts the mass flow by 3 %. It also overpredicts the isentropic efficiency.

| | $q_m$ (kg/s) | $\pi$ | $\eta_{is}$ |
|---|---|---|---|
| Measurements | 8.75 | 1.236 | 0.883 |
| Euler | 9.0 | 1.244 | 0.912 |
| Navier-Stokes | 8.77 | 1.24 | 0.881 |

Table 3.4: Comparison of the computed global performances to the measured ones for the Rolls-Royce compressor

In order to further establish the benefit brought by the Navier-Stokes model compared to the Euler one, a complete characteristic line, corresponding to the nominal rotational speed, has been computed with both models. The different operating points on the characteristic line are obtained by varying the back static pressure. The results are presented on the figures 3.13 (a) and (b) for the Navier-Stokes model and on the figure 3.14 (a) and (b) for the Euler model, in terms of pressure ratio and isentropic efficiency versus mass flow. These characteristics are well captured by the Navier-Stokes model but not so well by the Euler model.

The dynamic behaviour with the incidence, i.e. with the varying mass flow, is mainly given by the 2-D empirical correlations as the used 3-D losses correlations are valid only for the design point and do not include any effect of the incidence. The improvement brought by the Navier-Stokes model relies more or less in the correct level of loss and flow blockage. It only contributes weakly to the variation of the performance with the incidence. For that reason, the shape of the obtained characteristic for both models on the figures 3.13 and 3.14 are quite similar but the characteristics obtained with the Euler based model are shifted toward higher mass flows and lower losses.

(a) pressure ratio  (b) isentropic efficiency

Figure 3.13: Performance map of the Rolls-Royce compressor for the nominal speed line. The blockage factor is of the normal type



(a) pressure ratio  (b) isentropic efficiency
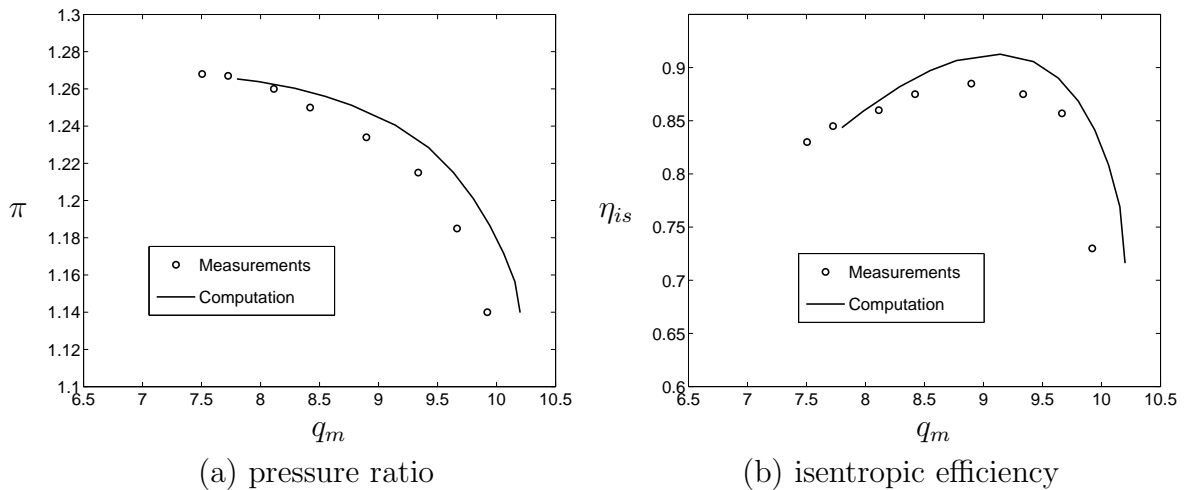
Figure 3.14: Performance map of the Rolls-Royce compressor for the nominal speed line. The computation is of the Euler type.

At low mass flow, the characteristics are limited by the non-convergence of the computational code. In the case of the Navier-Stokes computation, close to the (numerical) stall, a recirculation zone appears in front of the rotor. As the back pressure is further increased, the recirculation zone grows until it reaches the inlet of the computational domain. At that moment, the time integration diverges as improper boundary conditions are now apply with respect to the recirculation zone. The velocity vectors close to the inlet boundary have been represented on the figure 3.15 (a) for the lower back pressure leading to divergence. On the right of the figure the trace of the leading edge is shown. It can be seen that the flow is leaving the computational domain by the inlet plane. For the Euler model, the mode of divergence is similar (figure 3.15 (b)). The physical meaning of the recirculation is less obvious in this case.

(a) Navier-Stokes computation  (b) Euler computation
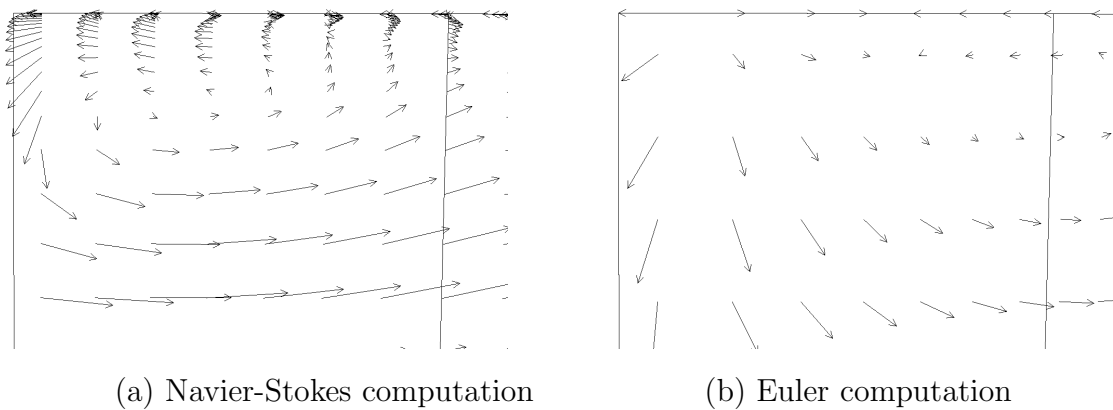
Figure 3.15: Velocity vectors at inlet of the domain and close to the casing of the Rolls-Royce compressor. This is for the stall operating point. The trace of the leading edge is visible on the right of the figure.

Finally, a Navier-Stokes computation has been run with the circumferential blockage instead of the normal blockage (equation 3.1). The resulting characteristics are given on the figures 3.16 (a) and (b). The solution is very close to the one obtained with the normal blockage (figure 3.13) over the major part of the characteristic. However at high mass flow, a chocking condition is obtained with the circumferential blockage. This advocates the use of the normal blockage not only for transonic compressors (see section 3.1) but also for fully subsonic compressors.
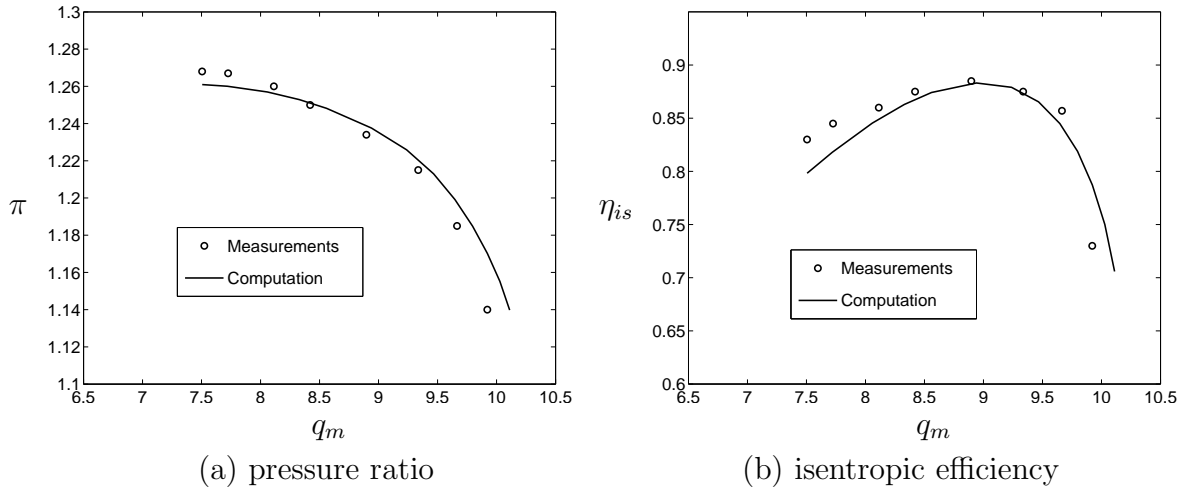




(a) pressure ratio  (b) isentropic efficiency.
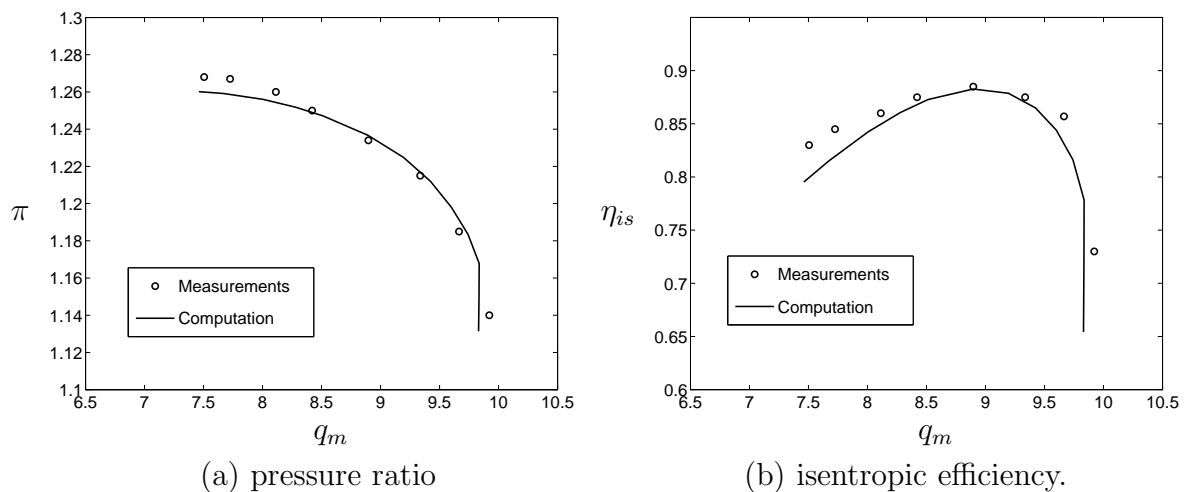
Figure 3.16: Performance map of the Rolls-Royce compressor for the nominal speed line. The blockage factor is of the circumferential type

# Chapter 4

# High order throughflow method

The main drawback of the throughflow models is that they heavily rely on empirical inputs such as the deviation angle correlation or the annulus endwall boundary layer model. While these models are able to produce accurate results for machines for which they have been devised or calibrated, it should not be expected that they work well for different machines with different bladings. It is obviously a problem from the designer point of view when new machines with new paremeters lying outside of the database of the known bladings are to be designed.

The Navier-Stokes throughflow model presented in chapter 1 represents a step in the direction of less empiricism by incorporating more physics in the model. However, as for classical throughflow models, some inputs of empirical nature must still be provided. A further step in the direction of less empiricism is presented in this chapter. It is based on the average cascade of Adamczyk (1984).

It is well known that the flow field inside a multistage turbomachine is extremely complex. It is 3-D, unsteady and turbulent. The time scales, as well as the space scales, that are involved in such a flow are numerous. The direct simulation of the Navier-Stokes equations for these problems is far beyond the capabilities of the today's most powerful computer. Even the Unsteady Reynolds-Averaged Navier-Stokes (URANS) simulation for multistage configuration, although possible with supercalculators, is too expensive to be used in the design process of a compressor or a turbine. In addition, it is not straightforward to extract useful guidelines for the designer from the information given by such a simulation. Therefore, more practical solutions must be sought.

With this idea in mind, Adamczyk (1984) has developed a model that allows to link the unsteady turbulent flow field to a steady representation of the flow field within a typical blade passage of a blade row embedded in a multistage configuration. The underlying model is referred to as the average-passage flow model. It consists in applying several filters or

averaging operators to the turbulent flow field and its associated equations. The resulting equations only resolve the flow structures that are not filtered out by the averaging process. The solution obtained with the averaged set of equations is (theoretically) identical to the one that would be obtained by *a posteriori* averaging the solution given by the non-averaged set of equations.

The first averaging operation defined in the Adamczyk model is the well known Reynolds ensemble-averaging. It eliminates the need to resolve the turbulent structure of the flow. Applied to the Navier-Stokes equations, it yields to the classical Reynolds-Averaged Navier-Stokes equations. Theses equations are similar to the Navier-Stokes equations but additional terms appear bringing back the mean effect of the turbulence on the mean flow field. The resulting flow field is still unsteady but deterministic.

The second average is a time-average. It removes the remaining deterministic unsteadiness which is linked to the rotation of the shaft. A typical deterministic unsteady phenomenon is the blade wake chopping by the downstream blade row. The application of this average to the unsteady RANS equations brings additional terms that represent the mean effect of the deterministic unsteadiness on the steady flow field.

For multistage configuration, the steady flow field is not in general spatially periodic from a blade passage to another blade passage of the same blade row. A typical aperiodic phenomenon is the blade indexing effect (the relative circumferential position of the blade rows placed on the same shaft). A third average, the passage-to-passage average, is introduced by Adamczyk. It allows to obtain a spatially periodic flow over the pitch. This average introduces also additional terms that represent the mean effect of the aperiodicity of the flow on the mean periodic flow. The resultant flow field is referred to as the average-passage flow and its associated set of equations is the average-passage set of equations of Adamczyk. A great introduction to the flow physics linked to the average-passage equations can be found in Adamczyk (1999) together with results from several simulations performed on both high and low-speed compressors and turbines.

As it is the throughflow level of approximation which is of interest here, an additional averaging operation is performed on the average-passage system of equations: a circumferential averaging. Here again, this procedure brings additional terms in the set of equations.

In the following, the different averaging procedures are detailed. As an example, each average is applied to the axial component of the momentum equation. The result of the application of the averaging to the complete Navier-Stokes equations is detailed in the appendix B.

In cylindrical coordinates, the axial component of the momentum of the instantaneous Navier-Stokes equations is written:

$$\frac{\partial \rho V_x}{\partial t} + \frac{\partial \left( \rho V_x V_x + p \right)}{\partial x} + \frac{1}{r} \frac{\partial r \rho V_r V_x}{\partial r} + \frac{1}{r} \frac{\partial \rho V_\theta V_x}{\partial \theta} = \frac{\partial \tau_{xx}}{\partial x} + \frac{1}{r} \frac{\partial r \tau_{rx}}{\partial r} + \frac{1}{r} \frac{\partial \tau_{r\theta}}{\partial \theta} \qquad (4.1)$$

## 4.1 Reynolds ensemble-averaging operator

The purpose of this average is to remove all the flow features that are not correlated to the rotation of the shaft while only retaining the unsteady deterministic part of the flow field. In particular, this average removes the turbulent fluctuations. The Reynolds ensemble-averaged form of the Navier-Stokes equations is obtained by averaging consecutive sets of data taken over a revolution of the shaft (figure 4.1). Mathematically it is written:

$$\overline{f}^e(x, r, \theta, t) = \lim_{M \to \infty} \frac{1}{M} \sum_{m=1}^{M} f(x, r, \theta, T.(m-1)) \tag{4.2}$$

where $T$ is the period of revolution of the shaft. $\overline{f}^e$ is unsteady but deterministic because all the turbulent fluctuations have been removed. This average also assumes that the flow field does not contain any global instabilities, such as the rotating stall or the surge, which are not correlated to the rotational speed. The flow field is next decomposed in a mean part, the deterministic part, and a fluctuating part, the non-deterministic part (figure 4.1):

$$f(x, r, \theta, T.(m-1)) = \overline{f}^e(x, r, \theta, t) + f'(x, r, \theta, T.(m-1)) \tag{4.3}$$

As compressible flows are studied, a density weighted average (Favre average) is used:

$$\widetilde{f}^e = \frac{\overline{\rho f}^e}{\overline{\rho}^e} \tag{4.4}$$

The Favre average is applied to the velocities and to the total flow quantities while the other quantities are averaged by a conventional procedure.
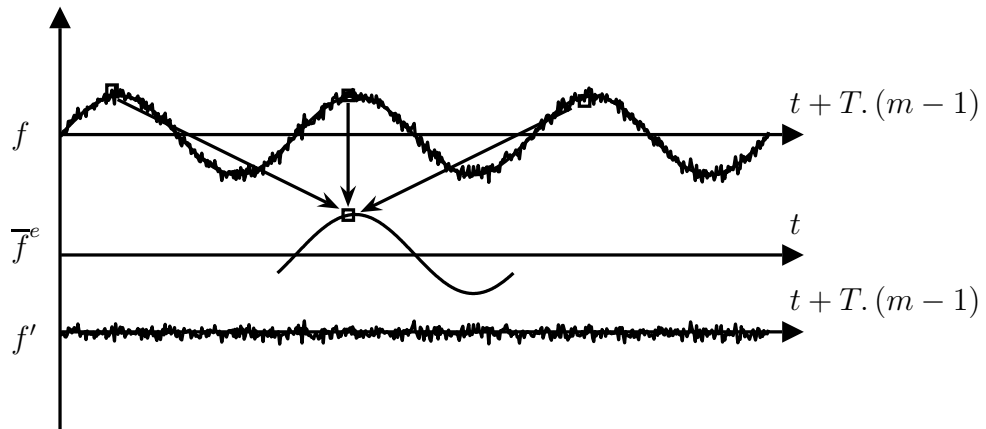


Figure 4.1: Decomposition of a signal in a deterministic part and a non-deterministic part

The application of the Reynolds ensemble-average to the Navier-Stokes equations is detailed in appendix B.2 and the result obtained for the axial momentum is reproduced hereafter:

$$
\frac{\partial \overline{\rho}^e \widetilde{V_x}^e}{\partial t} + \frac{\partial (\overline{\rho}^e \widetilde{V_x}^e \widetilde{V_x}^e + \overline{p}^e)}{\partial x} + \frac{1}{r}\frac{\partial r \overline{\rho}^e \widetilde{V_r}^e \widetilde{V_x}^e}{\partial r} + \frac{1}{r}\frac{\partial \overline{\rho}^e \widetilde{V_\theta}^e \widetilde{V_x}^e}{\partial \theta}
$$
$$
= \frac{\partial(\overline{\tau_{xx}}^e - \overline{\rho V_x' V_x'}^e)}{\partial x} + \frac{1}{r}\frac{\partial r(\overline{\tau_{rx}}^e - \overline{\rho V_r' V_x'}^e)}{\partial r} + \frac{1}{r}\frac{\partial(\overline{\tau_{\theta x}}^e - \overline{\rho V_\theta' V_x'}^e)}{\partial \theta}
\tag{4.5}
$$

The averaging process reveals additional terms compared to the instantaneous Navier-Stokes equations: the Reynolds stresses $\overline{\rho V_i' V_j'}^e$ in the momentum equations and an enthalpy flux $\overline{\rho V_i' H'}^e$ in the energy equation. They represent respectively the exchange of momentum and the exchange of energy between the non-deterministic and the deterministic flow fields.

## 4.2 Time-averaging operator

The second operator is a time-average. It removes the remaining unsteadiness of the flow. There is one time-average flow field by reference frame. Therefore, for a single shaft configuration, there are a time-average in the fixed reference frame and a time-average in the rotating reference frame. The time-average in the fixed reference frame of a quantity $\overline{f}^e$ is defined as follows:

$$
\overline{\overline{f}^e}^t = \frac{\dfrac{1}{T}\displaystyle\int_0^T H\left(x,r,\theta,t\right)\overline{f}^e\left(x,r,\theta,t\right)dt}{\dfrac{1}{T}\displaystyle\int_0^T H\left(x,r,\theta,t\right)dt}
$$

where H is a gate function. It is composed of a finite sum of unit step functions in such a way that the gate function is equal to one when at the time $t$, the point located at $(x, r, \theta)$ lies inside the flow field and it is equal to zero when the point lies inside a blade. For the rotating reference frame, the time-average is easily obtained by replacing the absolute circumferential position $\theta$ by the relative circumferential position $\theta_{rel}$. In the following, only the absolute reference frame will be considered without any loss of generality.

The integral of the gate function over the time defines the rotor blade blockage factor $b_R$ function:

$$
b_R\left(x,r\right) = \frac{1}{T}\int_0^T H\left(x,r,\theta,t\right)dt
$$

The flow field is decomposed in a steady part and in an unsteady fluctuation part:

$$
\overline{f}^e\left(x,r,\theta,t\right) = \overline{\overline{f}^e}^t\left(x,r,\theta\right) + f''\left(x,r,\theta,t\right)
$$

The Favre average is used for the velocities and for the total flow quantities, the other quantities being averaged classically.

Contrary to the ensemble averaging, particular rules arise for the average of the partial derivatives. This is due to the presence of the gate function. The time-average of the spatial derivative of a quantity $\overline{f}^e$ is written:

$$\overline{\frac{\partial \overline{f}^e}{\partial x_i}}^t = \frac{1}{b_R T} \int_0^T H\left(x, r, \theta, t\right) \frac{\partial \overline{f}^e}{\partial x_i}\left(x, r, \theta, t\right) dt$$

This can be rewritten as follows:

$$\overline{\frac{\partial \overline{f}^e}{\partial x_i}}^t = \frac{1}{b_R T} \int_0^T \frac{\partial \left(H\overline{f}^e\right)}{\partial x_i} dt - \frac{1}{b_R T} \int_0^T \frac{\partial H}{\partial x_i} \overline{f}^e dt \tag{4.6}$$

Since the limits of the integration do not depend on the spatial coordinates, the first term on the right hand-side is equal to

$$\frac{1}{b_R T} \int_0^T \frac{\partial \left(H\overline{f}^e\right)}{\partial x_i} dt = \frac{1}{b_R} \frac{\partial b_R \overline{\overline{f}^e}^t}{\partial x_i}$$

The second term contains the derivative of the gate function giving a sum of Dirac's delta functions. If a point lying at the location $(x, r, \theta)$ is considered, the Dirac's delta function will be non-zero at the instant of time when a blade side passes at this location. Mathematically, for the $n^{th}$ blade, this can be expressed by:

$$t_s\left(x, r, \theta, n\right) = \frac{\left(\theta_s\left(x, r\right) + \theta_{ref} - \dfrac{2\pi n}{N_R}\right) - \theta}{\Omega}$$

The subscript $s$ stands for the blade sides. The blade sides are not referenced here as pressure or suction sides but are referenced in the growing order of the circumferential coordinates so that $\theta_1(x, r) < \theta_2(x, r)$. In this way, the derived equations are independent of the reference frame and are valid for both compressors and turbines. The blade sides are both measured with respect to the blade mean line. $\theta_{ref}$ simply indicates the angular position of the blade mean line at the reference time $t = 0$. $N_R$ is the blade count in the rotor under consideration.

The spatial derivative of the gate function is expressed by:

$$\frac{\partial H}{\partial x_i} = \frac{1}{\Omega} \sum_{n=0}^{N_R-1} \left[\delta\left(t - t_1\right) \frac{\partial \theta_1}{\partial x_i} - \delta\left(t - t_2\right) \frac{\partial \theta_2}{\partial x_i}\right] \tag{4.7}$$

Reintroducing (4.7) in the last term of the equation (4.6) and reminding the following fundamental property of the Dirac's delta function:

$$\int_{a-\epsilon}^{a+\epsilon} f(x)\delta(x-a)\,dx = f(a) \tag{4.8}$$

for $\epsilon > 0$, one obtain:

$$\frac{1}{b_R T}\int_0^T \frac{\partial H}{\partial x_i}\overline{f}^e\,dt = \frac{1}{2\pi b_R}\sum_{n=0}^{N_R-1}\left(\overline{f_1}^e\frac{\partial\theta_1}{\partial x_i} - \overline{f_2}^e\frac{\partial\theta_2}{\partial x_i}\right)$$

where $\overline{f_1}^e$ and $\overline{f_2}^e$ are 3-D fields:

$$\overline{f_1}^e = \overline{f}^e(x,r,\theta,t=t_1) \quad\text{and}\quad \overline{f_2}^e = \overline{f}^e(x,r,\theta,t=t_2)$$

Finally, the time-average of the spatial derivative of a quantity $\overline{f}^e$ is equal to the spatial derivative of the time-average of the quantity plus an additional term:

$$\overline{\frac{\partial\overline{f}^e}{\partial x_i}}^t = \frac{1}{b_R}\frac{\partial b_R\overline{\overline{f}^e}^t}{\partial x_i} - \frac{1}{2\pi b_R}\sum_{n=0}^{N_R-1}\left(\overline{f_1}^e\frac{\partial\theta_1}{\partial x_i} - \overline{f_2}^e\frac{\partial\theta_2}{\partial x_i}\right) \tag{4.9}$$

This additional term is only non-zero for quantities that are not equal to zero on the blade walls, i.e. the pressure for example.

The application of the time-average to the unsteady RANS equations is given in appendix B.3. The result obtained for the axial momentum is reproduced hereafter:

$$\frac{1}{b_R}\frac{\partial b_R(\overline{\rho}^e{}^t\widetilde{\widetilde{V_x}}^e{}^t\widetilde{\widetilde{V_x}}^e{}^t + \overline{\overline{p}^e}^t)}{\partial x} + \frac{1}{rb_R}\frac{\partial rb_R\overline{\overline{\rho}^e}^t\widetilde{\widetilde{V_r}}^e{}^t\widetilde{\widetilde{V_x}}^e{}^t}{\partial r} + \frac{1}{rb_R}\frac{\partial b_R\overline{\overline{\rho}^e}^t\widetilde{\widetilde{V_\theta}}^e{}^t\widetilde{\widetilde{V_x}}^e{}^t}{\partial\theta}$$

$$= \frac{1}{b_R}\frac{\partial b_R(\overline{\overline{\tau_{xx}}^e}^t - \overline{\overline{\rho V_x'V_x'}^e}^t - \overline{\overline{\rho}^e V_x''V_x''}^t)}{\partial x}$$

$$+ \frac{1}{rb_R}\frac{\partial rb_R(\overline{\overline{\tau_{rx}}^e}^t - \overline{\overline{\rho V_r'V_x'}^e}^t - \overline{\overline{\rho}^e V_r''V_x''}^t)}{\partial r} \tag{4.10}$$

$$+ \frac{1}{rb_R}\frac{\partial b_R(\overline{\overline{\tau_{\theta x}}^e}^t - \overline{\overline{\rho V_\theta'V_x'}^e}^t - \overline{\overline{\rho}^e V_\theta''V_x''}^t)}{\partial\theta}$$

$$+ f_{bx}^R + f_{vx}^R$$

Compared to the unsteady RANS equations, additional terms show up:

1. The deterministic stresses $\overline{\overline{\rho^e V_i'' V_j''}}^t$ in the momentum equations and the enthalpy flux $\overline{\overline{\rho^e V_i'' H''}}^t$ in the energy equation represent the transport of respectively momentum and energy between the unsteady deterministic and the time-averaged flow fields. These terms have the same form as the additional terms brought by the Reynolds ensemble-average.

2. The blockage factor $b_R$ is due to the geometrical blockage resulting from the rotor blade thickness. It is less than one inside a rotor blade row and equal to one otherwise.

3. The momentum equations contain the blade forces $f_b^R$ and $f_v^R$ while the energy equation contains the source terms $e_b^R$ and $e_v^R$. These terms are due to the pressure field, the shear stresses and the heat fluxes acting on the rotor blade wall surfaces. They come directly from the additional terms of the equation (4.9). Their origin is similar to the blade force appearing in the throughflow equations through the Leibniz's rule (section 1.1).

An illustration of the averaging process and its impact on the flow field is presented on the figures 4.2 (a) and (b). These figures represent the flow field inside a transonic turbine at midspan. The flow field is given in terms of streamlines. They have been obtained by computing the time-average of the flow field in both reference frames. Due to the averaging process, the blade row that is not in the reference frame used to perform the average does not appear anymore as solid walls. It appears as a "ghost" row and its effect is smeared over the circumferential direction. The ghost row is brought by the deterministic stresses, the blockage factor and the blade forces. In the stator reference frame, the rotor blade surfaces have disappeared but the flow is deflected toward the axial direction, mainly due to the inviscid blade force contribution. In the same manner, in the rotor reference frame, the stator ghost row gives the turning of the flow in front of the rotor.

For a single stage configuration, operating in a stable mode (no rotating-stall or surge), and with uniform inflow and outflow boundary conditions, the time-average flow fields in both reference frames will be periodic over the pitch.

## 4.3   Passage-to-passage averaging operator

In general, the time-averaged flow is not periodic from one passage to another passage of a given blade row. Therefore an additional averaging operator is introduced to remove the aperiodicity of the flow in the different passages of the same blade row. This average is referred to as the passage-to-passage average. This average will not be used in the following

(a) stator reference frame                    (a) rotor reference frame
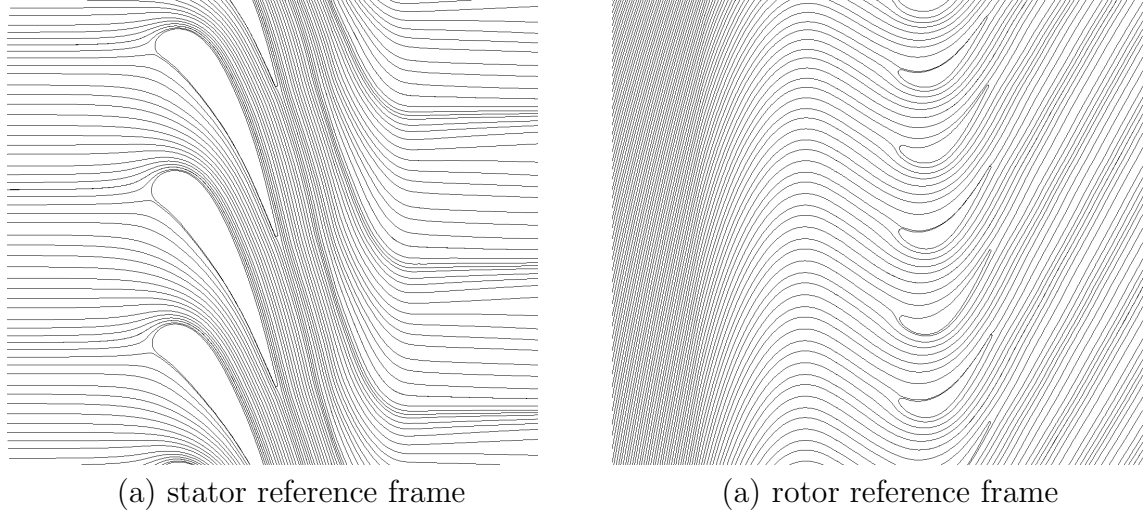
Figure 4.2: Time-averaging in both reference frames

sections as the focus will be put on single stage configuration but it is nevertheless presented here for the sake of completeness.

There is one passage-to-passage average per blade row. For a given stator, the passage-to-passage averaging is defined as follows:

$$
\overline{\overline{\overline{f}^{e^t}}}^a = \frac{\sum\limits_{n=0}^{N_{Sj}-1} G\left(x,r,\theta+\frac{2\pi n}{N_{Sj}}\right) \overline{\overline{f}^{e^t}}\left(x,r,\theta+\frac{2\pi n}{N_{Sj}}\right)}{\sum\limits_{n=0}^{N_{Sj}-1} G\left(x,r,\theta+\frac{2\pi n}{N_{Sj}}\right)}
$$

where $N_{Sj}$ is the blade count in the stator under consideration. The global gate function $G$ is composed of the product of $L$ gate functions $g_l$:

$$
G\left(x,r,\theta\right) = \prod_{l}^{L} g_l\left(x,r,\theta\right)
$$

where $L$ is the number of stator rows. A gate function $g_l$ is equal to one when the point located at position $(x,\ r,\ \theta)$ lies inside the (time-average) flow field. It is equal to zero otherwise.

For the $j^{th}$ stator, the integral over the circumferential coordinate of the product of the gate functions of the stators other than the stator $j$ gives the blade blockage factor $b_{Sj}$:

$$
b_{Sj}\left(x,r\right) = \frac{1}{2\pi} \int_{0}^{2\pi} \prod_{\substack{l=1 \\ l \neq j}}^{L} g_l\left(x,r,\theta\right) d\theta
$$

The flow field is next decomposed in a mean part, which is periodic for the reference blade row, and in an aperiodic fluctuating part:

$$\overline{\overline{f}^{e^t}}\left(x,r,\theta+\frac{2\pi n}{N_{Sj}}\right) = \overline{\overline{\overline{f}^{e^t}}}^a(x,r,\theta) + f'''\left(x,r,\theta+\frac{2\pi n}{N_{Sj}}\right)$$

Here again, the Favre average is used for the velocities and the total flow properties.

As for the time-average, the average of a derivative is not equal to the derivative of the average. An additional term brings the effects of the blade wall surfaces. The rule for passage-to-passage averaging a derivative is:

$$\overline{\frac{\partial \overline{\overline{f}^{e^t}}}{\partial x_i}}^a = \frac{1}{b_{Sj}}\frac{\partial b_S \overline{\overline{\overline{f}^{e^t}}}^a}{\partial x_i} - \frac{1}{2\pi b_{Sj}}\sum_{n=0}^{N_{Sj}-1}\left(\overline{\overline{f_3}^{e^t}}\frac{\partial \theta_3}{\partial x_i} - \overline{\overline{f_4}^{e^t}}\frac{\partial \theta_4}{\partial x_i}\right) \tag{4.11}$$

where

$$\overline{\overline{f_3}^{e^t}} = \overline{\overline{f}^{e^t}}\left(x,r,\theta = \theta_{ref}+\theta_3+\frac{2\pi n}{N_{Sj}}\right) \quad \text{and} \quad \overline{\overline{f_4}^{e^t}} = \overline{\overline{f}^{e^t}}\left(x,r,\theta = \theta_{ref}+\theta_4+\frac{2\pi n}{N_{Sj}}\right)$$

where $\theta_3$ and $\theta_4$ are respectively the locations of the blade sides in their order of appearance when rotating in the $\theta$ direction, i.e. $\theta_3(x,r) < \theta_4(x,r)$. They are measured with respect to the blade mean line. $\theta_{ref}$ simply indicates the angular position of the blade mean line of the first blade of the $j^{th}$ blade row. $N_{Sj}$ is the blade count of the stator $j$. The additional term is only non-zero for quantities that are not equal to zero on the blade walls.

The result of the application of the passage-to-passage average to the time-averaged equations is given in the appendix B.4 and the result obtained for the axial momentum is reproduced hereafter:

$$\frac{1}{b_{Sj}}\frac{\partial b_{Sj}(\overline{\overline{\rho}^{e^t}}^a \widetilde{\overline{V_x}^{e^t}}^a \widetilde{\overline{V_x}^{e^t}}^a + \overline{\overline{p}^{e^t}}^a)}{\partial x} + \frac{1}{rb_{Sj}}\frac{\partial rb_{Sj}\overline{\overline{\rho}^{e^t}}^a \widetilde{\overline{V_r}^{e^t}}^a \widetilde{\overline{V_x}^{e^t}}^a}{\partial r} + \frac{1}{rb_{Sj}}\frac{\partial b_{Sj}\overline{\overline{\rho}^{e^t}}^a \widetilde{\overline{V_\theta}^{e^t}}^a \widetilde{\overline{V_x}^{e^t}}^a}{\partial \theta}$$

$$= \frac{1}{b_{Sj}}\frac{\partial b_{Sj}(\overline{\overline{\overline{\tau_{xx}}^{e^t}}}^a - \overline{\overline{\rho V_x'V_x'}^{e^t}}^a - \overline{\overline{\rho^e V_x''V_x''}}^a - \overline{\overline{\rho}^{e^t}V_x'''V_x'''}^a)}{\partial x}$$

$$+ \frac{1}{rb_{Sj}}\frac{\partial rb_{Sj}(\overline{\overline{\overline{\tau_{rx}}^{e^t}}}^a - \overline{\overline{\rho V_r'V_x'}^{e^t}}^a - \overline{\overline{\rho^e V_r''V_x''}}^a - \overline{\overline{\rho}^{e^t}V_r'''V_x'''}^a)}{\partial r} \tag{4.12}$$

$$+ \frac{1}{rb_{Sj}}\frac{\partial b_{Sj}(\overline{\overline{\overline{\tau_{\theta x}}^{e^t}}}^a - \overline{\overline{\rho V_\theta'V_x'}^{e^t}}^a - \overline{\overline{\rho^e V_\theta''V_x''}}^a - \overline{\overline{\rho}^{e^t}V_\theta'''V_x'''}^a)}{\partial \theta}$$

$$+ \overline{f_{bx}^R}^a + \overline{f_{vx}^R}^a + f_{bx}^{Sj} + f_{vx}^{Sj}$$

Compared to the time-average equations additional terms appear:

1. The aperiodic stresses $\overline{\overline{\rho^{e}}^{t} V_i''' V_j'''}^{a}$ in the momentum equations and the enthalpy flux $\overline{\overline{\rho^{e}}^{t} V_i''' H''}^{a}$ in the energy equation. They represent the transport of respectively momentum and energy between the time-averaged aperiodic and the time-averaged periodic flow fields.

2. The blockage factor $b_{Sj}$ is due to the geometrical blockage resulting from the blade thickness. It is equal to $b_S$ inside the stators other than the one of interest (which is still in 3-D) and is equal to $b_R$ inside a rotor. It is equal to one otherwise.

3. The momentum equations contain the blade forces $f_b^{Sj}$ and $f_v^{Sj}$ while the energy equation contains the source term $e_v^{Sj}$. These terms are due to the pressure field, the shear stresses and the heat fluxes acting on the stator blade walls other than the one under consideration. They come directly from the additional terms of the equation (4.11).

The same reasoning can be applied to the relative reference frame for each rotor so that a flow field per blade row, which extends from the inlet to the outlet of the machine, is finally obtained. This flow field is periodic over the pitch of the blade row under consideration, the $j^{th}$ row. In each flow field, the only blade row that is still represented by its solid boundaries is the blade row under consideration. The other blade rows are represented by a distribution of blade blockage, blade forces and stresses. The obtained flow field represents the last step of the average-passage set of equations devised by Adamczyk (1984).

## 4.4 Circumferential-averaging operator

The last step to obtain an axisymmetric representation of the flow is to perform a circumferential average on the average-passage equations. There is only one axisymmetric flow field common to all average-passage flows (which are relative to each blade row). From this property of uniqueness, it appears that there are (at least) two ways to obtain the axisymmetric flow field and its associated equations. The first one is to take the average-passage flow in an arbitrary blade row that extents from the inlet to the outlet of the domain and to circumferentially average it. The other way is to circumferentially-average each average-passage flow that extents only in the zone of the blade row for which it is relative. From a practical point of view, when it comes to obtain the axisymmetric flow field, the difference between both methods can be important as it will be shown in section 5.7.

The circumferential-average can be defined with the help of a gate function in the same way as the time-average. An alternative consists in performing an integration from the pressure side to the suction side of a blade and to use the Leibniz's rule for the integration

with variable limits (see section 1.1). The first approach will be used here in order to be consistent with the previous averaging operators.

The circumferential average performed on the average-passage flow field of the $j^{th}$ blade row is defined as follows:

$$
\overline{\overline{f}^{e^{t^a}}}^c = \frac{\dfrac{1}{\Delta\theta} \displaystyle\int_0^{\Delta\theta} F(x,r,\theta) \overline{\overline{f}^{e^{t^a}}}(x,r,\theta)\,d\theta}{\dfrac{1}{\Delta\theta} \displaystyle\int_0^{\Delta\theta} F(x,r,\theta)\,d\theta}
$$

$\Delta\theta$ is equal to the pitch of the blade row under consideration, i.e. $2\pi/N$ where $N$ is the blade count. $F$ is a gate function. Its value is one when the point located at $(x,r,\theta)$ lies inside the flow field. It is equal to zero when the point lies inside the blade row. The integral of the gate function over the pitch is equal to the blade blockage factor $b_j$:

$$
b_j = \frac{1}{\Delta\theta} \int_0^{\Delta\theta} F(x,r,\theta)\,d\theta
$$

The flow field is next decomposed in an axisymmetric part and in a circumferential fluctuation part:

$$
\overline{\overline{f}^{e^{t^a}}}(x,r,\theta,t) = \overline{\overline{f}^{e^{t^a}}}^c(x,r,\theta) + f''''(x,r,\theta,t)
$$

The Favre average is used for the velocities and the total flow properties.

The rule for averaging the partial derivative is the following:

$$
\overline{\dfrac{\partial \overline{\overline{f}^{e^{t^a}}}^c}{\partial x_i}} = \frac{1}{b_j}\frac{\partial b_j \overline{\overline{f}^{e^{t^a}}}^c}{\partial x_i} - \frac{N}{2\pi b_j}\left( \overline{\overline{f_5}^{e^{t^a}}}\frac{\partial \theta_5}{\partial x_i} - \overline{\overline{f_6}^{e^{t^a}}}\frac{\partial \theta_6}{\partial x_i} \right) \tag{4.13}
$$

where

$$
\overline{\overline{f_5}^{e^{t^a}}} = \overline{\overline{f}^{e^{t^a}}}(x,r,\theta=\theta_5) \quad \text{and} \quad \overline{\overline{f_6}^{e^{t^a}}} = \overline{\overline{f}^{e^{t^a}}}(x,r,\theta=\theta_6)
$$

where $\theta_5$ and $\theta_6$ are the locations of the blade sides in their order of appearance when rotating in the $\theta$ direction. They are measured with respect to the blade mean line. The additional term is only non-zero for quantities that are not equal to zero on the blade walls. The result of the application of the circumferential average to the average-passage equations is given in

the appendix B.5 and the result obtained for the axial momentum is reproduced hereafter:

$$
\begin{aligned}
\frac{1}{b}\frac{\partial b(\overline{\overline{\rho}^{e^t}}^{a^c}\widetilde{\widetilde{V_x}}^{e^{t^a^c}}\widetilde{\widetilde{V_x}}^{e^{t^a^c}} + \overline{\overline{p}^{e^t}}^{a^c})}{\partial x} &+ \frac{1}{rb}\frac{\partial rb\overline{\overline{\rho}^{e^t}}^{a^c}\widetilde{\widetilde{V_r}}^{e^{t^a^c}}\widetilde{\widetilde{V_x}}^{e^{t^a^c}}}{\partial r} \\
&= \frac{1}{b}\frac{\partial b(\overline{\overline{\overline{\tau_{xx}}^{e^t}}}^{a^c} - \overline{\overline{\overline{\rho V_x'V_x'}}^{e^t}}^{a^c} - \overline{\overline{\rho^e V_x''V_x''}^{t}}^{a^c} - \overline{\overline{\rho^{e^t} V_x'''V_x'''}}^{a^c} - \overline{\overline{\rho^{e^t}} V_x''''V_x''''}^{c})}{\partial x} \\
&+ \frac{1}{rb}\frac{\partial rb(\overline{\overline{\overline{\tau_{rx}}^{e^t}}}^{a^c} - \overline{\overline{\overline{\rho V_r'V_x'}}^{e^t}}^{a^c} - \overline{\overline{\rho^e V_r''V_x''}^{t}}^{a^c} - \overline{\overline{\rho^{e^t} V_r'''V_x'''}}^{a^c} - \overline{\overline{\rho^{e^t}} V_r'''V_x'''}^{c})}{\partial r} \\
&+ \overline{\overline{f_{bx}^R}}^{a^c} + \overline{\overline{f_{vx}^R}}^{a^c} + \overline{f_{bx}^{Sj}}^{c} + \overline{f_{vx}^{Sj}}^{c} + f_{bx}^j + f_{vx}^j
\end{aligned} \tag{4.14}
$$

Compared to the average-passage equations additional terms appear.

1. The circumferential stresses $\overline{\overline{\rho}^{e^t}}^{a} V_i''''V_j''''^{c}$ in the momentum equations and the enthalpy flux $\overline{\overline{\rho}^{e^t}}V_i''''H''''^{a}$ in the energy equation. They represent the transport of respectively momentum and energy between the 3-D periodic and the axisymmetric flow fields.

2. The blockage factor $b$ is due to the geometrical blockage resulting from the blade thickness. It is equal to $b_S$ inside the stators others than the one of interest, to $b_R$ inside a rotor and to $b_j$ inside the current row. It is equal to one otherwise.

3. The momentum equations contain the blade forces $f_b^j$ and $f_v^j$ while the energy equation contains the source terms $e_b^j$ and $e_v^j$. These terms are due to the pressure field, the shear stresses and the heat fluxes acting on the wall surfaces of the blade row $j$. They come directly from the additional terms of the equation (4.13).

## 4.5 On the throughflow closure

The throughflow model defined by the set of equations (B.36) to (B.40) represents the ultimate throughflow model. It has been rigorously established from the 3-D instantaneous Navier-Stokes equations and only the assumptions that prevail to the establishment of these equations have been used. The equations governing the throughflow model are expressed in terms of the averaged conservative variables. Additionally to these primary unknowns, a large number of other unknown terms appear. These additional terms have to be modelled in order to solve the throughflow problem. This is the closure problem related to the meridional flow field. For example, for the momentum equations, the additional terms are:

- the averaged viscous (laminar) stresses,

- the Reynolds stresses,

- the deterministic stresses,

- the passage-to-passage stresses,

- the circumferential stresses,

- the inviscid blade forces,

- the viscous blade forces.

The energy equation also exhibits additional terms such as the product of velocity fluctuation and viscous stresses fluctuation or stresses composed of stagnation enthalpy and velocity fluctuations. If all these terms could be modelled adequately, one would obtain the perfect throughflow model that is able to predict the mean steady axisymmetric effect of the wake chopping phenomenon, the effect of the radial mixing or the mean effect of the blade clocking. Establishing a closure for that model is a tremendous task that is far beyond the scope of this work. In the present contribution, the focus will be rather put on the study of the system of equations which present certain particularities. Answers to the two following questions will also be sought:

- What are the relative importance of the different terms and, from there, the terms that are worth to be modelled ?

- What is the benefit of such a model compared to a classical throughflow model ?

These objectives will be achieved with the help of 3-D steady and unsteady simulations. The different contributions to the momentum and energy equations will be extracted from them to feed a throughflow model. These studies on real turbomachine testcases will be presented in the next chapter. A preliminary study will be first undertaken in the present chapter on simple two-dimensional testcases modelled by a one-dimensional set of equations.

Before that, a short introduction to the closure problem will be presented. It is focused on the deterministic and the circumferential averaging only. Although these closure problems will not be addressed directly in the present work (no set of equations for closing those problems will be provided at the end of this work), some of the concepts presented here will be useful later.

## 4.5.1 Deterministic stresses closure

The first approach for obtaining the deterministic stresses has been proposed by Adamczyk *et al.* (1986). It consists in decomposing the unsteadiness of the flow in two contributions: a

spatial part and a temporal part. To illustrate this concept, let us consider a compressor stage composed of a rotor followed by a stator. In the absolute reference frame, the unsteadiness viewed by the stator can be cast in two parts. A first part is steady in the reference frame of the rotor but appears to be unsteady in the stator reference frame due to the change of reference frame. The steady part of the rotor flow which appears unsteady in the stator reference frame is the non-axisymmetric one. This is the so-called spatial part. The same reasoning applies to the non-axisymmetric steady flow in the stator reference frame which is viewed in the rotor reference frame as unsteady. Mathematically, the following relation (valid for a constant rotational speed $\Omega$) links the time derivative in both reference frames:

$$\left.\frac{\partial}{\partial t}\right|_{rotor} = \left.\frac{\partial}{\partial t}\right|_{stator} + \Omega\frac{\partial}{\partial \theta} \qquad (4.15)$$

The second part of the unsteadiness is a part which is unsteady in both reference frames. This is the so-called purely temporal part. The main assumption of Adamczyk *et al.* (1986) is to neglect this part and to retain only the spatial contribution. Therefore, the unsteady behaviour can be captured by performing steady simulations in each of the reference frames and by exchanging information between the two flow fields such as the stresses, the blade forces and the blade blockage coefficients.

A procedure is schematically illustrated on the figure 4.3 for an inviscid closure. The blade forces and the circumferential stresses are exchanged between both steady computations in the rotor and the stator. Each computation extends over the complete domain but contains only one blade row in 3-D (full line on the figure 4.3). In the steady simulation of the rotor, the stator appears as a ghost row (dotted line on the figure 4.3) and in the steady simulation of the stator, the rotor appears as a ghost row. The 3-D steady simulation in the rotor provides the blade force and the circumferential stresses (superscript $R$) over the full domain to the steady computation in the stator and vice versa for the stator (superscript $S$).

Several authors have retained the main assumption of Adamczyk with some variants in the way of computing the stresses and the blade forces. Rhie *et al.* (1995) compute explicitly the blade forces and the deterministic stresses and neglect the viscous contributions. In the original inviscid approach of Adamczyk *et al.* (1986), extended to viscous flows by Adamczyk *et al.* (1989), all closure terms are computed implicitly by relying on an axisymmetric flow common to all blade rows. With the same assumption concerning the importance of the purely temporal contribution of the unsteadiness, Hall *et al.* (1995) proposed an empirical closure based on an analytic approach describing the wake development inside a downstream blade row. This approach does not necessitate any ghost rows.

In some cases, it has been shown that the purely unsteady part of the deterministic stresses plays an important role (see Bardoux (2000) for the transonic turbine stage VEGA2 that will be studied in the next chapter). Some models that do not neglect this part of the stresses have been proposed: the model of van de Wall *et al.* (2000) or the model of Charbonnier
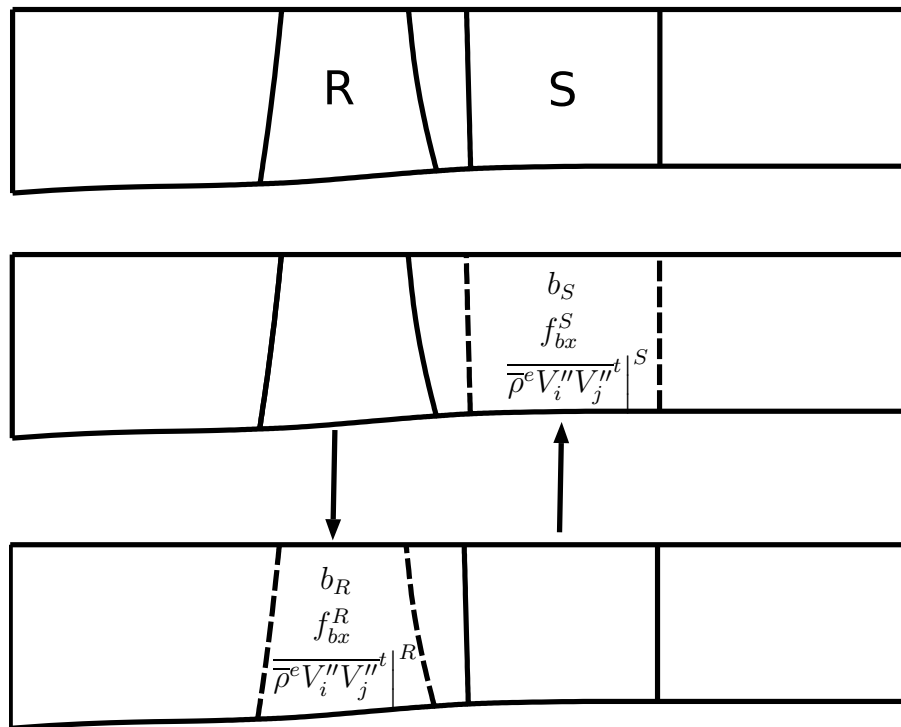
Figure 4.3: Adamczyk closure approach

(2004) for example. They are based on the assumption that the deterministic stresses are transported by the mean flow. One additional equation is therefore solved per stress. This approach has some similarity with the Reynolds stress transport modelling for the turbulent closure.

Finally, a promising approach is the harmonic method (He and Ning, 1998; Chen *et al.*, 2000). It consists in solving a separated set of equations for the unsteady perturbations (fluctuations of the unsteady flow with respect to mean steady flow) besides the mean set of equations including the deterministic stresses. The perturbation equations are solved in the frequency domain by injecting harmonic functions into the equations. There are as many sets of perturbation equations as twice the number of harmonics chosen to represent the perturbation behaviour. Contrary to the other methods presented above, the harmonic approach allows to reconstruct the unsteady flow field. Typically, three harmonics are used to obtain a converged mean steady solution. This is however not sufficient if the unsteady flow field is to be reconstructed. For application of the method to multistage compressors (rotor-stator, rotor-rotor and stator-stator interactions), see for example He *et al.* (2002), Stridh *et al.* (2005) or Vilmin *et al.* (2006).

The harmonic method has been compared to the transport method of van de Wall *et al.* (2000) by Stridh (2003) on a 2-D blade-to-blade testcase basis. The superiority of the

harmonic method has been demonstrated for that testcase. However, it must be noted that the comparison was not completely fair as some of the terms of the deterministic stresses transport model used by Stridh (2003) were missing in comparison to the original model of van de Wall *et al.* (2000), i.e. the pressure-velocity correlations. As shown by Charbonnier (2004) for a transonic turbine and for a centrifugal compressor, the pressure-velocity correlations are not negligible.

### 4.5.2   Circumferential stresses closure

Concerning the circumferential stresses closure, very few works have been done. Perrin and Leboeuf (1995) studied a rotor turbine cascade through numerical simulation in order to establish a hierarchy of the different contributions to the momentum balance. Some of their results will be recalled in a later section.

Baralon *et al.* (1999) performed a study on the influence of the different contributions to the momentum and energy balances for the transonic rotor NASA Rotor 67.

## 4.6   One-dimensional studies

### 4.6.1   Purpose of the one-dimensional study

The purpose of this section is to perform a preliminarily study of the different contributions arising from the circumferential averaging process as well as establishing a hierarchy in the importance of these contributions. The study will focus on the circumferential closure only and will not consider the deterministic stresses or the other terms arising from the time-averaging procedure.

It is obvious that the inviscid blade force will take a great importance in the momentum and energy balances. The relative importances of the circumferential stresses and of the viscous stresses are less clear. To help in evaluating these relative importances, two simple 1-D numerical experiments are performed. These experiments consist in averaging a 2-D flow and its associated equations thus obtaining a 1-D set of equations representative of the mean 2-D flow. Similarly to the meridional set of equations, the 1-D equations present additional unknowns brought by the averaging procedure. These additional terms can be computed from the 2-D flows and injected in the 1-D set of equations. In this way, the importance of the different contributions can be studied.

The two testcases that are presented here are representative of certain phenomena encountered in a 2-D steady blade-to-blade flow. The first one is the development of a boundary

layer over a flat plate and the second is a wake spreading due to the viscosity. It is true that these testcases lack of certain phenomena such as the generation of circumferential stresses due to the turning of the flow inside the blade passage but, as it will be seen, the results obtained here will be meaningful for the compressor testcase that will be presented later. The two studies also allow to get a first insight of the features of the averaged set of equations, principally the specificity brought by the density-average.

For the two studies to be presented, the circumferential average is replaced by a so-called spatial average and the circumferential stresses by the spatial stresses.

## 4.6.2  Averaging procedure

The 2-D Navier-Stokes equations are used here, coupled to the Baldwin-Lomax model for the computation of the turbulent viscosity. The usual simplifications that come with an algebraic model and non-hypersonic flows are performed here on the energy equation (Wilcox, 1993). The 2-D Navier-Stokes equations are written as follows:

Conservation of mass:

$$\frac{\partial \rho V_x}{\partial x} + \frac{\partial \rho V_y}{\partial y} = 0 \tag{4.16}$$

Conservation of momentum:

$$\frac{\partial (\rho V_x V_x + p)}{\partial x} + \frac{\partial \rho V_x V_y}{\partial y} = \frac{\partial \tau_{xx}}{\partial x} + \frac{\partial \tau_{xy}}{\partial y} \tag{4.17}$$

$$\frac{\partial (\rho V_y V_y + p)}{\partial y} + \frac{\partial \rho V_x V_y}{\partial x} = \frac{\partial \tau_{yy}}{\partial y} + \frac{\partial \tau_{xy}}{\partial x} \tag{4.18}$$

Conservation of energy:

$$\frac{\partial \rho V_x h^0}{\partial x} + \frac{\partial \rho V_y h^0}{\partial y} = \frac{\partial (\tau_{xx} V_x + \tau_{xy} V_y - q_x)}{\partial x} + \frac{\partial (\tau_{xy} V_x + \tau_{yy} V_y - q_y)}{\partial y} \tag{4.19}$$

The preceding set of equations is averaged in the y direction. The area-averaging and the Favre-averaging operators are defined as follows:

$$\overline{f} = \frac{1}{\Delta y} \int_0^{\Delta y} f \, dy \tag{4.20}$$

$$\widetilde{f} = \frac{1}{\Delta y \, \overline{\rho}} \int_0^{\Delta y} \rho f \, dy \tag{4.21}$$

where $\Delta y$ is the height of the computational domain. A quantity f is decomposed in a mean part and a fluctuating part:

$$f = \widetilde{f} + f' \tag{4.22}$$

$$f = \overline{f} + f'' \tag{4.23}$$

The rules for averaging the y-derivative is:

$$\overline{\frac{\partial f}{\partial y}} = \frac{1}{\Delta y} \left( f(\Delta y) - f(0) \right) = \frac{1}{\Delta y} [f]_0^{\Delta y} \tag{4.24}$$

For the two testcases presented hereafter, the averaging operator and the axial derivative operator commute:

$$\overline{\frac{\partial f}{\partial x}} = \frac{\partial \overline{f}}{\partial x} \tag{4.25}$$

### 4.6.3   Development of a boundary layer over a flat plate

The development of a boundary layer over a flat plate is studied here. The results of the 2-D computation have already been shown in section 2.9.1. The computational domain is reproduced at the figure 4.4. The focus is put here on the 1-D set of averaged equations representative of that 2-D problem.
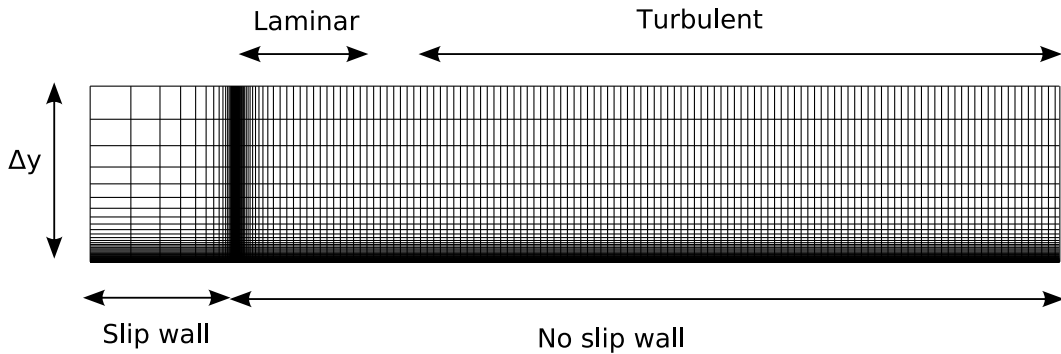


Figure 4.4: Flat plate definition and mesh

Applying the averaging operator defined above to the 2-D equations of conservation and to the flat plate problem gives the following set of equations.

Conservation of mass:

$$\frac{\partial \overline{\rho} \widetilde{V_x}}{\partial x} = 0 \tag{4.26}$$

Conservation of momentum:

$$\frac{\partial(\overline{\rho}\widetilde{V_x}\widetilde{V_x} + \overline{p})}{\partial x} + \frac{\partial\overline{\rho V_x'V_x'}}{\partial x} = \frac{\partial\overline{\tau_{xx}}}{\partial x} + \frac{1}{\Delta y}\tau_{xy}(0) \tag{4.27}$$

$$\frac{\partial\overline{\rho}\widetilde{V_x}\widetilde{V_y}}{\partial x} + \frac{\partial\overline{\rho V_x'V_y'}}{\partial x} = \frac{\partial\overline{\tau_{xy}}}{\partial x} + \frac{1}{\Delta y}\tau_{yy}(0) - \frac{1}{\Delta y}[p]_0^{\Delta y} \tag{4.28}$$

Conservation of energy:

$$\frac{\partial\overline{\rho}\widetilde{V_x}\widetilde{H}}{\partial x} + \frac{\partial\overline{\rho V_x'H'}}{\partial x} = \frac{\partial(\overline{\tau_{xx}V_x} + \overline{\tau_{xy}V_y} - \overline{q_x})}{\partial x} \tag{4.29}$$

where

$$\widetilde{H} = \widetilde{h} + \frac{1}{2}\widetilde{V}\widetilde{V} + \frac{1}{2}k \tag{4.30}$$

and

$$k = \frac{1}{\overline{\rho}}(\overline{\rho V_x'V_x'} + \overline{\rho V_y'V_y'}) \tag{4.31}$$

Similarly to the circumferentially averaged 3-D Navier-Stokes equations, additional terms appear in the momentum and in the energy equations. They can be cast in:

- wall stresses: $\frac{1}{\Delta y}\tau_{yy}(0)$, $\frac{1}{\Delta y}\tau_{xy}(0)$ and $\frac{1}{\Delta y}[p]_0^{\Delta y}$. It is well known that for a flat plate the normal viscous stress at the wall $\tau_{yy}(0)$ is negligible with respect to the shear stress $\tau_{xy}(0)$. It is also well known that pressure is nearly uniform in the direction perpendicular to the mean flow. The force at the wall reduces to the shear stress at the wall $\tau_{xy}(0)$,

- velocity-velocity stresses $\overline{\rho V_x'V_y'}$ and $\overline{\rho V_x'V_x'}$,

- velocity-enthalpy stress $\overline{\rho V_x'H'}$.

All preceding contributions can be computed from the 2-D flow field and included in the 1-D solver, as well as the averaged viscous stresses $\overline{\tau_{xy}}$, $\overline{\tau_{xx}}$ and the viscous contribution to the energy equation $\overline{\tau_{xx}V_x} + \overline{\tau_{xy}V_y} - \overline{q_x}$.

The unknowns of the 1-D system of equations are the averaged conservative variables: $\overline{\rho}$, $\overline{\rho}\widetilde{V_x}$, $\overline{\rho}\widetilde{V_y}$, $\overline{\rho}\widetilde{H}$. This system of equations is solved on a 1-D mesh. By switching on or off individually the terms computed from the 2-D flow field, their impacts on the 1-D averaged flow field can be evaluated and the predominant terms can be determined. These dominant terms are:

- the axial-axial spatial correlation $\overline{\rho V'_x V'_x}$,

- the viscous shear stress at the wall $\frac{1}{\Delta y}\tau_{xy}(0)$.

The effect of these two terms on the axial velocity and on the entropy is illustrated on the figure 4.5. The viscous force at the wall takes the greatest importance and it is the only viscous term that is worth to be modelled in order to close the system of equations.



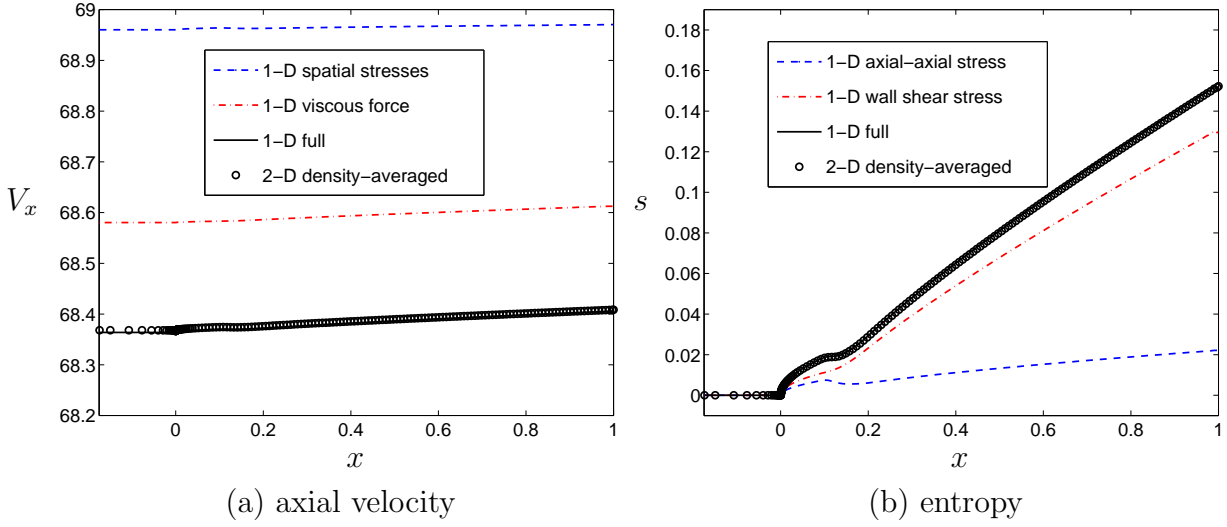(a) axial velocity                                    (b) entropy

Figure 4.5: Impact of the additional terms on the 1-D flat plate flow

The entropy plotted on the figure 4.5 has been computed with the Gibbs equation directly applied to the averaged variables, i.e:

$$\widetilde{T}\frac{\partial \widetilde{s}}{\partial x} = \frac{\partial \widetilde{h}}{\partial x} - \frac{1}{\overline{\rho}}\frac{\partial \overline{p}}{\partial x} \tag{4.32}$$

The rigorous and correct way to obtain the entropy is to apply the average operator directly to the Gibbs equation. This gives the following equation:

$$\widetilde{T}\frac{\partial \widetilde{s}}{\partial x} + \overline{T'\frac{\partial s'}{\partial x}} = \frac{\partial \widetilde{h}}{\partial x} - \frac{1}{\overline{\rho}}\frac{\partial \overline{p}}{\partial x} - \overline{\left(\frac{\frac{\partial p''}{\partial x}}{\rho''}\right)} \tag{4.33}$$

Recall that the sign $'$ is here relative to the fluctuation with respect to the Favre average and that the sign $''$ is relative to the fluctuation with respect to the classical average as defined by the equations (4.22) and (4.23).

This last relation gives the exact averaged entropy. The two different ways of computing the entropy are compared on the figure 4.6. For this testcase, characterised by a low level of the kinetic energy of the fluctuation, the difference between the two approaches is negligible.

Finally, the specific entropy is an intensive quantity that defines a property per unit of mass. Therefore, a meaningful entropy average is the mass-average. However, the solved set of equations is based on the density-average. The quantities that are obtained by solving this set of equations are therefore area-averaged or density-averaged quantities. The figure 4.6 highlights the difference between the density-averaged and the mass-averaged entropy. The difference is far to be negligible.
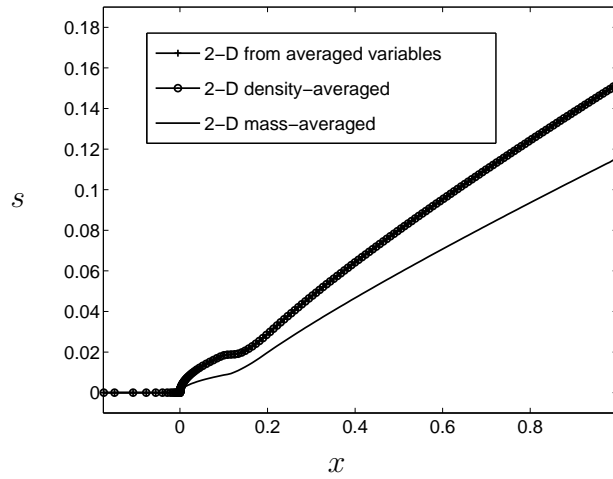


Figure 4.6: 1-D flat plate entropy computation

### 4.6.4 Wake mixing

The second testcase is a wake mixing due to the viscosity. The flow domain is a rectangle. The wake is injected as a deficit of total pressure through the left boundary of the domain and travels to the right (figure 4.7). Periodic boundary conditions are imposed on the top and on the bottom of the computational domain. The deficit of total pressure follows a cosine law and corresponds approximately to a deficit of half of the velocity at the inlet of the domain (figure 4.8). The mesh is uniform in both directions

Applying the averaging procedure to the 2-D equations of conservation for the wake mixing problem gives the following equations.

Conservation of mass:

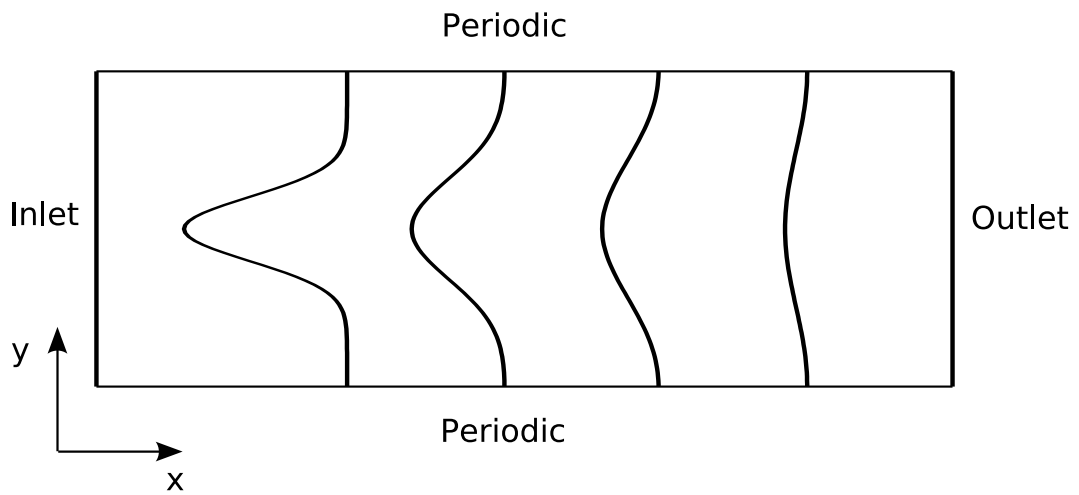$$\frac{\partial \overline{\rho} \widetilde{V_x}}{\partial x} = 0 \tag{4.34}$$
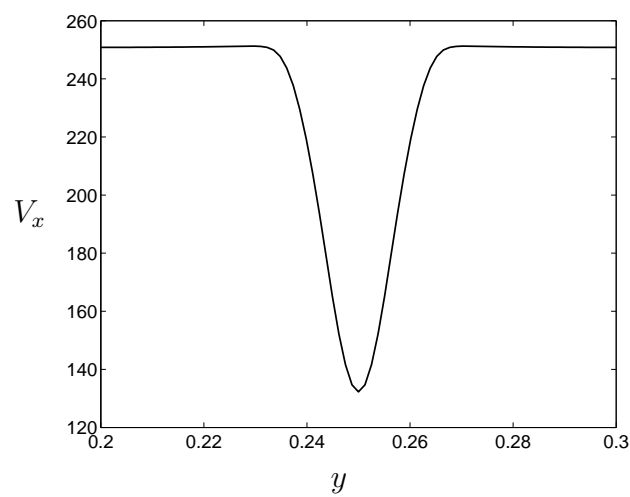
Figure 4.7: Wake mixing problem definition



Figure 4.8: Axial velocity profile at inlet of the domain

Conservation of momentum:

$$\frac{\partial(\overline{\rho \widetilde{V_x} \widetilde{V_x}} + \overline{p})}{\partial x} + \frac{\partial \overline{\rho V_x' V_x'}}{\partial x} = \frac{\partial \overline{\tau_{xx}}}{\partial x} \tag{4.35}$$

$$\frac{\partial \overline{\rho} \widetilde{V_x} \widetilde{V_y}}{\partial x} + \frac{\partial \overline{\rho V_x' V_y'}}{\partial x} = \frac{\partial \overline{\tau_{xy}}}{\partial x} \tag{4.36}$$

Conservation of energy:

$$\frac{\partial \overline{\rho} \widetilde{V_x} \widetilde{H}}{\partial x} + \frac{\partial \overline{\rho V_x' H'}}{\partial x} = \frac{\partial(\overline{\tau_{xx} V_x} + \overline{\tau_{xy} V_y} - \overline{q_x})}{\partial x} \tag{4.37}$$

where

$$\widetilde{H} = \widetilde{h} + \frac{1}{2}\widetilde{V}\widetilde{V} + \frac{1}{2}k \tag{4.38}$$

and

$$k = \frac{1}{\rho}(\overline{\rho V_x' V_x'} + \overline{\rho V_y' V_y'}) \tag{4.39}$$

Studying the evolution of the entropy is the main interest here. An equation for the entropy evolution is obtained by multiplying the equation of conservation of momentum by the velocity field, subtracting the conservation of energy and introducing the Gibbs equation. The following equation is obtained:

$$\overline{\rho} \widetilde{V_x} \overline{T} \frac{\partial \widetilde{s}}{\partial x} = -\frac{\partial \overline{\rho V_x' H'}}{\partial x} - \overline{\rho} \widetilde{V_x} \frac{1}{2} \frac{\partial k}{\partial x} + \frac{\partial \overline{\rho V_x' V_x'}}{\partial x} \widetilde{V_x} + \frac{\partial \overline{\rho V_x' V_y'}}{\partial x} \widetilde{V_y} +$$
$$\frac{\partial \overline{\tau_{xx} V_x'}}{\partial x} + \frac{\partial \overline{\tau_{xy} V_y'}}{\partial x} + \overline{\tau_{xx}} \frac{\partial V_x}{\partial x} + \overline{\tau_{xy}} \frac{\partial V_y}{\partial x} - \frac{\partial \overline{q_x}}{\partial x} \tag{4.40}$$

Compared to the equation of production of entropy in a non-averaged flow, additional terms show up, namely the spatial stresses. The figure 4.9 (a) summarises the different contributions to the entropy production. The more astonishing conclusion is that the mean viscous shear stresses exerts no influence on the 1-D evolution of entropy in a wake mixing.

The evolution of the entropy is given on the figure 4.9 (b). The density-averaged entropy exhibits a very unconventional evolution. It continuously decreases from the inlet to the outlet of the domain. This is due to the density averaging and is a common characteristic of the evolution of the density-averaged entropy in the main direction of propagation of a wake. Looking at the equation (4.40) and retaining only the main contribution, i.e. $\overline{\rho V_x' V_x'}$, it is now clear that the density-averaged entropy can only decrease in the direction of the

main velocity of the wake, i.e. the $x$ direction. Indeed, due to the homogenisation of the wake flow, $V_x'$ decreases in this direction. For this testcase, the error made by applying the Gibbs relation directly to the averaged variables is also weak as shown on figure 4.9 (b).



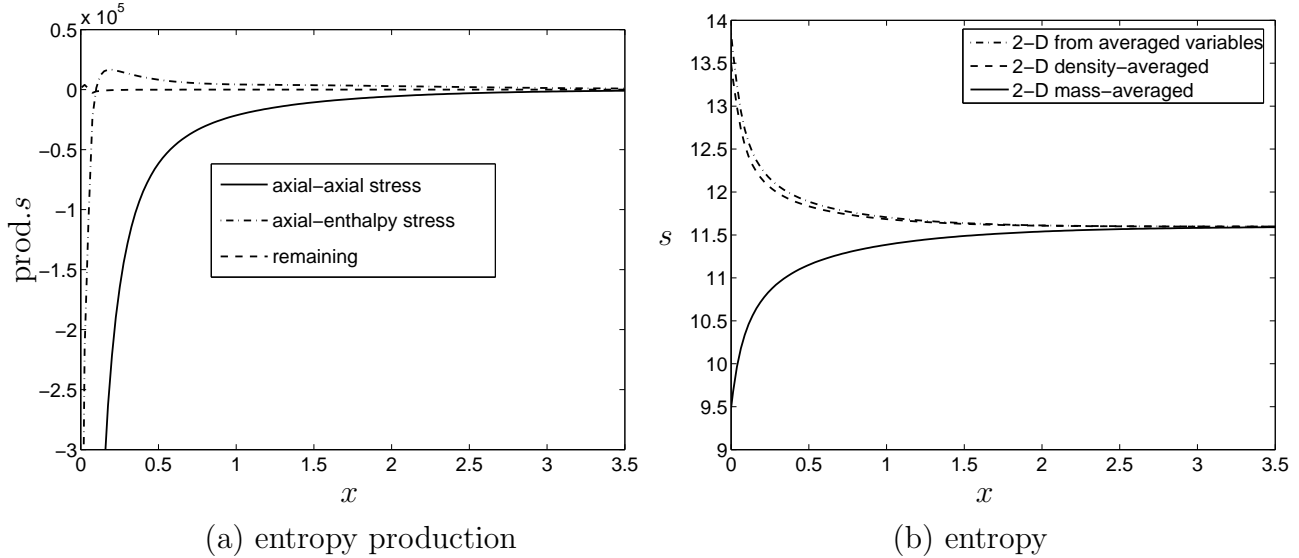(a) entropy production



(b) entropy

Figure 4.9: Contributions to entropy production and entropy evolution

Finally, a parametric study has been performed to evaluate the impact of the mesh resolution in the direction perpendicular to the wake propagation (y direction). The equations have been solved on three different uniform meshes with respectively 40, 20 and 13 grid points in the y direction. The spatial stresses have been extracted from each simulation and used to feed the 1-D model.

The obtained evolutions of the entropy are given on the figure 4.10. For a simulation with a sufficiently high number of nodes in the y direction, the stresses extracted from the 2-D simulation are able to correctly reproduce the entropy evolution. When the number of grid points is not sufficient, not only the 2-D solution departs from the reference one obtained on the fine mesh, which is an expected phenomenon, but the 1-D solution and the averaged 2-D solution differ. The stresses are not anymore able to reproduce the entropy evolution in the 2-D flow field. It seems that when the mesh resolution is not fine enough, the filtering through the average loses some information. In other words, the numerical dissipation in the reference 2-D problem is filtered out by the averaging process and cannot be reproduced by the resolution of the averaged set of equations.

This means that when the reference solution presents some non-negligible numerical errors, some differences may arise between the average of the reference solution and the solution of the averaged set of equations.
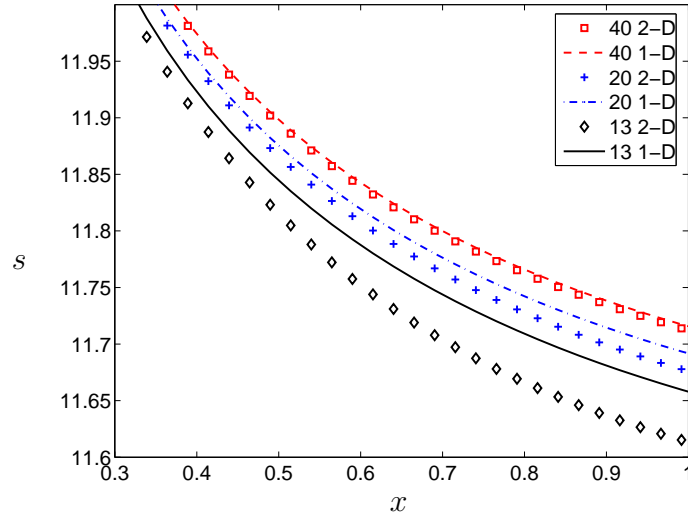
Figure 4.10: Effect of the mesh discretization on the averaged entropy

## 4.6.5  Concluding remarks and summary on 1-D testcases

From the two testcases presented above, the following conclusions and remarks are made:

1. The prioritization of the different contributions to the conservation equations has shown that among all viscous terms, the wall shear stress is the sole to be important. It is even the predominant term for the boundary layer development testcase. The spatial stresses are also important. In the case of a blade passage, some additional circumferential stresses will be generated due to the turning of the flow.

2. The error due to the application of the Gibbs equation directly to the averaged variables instead of the averaged form of the Gibbs equation seems to be weak. Especially when this difference is compared to the difference brought by the density-average with respect to the mass-average.

3. The difference observed between the mass-averaged and the density-averaged entropy increases with the non-uniformity of the flow. Extrapolated to the circumferential-average and to a turbomachine configuration, it means that sufficiently far from the inlet and the outlet of a blade row or a compressor, in the regions where the flow is circumferentially uniform, the two averages coincide (see figure 4.9 (b)). The global performances or radial surveys that would be obtained at the outlet of a machine with a density-average based computation would thus be correct. However, this is not fully satisfactory. A first and easy way to overcome this could be to develop a calibration of the mass-averaged and the density-averaged quantities in function of the level of kinetic energy of the circumferential fluctuations. These calibrations could be obtained from the large number of 3-D simulations performed in the turbomachine industry. A second and more attractive solution would be to devise a mass-averaged throughflow

model. Such an approach has been studied by a few authors. Noteworthy, Hirsch and Dring (1987) presented a rigorous derivation of a mass-averaged (momentum-averaged more precisely) throughflow model. In particular, they show the relation between the throughflow equations based on the density-average and the momentum-average. This relationship appears through the definition of six blockage coefficients. This theory has however not been applied here and the reference average will still be the density one in the following.

4. Continuing on the subject of the difference between the mass-average and the density-average, Bardoux (2000) has also observed the particular behaviour of the density-based average in the frame of 3-D steady simulations including the effect of the unsteady deterministic flow, i.e. for the time-average. The effect is however expected to be much smaller in that problem than in the circumferential-average problem because of the lower level of the kinetic energy of the involved fluctuations. The kinetic energy of the circumferential fluctuations can represent a great part of the total kinetic energy. For example, in a recirculation zone, where the averaged velocity reaches zero, the fluctuations represent 30 % of the maximum kinetic energy found in the complete flow field. This is in strong contrast with the turbulent kinetic energy or the deterministic kinetic energy and explains why the nature of the averaging is more critical in a throughflow problem.

5. Finally, it has been observed that some differences may occur between the 2-D averaged solution and the solution of the averaged equations with the numerical errors present in the 2-D simulation.

# Chapter 5

# Throughflow computations based on 3-D simulations

This chapter is dedicated to the application of the high order throughflow method described in chapter 4 to real turbomachine testcases. These testcases consist of two numerical simulations from which the additional terms necessary to run high order throughflow computations are extracted, i.e. the blade forces and the stresses. The first case is a 3-D simulation of the low speed CME2 compressor. The second is a 3-D unsteady simulation of the transonic VEGA2 turbine.

The notations used in the previous chapter and in the appendix B are not very practical due to the use of four averages. As the turbulence closure removes the explicit use of the Reynolds stress and as the passage-to-passage average is not considered here, their contributions in the average notation will therefore be forgotten in the following. Furthermore, for the steady simulation of the CME2 compressor, the deterministic average notation will also be removed, in such a way that the circumferential average will be denoted with one overline $(\overline{f}^c)$ and one prime sign $(f')$.

## 5.1   Information to be extracted from 3-D solutions

In section 4.6, it was shown that the viscous shear stresses (to the exception of the shear stresses at wall) do not play a significant role in the momentum and energy balances for an averaged 2-D flow.

Transposed to a 3-D flow circumferentially averaged, this result means that the viscous shear stresses acting in the blade-to-blade plane can be neglected. However, in the regions close to the annulus endwalls, it is obvious that the viscous shear stresses cannot be neglected

119

anymore. Contrary to the blade walls, the annulus endwalls are still present in the averaged flow and the contribution of the viscous stresses in these regions is important. Another way to look at this is to divide the viscous shear stresses (including both laminar and turbulent stresses) in three main contributions:

1. the viscous stresses acting in the blade-to-blade plane and which are similar to the ones that would be obtained with a 2-D blade-to-blade calculation,

2. the 2-D annulus endwalls viscous stresses. They result from the 2-D hub-to-tip development of the viscous flow and are similar to the ones that would be obtained in a channel flow,

3. the 3-D viscous stresses resulting from the interaction of the blades and the annulus endwall flows. They contain all viscous effects not included in the two first contributions.

This distinction between these three viscous contributions is maybe arbitrary and oversimplified but it will be useful for the discussion. The results presented in section 4.6 come to the conclusion that the contribution 1 reduces to the shear stresses at blade walls.

In the present work, the laminar viscous stresses and the turbulent stresses appearing in the momentum equations

$$\overline{\overline{\tau_{ij}}}^{ec} - \overline{\overline{\rho V_i' V_j'}}^{ec} \tag{5.1}$$

are approximated by the axisymmetric viscous stresses, the turbulent part being closed by the Baldwin-Lomax model. It is the model used in section 1.5 for the Navier-Stokes throughflow. This approach in fact neglects the viscous shear stresses resulting from the interaction of the blades and the annulus endwalls (the third contribution above). It is solely the viscous shear stresses part of the interaction that is neglected, the contributions of the circumferential stresses and of the blade wall shear stresses (the viscous blade force) are considered.

The following quantities will be extracted from the 3-D simulations: the inviscid and viscous blade forces and the circumferential stresses resulting from the $\theta$-average. The viscous blade force is directly computed from the blade wall shear stress $\tau_{wall}$ computed either using the wall functions (for the CME2 testcase) or by computing the primitive variables gradients at the wall (for the VEGA2 testcase). The inviscid blade force is computed from the pressure distribution on the blades. For the same reasons as those exposed in section 2.6.2 about the computation of the gradient of the blockage factor, the axial and radial blade forces are discretized with a finite volume approach. For example, for the radial component of the blade force (equation B.42)

$$f_{br} = \frac{1}{2\pi b} \sum_{n=0}^{N-1} \left( p_5 \frac{\partial \theta_5}{\partial r} - p_6 \frac{\partial \theta_6}{\partial r} \right) \tag{5.2}$$

the derivatives on both sides of the blade must be evaluated by the Green-Gauss theorem otherwise some numerical errors occur because of the unbalancing of the blade blockage term and of the blade force.

The circumferential stresses are extracted from the 3-D solutions by the following procedure:

1. A reference mesh must be generated in the meridional plane. On each node of this reference mesh, the circumferential stresses will be evaluated. From each node a circular arc is plotted and the variables on the 3-D domain are interpolated on it. Thanks to the axisymmetry of the blade-to-blade meshes composing the 3-D mesh, only 2-D interpolations are necessary to compute the variables on the circular arc.

2. Once the variables have been computed on the circular arcs, the circumferential averaging is easily performed by integrating the quantities over the circular arcs. It is necessary to compute the average of the conservative variables but also the average of the quadratic terms $\rho V_i V_j$ in order to compute the circumferential stresses by the following relation:

$$\overline{\rho V_i' V_j'}^c = \overline{\rho V_i V_j}^c - \overline{\rho}^c \widetilde{V_i}^c \widetilde{V_j}^c \tag{5.3}$$

3. The obtained stresses are interpolated on the middle of the edges of the throughflow mesh. The derivatives at the cell-centred are finally computed by the diamond path scheme from these middle egde values.

## 5.2  CME2 steady simulation

The CME2 is a single stage low speed compressor. Its global performances are presented on the table 5.1. The simulation used here has been obtained by Gourdain (2005) with the numerical code elsA developed by the ONERA. The turbulent viscosity is computed using the model of Spalart-Allmaras. Wall functions have been used. A blade-to-blade view of the mesh, illustrating the blade geometry, is presented on the figure 5.1 while a meridional view of the compressor is shown on the figure 5.2. The 3-D mesh is composed of approximately one million grid points. The simulation has been run for the nominal conditions. A comparison of the results of the simulation and the experimental measurements are presented in Gourdain (2005). The agreement is good.

The complete computational domain used by Gourdain extends further upstream and downstream of the boundaries shown on the figure 5.2. A smaller computational domain has been used here in order to reduce the computational time. It also helps in reducing the discrepancy between between the 3-D and the throughflow simulations that is brought by different boundary layer developments ahead of the rotor. This discrepancy arises because of the difference in the turbulence models and because of the different wall treatments used in both simulations (wall functions and Spalart-Allmaras versus Baldwin-Lomax).

| mass flow | 11 kg/s |
|---|---|
| pressure ratio | 1.14 |
| efficiency | 0.92 |
| rotation speed | 6300 RPM |

Table 5.1: Global parameters of the CME2 compressor
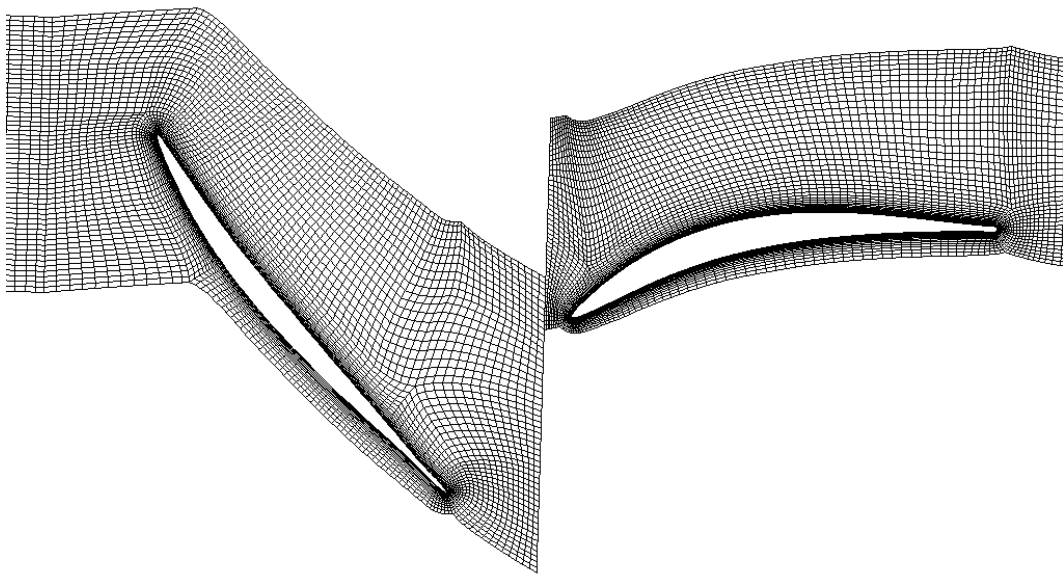


Figure 5.1: CME2 compressor blade-to-blade mesh at midspan
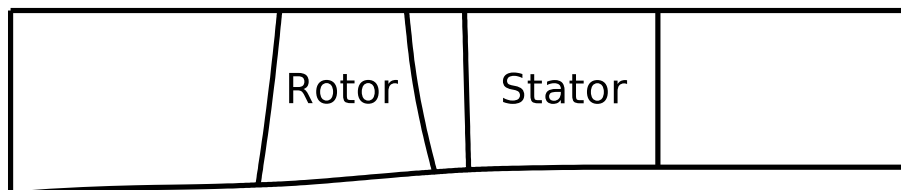


Figure 5.2: Meridional view of the CME2 compressor

The blade forces and the circumferential stresses obtained for this testcase are given in the appendix C.1. The observation of the evolution of the kinetic energy related to the circumferential stresses allows to highlight some of the main flow features. This evolution is given on the figure 5.3 for the whole 2-D field and on the figure 5.4 (a) for its axial distribution at midspan.

Some small spikes are visible in the region of the leading edges. This is a potential effect due to the flow going round the leading edge. At the trailing edges, spikes are also present. In these regions, the flow is subject to a strong reorganization due to the disappearance of the blade. Inside the blade passage, the kinetic energy evolves due to both the boundary layer development and the aerodynamic loading necessary to turn the flow. This quantity is shown on the figure 5.4 (b) by the circumferential component of the blade force. For both rows, the loading is concentrated in the region to the leading edge. This leads to a chordwise diminution of the kinetic energy, once the maximum loading is passed. For the stator row, the main characteristic is the strong non-uniformity of the flow close to the hub due to the corner stall (figure 5.3).
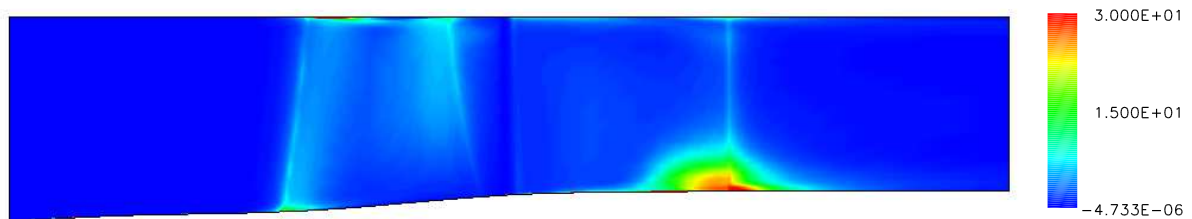


Figure 5.3: Kinetic energy of the circumferential stresses expressed in % of the total kinetic energy



(a) kinetic energy
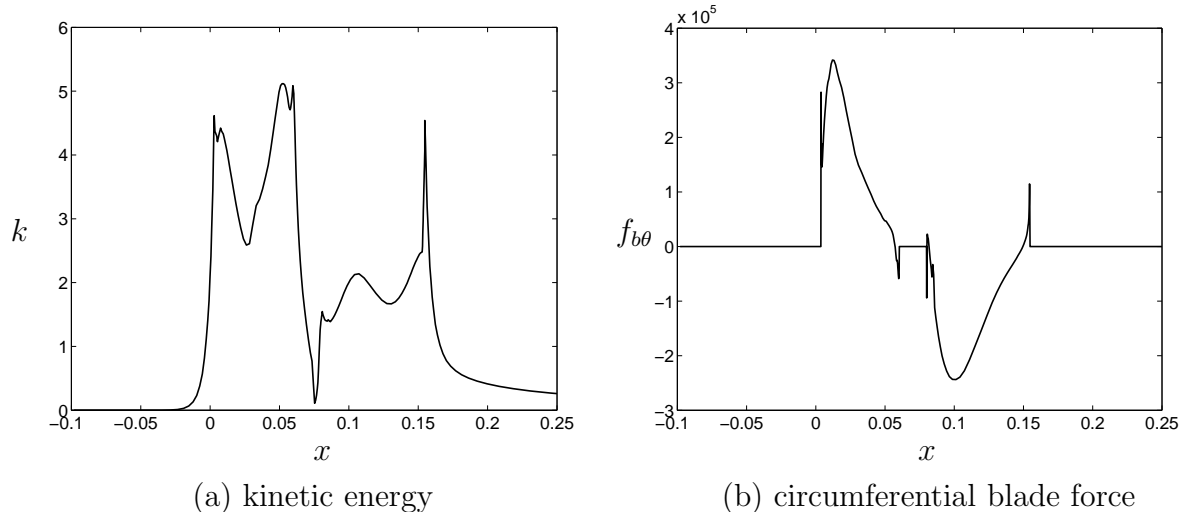
(b) circumferential blade force

Figure 5.4: (a) Kinetic energy of the circumferential stresses at midspan (in % of the total kinetic energy) and (b) circumferential blade force at midspan (in $N/m^3$)

## 5.3   CME2 throughflow analysis

The circumferential stresses and the blade forces computed in the previous section have been used to feed a throughflow computation. A typical mesh used for such computations is

presented at the figure 5.5. The mesh is clustered in the leading and trailing edges regions. This is necessary to correctly compute the strong gradients typical of these regions (see figures 5.3 and 5.4 (a)) .
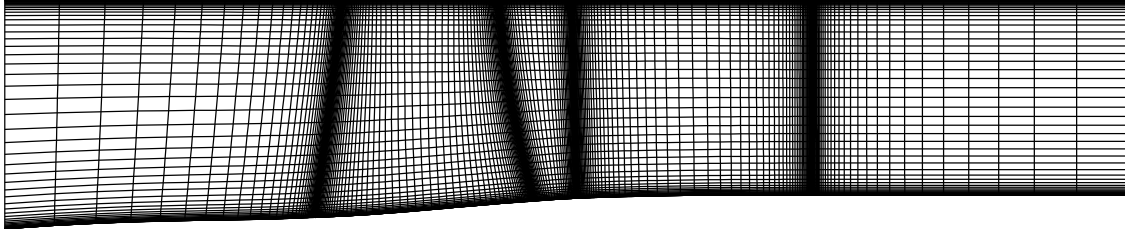


Figure 5.5: CME2 meridional mesh

A qualitative overview of the obtained solution is presented on the figures 5.6, 5.7 and 5.8. They compare three representative quantities of the flow field for the throughflow solution and the averaged 3-D solution. The agreement is very impressive. All the flow features are reproduced, such as the recirculation in the tip gap region with its associated high losses or the stator corner stall.

More quantitative investigations can be performed by inspecting radial surveys at inlet, outlet but also inside each blade rows as shown on figures 5.9 and 5.10 for respectively the rotor and the stator. The flow field inside the rotor is really well reproduced by the extracted 3-D terms and the viscous endwall model. For the stator row, the agreement is still good but some discrepancies occur in the corner stall region. This is mainly visible on the distribution of entropy and total pressure on the figure 5.9. The entropy turns out to be the most difficult quantity to correctly estimate. A small difference in pressure and temperature fields can lead to a substantial difference in the entropy.

The discrepancy can be attributed to either numerical errors or modelling errors. The numerical errors have several origins:

- firstly, errors arise from the different interpolation operations performed on the 3-D mesh and on the throughflow mesh in order to compute the forces and the stresses,

- secondly, the discretization of the stresses themselves by the Green-Gauss integration can also lead to some numerical errors,

- finally, the discretization error arising in the 3-D solution is viewed in the throughflow equations through a filter as shown in section 4.6.4.

The other errors are the modelling errors, i.e. error arising from the assumptions made to build the model:
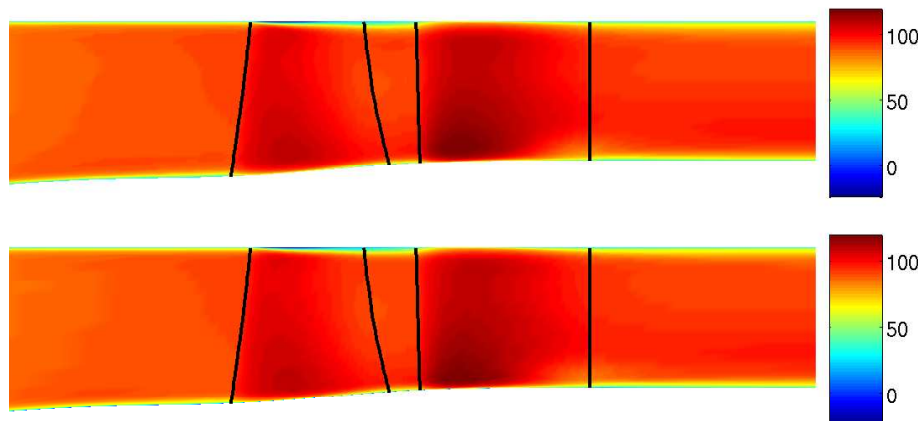
Figure 5.6: Axial velocity from 3-D averaged solution (top) and throughflow solution (bottom)
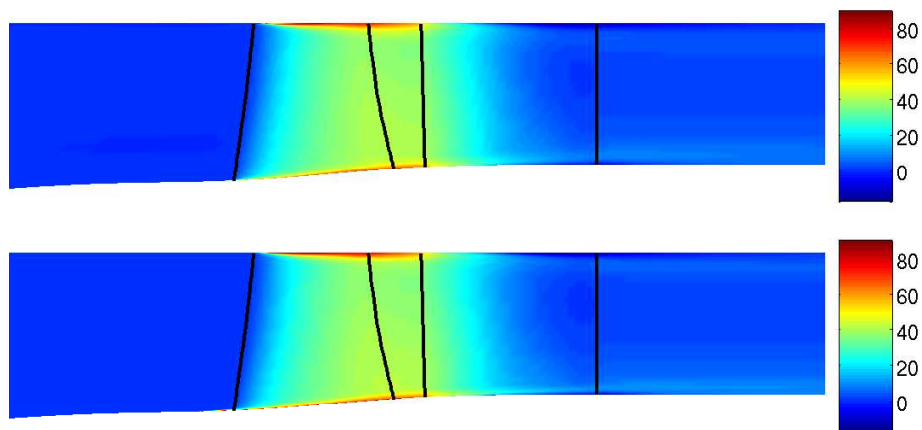


Figure 5.7: Absolute flow angle from 3-D averaged solution (top) and throughflow solution (bottom)



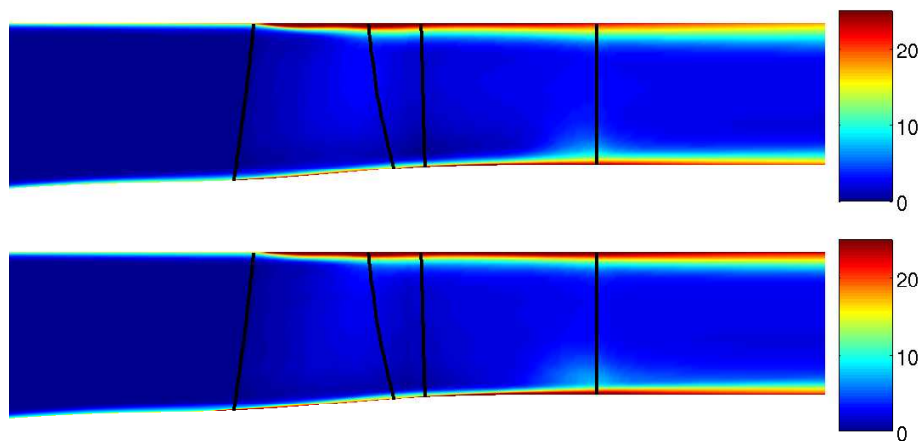Figure 5.8: Entropy from 3-D averaged solution (top) and throughflow solution (bottom)

Figure 5.9: Comparison between the throughflow solution (plain lines) and the 3-D solution circumferentially averaged (symbols) at 3 locations inside the rotor domain
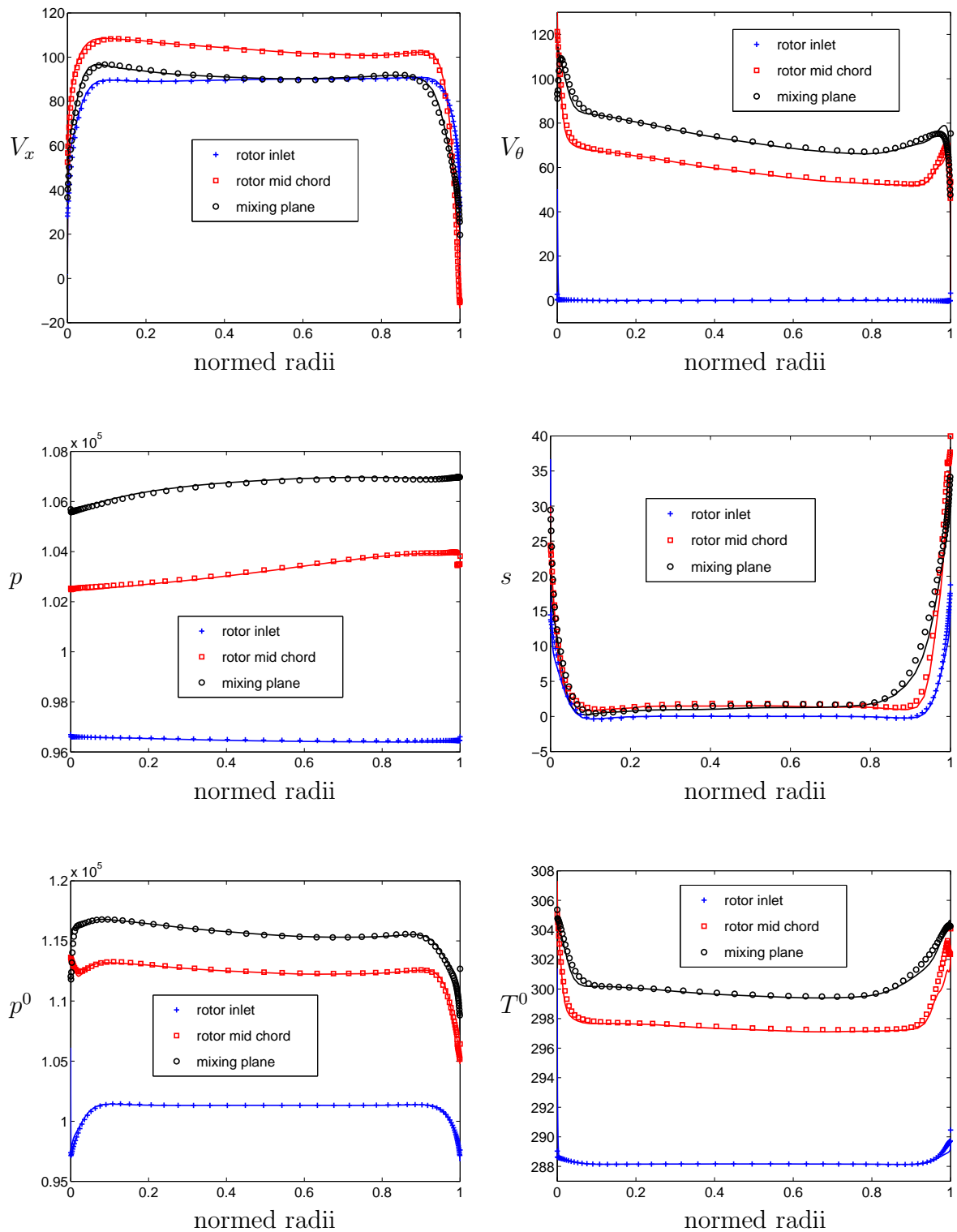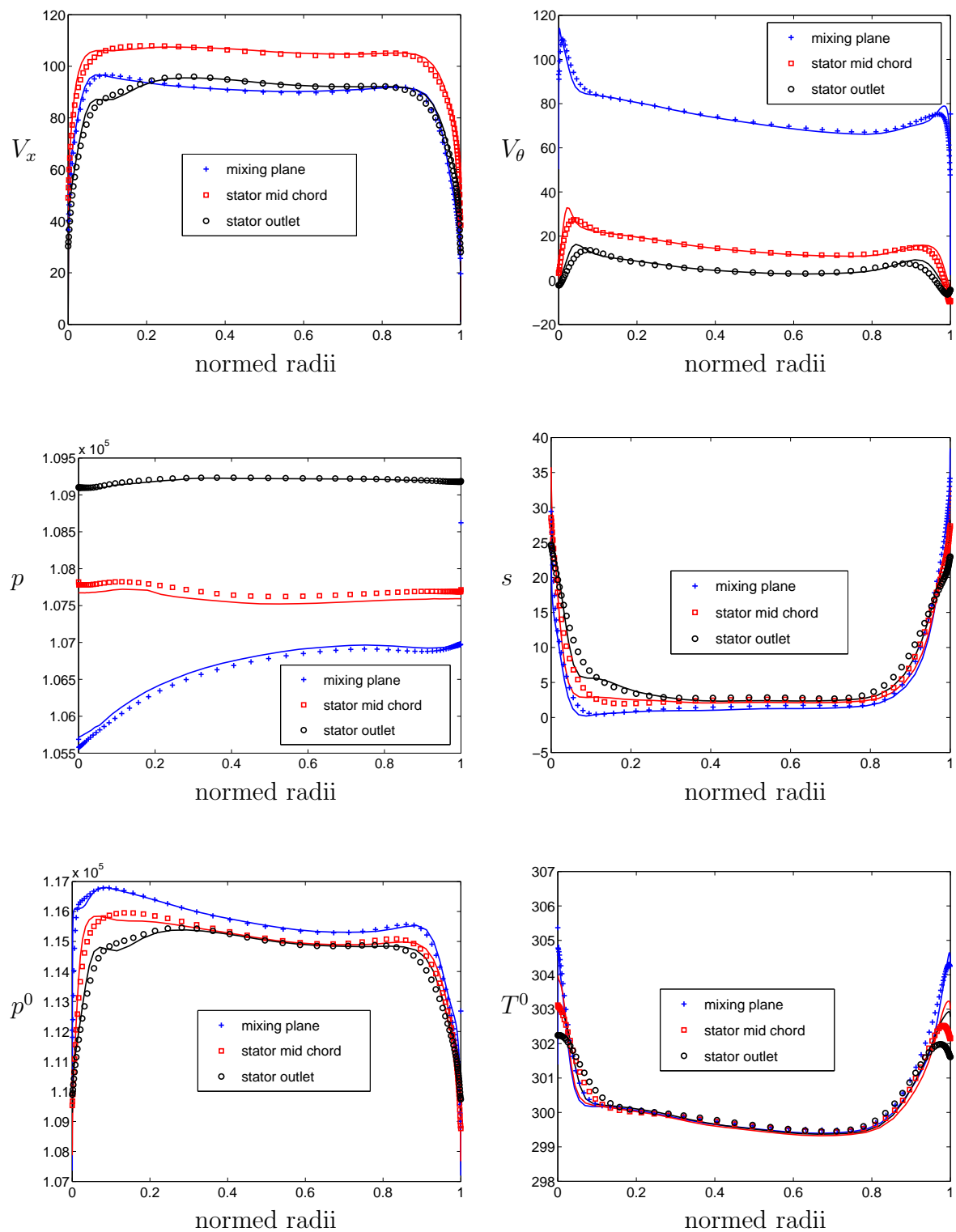
Figure 5.10: Comparison between the throughflow solution (plain lines) and the 3-D solution circumferentially averaged (symbols) at 3 locations inside the stator domain

- first, the sole blade-to-blade viscous contribution that is included is the viscous blade force. Other contributions such as the averaged viscous stresses are missing,

- secondly, the endwall losses are modelled by the axisymmetric Navier-Stokes terms and the Baldwin-Lomax turbulence model. This is a simplification compared to the real viscous terms circumferentially averaged,

- furthermore the turbulence model used here is different from the one used in the 3-D computation (the Spalart-Allmaras model).

Most of these errors are susceptible to be high in the regions of high flow non-uniformities such as the corner stall or the blades leading and trailing edges regions. It is therefore not easy to clearly determine which error predominates. Moreover, it is possible that combination of errors occurs. However, in the present case, the main discrepancy has been attributed to the 2-D Baldwin-Lomax turbulence model. The explanation is given hereafter.

To compute the viscosity in its outer layer, the Baldwin-Lomax model relies on the maximum of the momentum of vorticity and the distance from the wall at which this maximum occurs, i.e. the product $F_{max} y_{max}$ (see section 1.5.1 describing the Baldwin-Lomax model). However, close to the endwalls, the vorticity varies very quickly axially as one approaches the rotating hub. Due to this sharp variation and also due to the presence of the blades, the vorticity and the momentum of vorticity present a spurious behaviour. This is illustrated by the radial evolution of this quantity just upstream and downstream of the rotating hub at the figure 5.11 (a). It is mainly the variation in $y_{max}$ which gives a discontinuous behaviour of the outer turbulent viscosity. The axial evolution of this quantity is given on the figure 5.11 (b) for the hub wall. The drop of $y_{max}$ as one passes from a fixed wall to a rotating one (and conversely) is clearly highlighted.

The resulting turbulent viscosity is given on the lower part of the figure 5.12. It exhibits discontinuities for the above reasons. The drop of the turbulent viscosity causes an incorrect development of the boundary layer and partly explains the discrepancy observed on the figures 5.9 and 5.10.

The turbulent viscosity computed with the Baldwin-Lomax model is compared to the one computed by the 3-D simulation (via the Spalart-Allmaras model) which has been circumferentially averaged and plotted on the upper part of the figure 5.12. The most significant observation is that to the exception of the "resetting" of the turbulence viscosity in certain regions, the evolution of the turbulent viscosity computed by the Baldwin-Lomax is correctly predicted although this model is not based on the "history" of the flow.

Indeed, the localised zone of high turbulent viscosity at the rotor tip close to and downstream of the leading edge on the upper part of the figure 5.12 is also observed with the Baldwin-Lomax model on the lower part of the figure 5.12. The thickening of the boundary layer downstream of the compressor is also well predicted. This means that a throughflow model

with correct circumferential stresses and blade forces is able to reproduce the evolution of the viscous flow developing on the annulus endwalls with a simple 2-D turbulence model originally devised for channel flows. What is meant here is that no special treatment of the averaged turbulent stresses is necessary due to the presence of the blade, provided that one uses a model which solves the problem of the resetting of the boundary layer encountered with the Baldwin-Lomax model.

On this subject, several tweaks of the Baldwin-Lomax model have been tested. These tweaks consisted in taking only the axial and radial components of the velocity for computing the vorticity, or trying to take into account only a part of the decrease in $y_{max}$. None of the tested solutions was successful.

It is expected that this problem will also arise with the turbulence model of Cebeci and Smith (1974), which is another famous algebraic turbulence model. This model necessitates the determination of the edge of the boundary layer and that determination would probably be problematic due to the strong variations occurring at the rotating hub and in the blade rows. At this level it seems that a model based on the transport of the turbulence, such as the model of Spalart and Allmaras (1992) is a reasonable trade-off between accuracy and computational effort. It is based on the transport of $\mu_t$ and does not need to explicitly compute the length scale, which would avoid the resetting of the boundary layer. On the other hand, it is sufficiently fast and robust for a design method.

To be able to judge to which extent the Baldwin Lomax model is responsible for the difference observed in the radial distributions on the figures 5.9 and 5.10 and thus to figure out the benefit of its replacement in profit of a more evolved turbulence model, a computation has been run with a fixed turbulent viscosity extracted from the 3-D computation circumferentially averaged. This does not mean that the complete viscous effects are taken from the 3-D solution as it is only the turbulent viscosity and not the shear stresses that has been provided by it.

The figure 5.13 compares the total pressure distribution obtained at the outlet of the compressor for both simulations. The peaks in the boundary layer have disappeared on both walls. In these regions, the new distribution fits very well the averaged 3-D one. However, there is still a zone with more losses. This difference may be attributed to the numerical errors and not to the modelling errors. Indeed, as a too high level of losses is predicted, the difference cannot be attributed to the fact that the viscous shear stresses acting in the blade-to-blade plane have been neglected as their inclusion would have generated more losses.

In conclusion, the agreement between the throughflow solution and the 3-D averaged solution is considered to be very good. The main improvement lies in introducing a more elaborated turbulence model. A standard 2-D model in the hub-to-tip direction without modification (i.e. for channel flows) should be sufficient.

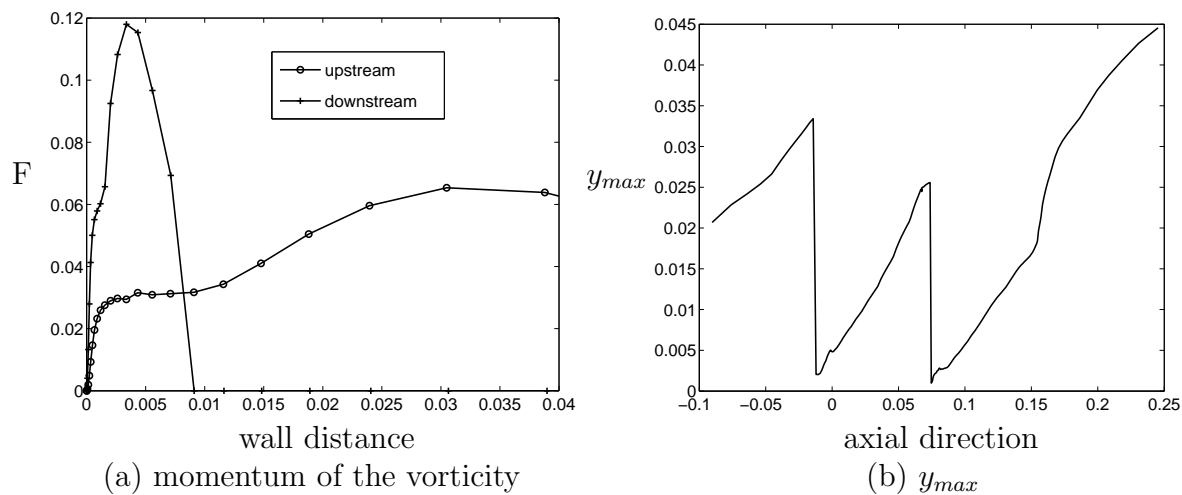(a) momentum of the vorticity           (b) $y_{max}$

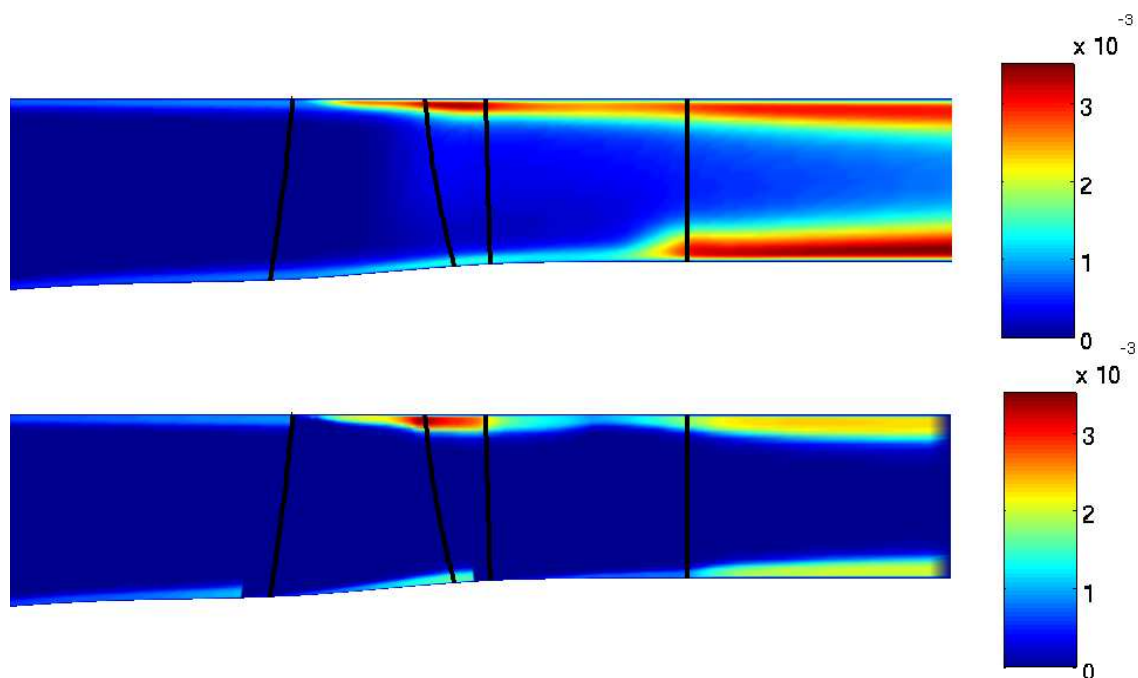Figure 5.11: Evolution of the outer viscosity parameters of the Baldwin-Lomax model



Figure 5.12: Comparison of the turbulent viscosity computed by the 3-D calculation (top) and computed by the throughflow model (bottom)
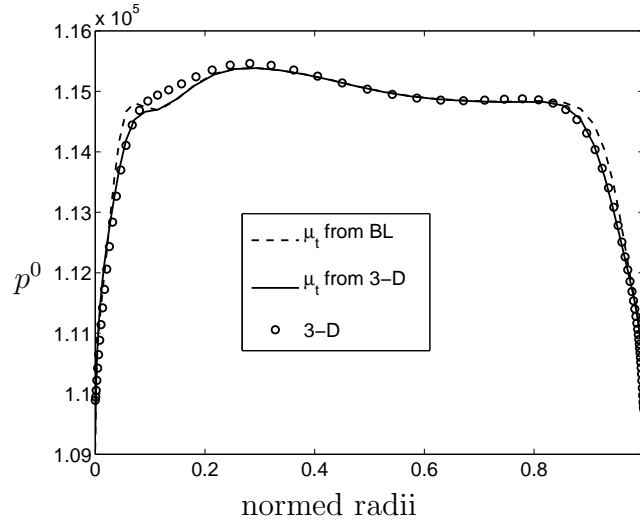
Figure 5.13: Total pressure at the outlet of the compressor. Comparison of the solutions obtained with the viscosity computed from the Baldwin-Lomax model and the one imposed from the 3-D computation circumferentially averaged.

## 5.4 Contributions to the momentum and energy equations

In this section, the relative importance of the different contributions taken from the 3-D simulation, i.e. the blade forces and the circumferential stresses, on the momentum and energy equations will be evaluated. First, the global impact of the blade forces and of the circumferential stresses on the flow field is investigated and next the contribution of each individual stress and component of the blade forces is analysed.

The figure 5.14 compares the entropy evolution for four computations. These computations are:

1. a computation with the inviscid blade force only ($f_b$),

2. a computation with both the inviscid and the viscous blade forces ($f_b + f_v$),

3. a computation with the inviscid blade force and the circumferential stresses ($f_b +$ stress),

4. a full computation containing all contributions ($f_b + f_v +$ stress (full)).

The first observation is that the simulation including only the inviscid blade force shows some entropy generation in the core flow region where the annulus endwall flows have no influence. This is an expected effect and is not a particularity of the density-average. This is due to

the unbalance of the momentum and energy equations. Indeed, let us consider a 3-D Euler simulation from which inviscid blade forces and circumferential stresses are extracted and injected in a throughflow model. An isentropic flow would be obtained with the throughflow only if all contributions are introduced in the conservation equations. Removing the stresses would lead to an unbalance of the equations and to an unphysical evolution of entropy.



(a) $f_b$

(b) $f_b + f_v$

(c) $f_b +$ stress

(d) $f_b + f_v +$ stress (full)
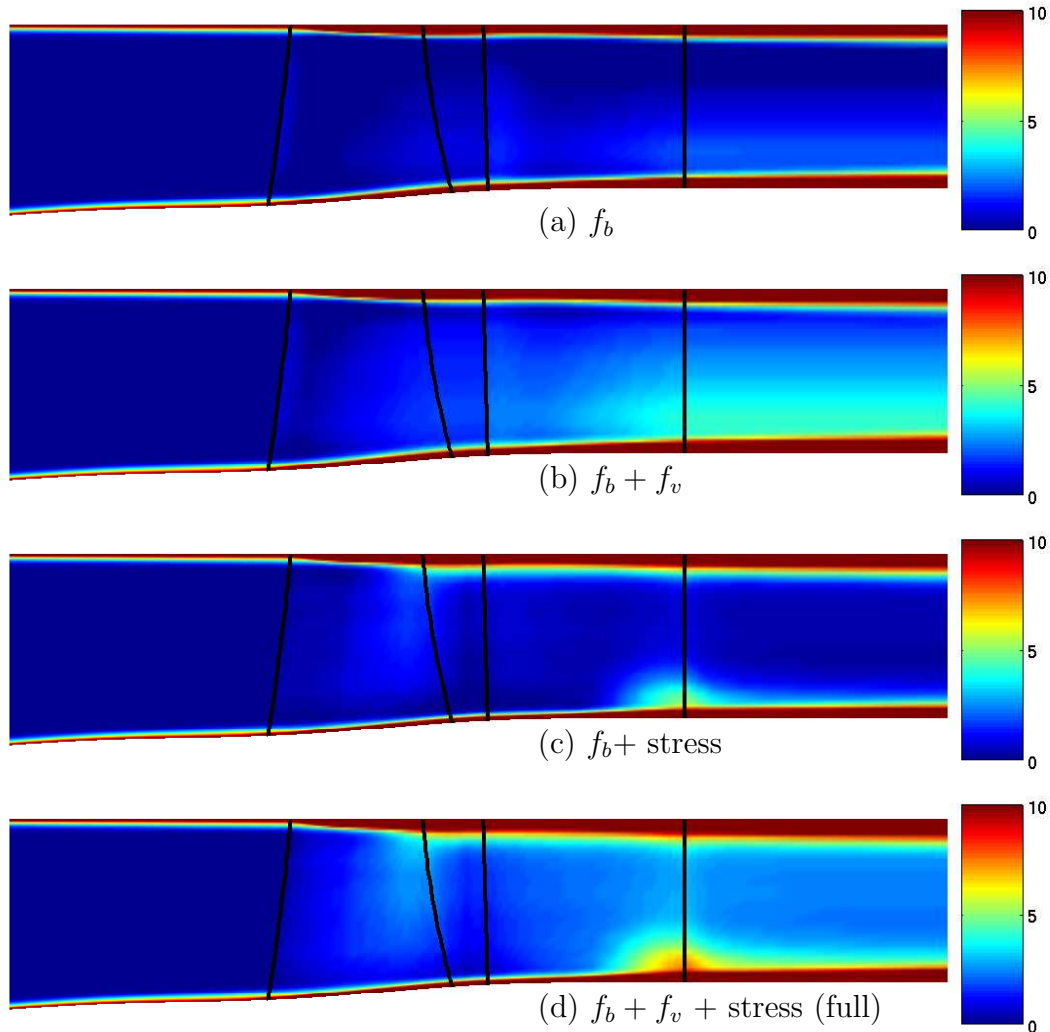
Figure 5.14: Impact of the blade forces and of the circumferential stresses on the entropy field

Both the viscous blade force and the circumferential stresses participate to the generation of entropy. However, it is the circumferential stresses that are responsible for the particular distribution of the entropy in the corner stall. It is also the circumferential stresses that are responsible for the increase-decrease of entropy along a streamline across the trailing edges. As explained in a preceding section, the decrease is due to the uniformisation of the flow just downstream of the trailing edges.

Overall, it seems that the viscous blade force is more or less responsible for the level of entropy while the circumferential stresses give the shape of the distribution. This is confirmed by the inspection of the radial distribution of the entropy half a chord downstream of the stator on the figure 5.15 (a). The same conclusion applies for the axial velocity distribution on the figure 5.15 (b). The blockage of the flow close to the hub caused by the corner stall is the result of the circumferential stresses only. It is also the circumferential stresses that are responsible for the radial mixing close to the endwalls as illustrated at the figure 5.15 (c) for the total temperature. The stresses reduce the gradients close to the endwalls. Finally, the figure 5.15 (d) shows the radial distribution of the radial velocity at the mid-chord of the stator. Only the circumferential stresses are able to reproduce the radial velocity generated by the corner stall.
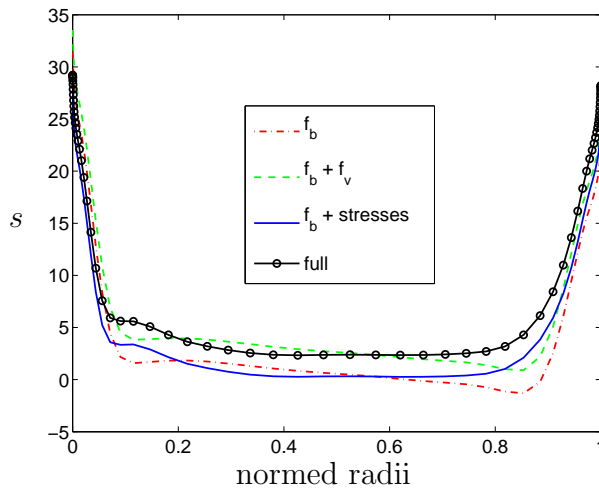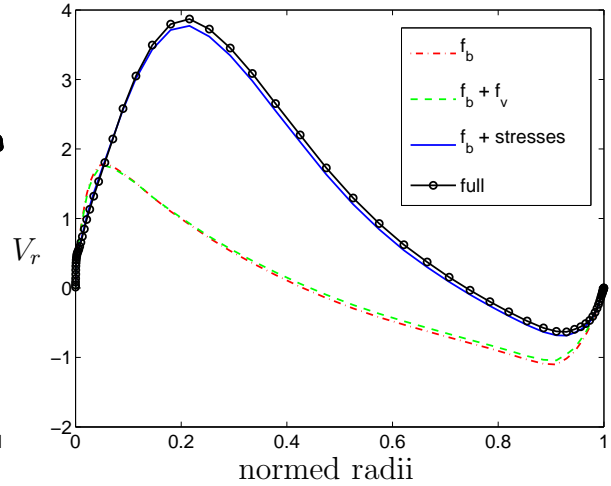


(a) entropy at the stator outlet
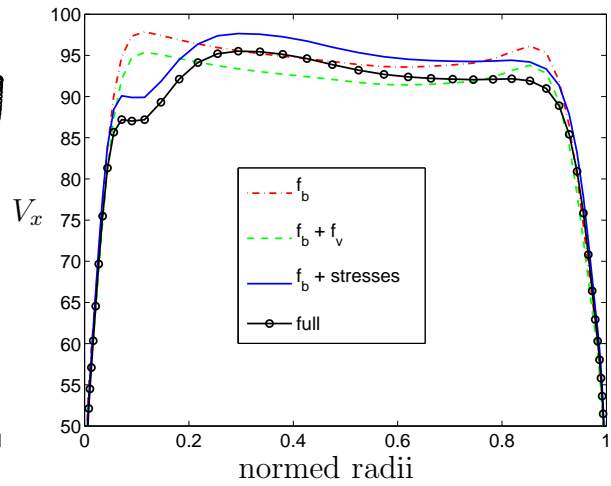
(b) axial velocity at the stator outlet
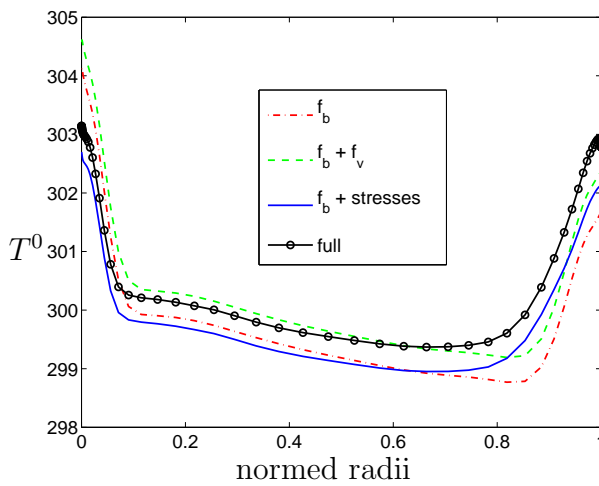
(c) total temperature at the stator outlet

(d) radial velocity at the stator mid-chord

Figure 5.15: Comparison of the impact of the different contributions extracted from the 3-D solution circumferentially averaged

It is possible to gain more insight on the effect of the different components of the forces and stresses on the flow field by analysing individually their effect. This means that each equation must be analysed separately. The appendix C.2 shows the balancing of each equation between the forces and the circumferential stresses. To be meaningful, the comparison of the blade forces components must be made with the derivatives of the stresses. It is clear from all the figures that the inviscid blade force dominates the momentum balance. Next come the circumferential stresses and finally the viscous blade forces.

Looking at the mean level of those last terms, it is tempting to conclude that it is not worth to include them in a simulation. This is misleading as another criterion must be taken into account, i.e. the direction of the force. Indeed, in section 1.3.1 devoted to the distributed loss model, it has been shown that the direction of the force is important for the loss generation mechanism. For the present testcase, neglecting the viscous blade force leads to a strong overestimation of the isentropic efficiency: 0.947 to be compared to 0.894 for the full simulation (0.891 for the 3-D simulation results). This result confirms the conclusion on the importance of the viscous blade force obtained on 1-D testcases in section 4.6

The observation made in this work concerning the importance of including the viscous blade force is in contradiction with results from other researchers studying the deterministic stress closure. As described in section 4.5.1, a way to address the deterministic stress closure is to consider the Adamczyk assumption, i.e. to neglect the purely temporal part of the deterministic stresses and to retain only the spatial part. Some approaches based on this assumption explicitly compute the required terms for the closure and neglect the viscous terms (Rhie *et al.* (1995) and Bardoux (2000)). Bardoux (2000) has presented some results obtained on the CME2 compressor that is studied here. He showed a comparison between the 3-D flow averaged in the stator and the same flow with the stator modelled by a "ghost row', consisting of an inviscid blade force and the circumferential stresses. He found some differences between the two computations. With the observation made in this work, the discrepancy observed by Bardoux can be attributed to the absence of the viscous blade force in its model. Indeed, the discrepancy observed by Bardoux is the same as the one observed between the full simulation and the $f_b+$ stress one on the figure 5.15.

Finally, eight computations have been performed, each one neglecting a given stress. The results are summarised on the figure 5.16. As expected from the analysis of the appendix C.2, the axial-axial stress takes the greatest importance, acting as a blockage term. This is the sole stress contribution appearing in an axial derivative that has some importance. All the other terms that impact the flow field are given by a radial derivative of a stress. These terms are: the axial-radial, the circumferential-radial and the enthalpy-radial stresses.
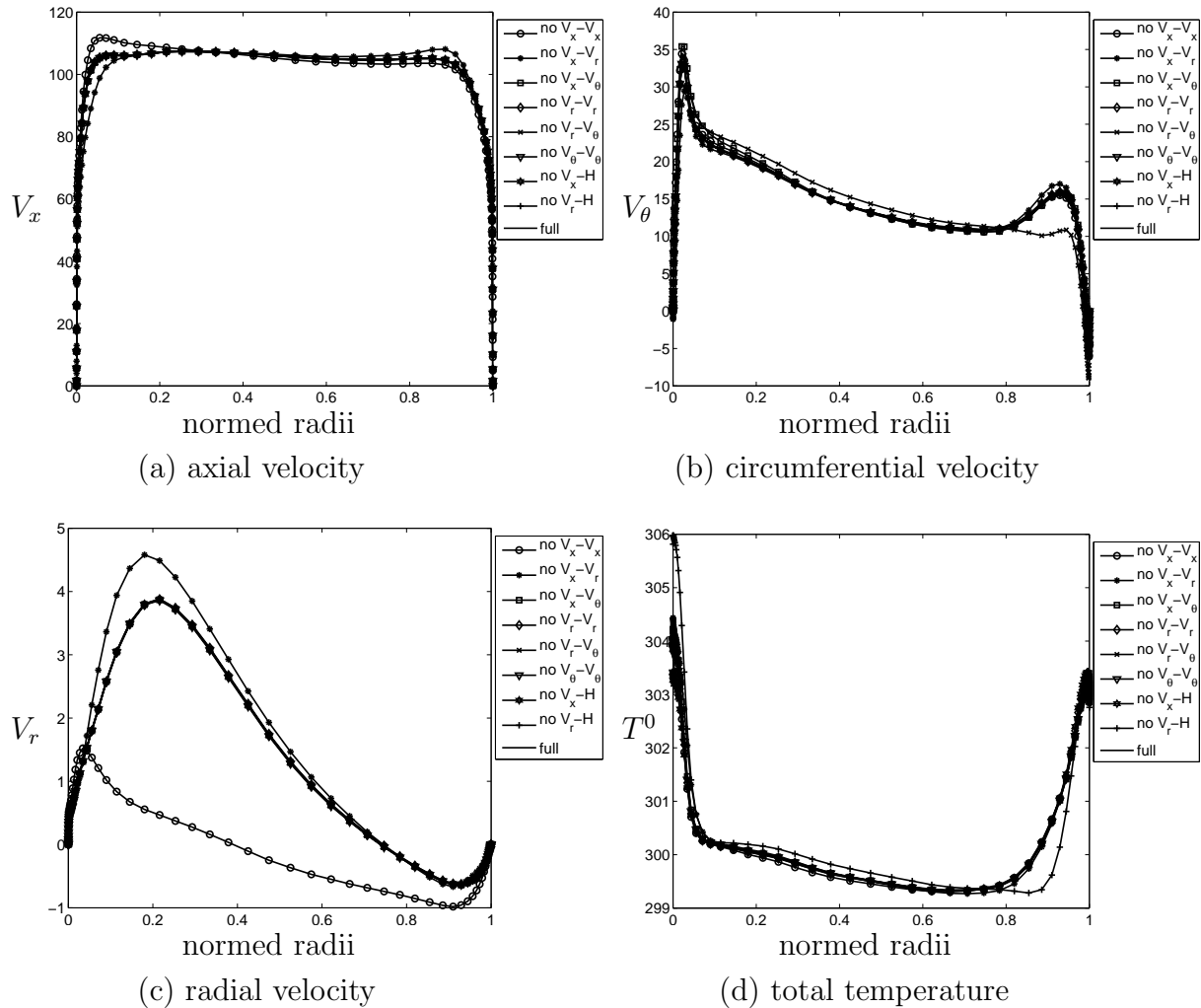
Figure 5.16: Comparison of the impact of the individual components of the circumferential stresses on the flow field

## 5.5 Classical throughflow and high order throughflow comparison

To end the analysis of the CME2 compressor, a comparison is performed between the high order throughflow and the more classical Navier-Stokes throughflow presented in chapter 1. It is not easy to compare both solutions because the high order throughflow is based on the density-average while the classical throughflow is not. The classical throughflow does not explicitly reveal any sort of circumferential averages. It is based on empirical correlations that allow to compute the flow angle (through the deviation) and the losses (through the loss coefficient). It is through these terms that an average type for the classical throughflow

(a) total temperature

(b) total pressure

Figure 5.17: Comparison of the 3-D solution density and mass-averaged

is specified and generally mass-averaged quantities are chosen. Therefore, the comparison between the throughflow computations has been performed downstream of the st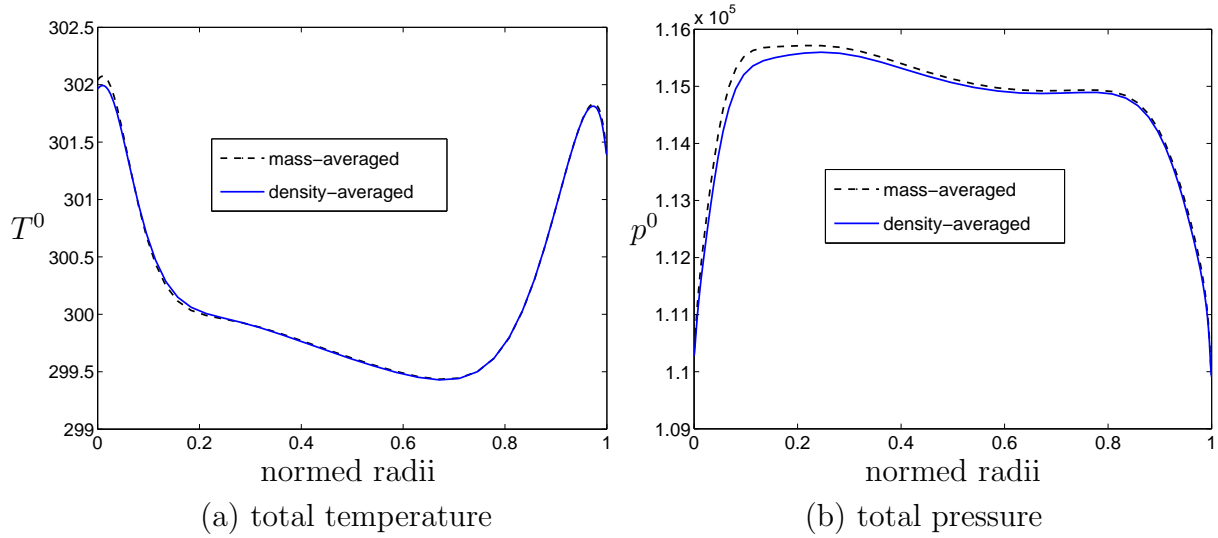ator, not too close to the stator trailing edge to avoid the difference between the density and the mass averages and not too far to avoid a completely mixed flow. At the chosen location, the mass-averaged and the density-averaged quantities nearly agree as it can be seen on the figure 5.17. The more significant difference appears in the region downstream of the hub corner stall for the total pressure. It is in that region that the kinetic energy of the fluctuations is the greatest.

The figure 5.18 compares three different results obtained with

1. a classical Navier-Stokes throughflow based on the Baldwin-Lomax closure,

2. a classical Navier-Stokes throughflow based on the Baldwin-Lomax closure plus a radial mixing model,

3. the high order throughflow based on the Baldwin-Lomax closure and the circumferential stresses.

The figure 5.18 (a) shows the axial velocity. The global agreement between the classical throughflow and the 3-D results is rather good. In the hub region, the problem arising from the use of the Baldwin-Lomax closure is visible at around 5 % of the span for both the high order throughflow and the classical throughflow without radial mixing model. For the high order throughflow, the problem is very weak. The classical throughflow with radial mixing model overpredicts the axial velocity close to the hub wall which results in an overprediction of the total pressure (not shown here) in that region.

(a) axial velocity

(b) radial velocity

(c) absolute flow angle

(d) total temperature
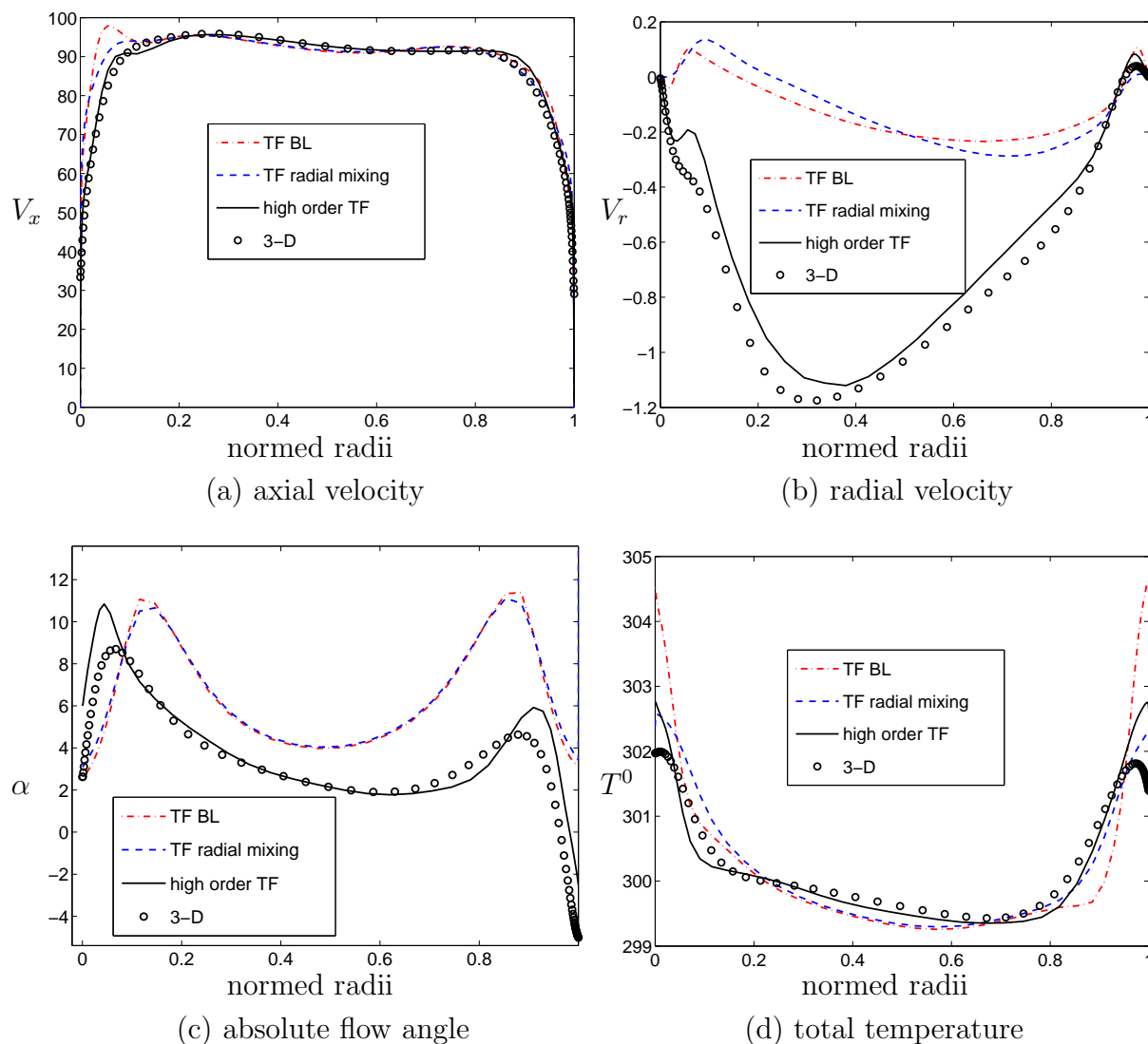
Figure 5.18: Comparison of the classical Navier-Stokes and the high order throughflows

From the figure 5.18 (b), it is clear that the (very weak) radial velocity at the outlet of the compressor can only be predicted by the circumferential stresses as it was already shown above. The absolute flow angle is given on the figure 5.18 (c). The empirical correlations used here for the classical throughflow computations are not able to correctly predict the mean level of the deviation angle at the outlet of the compressor and mispredict it by 2-3 degrees.

The 3-D loss correlations of Roberts, while providing the correct level of underturning, obviously fail to locate the passage vortex at the hub. The figure 5.18 (d), giving the total temperature, highlights the radial mixing phenomenon, which is relatively weak in this machine, but nevertheless present. The Navier-Stokes throughflow computation without radial mixing model overpredicts the temperature at the walls. Both the circumferential

stresses and the radial mixing model in the classical throughflow computations succeed in predicting the mixing phenomenon.

## 5.6    VEGA2 unsteady simulation

The transonic single stage turbine VEGA2 is representative of the first stage of a high pressure turbine. This turbine has been built by ONERA in association with three industrial partners (SNECMA, TURBOMECA and EDF). The hub and shroud walls are cylindrical. The figure 5.19 shows the meridional geometry of VEGA2.
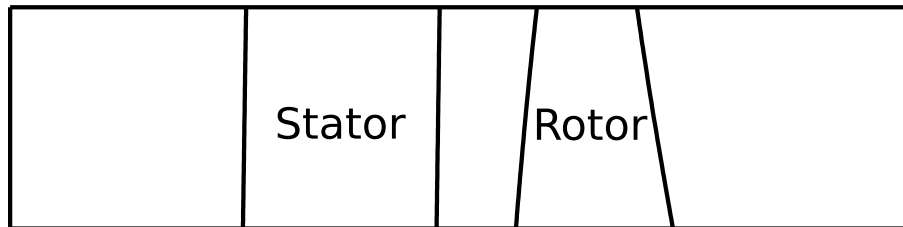


Figure 5.19: Vega2 meridional geometry

Two numerical simulations of VEGA2 have been run by Bardoux *et al.* (1999a), a steady one and an unsteady one. Both simulations have been run on the same multi-block structured mesh. The number of grid points is approximately two millions. A blade-to-blade representation of the mesh at midspan is shown on the figure 5.20. The simulations were run without tip clearance. The flow solver used is CANARI-COMET developed by the ONERA. The turbulence model is algebraic (Michel *et al.*, 1969).

The mean performances, extracted from the time-averaged simulation, and the main parameters of VEGA2 are given in the table 5.2

| | |
|---|---|
| mass flow | 3.09 kg/s |
| pressure ratio | 0.3101 |
| efficiency | 0.931 |
| rotation speed | 13000 RPM |

Table 5.2: Global parameters of the VEGA2 turbine

An analysis of the results of the unsteady simulation is provided in Bardoux *et al.* (1999a,b). A discussion is also available in Leboeuf (2001). A particularity of this testcase is the important difference between the unsteady solution and the steady one. This difference is

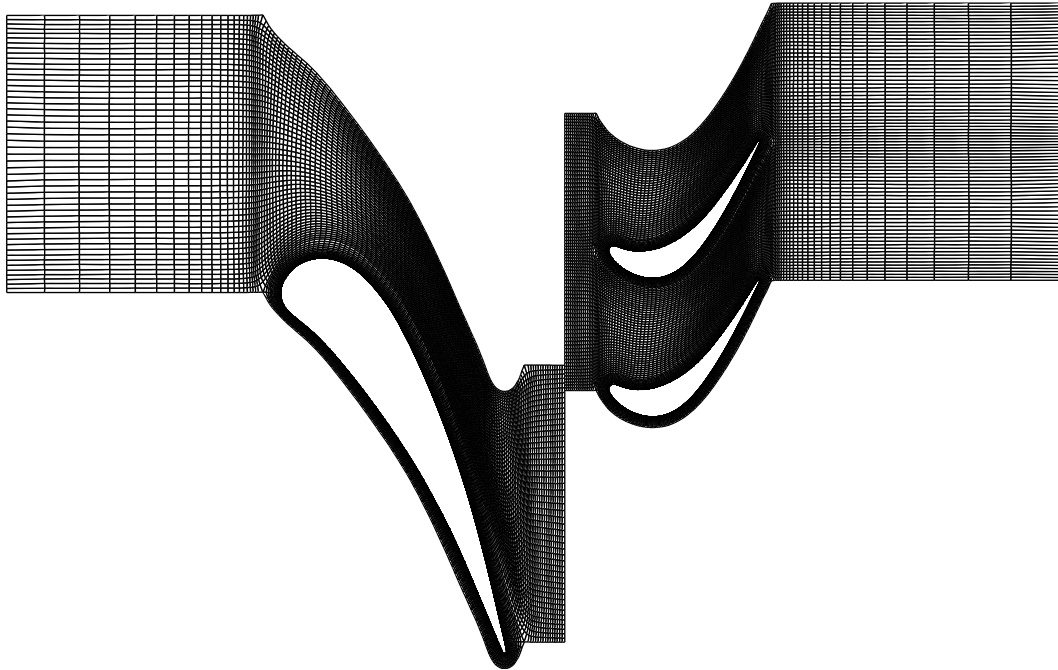Figure 5.20: Vega2 blade-to-blade mesh at midspan

mainly due to the radial migration of the stator wake. Indeed, considering that the static pressure is approximately constant across the stator wake, the same radial pressure gradient is applied to the core flow and to the wake flow. In the core flow, the centrifugal force generated by the circumferential velocity balances the radial pressure gradient. In the wake, however, the lower circumferential velocity and the lower centrifugal force cannot balance the radial pressure gradient, resulting in a radial migration toward the hub. This is illustrated on the figure 5.21 (a) where the radial migration of the wake flow is highlighted by the negative radial velocity.

The radial migration of the stator wake flow plus the stator passage vortex are responsible for an accumulation of low energy fluid at the wake foot (see entropy accumulation at the hub on the figure 5.21 (b)). This circumferential non-uniformity gives in turn a strong time variation of the inlet condition of the rotor close to the hub. As a consequence, the rotor passage vortex has a pulsating character. The time-averaged representation of the passage vortex therefore appears as spread compared to the passage vortex obtained by the steady mixing plane simulation. This is shown on the figure 5.22, giving the radial distribution of entropy at the outlet of the turbine for both simulations. Bardoux *et al.* (1999a,b) have also remarked that the radial transport of the stator wake toward the hub continues in the rotor domain. Consequently, the main part of the losses are located in the lower part of the span at the outlet of the turbine as illustrated on the figure 5.22.

(a) radial velocity                                   (b) entropy
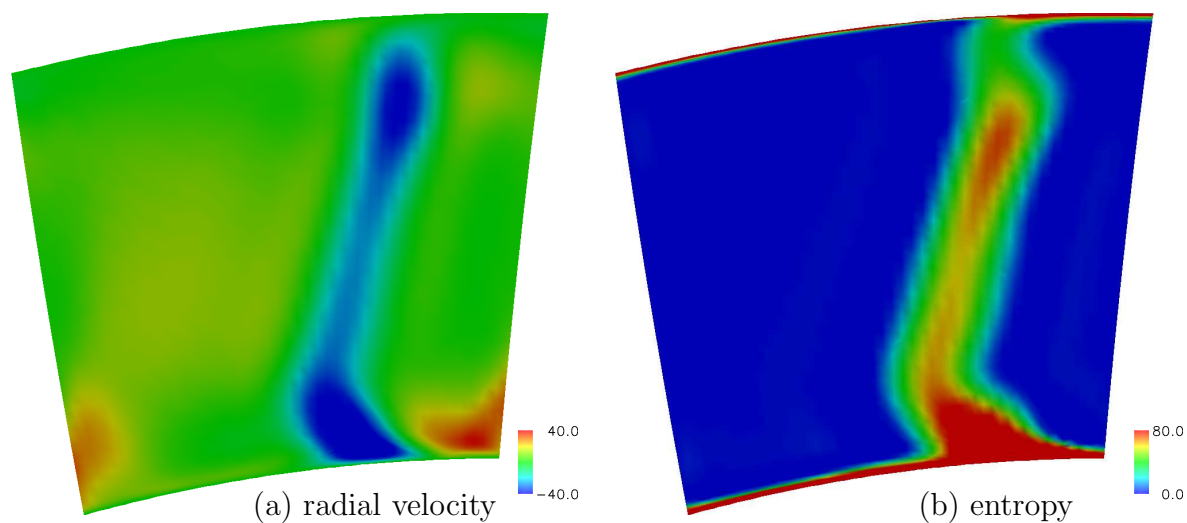
Figure 5.21: Time-averaged radial velocity and time-averaged entropy in plane orthogonal to the axis downstream of the stator trailing edge
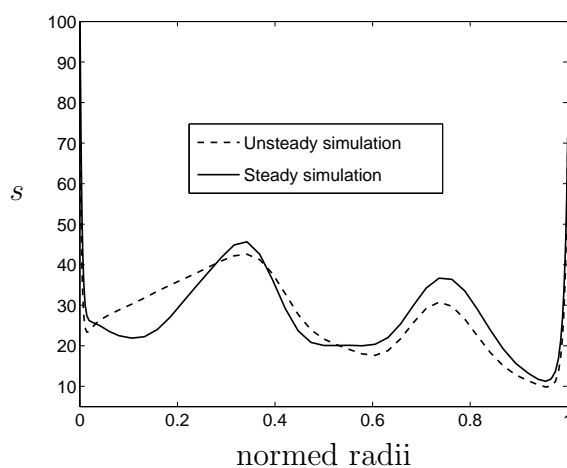


Figure 5.22: Comparison of the entropy at the outlet of the turbine for both steady mixing plane simulation and time-averaged unsteady one.

## 5.7 VEGA2 throughflow analysis

The following analysis focuses on the unsteady 3-D simulation and the introduction of the different stresses in the throughflow calculation. There are two ways of obtaining the stresses.

- The first solution is to start by time-averaging the unsteady simulation in one of the reference frame, the absolute one for example. This averaging requires to build a mesh that is fixed in the stator reference frame and covers the rotor domain. This reference

mesh is uniform in the circumferential direction. At each time step, the flow field inside the rotor domain is interpolated on the fixed reference mesh. At the end of the rotation of the rotor, a representation of the rotor flow field is obtained in the stator reference frame. An illustration of this has been given at the figure 4.2 with the streamlines computed in both reference frames for the present unsteady simulation. The drawback of this method is that the cell length in the circumferential direction of the (circumferentially uniform) reference mesh should be of the same size of the smallest cell of the rotor mesh in order to avoid any loss of information. The size of the first cell adjacent to the rotor wall is such that $y^+ = 1$. It is not practical to use a uniform mesh with such a resolution. A mesh with a lower resolution must therefore be used with some consequences on the accuracy.

- The other way for obtaining the stresses is to perform the time-averaging of the flow field for each row in their own reference frame. A time-averaged flow field is obtained in the stator reference frame and a time-averaged flow is obtained in the rotor reference frame. The time-averaged flow in the stator (rotor) reference frame extends spatially on the stator (rotor) domain only contrary to the previous method. The deterministic stresses are computed from these time-averaged flow fields and the instantaneous flow field. One has to remark that both time-averaged flow fields are different at the interface between the stator and the rotor so that the "flow field" is discontinuous as one passes from the stator domain to the rotor one. The same remark applies to the deterministic stresses. Next, a circumferential-averaging is performed on both time-averaged flow fields. The resulting flow field is now continuous at the stator-rotor interface as it exists only one axisymmetric flow field common to all blade rows, as described in section 4.4 devoted to the circumferential-averaging. Similarly, when the deterministic stresses are circumferentially averaged and added to the circumferential stresses, a continuous field of global stresses is obtained:

$$R_{ij} = \overline{\overline{\rho V_i' V_j'}^t}^c + \overline{\overline{\rho}^t V_i'' V_j''}^c \tag{5.4}$$

This method does not suffer from the loss of accuracy of the previous one and will therefore be used.

The blade forces are obtained from the time-averaged flow fields with the methodology used for the CME2 testcase.

A throughflow computation has been run from these extracted stresses and blade forces. As for the CME2 testcase, both global flow fields and radial distributions are compared. The figures 5.23 to 5.25 show the comparison of the averaged 3-D unsteady simulation and the throughflow solution for the complete flow field. The global agreement is not as good as for the CME2 testcase. The zone of high axial velocity at the stator wake foot is more extended in the throughflow calculation than in the 3-D one. The developments of the vortex, at hub and at shroud of the rotor blade, are also not correctly predicted.
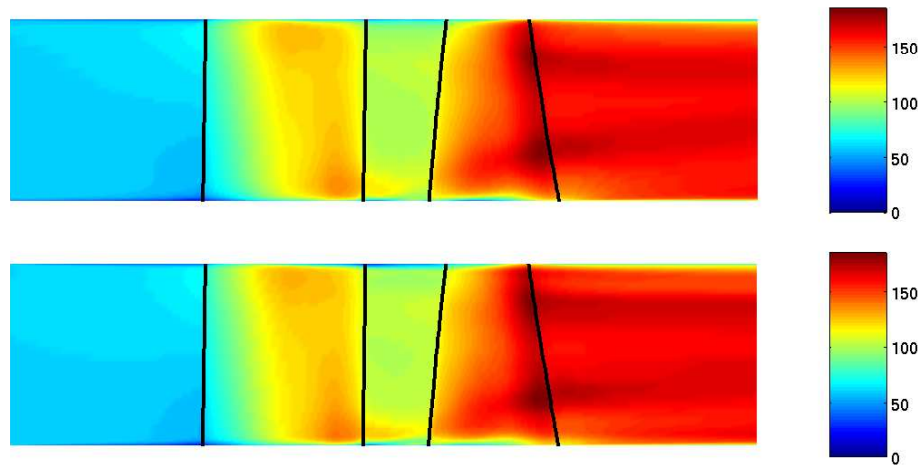
Figure 5.23: Axial velocity from 3-D averaged solution (top) and throughflow solution (bottom)
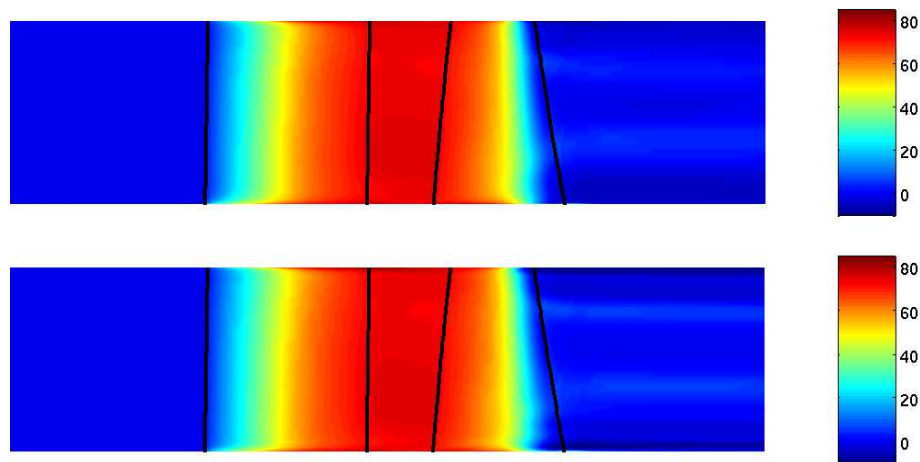


Figure 5.24: Absolute flow angle from 3-D averaged solution (top) and throughflow solution (bottom)



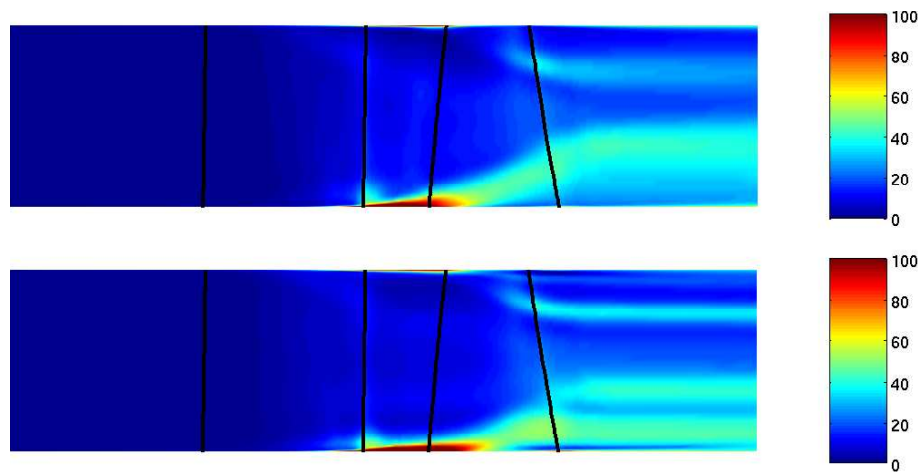Figure 5.25: Entropy from 3-D averaged solution (top) and throughflow solution (bottom)

Figure 5.26: Comparison between the throughflow solution (plain lines) and the averaged unsteady simulation (symbols) at 3 locations inside the stator domain
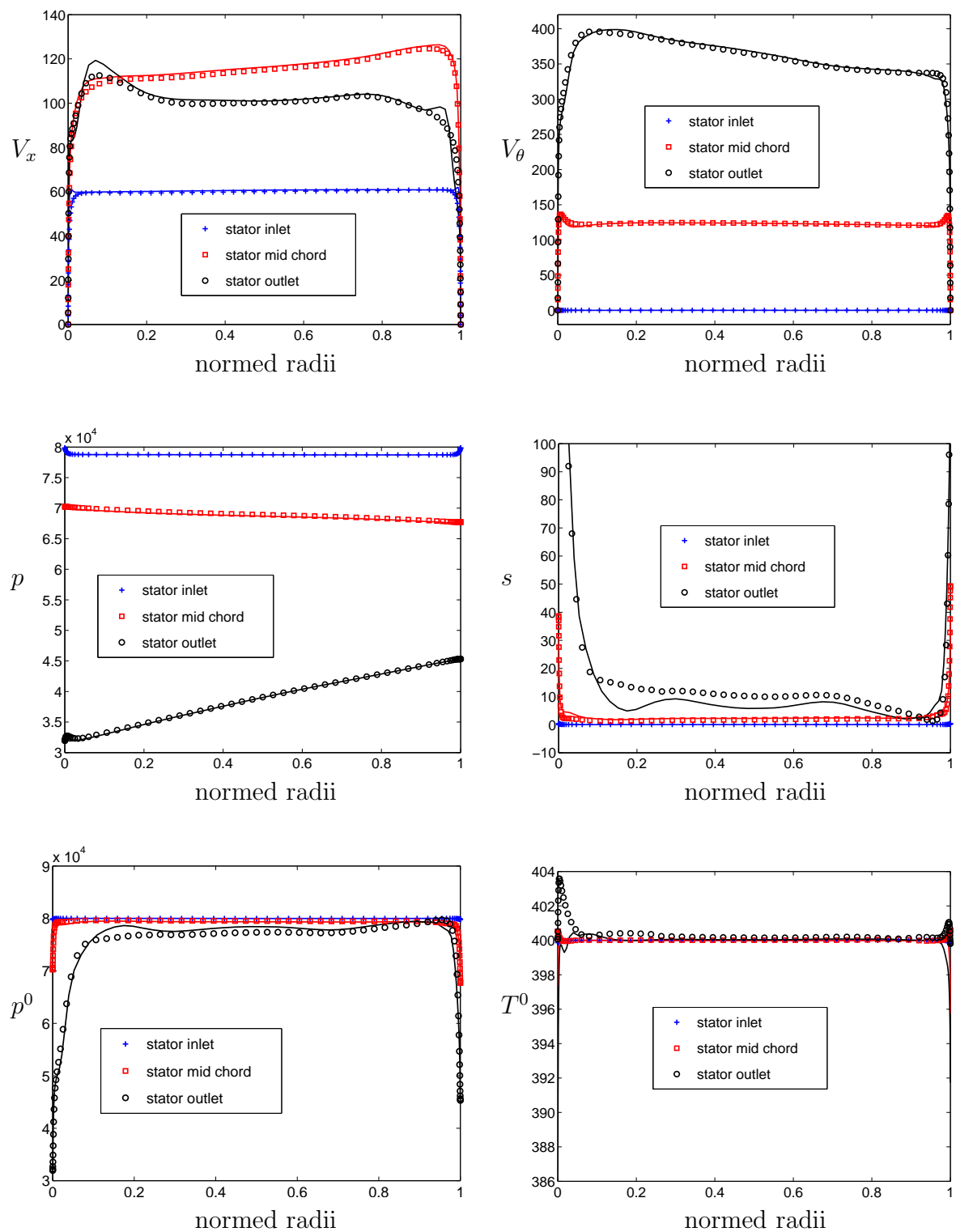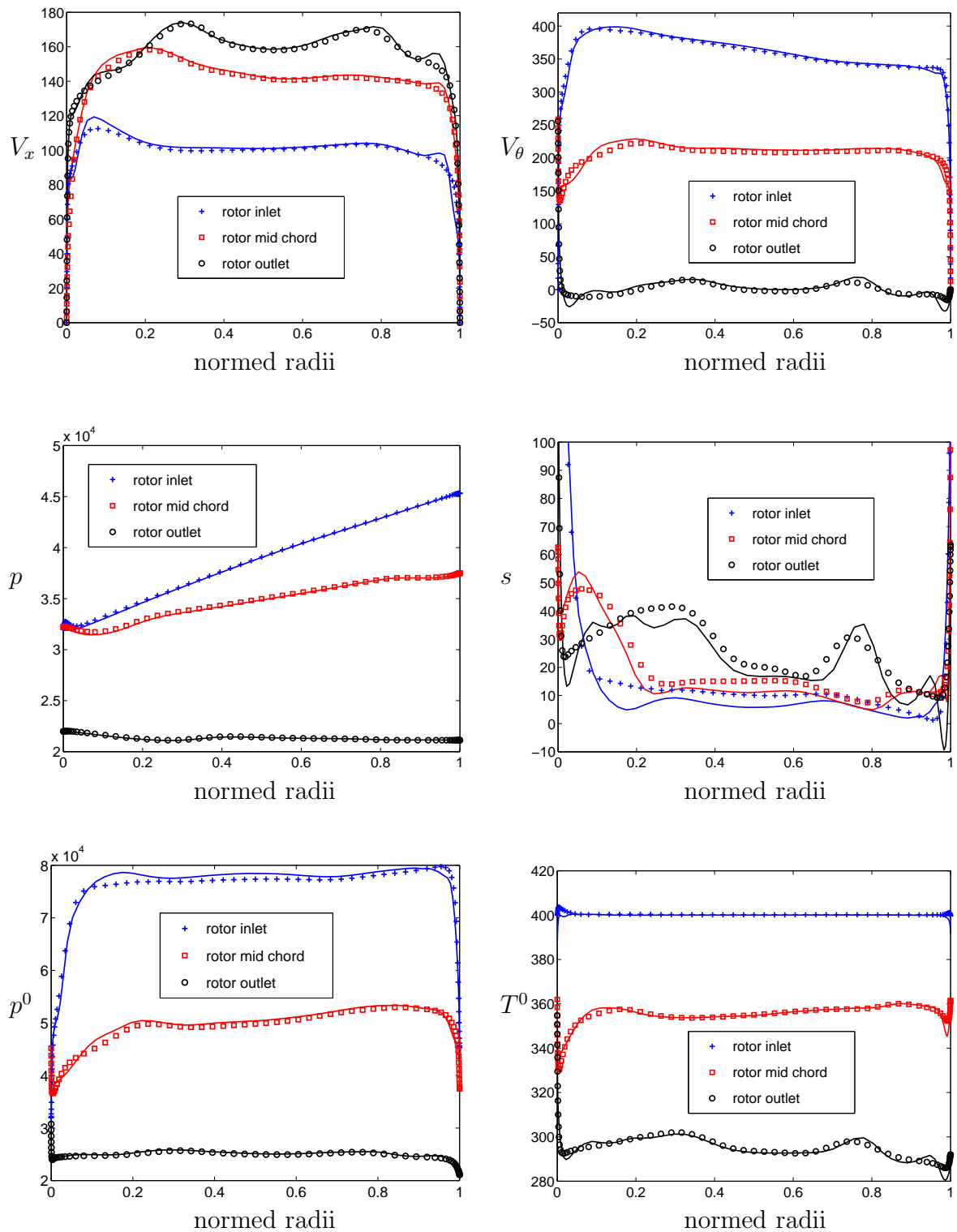
Figure 5.27: Comparison between the throughflow solution (plain lines) and the averaged unsteady simulation (symbols) at 3 locations inside the rotor domain

The main discrepancy occurs close to the stator trailing edge. The losses are underestimated at the outlet of the stator as shown by the radial distributions of entropy and total pressure on the figure 5.26. This discrepancy is best described on the figure 5.28 (a), comparing the axial distribution of entropy obtained by the throughflow with the one obtained from the 3-D simulation. These distributions are provided for the midspan section. The comparison shows that not enough losses are generated on the aft part of the stator in the throughflow simulation. In order to determine whether the discrepancy comes from the numerical losses at the throughflow level (with the numerical losses following the definition given in section 5.3), a throughflow computation with two times more grid points in the axial direction for the stator domain has been performed. At the same time, the number of grid points of the reference mesh used to compute the circumferential and the deterministic stresses has also been increased. No noticeable differences have been observed meaning that the discretization error are low.



(a) entropy                                          (b) axial velocity
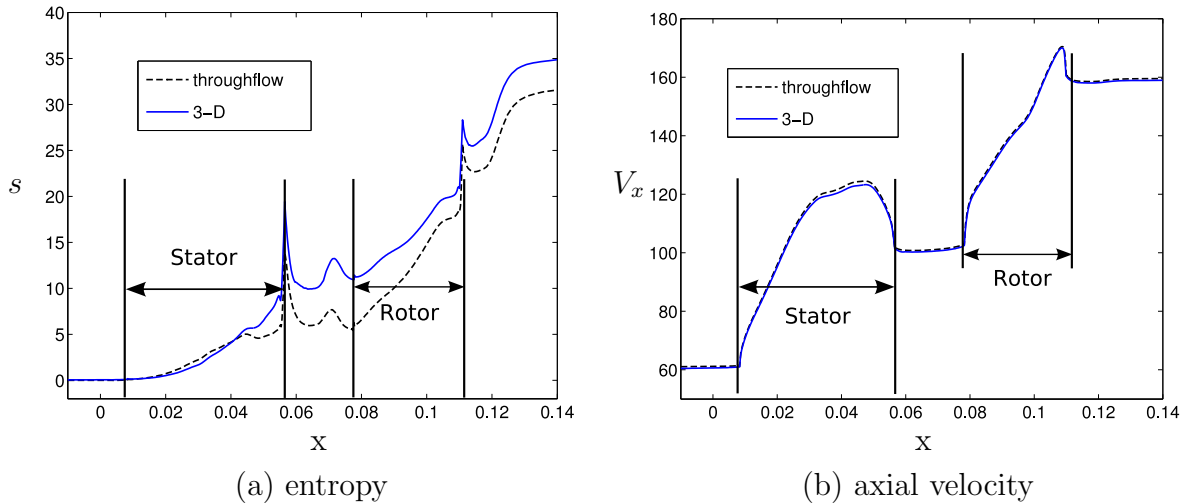
Figure 5.28: Comparison of the axial evolutions of the entropy and of the axial velocity at midspan for the throughflow solution and for the 3-D one

The figure 5.29 shows the turbulent viscosity. This quantity is plotted on an iso j-line of the O-mesh for the suction side of the stator. These iso j-lines are the lines that form the O-mesh. The region for which a discrepancy is observed on the figure 5.28, i.e. the aft part of the stator, is also the region where the turbulent viscosity is high. Therefore, a possible explanation for the discrepancy could be that the blade-to-blade viscous shear stresses have been neglected (contribution 1 defined in the section 5.1). The conclusions concerning the impact of these stresses that were elaborated on the flat plate testcase and that have hold for the CME2 testcase could be invalid here, for the aft-part of this high deflection stator.

On the other hand, Perrin and Leboeuf (1995) came to another conclusion concerning the importance of the blade-to-blade viscous shear stresses. They performed a 3-D Navier-Stokes computation on a high deflection turbine rotor cascade and analysed the momentum balance. They found that the blade wall shear stresses as well as the averaged shear stresses

Figure 5.29: Evolution of the turbulent viscosity on an iso j-line (parallel to the blade wall direction) for the suction side of the stator

are negligible everywhere except in the endwalls regions. They also found that the shear stresses have an indirect effect on the circumferential stresses through their dissipations. This last observation holds particularly downstream of the trailing edge. Their conclusion concerning the importance of the averaged viscous she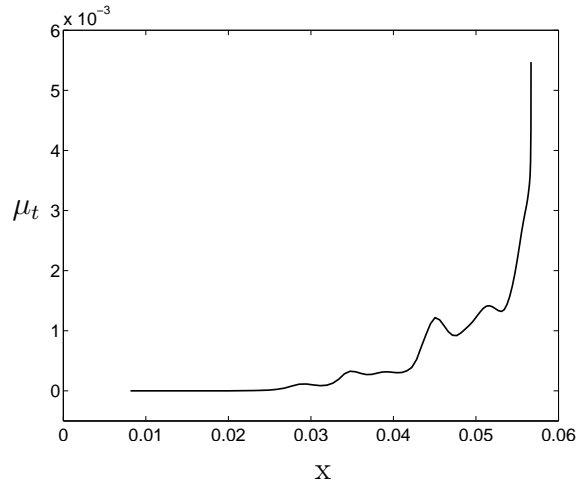ar stresses is in contradiction with the previously mentioned possible explanation for the aft part of the stator discrepancy.

Finally, another difference compared to the CME2 and the flat plate testcases is related to the relative importance of the viscous shear stresses at the blade walls, i.e. the viscous blade force. In the present case, it has only a slight effect and does not dictate the entropy generation. This goes in the direction of what Perrin and Leboeuf (1995) observed and weakens the proposed explanation for the discrepancy observed on the aft-part of the stator. However, the unavailability of the complete 3-D viscous stresses do not allow to go further on that subject.

As a side note, it should be mentioned that the discrepancy mainly affects the entropy and the other loss related quantities such as the total pressure. The other quantities are better predicted as can be seen on the figure 5.28 (b), comparing the axial distributions of the axial velocity at midspan or on the figure 5.24 giving the flow angle for the complete domain.

Continuing on the explanation of the observed discrepancies, the figure 5.25 highlights the evolution of both rotor corner vortex (hub and shroud). Close to the rotor trailing edge and just downstream of it, the vortex are spread and mixed for the 3-D averaged solution. This is not the case for the throughflow solution, and is attributed to the fact that the blade-to-blade viscous shear stresses were neglected and that a simplified model for the endwall viscous stresses was used. Indeed looking at the 3-D circumferentially averaged turbulent viscosity (figure 5.30), regions of high turbulent viscosity are found close to the rotor trailing edge and centred on the vortex. This phenomenon is not reproduced in the throughflow model.
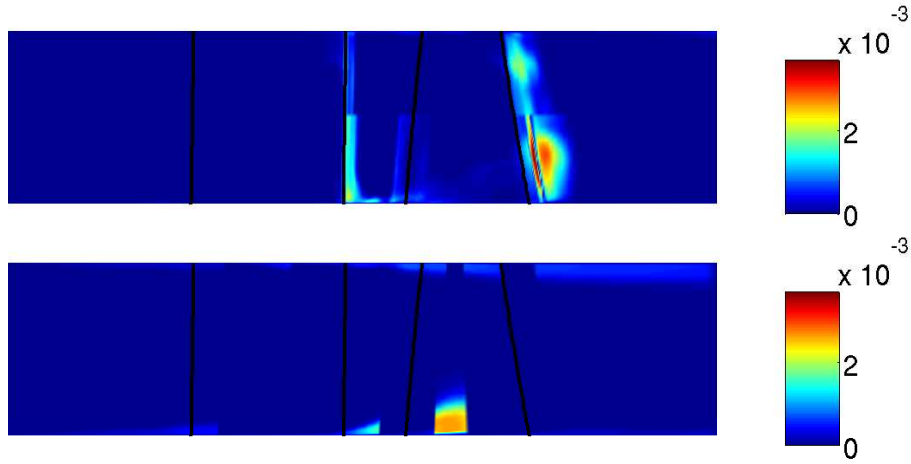
Figure 5.30: Turbulent viscosity from 3-D averaged solution (top) and throughflow solution (bottom)

On the figure 5.25, the vortex are progressively mixed out as they travel toward the outlet of the computational domain in the 3-D simulation. This phenomenon is not observed in the throughflow results. One possible explanation for this difference lies in the different numerical schemes used in both simulations and in the large stretching and mesh cell size used in the 3-D computation downstream of the rotor trailing edge. These mesh characteristics are highlighted on the figure 5.20. With the Jameson scheme used for the 3-D simulation the numerical dissipation is not negligible. With the Roe scheme and high order reconstruction embedded in the throughflow, this numerical dissipation is lower and does not lead to the same mixing of the vortex.

Similarly to the CME2 testcase, the "resetting" of the boundary layer brought by the Baldwin-Lomax turbulence model is present, mainly in the rotor domain (figure 5.27), resulting in peaks in the radial distributions of axial velocity or entropy close to the endwalls. Finally, at the outlet of the turbine, the agreement is relatively good and the global performances are well estimated (see table 5.3). However, the entropy distribution exhibits some oscillations.

|  | Throughflow | 3-D NS simulation |
|---|---|---|
| mass flow | 3.09 kg/s | 3.11 kg/s |
| pressure ratio | 0.3101 | 0.311 |
| efficiency | 0.931 | 0.934 |

Table 5.3: Comparison of the global performances computed by the throughflow and the 3-D simulation

# 5.8   Impact of the deterministic stresses

For the VEGA2 turbine, Bardoux (2000) showed that a strong difference exists between the steady and the unsteady behaviours of the turbine and that one of the main differences resides in the radial mixing of the rotor hub passage vortex. Bardoux also showed that including the deterministic stresses in the 3-D simulation of the VEGA2 rotor allows to capture the mean effect of the unsteadiness on the mean steady flow. He finally showed that the purely temporal part of the deterministic stresses cannot be neglected. Neglecting this part is one of the assumptions of the Adamczyk closure (section 4.5.1).

The study of Bardoux was focused on 3-D simulations and deterministic stresses. Therfore, a conclusion on the relative importance of the circumferential and deterministic stresses cannot be drawn from its study. This question of the relative importance of both stresses must be addressed at the throughflow level. This is the purpose of this section.

Three simulations are compared on the figures 5.31 and 5.32:

1. a simulation with the blade forces alone ($f_b$ calculation),

2. a simulation with the blade forces and the circumferential stresses ($f_b$ + circ stress calculation),

3. a full simulation including the blade forces, the circumferential stresses and the deterministic stresses ($f_b$ + circ stress + det stress calculation). This last computation is the reference one that has already been presented in the previous section.

The comparison of the first and second computations will allow to evaluate the impact of the circumferential stresses while the comparison of the two last ones will allow to evaluate the importance of the deterministic stresses.

As described in the model of Adamczyk, for a single shaft turbomachine, two steady flow fields exist, one per reference frame. The circumferential stresses are relative to a steady flow field in a given reference frame. This means that the flow field obtained by the $f_b$ + circ stresses calculation is not physical. In other words, the circumferential stresses field is discontinuous at the stator-rotor interface. The discontinuity disappears when the deterministic stresses are superimposed on the circumferential stresses as shown by the equation (5.4). This discontinuity is mainly present at the stator hub as it is a region of high unsteadiness. In order to evaluate the numerical losses introduced by this discontinuity, a computation with the circumferential stresses smoothed at the stator-rotor interface has been performed. No noticeable difference was observed meaning that the discontinuity does no perturb the flow field numerically.

At the stator outlet (figure 5.31), the difference between the full simulation and the one without the deterministic stresses is very low as the unsteadiness is weak upstream of this location. The simulation with the blade force only lacks some flow details brought by the circumferential stresses.



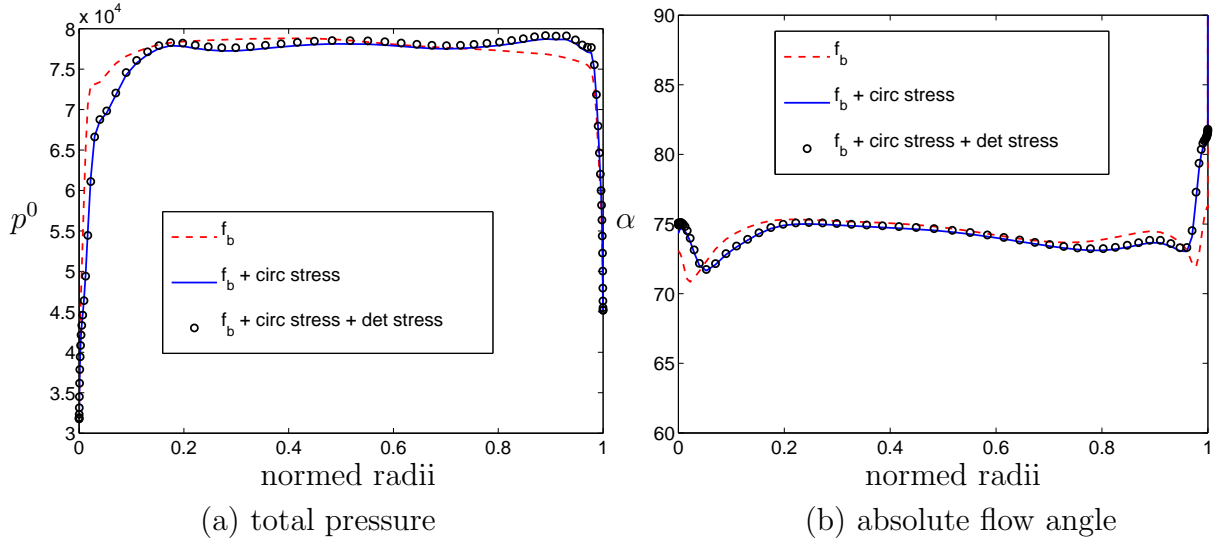(a) total pressure        (b) absolute flow angle

Figure 5.31: Comparison of the throughflow simulations with and without deterministic stresses (stator outlet)

The figure 5.32 shows the results of the three simulations at the outlet of the rotor. The circumferential stresses show a greater influence than the deterministic stresses. They are responsible for the trace of the passage vortex in the pressure distribution (figure 5.32 (d)) or the energy redistribution close to the hub and shroud (figure 5.32 (b)).

On the opposite the comparison of the full computation with the $f_b$ + circ stress one shows that the deterministic stresses have not a predominant impact on the resulting flow field to the exception of the hub region (figure 5.32 (b)). This is the region where the unsteadiness is the strongest.

A more detailed view of the influence of the deterministic stresses is given on the figure 5.33. It represents the contribution of the radial-radial stress to the radial momentum balance, i.e. the term

$$\frac{\partial \overline{\rho V_r' V_r'}}{\partial r} \tag{5.5}$$

The figure 5.33 (a) gives the contribution of the circumferential stress alone while the figure 5.33 (b) gives the full stress contribution, including the circumferential one and the deterministic one. The discontinuity of the circumferential stress can be viewed on the figure 5.33 (a). The results for the radial-radial contribution to the radial momentum balance is representative of the other contributions which are given in appendix D.
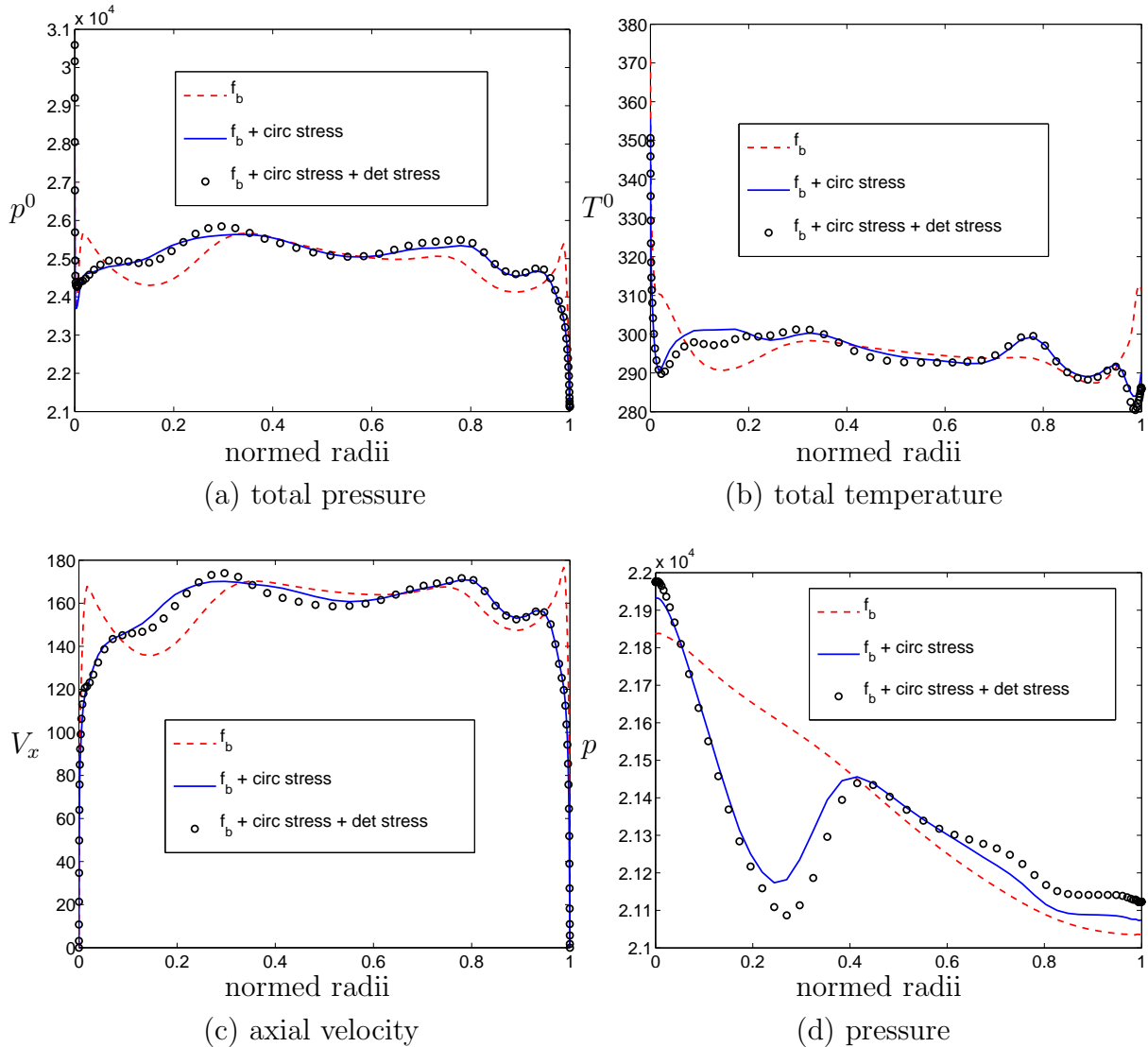
Figure 5.32: Comparison of the throughflow simulations with and without deterministic stresses (rotor outlet)

There are two main regions where the deterministic stresses contributions are not negligible compared to the circumferential stresses ones. The first one is the region just downstream of the stator where the potential interaction of the rotor with the stator wake is important. The second region is the rotor hub passage vortex. This is mainly observable for the radial derivative terms (see appendix D) and it highlights the radial mixing phenomenon brought by the deterministic stresses.

The previous observations would tend to show that it is not necessary to include the deterministic stresses in the throughflow closure. To further evaluate the error that would be brought by neglecting the deterministic stresses, three results are compared on the figure 5.34:

1. the result obtained without the deterministic stresses ($f_b$ + circ stress (unsteady)). This result has already been plotted on the figure 5.32,

2. the result obtained with the deterministic and the circumferential stresses extracted from the 3-D unsteady simulation (full (unsteady)). This result has already been plotted on the figure 5.32. The reference 3-D unsteady simulation from which the stresses have been extracted is also plotted on the figure 5.34 with symbols (3-D (unsteady)),

3. the result obtained with the circumferential stresses extracted from a 3-D steady mixing-plane simulation (full (steady)). The reference 3-D simulation from which the circumferential stresses have been extracted is also plotted on the figure 5.34 with symbols (3-D (steady)).

It is obvious from this comparison that the simulation without the deterministic stresses is not accurate enough. It is as far from the reference unsteady solution as the steady one is. Particularly, the radial mixing phenomenon brought but the unsteadiness is mispredicted (figure 5.34 (b)).

Concerning the impact of the unsteadiness on the flow, it must be recalled that circumferential stresses (as well as the blade forces) have been obtained from a time-averaged 3-D unsteady simulation. Therefore, they already include some part of the unsteadiness through these quantities.

For both steady and "unsteady" throughflow simulations, the 3-D solutions circumferentially averaged have been reproduced on the figure 5.34 (3-D unsteady and 3-D steady labels). They



(a) Circumferential stress contribution



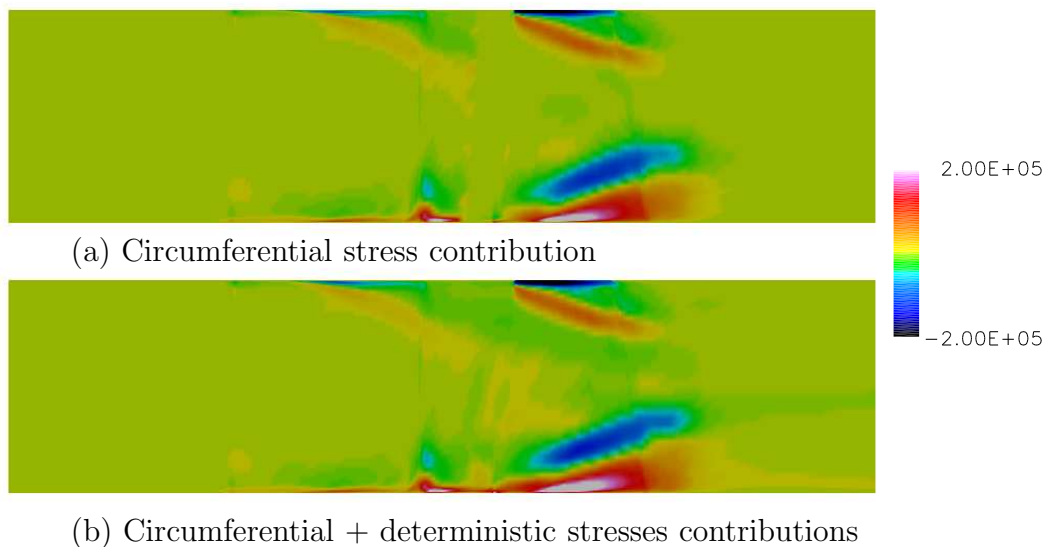(b) Circumferential + deterministic stresses contributions

Figure 5.33: Radial-radial stresses contributions to the radial momentum balance $\left( \dfrac{\partial \overline{\rho V_r' V_r'}}{\partial r} \right)$
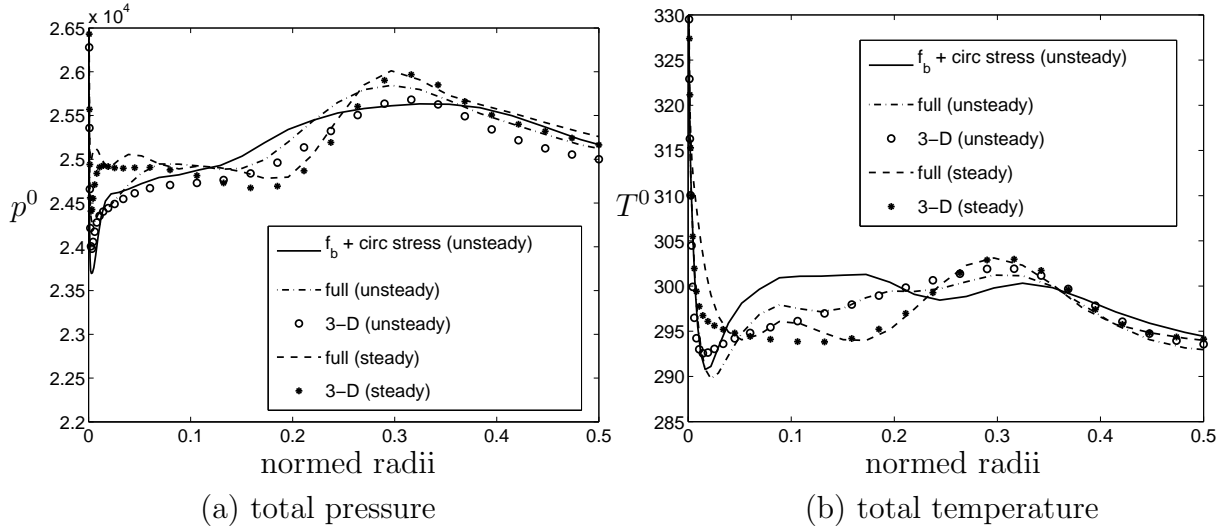
(a) total pressure

(b) total temperature

Figure 5.34: Comparison of the throughflow simulations for steady and unsteady cases at the outlet of the turbine. Close-up on the hub region.

allow to evaluate the accuracy of the throughflow solutions obtained. They are sufficiently accurate to distinguish the unsteady based solution and the steady based one but not much more. The use of a more elaborate turbulence model could cure some of the problems as mentioned earlier in this chapter.

## 5.9 Summary and concluding remarks

From the two numerical studies presented in this chapter, several conclusions can be drawn on the high order throughflow model:

1. First of all, it has been shown that it is possible to reproduce the 3-D averaged or 3-D unsteady averaged results in a throughflow model with injected stresses and blade forces. The quality of the results is generally very good with all the flow features captured by the throughflow simulation. This has been obtained without the need to introduce the averaged viscous shear stresses. An exception to this may be the flow on the aft part of the VEGA2 turbine stator for which a clear discrepancy has been observed between the throughflow results and the 3-D averaged ones. This discrepancy could be explained by the fact that the averaged viscous shear stresses were neglected.

2. The two-dimensional "hub-to-tip" turbulence model used in the present work has shown a deficiency in the endwall viscous flow calculation resulting in the "resetting" of the boundary layers at some places. An improvement would be brought by using a

more evolved turbulence model such as the one of Spalart-Allmaras. It has however been shown that a 2-D model is sufficient to capture the desired flow features, i.e. there is no need for a special treatment compared to the turbulence models used for channel flow computations.

3. Including the viscous blade force was mandatory in the low speed compressor case in order to capture the correct level of losses. This is in contradiction with results found in the literature.

4. The classical throughflow with viscous endwall treatment and radial mixing model cannot capture some of the flow features such as the radial velocity distribution and the radial mixing. These flow features are generated by the circumferential stresses.

5. For the unsteady VEGA2 simulation, including the deterministic stresses is mandatory in order to correctly predict the radial mixing phenomenon. The relative importance of the deterministic stresses compared to the circumferential stresses is low.

6. Finally, the results obtained for both testcases have been obtained with the exact stresses and blade forces extracted from 3-D solutions. It must be expected that modelling these terms will result in a lower accuracy.

# Conclusions

This work was dedicated to the throughflow modelling and the main motivation was to reduce the level of empiricism embedded in these models. This has been achieved through two approaches. The first one is the Navier-Stokes throughflow model and the second one is the high order throughflow model. Both approaches clearly get away from the classical approach used in the throughflow models. Besides these two main achievements, a general purpose throughflow model has been developed. It differs from the Euler throughflows found in the literature not only because of the endwall flow is computed consistently but also because it has a complete set of models to take into accounts different flow features: 2-D empirical correlations, 3-D empirical correlations, 3-D blade force effects, both analysis and design blade force approaches, etc. This level of completeness is seldom found in the literature for the Euler throughflow. These different features have been highlighted all along this document.

Coming back to the first contribution of this work, a throughflow model directly based on the Navier-Stokes equations circumferentially averaged has been devised. It resolves the viscous flows close to the endwalls and allows to capture the high gradient in these regions. It can sustain the high level of losses close to the endwall unlike the classical SLC method. Furthermore, the Navier-Stokes throughflow captures the correct level of losses and also the correct level of blockage. This removes the need of using the highly empirical aerodynamic blockage as well as the boundary layer calculation.

In the frame of the 3-D losses modelling, the potential of the viscous flow computation with local blade force modification has been shown. It allows to capture the overturning at the hub and the underturning at the tip for a rotor blade. However there are still some improvements to be brought to the method, such as the establishment of a relation between the deviation captured by the solver and the loss coefficient. Another way of improving the Navier-Stokes throughflow model and that has been revealed by the high order throughflow model studies is the replacement of the Baldwin-Lomax model with a more evolved turbulence model such as the one of Spalart-Allmaras. This should solve the problem encountered with the "resetting" of the boundary layers.

Another domain for which a finite volume Navier-Stokes throughflow presents a strong interest is the inclusion in computations of the effect of the flow path geometrical imperfections,

such as the backflow under compressor stators or axial steps in the casing. The inclusion of these effects is currently a much discussed topic for 3-D solvers. Some of these features can be included in a throughflow computation provided that they are axisymmetric and that a certain level of spatial discretization can be reached. This last point can not be achieved with SLC throughflows. Furthermore, as these imperfections strongly interact with the viscous flows developing on the endwalls, a viscous simulation would be necessary in order to correctly capture these effects.

Finally, a last way of improvement of the Navier-Stokes throughflow resides in the time integration algorithm to reduce the computational time. This is currently the main disadvantage of the time-marching throughflows when compared to the streamline curvature throughflows. In the present work, nothing has been done on that topic. The use of an implicit time integration or/and a multigrid acceleration should allow an order of magnitude gain in the convergence speed.

The other main part of this work was dedicated to the high order throughflow model. The potential of this method to capture all flow features has been demonstrated. Concerning the closure of the steady problem, it has been shown that the following terms are necessary in order to correctly reproduce the flow physics:

- the inviscid blade force,

- the circumferential stresses,

- the viscous blade force,

- a viscous model for the endwall flows.

When unsteadiness is considered, the deterministic stresses should also be included even though they are not preponderant compared to the circumferential ones.

The most important contribution in the list above is obviously the inviscid blade force. Concerning the circumferential stresses, their relative importance grows with the loading and thus has been found greater for the VEGA2 transonic turbine than for the CME2 compressor.

The need to include the viscous shear stress at the blade wall, i.e. the viscous blade force, has been stressed. This term should also be included in the deterministic stress closure models such as the one of Rhie *et al.* (1995) for example. This conclusion is in opposition to former results found in the literature.

It has also been shown that the last contribution in the list above can be obtained with the viscous terms of the axisymmetric Navier-Stokes equations and a model of turbulence similar to those used for channel flows. This means that no special treatment of the viscous

stresses is necessary. In summary, for the viscous contributions, the sole contributions that are worth to be included in a throughflow model are the viscous blade force and the "2-D hub-to-tip" viscous shear stresses.

The improvement brought by the high order throughflow model over a more conventional throughflow model has been shown for the CME2 testcase. It consists in a more accurate capture of the boundary layer and of the radial velocity field. The exact loss coefficient and deviation are also captured.

The features of the high order throughflow system of equations have also been highlighted in this work. The main particularity is probably the evolution of the entropy due to the Favre averaging chosen to derive the equations. This behaviour will be difficult to modify unless another system of equations is devised, such as one based on mass-averaged properties.

In summary, the work on the high order throughflow model has shown the particularities of its set of equations and has revealed the relative importance of the different unknown terms appearing in it. However nothing has been done on the modelling of the different terms needed to close the equations. Some thoughts on how to address this closure are given hereafter.

For the inviscid blade forces, we believe that two solutions are available:

- modify the current conventional way of computing the blade force which consists in imposing an orthogonality condition of the blade force to the mean flow. The modification should respect the obtention of an isentropic flow for an inviscid computation. However, adding the circumferential stresses to the blade force computed with the orthogonality constraint will violate this isentropic evolution. The blade force must thus be modified in order to reobtained the isentropic condition.

- use fast 3-D models to compute the pressure distribution on the blade walls, such as potential methods (singularity methods) or Euler ones.

For the circumferential stresses, adapting techniques inspired from the deterministic stresses closure seems a natural way, among them are transport equations for the circumferential stresses or the non linear harmonic modelling. As remarked in chapter 4, the latter method has allowed to obtain good results recently. Adapting this technique to the throughflow method seems therefore an attractive solution. A work studying the feasibility of a circumferential closure by a method inspired from the non linear harmonic method is currently undertaken by Léonard and Simon (2006). Some modifications of the original method will be necessary concerning the function chosen to represent the fluctuations. Harmonic functions may not be appropriate to describe the circumferential fluctuations due to the different length scales present in this problem: fluctuations due to the loading (inviscid one) and fluctuations due the development of the boundary layer (viscous). They are also not well

adapted to represent the fluctuations inside the blade passage as the fluctuations are equal to zero or not defined inside the blade.

Finally, for the viscous blade force, a simple model giving the skin friction on the blade walls could be obtained from typical law used in wall function formulations. Considering that the circumferential stresses closure will be able to bring some information on the evolution of the velocity in the direction orthogonal to the blade walls, it will be possible to compute the viscous blade force.

# Bibliography

Abzalilov, A.I., Ivanov, M.J., and Nigmatullin, R.Z. 2005. Steady and transient working mode simulation for turbojet bypass engines based on meridional axisymmetric approach. *ISABE 2005-1083.*

Adam, O., and Léonard, O. 2005. A Quasi-One Dimensional Model for Axial Compressor. *ISABE 2005-1011.*

Adamczyk, J.J. 1984. Model Equation for Simulating Flows in Multistage Turbomachinery. *NASA-TM-86869.*

Adamczyk, J.J. 1999. Aerodynamic Analysis of Multistage Turbomachinery Flows in Support of Aerodynamic Design. *ASME Paper 99-GT-80.*

Adamczyk, J.J., Mulac, R.A., and Celestina, M.L. 1986. A Model for Closing the Inviscid Form of the Average-Passage Equation System. *Transactions of the ASME Journal of Turbomachinery*, **108**, 180–186.

Adamczyk, J.J., Celestina, M.L., Beach, T.A., and Barnett, M. 1989. Simulation of Three-Dimensional Viscous Flow within a Multistage Turbine. *ASMA Paper 89-GT-152.*

Adkins, G.G., and Smith, L.H. 1982. Spanwise Mixing in Axial-Flow Turbomachines. *Transactions of the ASME Journal of Engineering for Power*, **104**, 97–110.

Arnone, A. 1994. Viscous Analysis of Three-Dimensional Rotor Flow Using a Multigrid Method. *Transactions of the ASME Journal of Turbomachinery*, **116**, 435–444.

Attia, M.S. 2005. Semiviscous Method for Compressor Performance Prediction. *AIAA Journal of propulsion and power*, **21**(5), 792–796.

Baldwin, B.S., and Lomax, H. 1978. Thin Layer Approximation and Algebraic Model for Separated Turbulent Flows. *AIAA Paper 78-257.*

Baralon, S. 2000. *On multistage Analysis of Transonic Compressors : From axisymmetric Throughflow Time Marching to Unsteady Three Dimensional Methods.* Ph.D. thesis, Chalmers University of Technology.

Baralon, S., Erikson, L-E, and Hall, Ulf. 1997. Viscous Throughflow Modelling of Transonic Compressors Using a Time-Marching Finite-Volume Solver. *13th International Symposium on Airbreathing Engines (ISABE), Chattanooga, USA.*

Baralon, S., Erikson, L-E, and Hall, Ulf. 1998. Validation of a Throughflow Time-Marching Finite-Volume Solver for Transonic Compressors. *ASME Paper 98-GT-47.*

Baralon, S., Erikson, L-E, and Hall, Ulf. 1999. Evaluation of High-Order Terms in the Throughflow Approximation Using 3D Navier-Stokes Computations of a Transonic Compressor Rotor. *ASME Paper 99-GT-74.*

Bardoux, F.. 2000. *Modélisation des interactions instationnaires rotor-stator en turbomachine multi-étages.* Ph.D. thesis, Ecole centrale de Lyon.

Bardoux, F., Leboeuf, F., Dano, C., and Toussaint, C. 1999a. Characterization of Deterministic Correlations for a Turbine Stage. Part 1 : Time Averaged Flow Analysis. *ASME Paper 99-GT-100.*

Bardoux, F., Leboeuf, F., Dano, C., and Toussaint, C. 1999b. Characterization of Deterministic Correlations for a Turbine Stage. Part 2 : Unsteady Flow Analysis. *ASME Paper 99-GT-100.*

Behlke, R.F., Burdsall, E.A., Canal, E., Jr., and Korn, N.D. 1979. *Core Compressor Exit Stage Study - II. Final Report.* Tech. rept. NASA CR-159812.

Bermudez, A., and Vazquez, E. 1994. Upwind Methods for Hyperbolic Conservation Laws with Source Terms. *Computer Fluids*, **23**(8), 1049–1071.

Bosman, C., and Marsh, H. 1974. An improved Method for Calculating the Flow in Turbo-Machines, Including a Consistent Loss Model. *Journal of Mechanical Engineering Sciences*, **16**, 25–31.

Boure, G., and Gillant, P. 1985. Aerodynamic Modelling of a Transonic Radial Equilibrium of a Multistage Compressorl. *Turbomachinery—Fluid Dynamic and Thermodynamic Aspects, VDI Berichte 1185, Journal of Mechanical Engineering Sciences*, 143–155.

Boyer, K. M., and O'Brien, W. F. 2002. An Improved Streamline Curvature Approach for Off-Design Analysis of Transonic Axial Compression Systems. *ASME Paper GT-2002-30444.*

Brandt, A. 1977. Multi-Level Adaptatives Solution to Boundary-Value Problems. *Mathematics of Computation*, **31**, 333–390.

Burdsall, E.A., Canal, E., Jr., and Lyons, K.A. 1979. *Core Compressor Exit Stage Study - I. Aerodynamic and Mechanical Design.* Tech. rept. NASA CR-159714.

Carter, A.D.S. 1950. The Low Speed Performance of Related Aerofoils in Cascades. *ARC CP 29.*

Çetin, M., Üçer, A.Ş., Hirsch, C., and Serovy, G.K. 1987. Application of Modified Loss and Deviation Correlations to Transonic Axial Compressors. *AGARD R-745*.

Cebeci, T., and Smith, A.M.O. 1974. Analysis of the Turbulent Boundary Layers. *Academic Press*.

Chakravaty, S., and Osher, S. 1983. High Resolution Applications of the Osher Upwind Schemes for the Euler Equations. *AIAA 6th CFD Conference*, 363–373.

Charbonnier, D. 2004. *Développement d'un modèle de tensions déterministes instationnaires adapté à la simulation de turbomachines multi-étagées*. Ph.D. thesis, Ecole centrale de Lyon.

Chen, T., Vasanthakumar, P., and He, L. 2000. Analysis of Unsteady Blade Row Interaction Using Nonlinear Harmonic Approach. *ASME 2000-GT-431*.

Coirier, W.J. 1994. *An Adaptively-Refined, Cartesian, Cell-Based Scheme for the Euler and Navier-Stokes Equations*. Ph.D. thesis, University of Michigan.

Creveling, H.F. 1968. Axial-Flow Compressor Computer Program for Calculating Off-Design Performance. *NASA CR 72472*.

Cumpsty, N.A. 1989. *Compressor Aerodynamics*. Longman Scientific and Technical.

Damle, S. V., Dang, T.Q., and Reddy, D.R. 1997. Throughflow Method for Turbomachines Applicable for All Regimes. *Transactions of the ASME Journal of Turbomachinery*.

Dawes, W.N. 1992. Toward Improved Throughflow Capability : The Use of Three Dimensional Viscous Flow Solvers in a Multistage Environment. *Transactions of the ASME Journal of Turbomachinery*, **114**, 8–17.

De Ruyck, J., Hirsch, C., and Segaert, P. 1989. Secondary Flow and Radial Mixing Predictions in Axial Compressor. *AGARD CP-469*.

Deconinck, H., and Struijs, R. 1988. A Consistent Boundary Condition for Cell Center Upwind Finite Volume Euler Solvers. *Numerical Methods for Fluid Dynamics III, Clarendon Press, Oxford*.

Delanaye, M. 1996. *Polynomial Reconstruction Finite Volume Schemes for the Compressible Euler and Navier-Stokes Equations on Unstructured Adaptative Grids*. Ph.D. thesis, Université de Liège.

Demeulenaere, A. 1997. *Conception et Développement d'une méthode inverse pour la Génération d'Aubes de Turbomachines*. Ph.D. thesis, Université de Liège et Institut von Karman.

Denton, J.D, and Dawes, W.N. 1999. Computational Fluid Dynamics for Turbomachinery Design. *In:* denton, John (ed), *Developments in Turbomachinery Design*. Professional Engineering Publishing.

Denton, J.D, and Xu, L. 1999. The Exploitation of Three-Dimensional Flow in Turbomachinery Design. *In:* denton, John (ed), *Developments in Turbomachinery Design.* Professional Engineering Publishing.

Dring, R.P. 1993. Radial Transport and Momentum Exchange in an Axial Compressor. *Transactions of the ASME Journal of Turbomachinery*, **115**, 477–486.

Dunham, J. 1995. A New Endwall Model for Axial Compressor Throughflow Calculations. *Transactions of the ASME Journal of Turbomachinery*, **117**.

Enander, R. 1997. Implicit Explicit Residual Smoothing for the Multidimensional Euler and Navier-Stokes Equations. *SIAM J. Sci. Comput.*, **18**, 1243–1254.

Escuret, J. F., and Garnier, V. 1994. Numerical Simulations of Surge and Rotating Stall in Multi-Stage Axial-Flow Compressors. *AIAA Paper 94-3202.*

Essers, J.A. 2003. *Cours de Compléments d'Analyse Numérique.* Tech. rept. Université de Liège, Faculté des Sciences Appliquées.

Fay, G., Lawerenz, M., and Przewozny, H. 1999. Calculation of pitch averaged viscous flow in annular compressor cascade. *Computational Methods in Experimental Measurements IX*, **22**, 185–194.

Gallimore, S.J. 1986. Spanwise Mixing in Multistage Axial Flow Compressors: Part 2 - Throughflow Calculations Including Mixing. *Transactions of the ASME Journal of Turbomachinery*, **108**, 10–16.

Gallimore, S.J. 1997. Viscous Throughflow Modelling of Axial Compressor bladerows Using a Tangential Blade Force Hypothesis. *ASME Paper 97-GT-415.*

Gallimore, S.J., and Cumpsty, N.A. 1986. Spanwise Mixing in Multistage Axial Flow Compressors : Part 1 - Experimental Investigation. *Transactions of the ASME Journal of Turbomachinery*, **108**, 2–9.

Gallimore, S.J., Bolger, J.J., Cumpsty, N.A., Taylor, M.J., Wright, P.I., and Place, J.M.M. 2002. The Use of Sweep and Dihedral in Multistage Axial Flow Compressor Blading: Part I: University Research and Methods Development. *ASME Paper GT-2002-30328.*

Geuzaine, P. 1999. *An Implicit Finite Volume Method for Compressible Turbulent Flows on Unstructured Meshes.* Ph.D. thesis, Université de Liège.

Ginder, R.B., and Harris, D. 1990. Test-Case E/CO-3 Single Subsonic Compressor Stage. *AGARD AR-275.*

Godunov, S.K. 1959. A Finite-Difference Method for the Numerical Computation of Discontinuous Solutions of the Equations of Fluid Dynamics. *Math. Sbornik. Translated US Joint Publ. Res. Service, JPRS 7226.*

Gourdain, N. 2005. *Simulation Numérique des Phénomènres de Décollement Tournant dans les Compresseurs Axiaux*. Ph.D. thesis, Ecole Centrale de Lyon.

Hall, E., Topp, D., and Delaney, R. 1995. Task 7 - ADPAC User's Manual. *NASA CR195472*.

Han, W., Wang, Z., Tan, C., Shi, H., and Zhou, M. 1994. Effects of Leaning and Curving of Blades with Hign Turning Angles on the Aerodynamic Characteristics of Turbine Rectangular Cascades. *Transactions of the ASME Journal of Turbomachinery*.

Harten, A., P.D., Lax, and Van Leer, B. 1983. On Upstream Differencing and Godunov-Type Schemes for Hyperbolic Conservation Laws'. *SIAM Review*, **25**, 35–67.

He, L., and Ning, W. 1998. Efficient Approach for Analysis of Unsteady Viscous Flows in Turbomachines. *AIAA journal*, **36**, 2005–2012.

He, L., Chen, T., Wells, R.G., Li, Y.S., and Ning, W. 2002. Analysis of Rotor-Rotor and Stator-Stator interference in Multi-Stage Turbomachines. *Transactions of the ASME Journal of Turbomachinery*, **124**, 564–571.

Hirsch, C. 1988. *Numerical Computation of Internal and External Flows, Volume 1 : Fundamentals of Numerical Discretisation*. Wiley.

Hirsch, C. 1994. CFD Methodology and Validation for Turbomachinery Flows. *AGARD LS-195*.

Hirsch, C., and Dring, R. P. 1987. Throughflow Models for Mass and Momentum-Averaged Variables. *Transactions of the ASME Journal of Turbomachinery*, **109**, 362–370.

Horlock, J.H. 1971. On Entropy Production in Adiabatic Flow in Turbomachines. *Transactions of the ASME Journal of Basic Engineering*, December, 587–593.

Horlock, J.H., and Denton, J.D. 2005. A review of Some Early Design Practice Using Computational Fluid Dynamics and a Current Perspective. *Transactions of the ASME Journal of Turbomachinery*, **127**, 5–13.

Horlock, J.H., and Perkins, H.J. 1974. Annulus Wall Boundary Layers in Turbomachines. *AGARD AG-185*.

Howard, M.A., and Gallimore, S.J. 1993. Viscous Throughflow Modelling for Multistage Compressor Design. *Transactions of the ASME Journal of Turbomachinery*, **115**, 296–304.

Jameson, A., and Baker, T. J. 1983. Solution of the Euler Equations for Complex Configurations. *AIAA Paper 83-1929*.

Jameson, A., Schmidt, W., and Turkel, E. 1981. Numerical Solution of the Euler Equations by Finite Volume Methods Using Runge-Kutta Time Stepping Scheme. *AIAA Paper 81-1259*.

Jasak, H. 1996. *Error Analysis and Estimation for the Finite Volume Method with Applications to Fluid Flows.* Ph.D. thesis, University of London.

Jennions, I. K., and Stow, P. 1985a. A Quasi-Three Dimensionnal Turbomachinery Blade Design System : Part I - Throughflow analysis. *Transactions of the ASME Journal of Engineering for Power.*

Jennions, I. K., and Stow, P. 1985b. A Quasi-Three Dimensionnal Turbomachinery Blade Design System : Part II - Computerized System. *Transactions of the ASME Journal of Engineering for Power.*

Jennions, I. K., and Stow, P. 1986. The Importance of Circumferential Non-Uniformities in a Passage Average Quasi-Three Dimensional Turbomachinery Design System. *Transactions of the ASME Journal of Engineering for Power.*

Koch, C. C., and Smith, L.H. 1976. Loss Sources and Magnitudes in Axial-Flow Compressors. *Transactions of the ASME Journal of Engineering for Power*, **98**, 411–424.

Koiro, M.J., Myers, R.A., and R.A., Delaney. 1999. TADS - A CFD-Based Turbomachinery Analysis and Design System with GUI - Version 2.0 - Methods and Results. *NASA/CR-1999-206603.*

Kroll, N., and Jain, R.K. 1987. Solution of Two-Dimensional Euler Equations - Experience with a Finite Volume Code. *DFVLR Forschungbericht 87-41.*

König, W. M., Hennecke, D. K., and Fottner, L. 1996. Improved Blade Profile Loss and Deviation Angle Models for Advanced Transonic Compressor Blading : Part I-A Model for Subsonic Flow, Part II-A Model for Supersonic Flow. *Transactions of the ASME Journal of Turbomachinery*, **118**, 73–80.

Leboeuf, F. 2001. Recent Developments in Numerical Methods for Turbomachinery Flows. *VKI-LS 2002-01.*

Lewis, K.L. 1993. Spanwise Transport in Axial-Flow Turbines: Part 1 - The Multistage Environment. Part 2 - Throughflow Calculations Including Spanwise Transport. *ASME Paper 93-GT-299 and 93-GT-300.*

Liu, B., Chen, S., and Martin, H. F. 2000. A Primary Variable Throughflow Code and Its Application to Last Stage Reverse Flow in LP Steam Turbine. *Paper IJPGC2000 - 15010.*

Léonard, O., and Simon, J.F. 2006. Modélisation harmonique des tensions circonférentielles dans le cadre d'une approche méridienne en turbomachines. *Rapport interne.*

Léonard, O., Rogiest, P., and Delanaye, M. 1997. Blade Analysis and Design Using an Implicit Flow Solver. *Proc. 2nd European Conference on Turbomachinery - Fluid Dynamics and Thermodynamics, AntwerpenVKI-LS 2002-01.*

Manna, M. 1992. *A Three Dimensionnal High Resolution Compressible Flow Solver.* Ph.D. thesis, Université Caholique de Louvain et Insistut von Karman.

Michel, R., Quémard, C., and Durant, R. 1969. Application d'un schéma de longueur de mélange à l'étude des couches limites turbulentes d'équilibre. *ONEAR NT n° 154.*

Müller, B., and Jenny, P. 1999. Rankine-Hugoniot-Riemann Solver and Convergence Acceleration for Low Speed Combustion. *VKI-LS 1999-03.*

Nicks, A. 2006. *Simulation des Effets Pariétaux et de Jeu dans un Code de Calcul Méridien.* Travail de fin d'Etudes, Université de Liège.

Nigmatullin, R.Z., and Ivanov, M.J. 1994. The Mathematical models of Flow Passage for Gas Turbine Engines and their Components. *AGARD LS-198.*

Patankar, S.W., and Spalding, D.B. 1972. A Calculation Procedure for Heat, Mass and Momentum Transfert in Three-Dimensional Parabolic Flows. *International Journal of Heat and Mass Transfer.*

Perrin, G., and Leboeuf, F. 1995. Investigation of Throughflow Hypothesis in a Turbine Cascade Using a Three-Dimensionnal Navier-Stokes Computation. *Transactions of the ASME Journal of Turbomachinery*, **117**, 126–132.

Pfitzinger, E.W., and Reiss, W. 1997. A New Concept for Loss and Deviation Prediction in Throughflow Calculations of Axial Flow Compressors. *Proc. 2nd European Conference on Turbomachinery - Fluid Dynamics and Thermodynamics, Antwerpen.*

Rhie, C.M., Gleixner, A.J., Fischberg, C.J., and Zacharias, R.M. 1995. Development and Application of a Multistage Navier-Stokes Solver - Part I:Multistage Modeling Using Body-forces and Deterministic Stresses. *ASME Paper 95-GT-342.*

Roberts, W.B., G.K., Serovy, and Sandercock, D.M. 1986. Modeling the 3-D Flow effects on Deviation for Axial Compressor Middle Stages. *Transactions of the ASME Journal of Engineering for Gas Turbines and Power*, **108**, 131–137.

Roberts, W.B., G.K., Serovy, and Sandercock, D.M. 1988. Design Point Variation of 3-D Loss and Deviation for Axial Compressor Middle Stages. *ASME Paper 88-GT-57.*

Roe, P.L. 1981. Approximate Riemann Solvers, Parameter Vectors and Difference Schemes. *Journal of Computaional Physics*, **43**, 357–372.

Roe, P.L. 1987. Upwind Differencing Schemes for Hyperbolic Conservation Laws with Source Terms. *Lecture Notes in Mathematics 1270.*

Roy, B., Laxmiprasanna, P.A., V., Borikan, and Batra, A. 2002. Low Speed Studies of Sweep and Dihedral Effects on Compressor Cascades. *ASME Paper GT-2002-30441.*

Rábai, G., Vad, J., and Lohász, M.M. 2007. Aerodynamic Study on Linear Cascades of Straight, Arc-Swept and Twisted Blades. *Proc. 7rd European conference on turbomachinery, Athens.*

Sasaki, T., and Breugelmans, F. 1998. Comparison of Sweep and Dihedral Effects on Compressor Cascade Performance. *Transactions of the ASME Journal of Turbomachinery*, **120**, 454–464.

Sayari, N., and Bölcs, A. 1995. A New Throughflow Approach for Transonic Axial Compressor Stage Analysis. *ASME Paper 95-GT-195.*

Spalart, P.R., and Allmaras, S.R. 1992. A One-Equation Turbulence Model for Aerodynamic Flows. *AIAA Paper 92-0439.*

Spurr, A. 1980. The Prediction of 3D Transonnic Flow in Turbomachinery Using a Combined Throughflow and Blade-to-Blade Time Marching Method. *Int. J. Heat and Fluid Flow*, **2**(4), 189–199.

Stewart, M. E. M. 1995. Axisymmetric Aerodynamic Numerical Analysis of a Turbofan Engine. *ASME Paper 95-GT-338.*

Storer, J.A., and Cumpsty, N.A. 1991. Tip Leakage Flow in Axial Compressors. *Transactions of the ASME Journal of Turbomachinery*, **113**, 252.

Strazisar, A.J., Wood, J.R., Hathaway, M.D., and Suder, K. 1989. Laser Anemometer Measurements in a Transonic Axial-Flow Fan Rotor. *NASA-TP-2879.*

Stridh, M. 2003. *Modeling of Unsteady Flow Effects in Throughflow Calculations.* Licenciate thesis, Chalmers University of Technology.

Stridh, M., , and Eriksson, L.E. 2005. Modeling Unsteady Flow Effects in a 3-D Transonic Compressor. *ASME GT2005-68149.*

Sturmayr, A. 2004. *Evolution of a 3D Structured Navier-Stokes Solver Towards Advanced Turbomachinery Applications.* Ph.D. thesis, Vrije Universiteit Brussel.

Sturmayr, A., and Hirsch, C. 1999a. Shock Representation by Euler Throughflow Models and Comparison with Pitch-Averaged Navier-Stokes Solutions. *ISABE 99-7281.*

Sturmayr, A., and Hirsch, C. 1999b. Through-Flow Model for Design and Analysis Integrated in a 3D Navier-Stokes Solver. *Proc. 3rd European conference on turbomachinery, London.*

Üçer, A.Ş., and Shreeve, R.P. 1992. A Viscous Axisymmetric Throughflow Prediction Method for Multi-Stage Compressors. *ASME Paper 92-GT-293.*

Vaassen, J.M. 2005. Etudes des Schémas Utilisés dans la Discrétisation des Termes de Diffusion. *Rapport Interne - Université de Liège - Service d'Aérodynamique.*

van de Wall, A., Kadambi, J.R., and Adamczyk, J.J.. 2000. A Transport Model for the Deterministic Stresses Associated With Turbomachinery Blade Row Interactions. *Transactions of the ASME Journal of Turbomachinery*, **122**, 593–603.

Van Leer, B. 1974. Towards the Ultimate Conservative Difference Scheme, II : Monotonicity and Conservation Combined in a Second-Order Scheme. *Journal of Computational Physics*, **14**, 361–370.

Van Leer, B. 1977. Towards the Ultimate Conservative Difference Scheme, IV : A New Approach to Numerical Convection. *Journal of Computational Physics*, **23**, 276–299.

Van Leer, B. 1982. Flux-Vector Splitting for the Euler Equations. *Lecture Notes in Physics*, **170**, 507–512.

Vilmin, S., Lorrain, E., Hirsch, C., and Swoboda, M. 2006. Unsteady Flow Modeling Across the Rotor/Stator Interface Using the Nonlinear Harmonic Method. *ASME Paper GT2006-90219*.

Wadia, A.R., Szucs, P.N., and Crall, D.W. 1997. Inner Working of Aerodynamic Sweep. *ASME Paper 97-GT-401*.

Weingold, H.D., Neubert, R.J, Behlke, R.F., and Potter, G.E. 1997. Bowed Stators : An example of CFD Applied to Improve Multistage Compressor Efficiency. *Transactions of the ASME Journal of Turbomachinery*, **119**.

Wennerstrom, A.J. 1991. A Review of Predictive Efforts for Transport Phenomena in Axial Flow Compressors. *Transactions of the ASME Journal of Turbomachinery*, **113**.

Wilcox, D. C. 1993. *Turbulence Modeling for CFD*. DCW Industries.

Yao, Z., and Hirsch, Ch. 1995. Throughflow Model Using 3D Euler or Navier-Stokes Solver. *Proc. 1st European conference on turbomachinery fluid dynamics and thermodynamics, Eerlangen*.

Yee, H. C. 1989. A Class of High Resolution Explicit and Implicit Shock Capturing Methods. *VKI-LS 1989-04*.

Yoder, D. A. 1998. Turbulent Flat Plate: Study #1, NPARC Alliance Validation Archive. *NASA Glenn Research Center, MS 86-7*.

# Appendix A

# Numerical fluxes

## A.1 Axisymmetric flux of Van Leer

The flux at the cell face is computed from the left and right states:

$$H_i\left(U^L, U^R\right) = H_i^+\left(U^L\right) + H_i^-\left(U^R\right) \tag{A.1}$$

For $-1 < M_n < 1$:

$$H_i^\pm = \pm \frac{\rho a}{4}\left(1 \pm M_n\right)^2 \begin{pmatrix} 1 \\ V_x \pm \left(2 \mp M_n\right)\dfrac{an_x}{\gamma} \\ V_r \pm \left(2 \mp M_n\right)\dfrac{an_r}{\gamma} \\ V_\theta \\ \dfrac{a^2}{\gamma+1}\left(\dfrac{2}{\gamma-1} \mp 2M_n - M_n^2\right) + \dfrac{V_x^2 + V_r^2 + V_\theta^2}{2} + \dfrac{k^2}{2} \end{pmatrix} \tag{A.2}$$

where $M_n = \dfrac{V_n}{a}$ et $V_n = V_x n_x + V_r n_r$

For the computations including circumferential or deterministic stresses, the kinetic energy $k$ of that stresses has been added to the definition of the total energy.

## A.2   Axisymmetric fluxes of Roe

The flux at the cell face is approximated by:

$$H_i = \frac{1}{2}\left(H_i\left(U^L\right) + H_i\left(U^R\right)\right) - \frac{1}{2}\sum_{j=1}^{5}\left|\lambda^j\right| r^j \delta W^j \tag{A.3}$$

The computation of the flux involves the following stages:

1. Computation of the Roe-averaged quantities:

$$R = \sqrt{\frac{\rho^R}{\rho^L}} \tag{A.4}$$

$$\tilde{\rho} = R\rho^L \tag{A.5}$$

$$\tilde{V}_x = \frac{RV_x^R + V_x^L}{R+1} \tag{A.6}$$

$$\tilde{V}_r = \frac{RV_r^R + V_r^L}{R+1} \tag{A.7}$$

$$\tilde{V}_\theta = \frac{RV_\theta^R + V_\theta^L}{R+1} \tag{A.8}$$

$$\tilde{h}^0 = \frac{Rh^{0R} + h^{0L}}{R+1} \tag{A.9}$$

$$\tilde{t} = \frac{Rt^R + t^L}{R+1} \tag{A.10}$$

$$\tilde{k} = \frac{Rk^R + k^L}{R+1} \tag{A.11}$$

$$\tilde{a} = \sqrt{\gamma\tilde{t}} \tag{A.12}$$

$$\tilde{V}_n = \tilde{V}_x n_x + \tilde{V}_r n_r \tag{A.13}$$

2. Computation of the eigenvalues:

$$\lambda^1 = \tilde{V}_n \tag{A.14}$$

$$\lambda^2 = \tilde{V}_n \tag{A.15}$$

$$\lambda^3 = \tilde{V}_n \tag{A.16}$$

$$\lambda^4 = \tilde{V}_n + \tilde{a} \tag{A.17}$$

$$\lambda^5 = \tilde{V}_n - \tilde{a} \tag{A.18}$$

3. Computation of the right eigenvectors:

$$
r^1 = \begin{pmatrix} 1 \\ \tilde{V}_x \\ \tilde{V}_r \\ \tilde{V}_\theta \\ \dfrac{\tilde{V}_x^2 + \tilde{V}_\theta^2 + \tilde{V}_r^2 + \tilde{k}^2}{2} \end{pmatrix}
\qquad
r^2 = \begin{pmatrix} 0 \\ \tilde{\rho} n_r \\ -\tilde{\rho} n_x \\ 0 \\ \tilde{\rho}\left(\tilde{V}_x n_r - \tilde{V}_r n_x\right) \end{pmatrix}
\qquad
r^3 = \begin{pmatrix} 0 \\ 0 \\ 0 \\ \tilde{\rho} \\ \tilde{\rho}\tilde{V}_\theta \end{pmatrix}
$$

$$\tag{A.19}$$

$$
r^4 = \frac{\tilde{\rho}}{2\tilde{a}}\begin{pmatrix} 1 \\ \tilde{V}_x + \tilde{a} n_x \\ \tilde{V}_r + \tilde{a} n_r \\ \tilde{V}_\theta \\ \tilde{h}^0 + \tilde{a} V_n \end{pmatrix}
\qquad
r^5 = \frac{\tilde{\rho}}{2\tilde{a}}\begin{pmatrix} 1 \\ \tilde{V}_x - \tilde{a} n_x \\ \tilde{V}_r - \tilde{a} n_r \\ \tilde{V}_\theta \\ \tilde{h}^0 - \tilde{a} V_n \end{pmatrix}
\qquad
r^6 = \begin{pmatrix} 0 \\ 0 \\ 0 \\ 0 \\ \tilde{h}^0 - \tilde{a}\tilde{V}_n \end{pmatrix}
$$

$$\tag{A.20}$$

4. Computation of the wave strengths:

$$\delta W^1 = \delta\rho - \frac{\delta p}{\tilde{c}^2} \tag{A.21}$$

$$\delta W^2 = \delta V_x n_r - \delta V_r n_x \tag{A.22}$$

$$\delta W^4 = \frac{\delta p}{\tilde{\rho}\tilde{a}} + \delta V_x\, n_x + \delta V_r\, n_r \tag{A.23}$$

$$\delta W^3 = \delta V_\theta \tag{A.24}$$

$$\delta W^5 = \frac{\delta p}{\tilde{\rho}\tilde{a}} - \delta V_x\, n_x - \delta V_r\, n_r \tag{A.25}$$

where

$$\delta\rho = \rho^R - \rho^L \tag{A.26}$$

$$\delta V_x = V_x^R - V_x^L \tag{A.27}$$

$$\delta V_r = V_r^R - V_r^L \tag{A.28}$$

$$\delta V_\theta = V_\theta^R - V_\theta^L \tag{A.29}$$

$$\delta p = p^R - p^L \tag{A.30}$$

$$\delta k = k^R - k^L \tag{A.31}$$

For computations including circumferential or deterministic stresses, the kinetic energy $k$ of that stresses has been added to the definition of the total energy. Moreover, the quantity

$$\tilde{\rho}\,\lambda^1\,\delta k \tag{A.32}$$

must be added to the sum in the equation (A.3) for the energy equation.

# Appendix B

# Averaged forms of the Navier-Stokes equations

This appendix presents the different averaged forms of the Navier-Stokes equations used in this work: the Reynolds ensemble-averaged form, the time-averaged form, the average-passage form and the circumferential-averaged form. Without any loss of generality, the time-average is performed in the stator reference frame. The next averages, the passage-to-passage average and the circumferential-average, are performed on the stator rows.

## B.1    Navier-Stokes equations

In cylindrical coordinates, the instantaneous Navier-Stokes equations are written as follows:

**Equation of conservation of mass**

$$\frac{\partial \rho}{\partial t} + \frac{\partial \rho V_x}{\partial x} + \frac{1}{r}\frac{\partial r \rho V_r}{\partial r} + \frac{1}{r}\frac{\partial \rho V_\theta}{\partial \theta} = 0 \tag{B.1}$$

**Axial, radial and circumferential components of the equation of conservation of momentum**

$$\frac{\partial \rho V_x}{\partial t} + \frac{\partial (\rho V_x V_x + p)}{\partial x} + \frac{1}{r}\frac{\partial r \rho V_r V_x}{\partial r} + \frac{1}{r}\frac{\partial \rho V_\theta V_x}{\partial \theta} = \frac{\partial \tau_{xx}}{\partial x} + \frac{1}{r}\frac{\partial r \tau_{rx}}{\partial r} + \frac{1}{r}\frac{\partial \tau_{\theta x}}{\partial \theta} \tag{B.2}$$

$$\frac{\partial \rho V_r}{\partial t} + \frac{\partial \rho V_x V_r}{\partial x} + \frac{1}{r}\frac{\partial r (\rho V_r V_r + p)}{\partial r} + \frac{1}{r}\frac{\partial \rho V_\theta V_r}{\partial \theta} = \frac{\partial \tau_{xr}}{\partial x} + \frac{1}{r}\frac{\partial r \tau_{rr}}{\partial r} + \frac{1}{r}\frac{\partial \tau_{\theta r}}{\partial \theta}$$
$$+ \frac{1}{r}(\rho V_\theta V_\theta + p - \tau_{\theta\theta}) \tag{B.3}$$

$$\frac{\partial \rho V_\theta}{\partial t} + \frac{\partial \rho V_x V_\theta}{\partial x} + \frac{1}{r}\frac{\partial r \rho V_r V_\theta}{\partial r} + \frac{1}{r}\frac{\partial (\rho V_\theta V_\theta + p)}{\partial \theta} = \frac{\partial \tau_{x\theta}}{\partial x} + \frac{1}{r}\frac{\partial r \tau_{r\theta}}{\partial r} + \frac{1}{r}\frac{\partial \tau_{\theta\theta}}{\partial \theta}$$
$$+\frac{1}{r}(\tau_{r\theta} - \rho V_r V_\theta) \tag{B.4}$$

**Equation of conservation of energy**

$$\frac{\partial \rho E}{\partial t} + \frac{\partial (\rho V_x E + p V_x)}{\partial x} + \frac{1}{r}\frac{\partial r (\rho V_r E + p V_r)}{\partial r} + \frac{1}{r}\frac{\partial (\rho V_\theta E + p V_\theta)}{\partial \theta}$$
$$= \frac{\partial (\tau_{xj} V_j - q_x)}{\partial x} + \frac{1}{r}\frac{\partial r (\tau_{rj} V_j - q_r)}{\partial r} + \frac{1}{r}\frac{\partial (\tau_{\theta j} V_j - q_\theta)}{\partial \theta} \tag{B.5}$$

# B.2 Reynolds ensemble-averaged Navier-Stokes equations

Applying the ensemble average (defined by the equation (4.2)) to the instantaneous Navier-Stokes equations, the Reynolds ensemble-averaged Navier-Stokes equations are obtained::

**Equation of conservation of mass**

$$\frac{\partial \overline{\rho}^e}{\partial t} + \frac{\partial \overline{\rho}^e \widetilde{V_x}^e}{\partial x} + \frac{1}{r}\frac{\partial r \overline{\rho}^e \widetilde{V_r}^e}{\partial r} + \frac{1}{r}\frac{\partial \overline{\rho}^e \widetilde{V_\theta}^e}{\partial \theta} = 0 \tag{B.6}$$

**Axial, radial and circumferential components of the equation of conservation of momentum**

$$\frac{\partial \overline{\rho}^e \widetilde{V_x}^e}{\partial t} + \frac{\partial (\overline{\rho}^e \widetilde{V_x}^e \widetilde{V_x}^e + \overline{p}^e)}{\partial x} + \frac{1}{r}\frac{\partial r \overline{\rho}^e \widetilde{V_r}^e \widetilde{V_x}^e}{\partial r} + \frac{1}{r}\frac{\partial \overline{\rho}^e \widetilde{V_\theta}^e \widetilde{V_x}^e}{\partial \theta}$$
$$= \frac{\partial (\overline{\tau_{xx}}^e - \overline{\rho V_x' V_x'}^e)}{\partial x} + \frac{1}{r}\frac{\partial r(\overline{\tau_{rx}}^e - \overline{\rho V_r' V_x'}^e)}{\partial r} + \frac{1}{r}\frac{\partial (\overline{\tau_{\theta x}}^e - \overline{\rho V_\theta' V_x'}^e)}{\partial \theta} \tag{B.7}$$

$$\frac{\partial \overline{\rho}^e \widetilde{V_r}^e}{\partial t} + \frac{\partial \overline{\rho}^e \widetilde{V_x}^e \widetilde{V_r}^e}{\partial x} + \frac{1}{r}\frac{\partial r(\overline{\rho}^e \widetilde{V_r}^e \widetilde{V_r}^e + \overline{p}^e)}{\partial r} + \frac{1}{r}\frac{\partial \overline{\rho}^e \widetilde{V_\theta}^e \widetilde{V_r}^e}{\partial \theta}$$
$$= \frac{\partial (\overline{\tau_{xr}}^e - \overline{\rho V_x' V_r'}^e)}{\partial x} + \frac{1}{r}\frac{\partial r(\overline{\tau_{rr}}^e - \overline{\rho V_r' V_r'}^e)}{\partial r} + \frac{1}{r}\frac{\partial (\overline{\tau_{\theta r}}^e - \overline{\rho V_\theta' V_r'}^e)}{\partial \theta}$$
$$+ \frac{1}{r}(\overline{\rho}^e \widetilde{V_\theta}^e \widetilde{V_\theta}^e + \overline{p}^e - \overline{\tau_{\theta\theta}}^e + \overline{\rho V_\theta' V_\theta'}^e) \tag{B.8}$$

$$\frac{\partial \overline{\rho}^e \widetilde{V_\theta}^e}{\partial t} + \frac{\partial \overline{\rho}^e \widetilde{V_x}^e \widetilde{V_\theta}^e}{\partial x} + \frac{1}{r}\frac{\partial r \overline{\rho}^e \widetilde{V_r}^e \widetilde{V_\theta}^e}{\partial r} + \frac{1}{r}\frac{\partial (\overline{\rho}^e \widetilde{V_\theta}^e \widetilde{V_\theta}^e + \overline{p}^e)}{\partial \theta}$$
$$= \frac{\partial (\overline{\tau_{x\theta}}^e - \overline{\rho V_x' V_\theta'}^e)}{\partial x} + \frac{1}{r}\frac{\partial r(\overline{\tau_{r\theta}}^e - \overline{\rho V_r' V_\theta'}^e)}{\partial r} + \frac{1}{r}\frac{\partial (\overline{\tau_{\theta\theta}}^e - \overline{\rho V_\theta' V_\theta'}^e)}{\partial \theta}$$
$$+ \frac{1}{r}(\overline{\tau_{r\theta}}^e - \overline{\rho}^e \widetilde{V_r}^e \widetilde{V_\theta}^e - \overline{\rho V_r' V_\theta'}^e) \tag{B.9}$$

**Equation of conservation of energy**

$$\frac{\partial \overline{\rho}^e \widetilde{E}^e}{\partial t} + \frac{\partial \overline{\rho}^e \widetilde{V_x}^e \widetilde{H}^e}{\partial x} + \frac{1}{r}\frac{\partial r \overline{\rho}^e \widetilde{V_r}^e \widetilde{H}^e}{\partial r} + \frac{1}{r}\frac{\partial \overline{\rho}^e \widetilde{V_\theta}^e \widetilde{H}^e}{\partial \theta}$$
$$= \frac{\partial (\overline{\tau_{xj}}^e \widetilde{V_j}^e - \overline{q_x}^e - \overline{\rho V_x' H'}^e + \overline{\tau_{xj}' V_j'}^e)}{\partial x}$$
$$+ \frac{1}{r}\frac{\partial r(\overline{\tau_{rj}}^e \widetilde{V_j}^e - \overline{q_r}^e - \overline{\rho V_r' H'}^e + \overline{\tau_{rj}' u_j'}^e)}{\partial r}$$
$$+ \frac{1}{r}\frac{\partial (\overline{\tau_{\theta j}}^e \widetilde{V_j}^e - \overline{q_\theta}^e - \overline{\rho V_\theta' H'}^e + \overline{\tau_{\theta j}' V_j'}^e)}{\partial \theta} \tag{B.10}$$

The Reynolds stresses $\overline{\rho V_i' V_j'}^e$ that appear in the momentum equations represent the exchange of momentum between the non-deterministic and the deterministic flow fields. Similarly, the enthalpy flux $\overline{\rho V_i' H'}^e$ represents the exchange of energy between the non-deterministic and the deterministic flow fields.

# B.3   Time-averaged Navier-Stokes equations

The application of the time-average operator to the Reynolds ensemble-average Navier-Stokes equations leads to the time-average Navier-Stokes equations:

**Equation of conservation of mass**

$$\frac{1}{b_R}\frac{\partial b_R\overline{\overline{\rho}^{e}}^{t}\widetilde{\widetilde{V}_x^{e}}^{t}}{\partial x} + \frac{1}{rb_R}\frac{\partial rb_R\overline{\overline{\rho}^{e}}^{t}\widetilde{\widetilde{V}_r^{e}}^{t}}{\partial r} + \frac{1}{rb_R}\frac{\partial b_R\overline{\overline{\rho}^{e}}^{t}\widetilde{\widetilde{V}_\theta^{e}}^{t}}{\partial \theta} = 0 \tag{B.11}$$

**Axial, radial and circumferential components of the equation of conservation of momentum**

$$\frac{1}{b_R}\frac{\partial b_R(\overline{\overline{\rho}^{e}}^{t}\widetilde{\widetilde{V}_x^{e}}^{t}\widetilde{\widetilde{V}_x^{e}}^{t} + \overline{\overline{p}^{e}}^{t})}{\partial x} + \frac{1}{rb_R}\frac{\partial rb_R\overline{\overline{\rho}^{e}}^{t}\widetilde{\widetilde{V}_r^{e}}^{t}\widetilde{\widetilde{V}_x^{e}}^{t}}{\partial r} + \frac{1}{rb_R}\frac{\partial b_R\overline{\overline{\rho}^{e}}^{t}\widetilde{\widetilde{V}_\theta^{e}}^{t}\widetilde{\widetilde{V}_x^{e}}^{t}}{\partial \theta}$$

$$= \frac{1}{b_R}\frac{\partial b_R(\overline{\overline{\tau_{xx}}^{e}}^{t} - \overline{\overline{\rho V_x'V_x'}^{e}}^{t} - \overline{\rho^e V_x''V_x''}^{t})}{\partial x}$$

$$+ \frac{1}{rb_R}\frac{\partial rb_R(\overline{\overline{\tau_{rx}}^{e}}^{t} - \overline{\overline{\rho V_r'V_x'}^{e}}^{t} - \overline{\rho^e V_r''V_x''}^{t})}{\partial r} \tag{B.12}$$

$$+ \frac{1}{rb_R}\frac{\partial b_R(\overline{\overline{\tau_{\theta x}}^{e}}^{t} - \overline{\overline{\rho V_\theta'V_x'}^{e}}^{t} - \overline{\rho^e V_\theta''V_x''}^{t})}{\partial \theta}$$

$$+ f_{bx}^R + f_{vx}^R$$

$$\frac{1}{b_R}\frac{\partial b_R\overline{\overline{\rho}^{e}}^{t}\widetilde{\widetilde{V}_x^{e}}^{t}\widetilde{\widetilde{V}_r^{e}}^{t}}{\partial x} + \frac{1}{rb_R}\frac{\partial rb_R(\overline{\overline{\rho}^{e}}^{t}\widetilde{\widetilde{V}_r^{e}}^{t}\widetilde{\widetilde{V}_r^{e}}^{t} + \overline{\overline{p}^{e}}^{t})}{\partial r} + \frac{1}{rb_R}\frac{\partial b_R\overline{\overline{\rho}^{e}}^{t}\widetilde{\widetilde{V}_\theta^{e}}^{t}\widetilde{\widetilde{V}_r^{e}}^{t}}{\partial \theta}$$

$$= \frac{1}{b_R}\frac{\partial b_R(\overline{\overline{\tau_{xr}}^{e}}^{t} - \overline{\overline{\rho V_x'V_r'}^{e}}^{t} - \overline{\rho^e V_x''V_r''}^{t})}{\partial x}$$

$$+ \frac{1}{rb_R}\frac{\partial rb_R(\overline{\overline{\tau_{rr}}^{e}}^{t} - \overline{\overline{\rho V_r'V_r'}^{e}}^{t} - \overline{\rho^e V_r''V_r''}^{t})}{\partial r} \tag{B.13}$$

$$+ \frac{1}{rb_R}\frac{\partial b_R(\overline{\overline{\tau_{\theta r}}^{e}}^{t} - \overline{\overline{\rho V_\theta'V_r'}^{e}}^{t} - \overline{\rho^e V_\theta''V_r''}^{t})}{\partial \theta}$$

$$+ \frac{1}{r}(\overline{\overline{\rho}^{e}}^{t}\widetilde{\widetilde{V}_\theta^{e}}^{t}\widetilde{\widetilde{V}_\theta^{e}}^{t} + \overline{\overline{p}^{e}}^{t} - \overline{\overline{\tau_{\theta\theta}}^{e}}^{t} + \overline{\overline{\rho V_\theta'V_\theta'}^{e}}^{t} + \overline{\rho^e V_\theta''V_\theta''}^{t})$$

$$+ f_{br}^R + f_{vr}^R$$

$$
\frac{1}{b_R}\frac{\partial b_R \overline{\overline{\rho}^e}^t \widetilde{\widetilde{V_x}^e}^t \widetilde{\widetilde{V_\theta}^e}^t}{\partial x} + \frac{1}{rb_R}\frac{\partial rb_R \overline{\overline{\rho}^e}^t \widetilde{\widetilde{V_r}^e}^t \widetilde{\widetilde{V_\theta}^e}^t}{\partial r} + \frac{1}{rb_R}\frac{\partial b_R (\overline{\overline{\rho}^e}^t \widetilde{\widetilde{V_\theta}^e}^t \widetilde{\widetilde{V_\theta}^e}^t + \overline{\overline{p}^e}^t)}{\partial \theta}
$$

$$
= \frac{1}{b_R}\frac{\partial b_R (\overline{\overline{\tau_{x\theta}}^e}^t - \overline{\overline{\rho V_x' V_\theta'}^e}^t - \overline{\overline{\rho}^e V_x'' V_\theta''}^t)}{\partial x}
$$

$$
+ \frac{1}{rb_R}\frac{\partial rb_R (\overline{\overline{\tau_{r\theta}}^e}^t - \overline{\overline{\rho V_r' V_\theta'}^e}^t - \overline{\overline{\rho}^e V_r'' V_\theta''}^t)}{\partial r}
$$

$$
+ \frac{1}{rb_R}\frac{\partial b_R (\overline{\overline{\tau_{\theta\theta}}^e}^t - \overline{\overline{\rho V_\theta' V_\theta'}^e}^t - \overline{\overline{\rho}^e V_\theta'' V_\theta''}^t)}{\partial \theta} \qquad (B.14)
$$

$$
+ \frac{1}{r}(\overline{\overline{\tau_{r\theta}}^e}^t - \overline{\overline{\rho}^e}^t \widetilde{\widetilde{V_r}^e}^t \widetilde{\widetilde{V_\theta}^e}^t - \overline{\overline{\rho V_r' V_\theta'}^e}^t - \overline{\overline{\rho}^e V_r'' V_\theta''}^t))
$$

$$
+ f_{b\theta}^R + f_{v\theta}^R
$$

**Equation of conservation of energy**

$$
\frac{1}{b_R}\frac{\partial b_R \overline{\overline{\rho}^e}^t \widetilde{\widetilde{V_x}^e}^t \widetilde{\widetilde{H}^e}^t}{\partial x} + \frac{1}{rb_R}\frac{\partial rb_R \overline{\overline{\rho}^e}^t \widetilde{\widetilde{V_r}^e}^t \widetilde{\widetilde{H}^e}^t}{\partial r} + \frac{1}{rb_R}\frac{\partial b_R \overline{\overline{\rho}^e}^t \widetilde{\widetilde{V_\theta}^e}^t \widetilde{\widetilde{H}^e}^t}{\partial \theta}
$$

$$
= \frac{1}{b_R}\frac{\partial b_R (\overline{\overline{\tau_{xj}}^e}^t \widetilde{\widetilde{V}^e}_j^t - \overline{\overline{q_x}^e}^t + \overline{\overline{\tau_{xj}' V_j'}^e}^t + \overline{\tau_{xj}'' V_j''}^t - \overline{\overline{\rho V_x' H'}^e}^t - \overline{\overline{\rho}^e V_x'' H''}^t)}{\partial x}
$$

$$
+ \frac{1}{rb_R}\frac{\partial rb_R (\overline{\overline{\tau_{rj}}^e}^t \widetilde{\widetilde{V}^e}_j^t - \overline{\overline{q_r}^e}^t + \overline{\overline{\tau_{rj}' V_j'}^e}^t + \overline{\tau_{rj}'' V_j''}^t - \overline{\overline{\rho V_r' H'}^e}^t - \overline{\overline{\rho}^e V_r'' H''}^t)}{\partial r} \qquad (B.15)
$$

$$
+ \frac{1}{rb_R}\frac{\partial b_R (\overline{\overline{\tau_{\theta j}}^e}^t \widetilde{\widetilde{V}^e}_j^t - \overline{\overline{q_\theta}^e}^t + \overline{\overline{\tau_{\theta j}' V_j'}^e}^t + \overline{\tau_{\theta j}'' V_j''}^t - \overline{\overline{\rho V_\theta' H'}^e}^t - \overline{\overline{\rho}^e V_\theta'' H''}^t)}{\partial \theta}
$$

$$
+ e_b^R + e_v^R
$$

The deterministic stresses $\overline{\overline{\rho}^e V_i'' V_j''}^t$ that appear in the momentum equations represent the exchange of momentum between the deterministic and the time-averaged flow fields. Similarly, the enthalpy flux $\overline{\overline{\rho}^e V_i'' H''}^t$ represents the exchange of energy between the deterministic and the time-average flow fields.

The blockage factor $b_R$ is due to the geometrical blockage resulting from the blade thickness. It is lesser than one inside a rotor blade row and equal to one otherwise.

Additionally, the momentum equations contain the blade forces $f_b^R$ and $f_v^R$ and the energy equation contains the source terms $e_b^R$ and $e_v^R$. These terms are due to the pressure field, the shear stresses and the heat fluxes acting on the rotor blade wall surfaces. They directly

come from the additional term of the equation (4.9). They are written as follows:

$$f_{bx}^R = \frac{1}{2\pi b_R} \sum_{n=0}^{N_R-1} \left( \overline{p_1}^e \frac{\partial \theta_1}{\partial x} - \overline{p_2}^e \frac{\partial \theta_2}{\partial x} \right) \tag{B.16}$$

$$f_{br}^R = \frac{1}{2\pi b_R} \sum_{n=0}^{N_R-1} \left( \overline{p_1}^e \frac{\partial \theta_1}{\partial r} - \overline{p_2}^e \frac{\partial \theta_2}{\partial r} \right) \tag{B.17}$$

$$f_{b\theta}^R = \frac{1}{2\pi b_R} \sum_{n=0}^{N_R-1} \left( \frac{\overline{p_2}^e - \overline{p_1}^e}{r} \right) \tag{B.18}$$

$$e_b^R = r\omega f_{b\theta}^R \tag{B.19}$$

$$f_{vx}^R = \frac{1}{2\pi b_R} \sum_{n=0}^{N_R-1} \left[ \left( \overline{\tau_{xx2}}^e \frac{\partial \theta_2}{\partial x} + \overline{\tau_{rx2}}^e \frac{\partial \theta_2}{\partial r} - \frac{\overline{\tau_{\theta x2}}^e}{r} \right) - \left( \overline{\tau_{xx1}}^e \frac{\partial \theta_1}{\partial x} + \overline{\tau_{rx1}}^e \frac{\partial \theta_1}{\partial r} - \frac{\overline{\tau_{\theta x1}}^e}{r} \right) \right] \tag{B.20}$$

$$f_{vr}^R = \frac{1}{2\pi b_R} \sum_{n=0}^{N_R-1} \left[ \left( \overline{\tau_{xr2}}^e \frac{\partial \theta_2}{\partial x} + \overline{\tau_{rr2}}^e \frac{\partial \theta_2}{\partial r} - \frac{\overline{\tau_{\theta r2}}^e}{r} \right) - \left( \overline{\tau_{xr1}}^e \frac{\partial \theta_1}{\partial x} + \overline{\tau_{rr1}}^e \frac{\partial \theta_1}{\partial r} - \frac{\overline{\tau_{\theta r1}}^e}{r} \right) \right] \tag{B.21}$$

$$f_{v\theta}^R = \frac{1}{2\pi b_R} \sum_{n=0}^{N_R-1} \left[ \left( \overline{\tau_{x\theta2}}^e \frac{\partial \theta_2}{\partial x} + \overline{\tau_{r\theta2}}^e \frac{\partial \theta_2}{\partial r} - \frac{\overline{\tau_{\theta\theta2}}^e}{r} \right) - \left( \overline{\tau_{x\theta1}}^e \frac{\partial \theta_1}{\partial x} + \overline{\tau_{r\theta1}}^e \frac{\partial \theta_1}{\partial r} - \frac{\overline{\tau_{\theta\theta1}}^e}{r} \right) \right] \tag{B.22}$$

$$e_v^R = r\omega f_{v\theta}^R - \frac{1}{2\pi b_R} \sum_{n=0}^{N_R-1} \left[ \left( \overline{q_{x2}}^e \frac{\partial \theta_2}{\partial x} + \overline{q_{r2}}^e \frac{\partial \theta_2}{\partial r} - \frac{\overline{q_{\theta2}}^e}{r} \right) - \left( \overline{q_{x1}}^e \frac{\partial \theta_1}{\partial x} + \overline{q_{r1}}^e \frac{\partial \theta_1}{\partial r} - \frac{\overline{q_{\theta1}}^e}{r} \right) \right] \tag{B.23}$$

## B.4   Passage-to-passage averaged Navier-Stokes equations

The application of the passage-to-passage average to the time-averaged Navier-Stokes equations leads, for the $j^{th}$ stator, to the average-passage equations:

**Equation of conservation of mass**

$$\frac{1}{b_{Sj}}\frac{\partial b_{Sj}\overline{\overline{\rho^{e}}}^{t^{a}}\widetilde{\widetilde{V_{x}}^{e}}^{t^{a}}}{\partial x} + \frac{1}{rb_{Sj}}\frac{\partial rb_{Sj}\overline{\overline{\rho^{e}}}^{t^{a}}\widetilde{\widetilde{V_{r}}^{e}}^{t^{a}}}{\partial r} + \frac{1}{rb_{Sj}}\frac{\partial b_{Sj}\overline{\overline{\rho^{e}}}^{t^{a}}\widetilde{\widetilde{V_{\theta}}^{e}}^{t^{a}}}{\partial \theta} = 0 \tag{B.24}$$

**Axial, radial and circumferential components of the equation of conservation of momentum**

$$\frac{1}{b_{Sj}}\frac{\partial b_{Sj}(\overline{\overline{\rho^{e}}}^{t^{a}}\widetilde{\widetilde{V_{x}}^{e}}^{t^{a}}\widetilde{\widetilde{V_{x}}^{e}}^{t^{a}} + \overline{\overline{p^{e}}}^{t^{a}})}{\partial x} + \frac{1}{rb_{Sj}}\frac{\partial rb_{Sj}\overline{\overline{\rho^{e}}}^{t^{a}}\widetilde{\widetilde{V_{r}}^{e}}^{t^{a}}\widetilde{\widetilde{V_{x}}^{e}}^{t^{a}}}{\partial r} + \frac{1}{rb_{Sj}}\frac{\partial b_{Sj}\overline{\overline{\rho^{e}}}^{t^{a}}\widetilde{\widetilde{V_{\theta}}^{e}}^{t^{a}}\widetilde{\widetilde{V_{x}}^{e}}^{t^{a}}}{\partial \theta}$$

$$= \frac{1}{b_{Sj}}\frac{\partial b_{Sj}(\overline{\overline{\tau_{xx}}^{e}}^{t^{a}} - \overline{\overline{\rho V_{x}'V_{x}'}^{e}}^{t^{a}} - \overline{\overline{\rho^{e}V_{x}''V_{x}''}}^{t^{a}} - \overline{\overline{\rho^{e}}^{t}V_{x}'''V_{x}'''}^{a})}{\partial x}$$

$$+ \frac{1}{rb_{Sj}}\frac{\partial rb_{Sj}(\overline{\overline{\tau_{rx}}^{e}}^{t^{a}} - \overline{\overline{\rho V_{r}'V_{x}'}^{e}}^{t^{a}} - \overline{\overline{\rho^{e}V_{r}''V_{x}''}}^{t^{a}} - \overline{\overline{\rho^{e}}^{t}V_{r}'''V_{x}'''}^{a})}{\partial r} \tag{B.25}$$

$$+ \frac{1}{rb_{Sj}}\frac{\partial b_{Sj}(\overline{\overline{\tau_{\theta x}}^{e}}^{t^{a}} - \overline{\overline{\rho V_{\theta}'V_{x}'}^{e}}^{t^{a}} - \overline{\overline{\rho^{e}V_{\theta}''V_{x}''}}^{t^{a}} - \overline{\overline{\rho^{e}}^{t}V_{\theta}'''V_{x}'''}^{a})}{\partial \theta}$$

$$+ \overline{f_{bx}^{R}}^{a} + \overline{f_{vx}^{R}}^{a} + f_{bx}^{Sj} + f_{vx}^{Sj}$$

$$\frac{1}{b_{Sj}}\frac{\partial b_{Sj}\overline{\overline{\rho^{e}}}^{t^{a}}\widetilde{\widetilde{V_{x}}^{e}}^{t^{a}}\widetilde{\widetilde{V_{r}}^{e}}^{t^{a}}}{\partial x} + \frac{1}{rb_{Sj}}\frac{\partial rb_{Sj}(\overline{\overline{\rho^{e}}}^{t^{a}}\widetilde{\widetilde{V_{r}}^{e}}^{t^{a}}\widetilde{\widetilde{V_{r}}^{e}}^{t^{a}} + \overline{\overline{p^{e}}}^{t^{a}})}{\partial r} + \frac{1}{rb_{Sj}}\frac{\partial b_{Sj}\overline{\overline{\rho^{e}}}^{t^{a}}\widetilde{\widetilde{V_{\theta}}^{e}}^{t^{a}}\widetilde{\widetilde{V_{r}}^{e}}^{t^{a}}}{\partial \theta}$$

$$= \frac{1}{b_{Sj}}\frac{\partial b_{Sj}(\overline{\overline{\tau_{xr}}^{e}}^{t^{a}} - \overline{\overline{\rho V_{x}'V_{r}'}^{e}}^{t^{a}} - \overline{\overline{\rho^{e}V_{x}''V_{r}''}}^{t^{a}} - \overline{\overline{\rho^{e}}^{t}V_{x}'''V_{r}'''}^{a})}{\partial x}$$

$$+ \frac{1}{rb_{Sj}}\frac{\partial rb_{Sj}(\overline{\overline{\tau_{rr}}^{e}}^{t^{a}} - \overline{\overline{\rho V_{r}'V_{r}'}^{e}}^{t^{a}} - \overline{\overline{\rho^{e}V_{r}''V_{r}''}}^{t^{a}} - \overline{\overline{\rho^{e}}^{t}V_{r}'''V_{r}'''}^{a})}{\partial r} \tag{B.26}$$

$$+ \frac{1}{rb_{Sj}}\frac{\partial b_{Sj}(\overline{\overline{\tau_{\theta r}}^{e}}^{t^{a}} - \overline{\overline{\rho V_{\theta}'V_{r}'}^{e}}^{t^{a}} - \overline{\overline{\rho^{e}V_{\theta}''V_{r}''}}^{t^{a}} - \overline{\overline{\rho^{e}}^{t}V_{\theta}'''V_{r}'''}^{a})}{\partial \theta}$$

$$+ \frac{1}{r}(\overline{\overline{\rho^{e}}}^{t^{a}}\widetilde{\widetilde{V_{\theta}}^{e}}^{t^{a}}\widetilde{\widetilde{V_{\theta}}^{e}}^{t^{a}} + \overline{\overline{p^{e}}}^{t^{a}} - \overline{\overline{\tau_{\theta\theta}}^{e}}^{t^{a}} + \overline{\overline{\rho V_{\theta}'V_{\theta}'}^{e}}^{t^{a}} + \overline{\overline{\rho^{e}V_{\theta}''V_{\theta}''}}^{t^{a}} + \overline{\overline{\rho^{e}}^{t}V_{\theta}'''V_{\theta}'''}^{a})$$

$$+ \overline{f_{br}^{R}}^{a} + \overline{f_{vr}^{R}}^{a} + f_{br}^{Sj} + f_{vr}^{Sj}$$

$$
\frac{1}{b_{Sj}}\frac{\partial b_{Sj}\overline{\overline{\rho}^{e}}^{t^{a}}\widetilde{\widetilde{V}_{x}^{e}}^{t^{a}}\widetilde{\widetilde{V}_{\theta}^{e}}^{t^{a}}}{\partial x} + \frac{1}{rb_{Sj}}\frac{\partial rb_{Sj}\overline{\overline{\rho}^{e}}^{t^{a}}\widetilde{\widetilde{V}_{r}^{e}}^{t^{a}}\widetilde{\widetilde{V}_{\theta}^{e}}^{t^{a}}}{\partial r} + \frac{1}{rb_{Sj}}\frac{\partial b_{Sj}(\overline{\overline{\rho}^{e}}^{t^{a}}\widetilde{\widetilde{V}_{\theta}^{e}}^{t^{a}}\widetilde{\widetilde{V}_{\theta}^{e}}^{t^{a}} + \overline{\overline{p}^{e}}^{t^{a}})}{\partial \theta}
$$

$$
= \frac{1}{b_{Sj}}\frac{\partial b_{Sj}(\overline{\overline{\tau_{x\theta}}^{e}}^{t^{a}} - \overline{\overline{\rho V_{x}'V_{\theta}'}^{e}}^{t^{a}} - \overline{\overline{\rho}^{e}V_{x}''V_{\theta}''}^{t^{a}} - \overline{\overline{\rho}^{e^{t}}V_{x}'''V_{\theta}'''}^{a})}{\partial x}
$$

$$
+ \frac{1}{rb_{Sj}}\frac{\partial rb_{Sj}(\overline{\overline{\tau_{r\theta}}^{e}}^{t} - \overline{\overline{\rho V_{r}'V_{\theta}'}^{e}}^{t^{a}} - \overline{\overline{\rho}^{e}V_{r}''V_{\theta}''}^{t^{a}} - \overline{\overline{\rho}^{e^{t}}V_{r}'''V_{\theta}'''}^{a})}{\partial r}
$$

$$
+ \frac{1}{rb_{Sj}}\frac{\partial b_{Sj}(\overline{\overline{\tau_{\theta\theta}}^{e}}^{t} - \overline{\overline{\rho V_{\theta}'V_{\theta}'}^{e}}^{t^{a}} - \overline{\overline{\rho}^{e}V_{\theta}''V_{\theta}''}^{t^{a}} - \overline{\overline{\rho}^{e^{t}}V_{\theta}'''V_{\theta}'''}^{a})}{\partial \theta} \tag{B.27}
$$

$$
+ \frac{1}{r}(\overline{\overline{\tau_{r\theta}}^{e}}^{t^{a}} - \overline{\overline{\rho}^{e}}^{t^{a}}\widetilde{\widetilde{V}_{r}^{e}}^{t^{a}}\widetilde{\widetilde{V}_{\theta}^{e}}^{t^{a}} - \overline{\overline{\rho V_{r}'V_{\theta}'}^{e}}^{t^{a}} - \overline{\overline{\rho}^{e}V_{r}''V_{\theta}''}^{t^{a}} - \overline{\overline{\rho}^{e^{t}}V_{r}'''V_{\theta}'''}^{a})
$$

$$
+ \overline{f_{b\theta}^{R}}^{a} + \overline{f_{v\theta}^{R}}^{a} + f_{b\theta}^{Sj} + f_{v\theta}^{Sj}
$$

**Equation of conservation of energy**

$$
\frac{1}{b_{Sj}}\frac{\partial b_{Sj}\overline{\overline{\rho}^{e}}^{t^{a}}\widetilde{\widetilde{V}_{x}^{e}}^{t^{a}}\widetilde{\widetilde{H}^{e}}^{t^{a}}}{\partial x} + \frac{1}{rb_{Sj}}\frac{\partial rb_{Sj}\overline{\overline{\rho}^{e}}^{t^{a}}\widetilde{\widetilde{V}_{r}^{e}}^{t^{a}}\widetilde{\widetilde{H}^{e}}^{t^{a}}}{\partial r} + \frac{1}{rb_{Sj}}\frac{\partial b_{Sj}\overline{\overline{\rho}^{e}}^{t^{a}}\widetilde{\widetilde{V}_{\theta}^{e}}^{t^{a}}\widetilde{\widetilde{H}^{e}}^{t^{a}}}{\partial \theta}
$$

$$
= \frac{1}{b_{Sj}}\frac{\partial b_{Sj}(\overline{\overline{\tau_{xj}}^{e}}^{t^{a}}\widetilde{\widetilde{V}_{j}^{e}}^{t^{a}} - \overline{\overline{q_{x}}^{e}}^{t^{a}} + \overline{\overline{\tau_{xj}'V_{j}'}^{e}}^{t^{a}} + \overline{\overline{\tau_{xj}''V_{j}''}^{t^{a}}} + \overline{\tau_{xj}'''V_{j}'''}^{a})}{\partial x}
$$

$$
- \frac{1}{b_{Sj}}\frac{\partial b_{Sj}(\overline{\overline{\rho V_{x}'H'}^{e}}^{t^{a}} - \overline{\overline{\rho}^{e}V_{x}''H''}^{t^{a}} - \overline{\overline{\rho}^{e^{t}}V_{x}'''H'''}^{a})}{\partial x}
$$

$$
+ \frac{1}{rb_{Sj}}\frac{\partial rb_{Sj}(\overline{\overline{\tau_{rj}}^{e}}^{t^{a}}\widetilde{\widetilde{V}_{j}^{e}}^{t^{a}} - \overline{\overline{q_{r}}^{e}}^{t^{a}} + \overline{\overline{\tau_{rj}'V_{j}'}^{e}}^{t^{a}} + \overline{\overline{\tau_{rj}''V_{j}''}^{t^{a}}} + \overline{\tau_{rj}'''V_{j}'''}^{a})}{\partial r} \tag{B.28}
$$

$$
- \frac{1}{rb_{Sj}}\frac{\partial rb_{Sj}(\overline{\overline{\rho V_{r}'H'}^{e}}^{t^{a}} - \overline{\overline{\rho}^{e}V_{r}''H''}^{t^{a}} - \overline{\overline{\rho}^{e^{t}}V_{r}'''H'''}^{a})}{\partial r}
$$

$$
+ \frac{1}{rb_{Sj}}\frac{\partial b_{Sj}(\overline{\overline{\tau_{\theta j}}^{e}}^{t^{a}}\widetilde{\widetilde{V}_{j}^{e}}^{t^{a}} - \overline{\overline{q_{\theta}}^{e}}^{t^{a}} + \overline{\overline{\tau_{\theta j}'V_{j}'}^{e}}^{t^{a}} + \overline{\overline{\tau_{\theta j}''V_{j}''}^{t^{a}}} + \overline{\tau_{\theta j}'''V_{j}'''}^{a})}{\partial \theta}
$$

$$
- \frac{1}{rb_{Sj}}\frac{\partial b_{Sj}(\overline{\overline{\rho V_{\theta}'H'}^{e}}^{t^{a}} - \overline{\overline{\rho}^{e}V_{\theta}''H''}^{t^{a}} - \overline{\overline{\rho}^{e^{t}}V_{\theta}'''H'''}^{a})}{\partial \theta}
$$

$$
+ \overline{e_{b}^{R}}^{t} + \overline{e_{v}^{R}}^{t} + e_{v}^{Sj}
$$

The aperiodic stresses $\overline{\overline{\rho}^{e^{t}}V_{i}'''V_{j}'''}^{a}$ that appear in the momentum equations represent the ex-

change of momentum between the time-averaged and the average-passage flow fields. Similarly, the enthalpy flux $\overline{\overline{\rho}^e{}^t V_i''' H'''}^a$ represents the exchange of energy between the time-average and the average-passage flow fields.

The blockage factor $b_{Sj}$ is due to the geometrical blockage resulting from the blade thickness. It is equal to $b_S$ inside the stators other than one of interest (which is still in 3-D) and is equal to $b_R$ inside a rotor. It is equal to one otherwise.

Additionally, the momentum equations contain the blade forces $f_b^{Sj}$ and $f_v^{Sj}$ and the energy equation contains the source term $e_v^{Sj}$. These terms are due to the pressure field, the shear stresses and the heat fluxes acting on the stator blade wall surfaces other than the one under consideration. They directly come from the additional term of the equation (4.11). They are written as follows:

$$f_{bx}^{Sj} = \frac{1}{2\pi b_j} \sum_{n=0}^{N_S-1} \left( \overline{\overline{p_3}^e}^t \frac{\partial \theta_3}{\partial x} - \overline{\overline{p_4}^e}^t \frac{\partial \theta_4}{\partial x} \right) \tag{B.29}$$

$$f_{br}^{Sj} = \frac{1}{2\pi b_j} \sum_{n=0}^{N_S-1} \left( \overline{\overline{p_3}^e}^t \frac{\partial \theta_3}{\partial r} - \overline{p_4}^e \frac{\partial \theta_4}{\partial r} \right) \tag{B.30}$$

$$f_{b\theta}^{Sj} = \frac{1}{2\pi b_j} \sum_{n=0}^{N_S-1} \left( \frac{\overline{\overline{p_4}^e}^t - \overline{\overline{p_3}^e}^t}{r} \right) \tag{B.31}$$

$$f_{vx}^{Sj} = \frac{1}{2\pi b_j} \sum_{n=0}^{N_S-1} \left[ \left( \overline{\overline{\tau_{xx4}}^e}^t \frac{\partial \theta_4}{\partial x} + \overline{\overline{\tau_{rx4}}^e}^t \frac{\partial \theta_4}{\partial r} - \frac{\overline{\overline{\tau_{\theta x4}}^e}^t}{r} \right) - \left( \overline{\overline{\tau_{xx3}}^e}^t \frac{\partial \theta_3}{\partial x} + \overline{\overline{\tau_{rx3}}^e}^t \frac{\partial \theta_3}{\partial r} - \frac{\overline{\overline{\tau_{\theta x3}}^e}^t}{r} \right) \right] \tag{B.32}$$

$$f_{vr}^{Sj} = \frac{1}{2\pi b_j} \sum_{n=0}^{N_S-1} \left[ \left( \overline{\overline{\tau_{xr4}}^e}^t \frac{\partial \theta_4}{\partial x} + \overline{\overline{\tau_{rr4}}^e}^t \frac{\partial \theta_4}{\partial r} - \frac{\overline{\overline{\tau_{\theta r4}}^e}^t}{r} \right) - \left( \overline{\overline{\tau_{xr3}}^e}^t \frac{\partial \theta_3}{\partial x} + \overline{\overline{\tau_{rr3}}^e}^t \frac{\partial \theta_3}{\partial r} - \frac{\overline{\overline{\tau_{\theta r3}}^e}^t}{r} \right) \right] \tag{B.33}$$

$$f_{v\theta}^{Sj} = \frac{1}{2\pi b_j} \sum_{n=0}^{N_S-1} \left[ \left( \overline{\overline{\tau_{x\theta4}}^e}^t \frac{\partial \theta_4}{\partial x} + \overline{\overline{\tau_{r\theta4}}^e}^t \frac{\partial \theta_4}{\partial r} - \frac{\overline{\overline{\tau_{\theta\theta4}}^e}^t}{r} \right) - \left( \overline{\overline{\tau_{x\theta3}}^e}^t \frac{\partial \theta_3}{\partial x} + \overline{\overline{\tau_{r\theta3}}^e}^t \frac{\partial \theta_3}{\partial r} - \frac{\overline{\overline{\tau_{\theta\theta3}}^e}^t}{r} \right) \right] \tag{B.34}$$

$$e_v^{Sj} = -\frac{1}{2\pi b_j} \sum_{n=0}^{N_S-1} \left[ \left( \overline{\overline{q_{x4}}^e}^t \frac{\partial \theta_4}{\partial x} + \overline{\overline{q_{r4}}^e}^t \frac{\partial \theta_4}{\partial r} - \frac{\overline{\overline{q_{\theta4}}^e}^t}{r} \right) - \left( \overline{\overline{q_{x3}}^e}^t \frac{\partial \theta_3}{\partial x} + \overline{\overline{q_{r3}}^e}^t \frac{\partial \theta_3}{\partial r} - \frac{\overline{\overline{q_{\theta3}}^e}^t}{r} \right) \right] \tag{B.35}$$

# B.5    Circumferentially-averaged Navier-Stokes equations

The application of the circumferential-average to the average-passage equations for the $j^{th}$ stator leads to the circumferentially-averaged Navier-Stokes equations or the throughflow equations:

**Equation of conservation of mass**

$$\frac{1}{b}\frac{\partial b\overline{\overline{\rho}^{e^t}}^{a^c}\widetilde{\overline{\widetilde{V_x}}^{e^t}}^{a^c}}{\partial x} + \frac{1}{rb}\frac{\partial rb\overline{\overline{\rho}^{e^t}}^{a^c}\widetilde{\overline{\widetilde{V_r}}^{e^t}}^{a^c}}{\partial r} = 0 \tag{B.36}$$

**Axial, radial and circumferential components of the equation of conservation of momentum**

$$
\begin{aligned}
&\frac{1}{b}\frac{\partial b(\overline{\overline{\rho}^{e^t}}^{a^c}\widetilde{\overline{\widetilde{V_x}}^{e^t}}^{a^c}\widetilde{\overline{\widetilde{V_x}}^{e^t}}^{a^c} + \overline{\overline{p}^{e^t}}^{a^c})}{\partial x} + \frac{1}{rb}\frac{\partial rb\overline{\overline{\rho}^{e^t}}^{a^c}\widetilde{\overline{\widetilde{V_r}}^{e^t}}^{a^c}\widetilde{\overline{\widetilde{V_x}}^{e^t}}^{a^c}}{\partial r} \\
&= \frac{1}{b}\frac{\partial b(\overline{\overline{\overline{\tau_{xx}}}^{e^t}}^{a^c} - \overline{\overline{\overline{\rho V_x'V_x'}}^{e^t}}^{a^c} - \overline{\overline{\overline{\rho^e V_x''V_x''}}^{t}}^{a^c} - \overline{\overline{\rho^{e^t} V_x'''V_x'''}}^{a^c} - \overline{\overline{\rho^{e^t}}^a V_x''''V_x''''}^{c})}{\partial x} \tag{B.37} \\
&+ \frac{1}{rb}\frac{\partial rb(\overline{\overline{\overline{\tau_{rx}}}^{e^t}}^{a^c} - \overline{\overline{\overline{\rho V_r'V_x'}}^{e^t}}^{a^c} - \overline{\overline{\overline{\rho^e V_r''V_x''}}^{t}}^{a^c} - \overline{\overline{\rho^{e^t} V_r'''V_x'''}}^{a^c} - \overline{\overline{\rho^{e^t}}^a V_r''''V_x''''}^{c})}{\partial r} \\
&+ \overline{\overline{f_{bx}^R}}^{a^c} + \overline{\overline{f_{vx}^R}}^{a^c} + \overline{f_{bx}^{Sj}}^c + \overline{f_{vx}^{Sj}}^c + f_{bx}^j + f_{vx}^j
\end{aligned}
$$

$$
\begin{aligned}
&\frac{1}{b}\frac{\partial b\overline{\overline{\rho}^{e^t}}^{a^c}\widetilde{\overline{\widetilde{V_x}}^{e^t}}^{a^c}\widetilde{\overline{\widetilde{V_r}}^{e^t}}^{a^c}}{\partial x} + \frac{1}{rb}\frac{\partial rb(\overline{\overline{\rho}^{e^t}}^{a^c}\widetilde{\overline{\widetilde{V_r}}^{e^t}}^{a^c}\widetilde{\overline{\widetilde{V_r}}^{e^t}}^{a^c} + \overline{\overline{p}^{e^t}}^{a^c})}{\partial r} \\
&= \frac{1}{b}\frac{\partial b(\overline{\overline{\overline{\tau_{xr}}}^{e^t}}^{a^c} - \overline{\overline{\overline{\rho V_x'V_r'}}^{e^t}}^{a^c} - \overline{\overline{\overline{\rho^e V_x''V_r''}}^{t}}^{a^c} - \overline{\overline{\rho^{e^t} V_x'''V_r'''}}^{a^c} - \overline{\overline{\rho^{e^t}}^a V_x''''V_r''''}^{c})}{\partial x} \\
&+ \frac{1}{rb}\frac{\partial rb(\overline{\overline{\overline{\tau_{rr}}}^{e^t}}^{a^c} - \overline{\overline{\overline{\rho V_r'V_r'}}^{e^t}}^{a^c} - \overline{\overline{\overline{\rho^e V_r''V_r''}}^{t}}^{a^c} - \overline{\overline{\rho^{e^t} V_r'''V_r'''}}^{a^c} - \overline{\overline{\rho^{e^t}}^a V_r''''V_r''''}^{c})}{\partial r} \tag{B.38} \\
&+ \frac{1}{r}(\overline{\overline{\rho}^{e^t}}^{a^c}\widetilde{\overline{\widetilde{V_\theta}}^{e^t}}^{a^c}\widetilde{\overline{\widetilde{V_\theta}}^{e^t}}^{a^c} + \overline{\overline{p}^{e^t}}^{a^c} - \overline{\overline{\tau_{\theta\theta}}^{e^t}}^{a^c} \\
&+ \overline{\overline{\overline{\rho V_\theta'V_\theta'}}^{e^t}}^{a^c} + \overline{\overline{\overline{\rho^e V_\theta''V_\theta''}}^{t}}^{a^c} + \overline{\overline{\rho^{e^t} V_\theta'''V_\theta'''}}^{a^c} + \overline{\overline{\rho^{e^t}}^a V_\theta'''V_\theta'''}^{c}) \\
&+ \overline{\overline{f_{br}^R}}^{a^c} + \overline{\overline{f_{vr}^R}}^{a^c} + \overline{f_{br}^{Sj}}^c + \overline{f_{vr}^{Sj}}^c + f_{br}^j + f_{vr}^j
\end{aligned}
$$

$$
\frac{1}{b}\frac{\partial b\overline{\overline{\overline{\rho}^{e^t}}}^{ac}\widetilde{\widetilde{\widetilde{V_x}^e}}^{t^{ac}}\widetilde{\widetilde{\widetilde{V_\theta}^e}}^{t^{ac}}}{\partial x}+\frac{1}{rb}\frac{\partial rb\overline{\overline{\overline{\rho}^{e^t}}}^{ac}\widetilde{\widetilde{\widetilde{V_r}^e}}^{t^{ac}}\widetilde{\widetilde{\widetilde{V_\theta}^e}}^{t^{ac}}}{\partial r}
$$

$$
=\frac{1}{b}\frac{\partial b(\overline{\overline{\overline{\tau_{x\theta}}^e}}^{t^a}-\overline{\overline{\overline{\rho V_x'V_\theta'}^e}}^{t^{ac}}-\overline{\overline{\overline{\rho^e V_x''V_\theta''}}^{t}}^{ac}-\overline{\overline{\overline{\rho}^{e^t}V_x'''V_\theta'''}}^{ac}-\overline{\overline{\overline{\rho}^{e^t}}^a V_x''''V_\theta''''}^c)}{\partial x}
$$

$$
+\frac{1}{rb}\frac{\partial rb(\overline{\overline{\overline{\tau_{r\theta}}^e}}^t-\overline{\overline{\overline{\rho V_r'V_\theta'}^e}}^{t^{ac}}-\overline{\overline{\overline{\rho^e V_r''V_\theta''}}^{t}}^{ac}-\overline{\overline{\overline{\rho}^{e^t}V_r'''V_\theta'''}}^{ac}-\overline{\overline{\overline{\rho}^{e^t}}^a V_r''''V_\theta''''}^c)}{\partial r}
$$

$$
+\frac{1}{r}(\overline{\overline{\overline{\tau_{r\theta}}^e}}^{t^{ac}}-\overline{\overline{\rho}^{e^t}}^{ac}\widetilde{\widetilde{V_r}^e}^{t^{ac}}\widetilde{\widetilde{V_\theta}^e}^{t^{ac}}-\overline{\overline{\overline{\rho V_r'V_\theta'}^e}}^{t^{ac}}-\overline{\overline{\overline{\rho^e V_r''V_\theta''}}^{t}}^{ac}-\overline{\overline{\overline{\rho}^{e^t}V_r'''V_\theta'''}}^{ac}-\overline{\overline{\overline{\rho}^{e^t}}^a V_r''''V_\theta''''}^c)
$$

$$
+\overline{\overline{f_{b\theta}^R}}^{ac}+\overline{\overline{f_{v\theta}^R}}^{ac}+\overline{f_{b\theta}^{Sj}}^c+\overline{f_{v\theta}^{Sj}}^c+f_{b\theta}^j+f_{v\theta}^j
$$

$$
\tag{B.39}
$$

**Equation of conservation of energy**

$$
\frac{1}{b}\frac{\partial b\overline{\overline{\overline{\rho}^{e^t}}}^{ac}\widetilde{\widetilde{\widetilde{V_x}^e}}^{t^{ac}}\widetilde{\widetilde{\widetilde{H}^e}}^{t^{ac}}}{\partial x}+\frac{1}{rb}\frac{\partial rb\overline{\overline{\overline{\rho}^{e^t}}}^{ac}\widetilde{\widetilde{\widetilde{V_r}^e}}^{t^{ac}}\widetilde{\widetilde{\widetilde{H}^e}}^{t^{ac}}}{\partial r}
$$

$$
=\frac{1}{b}\frac{\partial b(\overline{\overline{\overline{\tau_{xj}}^e}}^{t^{ac}}\widetilde{\widetilde{V_j}^e}^{t^{ac}}-\overline{\overline{\overline{q_x}^e}}^{t^{ac}}+\overline{\overline{\overline{\tau_{xj}'V_j'}^e}}^{t^{ac}}+\overline{\overline{\overline{\tau_{xj}''V_j''}}^{t}}^{ac}+\overline{\overline{\tau_{xj}'''V_j'''}}^{ac}+\overline{\tau_{xj}''''V_j''''}^c)}{\partial x}
$$

$$
-\frac{1}{b}\frac{\partial b(\overline{\overline{\overline{\rho V_x'H'}^e}}^{t^{ac}}\overline{\overline{\overline{\rho^e V_x''H''}}^{t}}^{ac}-\overline{\overline{\overline{\rho}^{e^t}V_x'''H'''}}^{ac}-\overline{\overline{\overline{\rho}^{e^t}}^a V_x''''H''''}^c)}{\partial x}
$$

$$
+\frac{1}{rb}\frac{\partial rb(\overline{\overline{\overline{\tau_{rj}}^e}}^{t^{ac}}\widetilde{\widetilde{V_j}^e}^{t^{ac}}-\overline{\overline{\overline{q_r}^e}}^{t^{ac}}+\overline{\overline{\overline{\tau_{rj}'V_j'}^e}}^{t^{ac}}+\overline{\overline{\overline{\tau_{rj}''V_j''}}^{t}}^{ac}+\overline{\overline{\tau_{rj}'''V_j'''}}^{ac}+\overline{\tau_{rj}''''V_j''''}^c)}{\partial r}
$$

$$
-\frac{1}{rb}\frac{\partial rb(\overline{\overline{\overline{\rho V_r'H'}^e}}^{t^{ac}}-\overline{\overline{\overline{\rho^e V_r''H''}}^{t}}^{ac}-\overline{\overline{\overline{\rho}^{e^t}V_r'''H'''}}^{ac}-\overline{\overline{\overline{\rho}^{e^t}}^a V_r''''H''''}^c)}{\partial r}
$$

$$
+\overline{\overline{e_b^R}}^{ac}+\overline{\overline{e_v^R}}^{ac}+\overline{e_v^{Sj}}^c+e_v^j
$$

$$
\tag{B.40}
$$

The circumferential stresses $\overline{\overline{\overline{\rho}^{e^t}}^a V_i''''V_j''''}^c$ that appear in the momentum equations represent the exchange of momentum between the average-passage and the axisymmetric flow fields. Similarly, the enthalpy flux $\overline{\overline{\overline{\rho}^{e^t}}^a V_i''''H''''}^c$ represents the exchange of energy between the average-passage and the axisymmetric fields.

The blockage factor $b$ is due to the geometrical blockage resulting from the blade thickness. It is equal to $b_S$ inside the stators other than one of interest, to $b_R$ inside a rotor and to $b_j$ inside the $j^{th}$ stator. It is equal to one otherwise.

Additionally, the momentum equations contain the blade forces $f_b^j$ and $f_v^j$ and the energy equation contains the source terms $e_b^j$ and $e_v^j$. These terms are due to the pressure field, the shear stresses and the heat fluxes acting on the stator $j$. They directly come from the additional term of the equation (4.13). They are written as follows:

$$f_{bx}^j = \frac{1}{2\pi b} \sum_{n=0}^{N-1} \left( \overline{\overline{p_5 e}}^{t a} \frac{\partial \theta_5}{\partial x} - \overline{\overline{p_6 e}}^{t a} \frac{\partial \theta_6}{\partial x} \right) \tag{B.41}$$

$$f_{br}^j = \frac{1}{2\pi b} \sum_{n=0}^{N-1} \left( \overline{\overline{p_5 e}}^{t a} \frac{\partial \theta_5}{\partial r} - \overline{\overline{p_6 e}}^{t a} \frac{\partial \theta_6}{\partial r} \right) \tag{B.42}$$

$$f_{b\theta}^j = \frac{1}{2\pi b} \sum_{n=0}^{N-1} \left( \frac{\overline{\overline{p_6 e}}^{t a} - \overline{\overline{p_5 e}}^{t a}}{r} \right) \tag{B.43}$$

$$f_{vx}^j = \frac{1}{2\pi b} \sum_{n=0}^{N-1} \left[ \left( \overline{\overline{\tau_{xx6} e}}^{t a} \frac{\partial \theta_6}{\partial x} + \overline{\overline{\tau_{rx6} e}}^{t a} \frac{\partial \theta_6}{\partial r} - \frac{\overline{\overline{\tau_{\theta x6} e}}^{t a}}{r} \right) - \left( \overline{\overline{\tau_{xx5} e}}^{t a} \frac{\partial \theta_5}{\partial x} + \overline{\overline{\tau_{rx5} e}}^{t a} \frac{\partial \theta_5}{\partial r} - \frac{\overline{\overline{\tau_{\theta x5} e}}^{t a}}{r} \right) \right] \tag{B.44}$$

$$f_{vr}^j = \frac{1}{2\pi b} \sum_{n=0}^{N-1} \left[ \left( \overline{\overline{\tau_{xr6} e}}^{t a} \frac{\partial \theta_6}{\partial x} + \overline{\overline{\tau_{rr6} e}}^{t a} \frac{\partial \theta_6}{\partial r} - \frac{\overline{\overline{\tau_{\theta r6} e}}^{t a}}{r} \right) - \left( \overline{\overline{\tau_{xr5} e}}^{t a} \frac{\partial \theta_5}{\partial x} + \overline{\overline{\tau_{rr5} e}}^{t a} \frac{\partial \theta_5}{\partial r} - \frac{\overline{\overline{\tau_{\theta r5} e}}^{t a}}{r} \right) \right] \tag{B.45}$$

$$f_{v\theta}^j = \frac{1}{2\pi b} \sum_{n=0}^{N-1} \left[ \left( \overline{\overline{\tau_{x\theta6} e}}^{t a} \frac{\partial \theta_6}{\partial x} + \overline{\overline{\tau_{r\theta6} e}}^{t a} \frac{\partial \theta_6}{\partial r} - \frac{\overline{\overline{\tau_{\theta\theta6} e}}^{t a}}{r} \right) - \left( \overline{\overline{\tau_{x\theta5} e}}^{t a} \frac{\partial \theta_5}{\partial x} + \overline{\overline{\tau_{r\theta5} e}}^{t a} \frac{\partial \theta_5}{\partial r} - \frac{\overline{\overline{\tau_{\theta\theta5} e}}^{t a}}{r} \right) \right] \tag{B.46}$$

$$e_v^j = -\frac{1}{2\pi b} \sum_{n=0}^{N-1} \left[ \left( \overline{\overline{q_{x6} e}}^{t a} \frac{\partial \theta_6}{\partial x} + \overline{\overline{q_{r6} e}}^{t a} \frac{\partial \theta_6}{\partial r} - \frac{\overline{\overline{q_{\theta6} e}}^{t a}}{r} \right) - \left( \overline{\overline{q_{x5} e}}^{t a} \frac{\partial \theta_5}{\partial x} + \overline{\overline{q_{r5} e}}^{t a} \frac{\partial \theta_5}{\partial r} - \frac{\overline{\overline{q_{\theta5} e}}^{t a}}{r} \right) \right] \tag{B.47}$$

# Appendix C

# CME2 blade forces and stresses

## C.1   Blade force and circumferential stresses
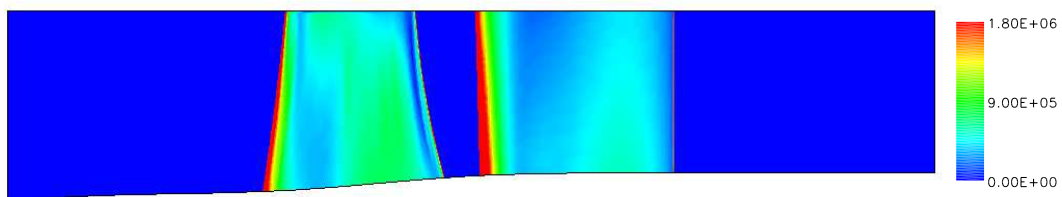


Figure C.1: Modulus of the inviscid blade force
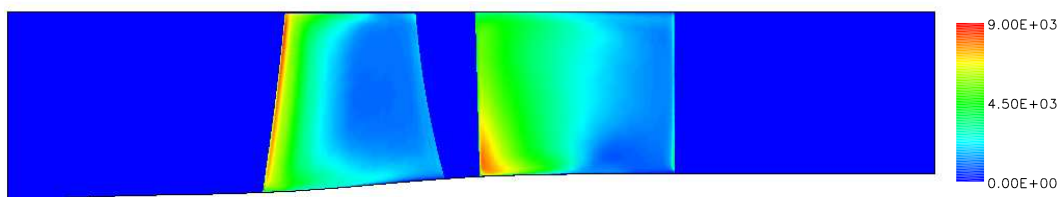


Figure C.2: Modulus of the viscous blade force
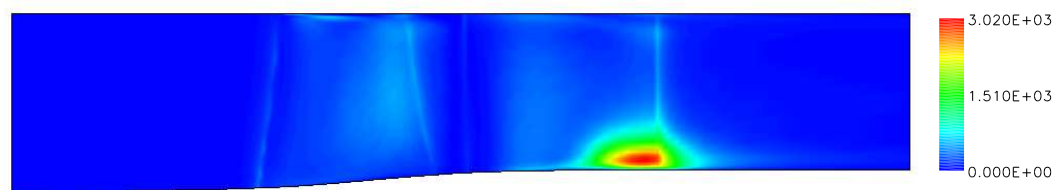


Figure C.3: Axial-axial circumferential stress
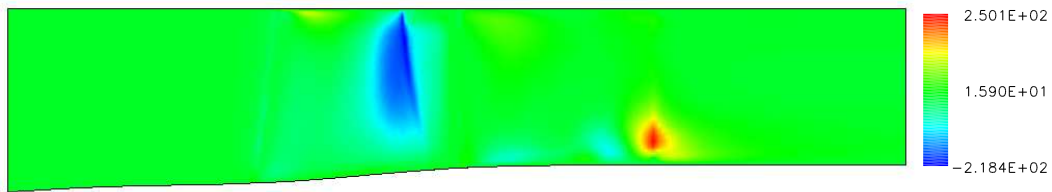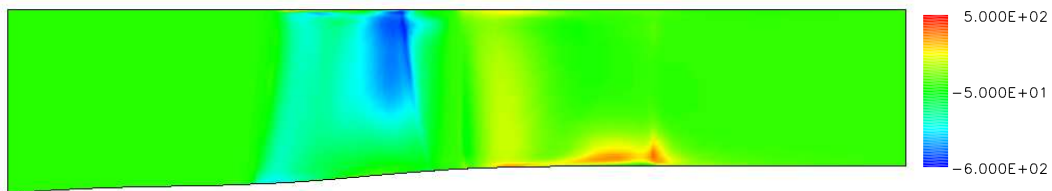
Figure C.4: Axial-radial circumferential stress



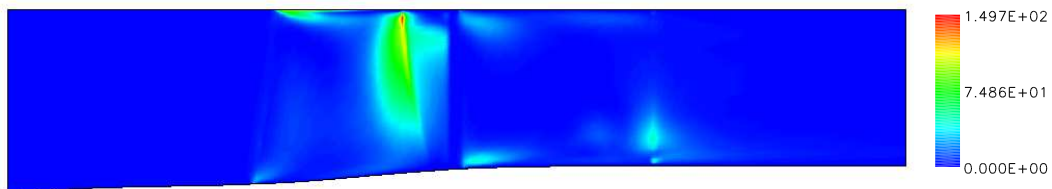Figure C.5: Axial-circumferential circumferential stress



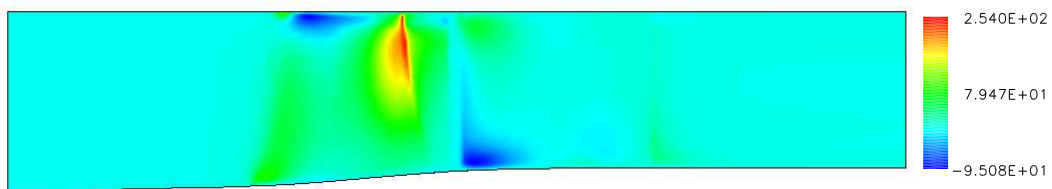Figure C.6: Radial-radial circumferential stress

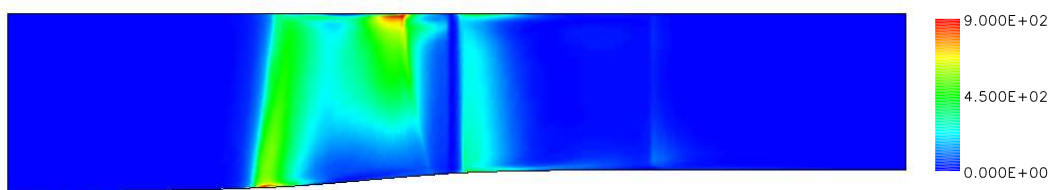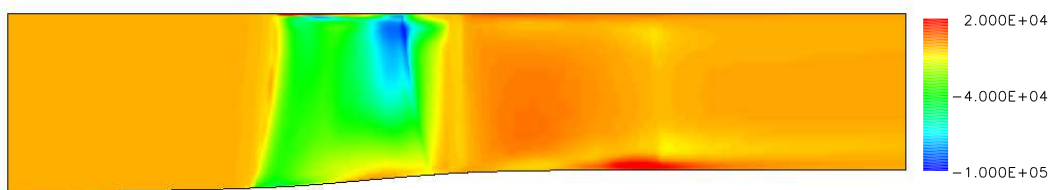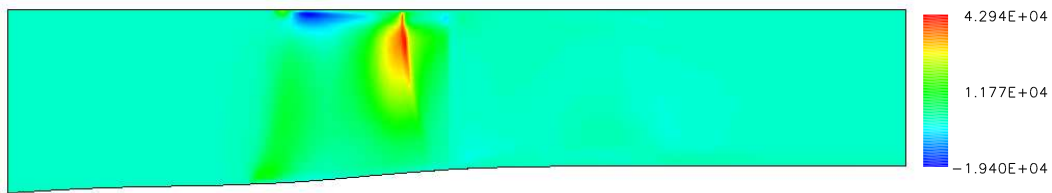

Figure C.7: Radial-circumferential circumferential stress



Figure C.8: Circumferential-circumferential circumferential stress



Figure C.9: Axial velocity-enthalpy circumferential stress

Figure C.10: Radial velocity-enthalpy circumferential stress

## C.2  Contributions to the momentum and energy balances
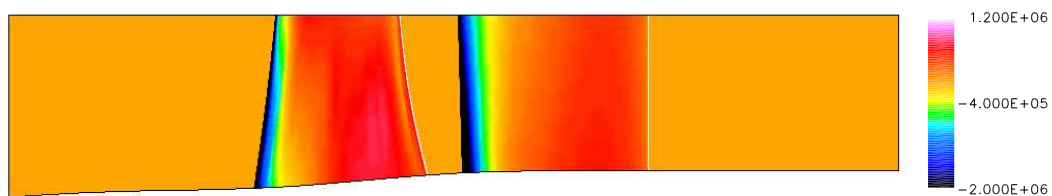


(a) inviscid blade force $f_{bx}$
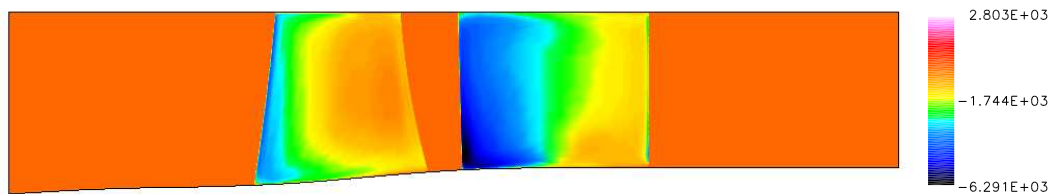


(b) viscous blade force $f_{vx}$
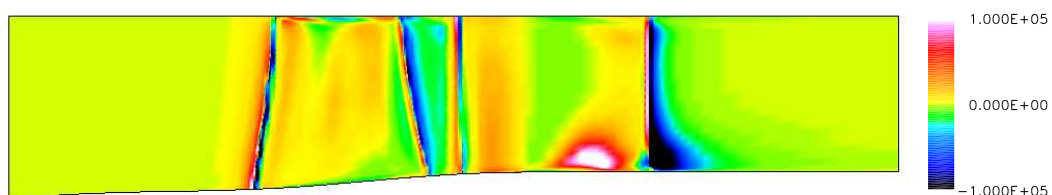


(c) axial-axial stress $\dfrac{\partial \overline{\rho V_x' V_x'}^c}{\partial x}$
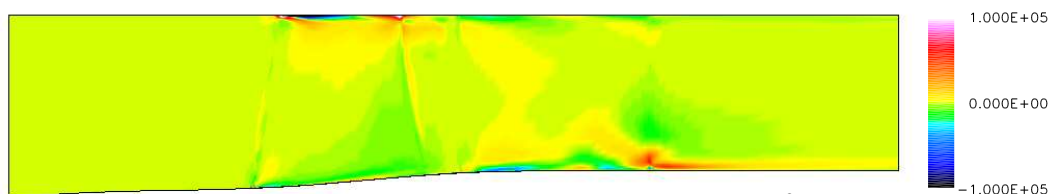


(d) radial-axial stress $\dfrac{\partial \overline{\rho V_r' V_x'}^c}{\partial r}$

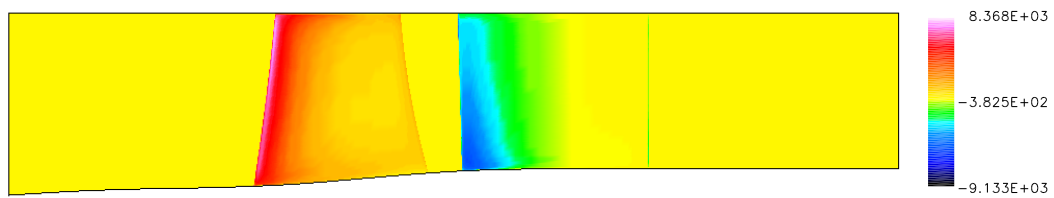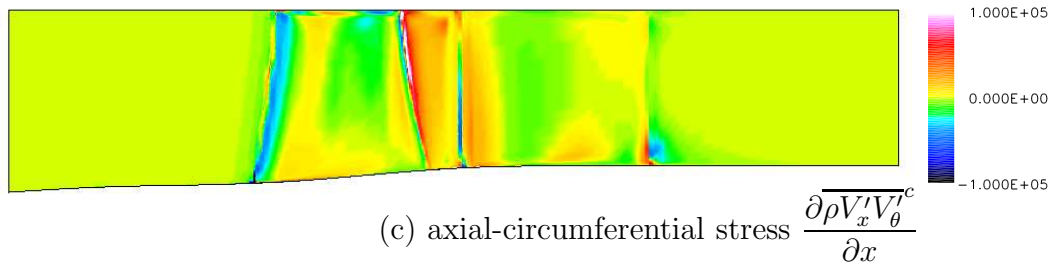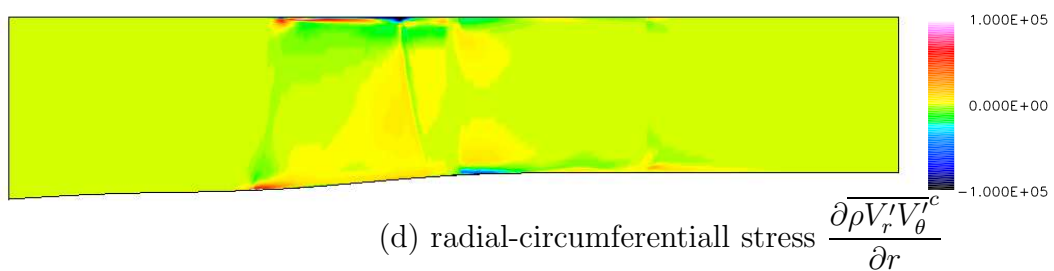Figure C.11: Contributions to the axial momentum balance
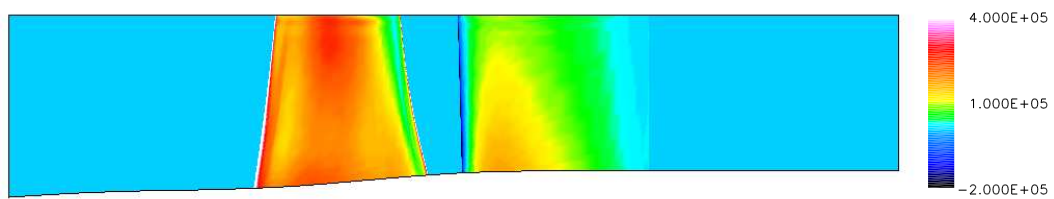
(a) inviscid blade force $f_{br}$
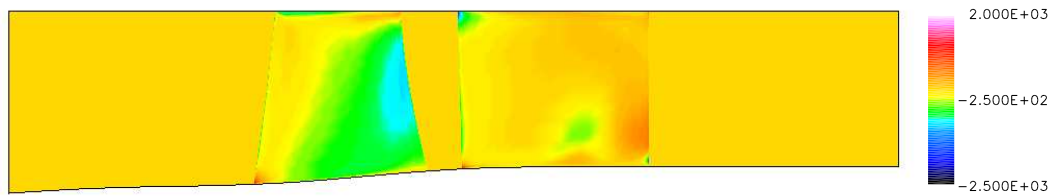


(b) viscous blade force $f_{vr}$
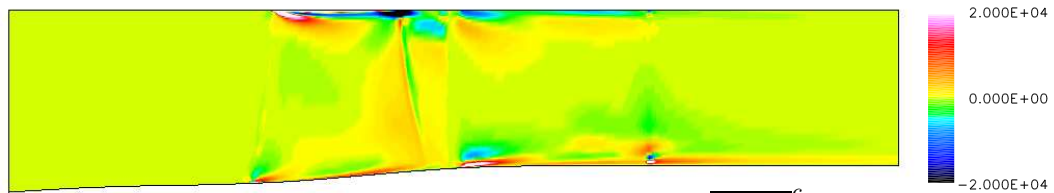


(c) radial-radial stress $\dfrac{\partial \overline{\rho V_r' V_r'}^c}{\partial r}$
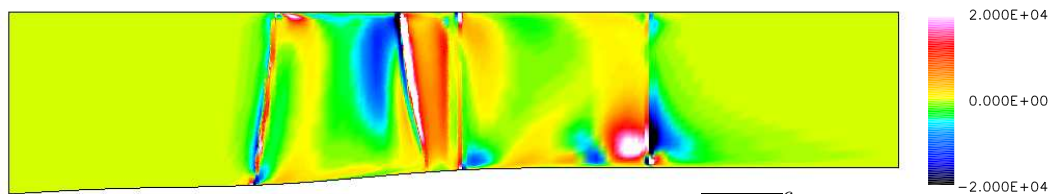


(d) axial-radial stress $\dfrac{\partial \overline{\rho V_x' V_r'}^c}{\partial x}$

Figure C.12: Contributions to the radial momentum balance
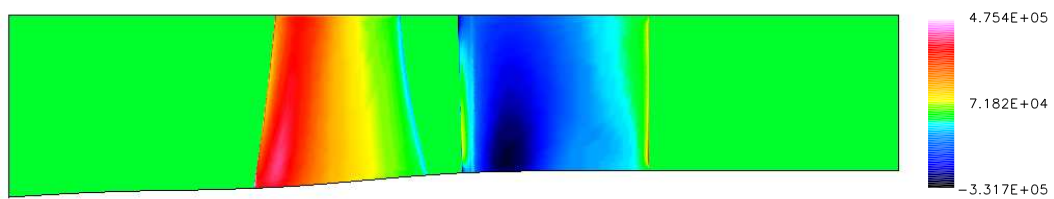
(a) inviscid blade force $f_{bt}$



(b) viscous blade force $f_{vt}$



(c) axial-circumferential stress $\dfrac{\partial \overline{\rho V_x' V_\theta'}^c}{\partial x}$



(d) radial-circumferentiall stress $\dfrac{\partial \overline{\rho V_r' V_\theta'}^c}{\partial r}$

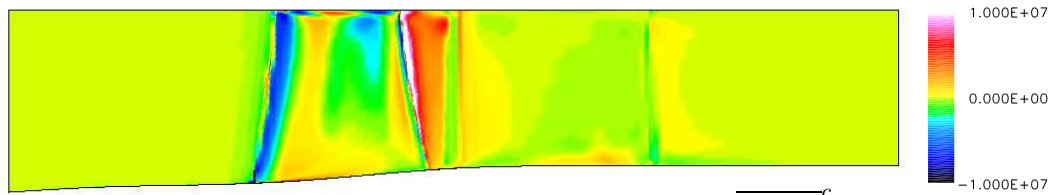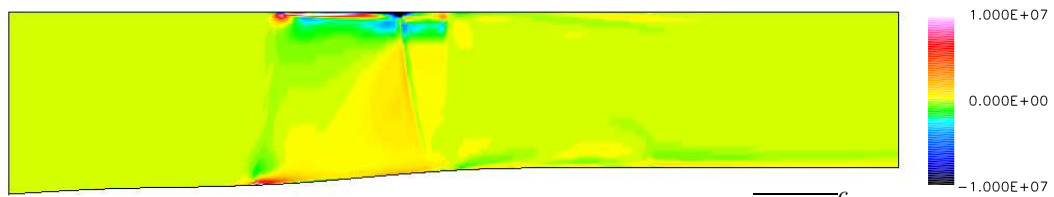Figure C.13: Contributions to the circumferential momentum balance

(a) inviscid blade force $f_{bt}\Omega r$



(b) viscous blade force $f_{vt}\Omega r$



(c) axial-enthalpy stress $\dfrac{\partial \overline{\rho V_x' H'}^c}{\partial x}$



(d) radial-enthalpy stress $\dfrac{\partial \overline{\rho V_r' H'}^c}{\partial r}$

Figure C.14: Contributions to the energy balance

# Appendix D

# VEGA2 circumferential and deterministic stresses

The contributions to the momentum and energy balances from the circumferential and the deterministic stresses are presented below. For each term of each conservation equation, the circumferential stress and the full stress, consisting of the circumferential and the deterministic stresses, are given.
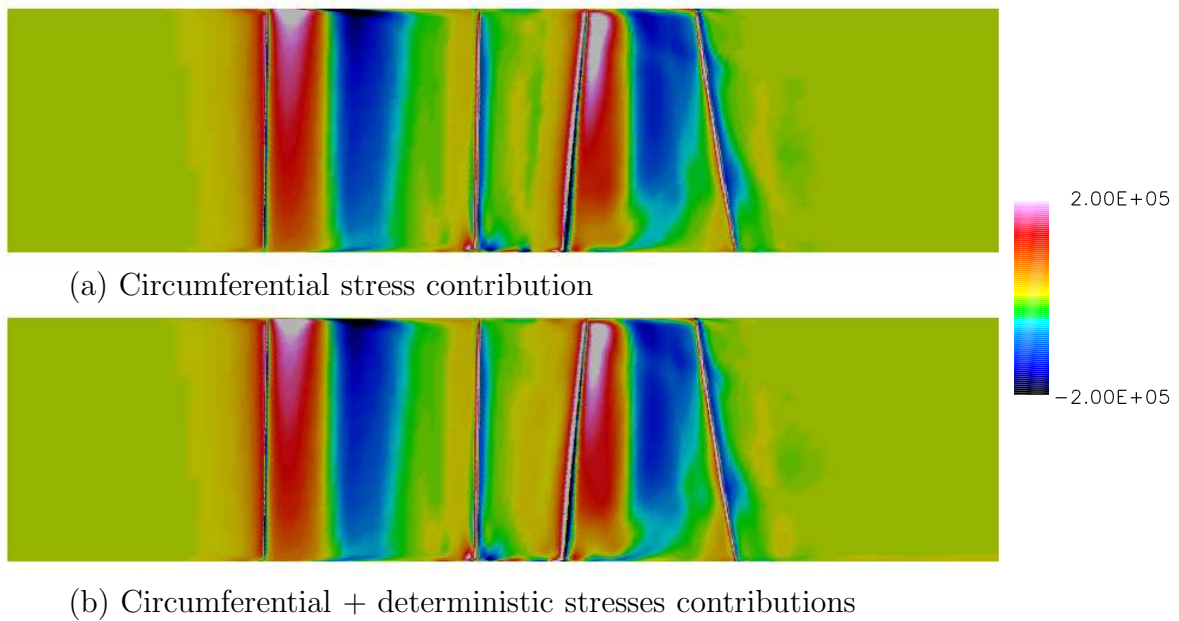


(a) Circumferential stress contribution



(b) Circumferential + deterministic stresses contributions

Figure D.1: Axial-axial stresses contributions to the axial momentum balance $\left( \frac{\partial \overline{\rho V_x' V_x'}}{\partial x} \right)$
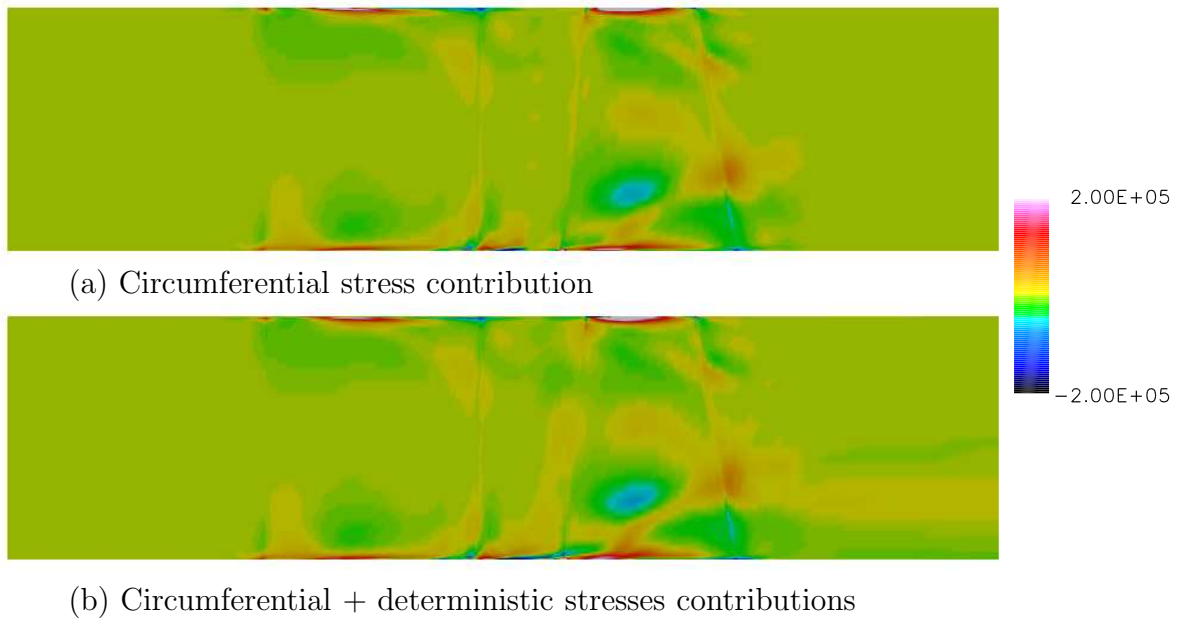
(a) Circumferential stress contribution



(b) Circumferential + deterministic stresses contributions

Figure D.2: Radial-axial stresses contributions to the axial momentum balance $\left( \dfrac{\partial \overline{\rho V_r' V_x'}}{\partial r} \right)$
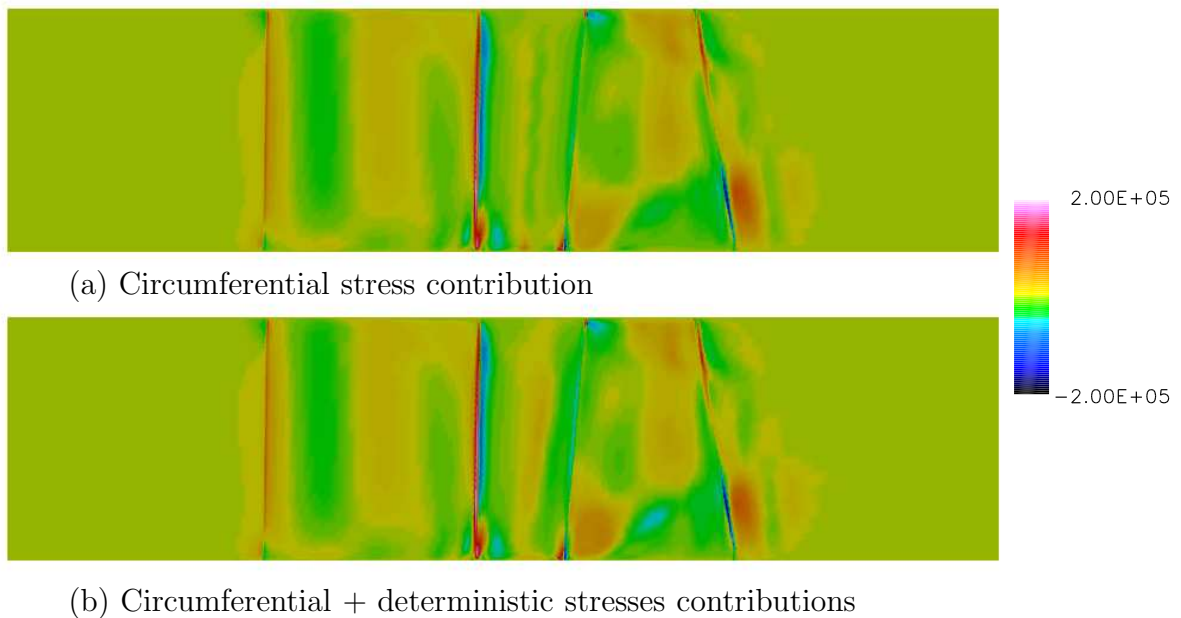


(a) Circumferential stress contribution



(b) Circumferential + deterministic stresses contributions

Figure D.3: Axial-radial stresses contributions to the radial momentum balance $\left( \dfrac{\partial \overline{\rho V_x' V_r'}}{\partial x} \right)$
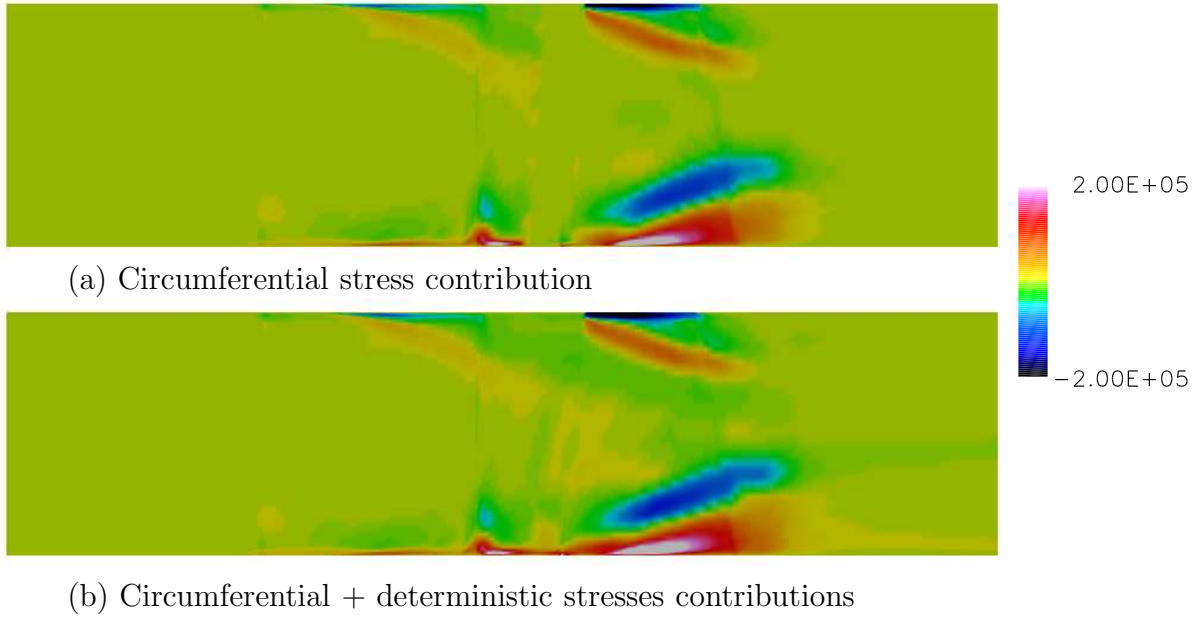
(a) Circumferential stress contribution



(b) Circumferential + deterministic stresses contributions

Figure D.4: Radial-radial stresses contributions to the radial momentum balance $\left(\dfrac{\partial \overline{\rho V_r' V_r'}}{\partial r}\right)$



(a) Circumferential stress contribution



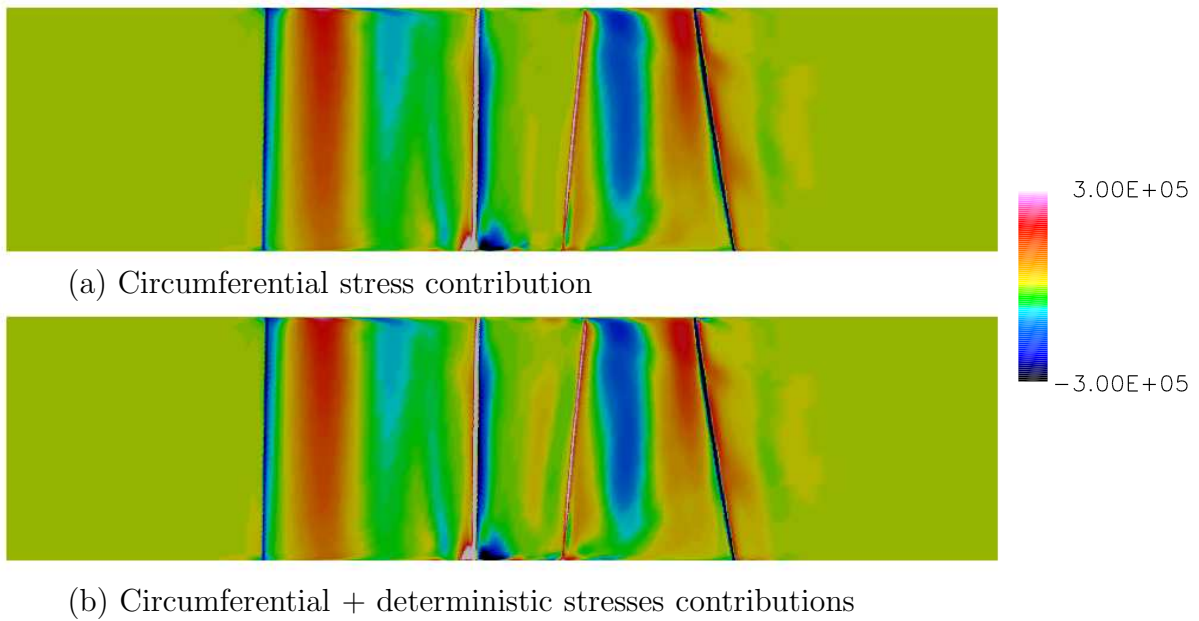(b) Circumferential + deterministic stresses contributions

Figure D.5: Axial-circumferential stresses contributions to the circumferential momentum balance $\left(\dfrac{\partial \overline{\rho V_x' V_\theta'}}{\partial x}\right)$
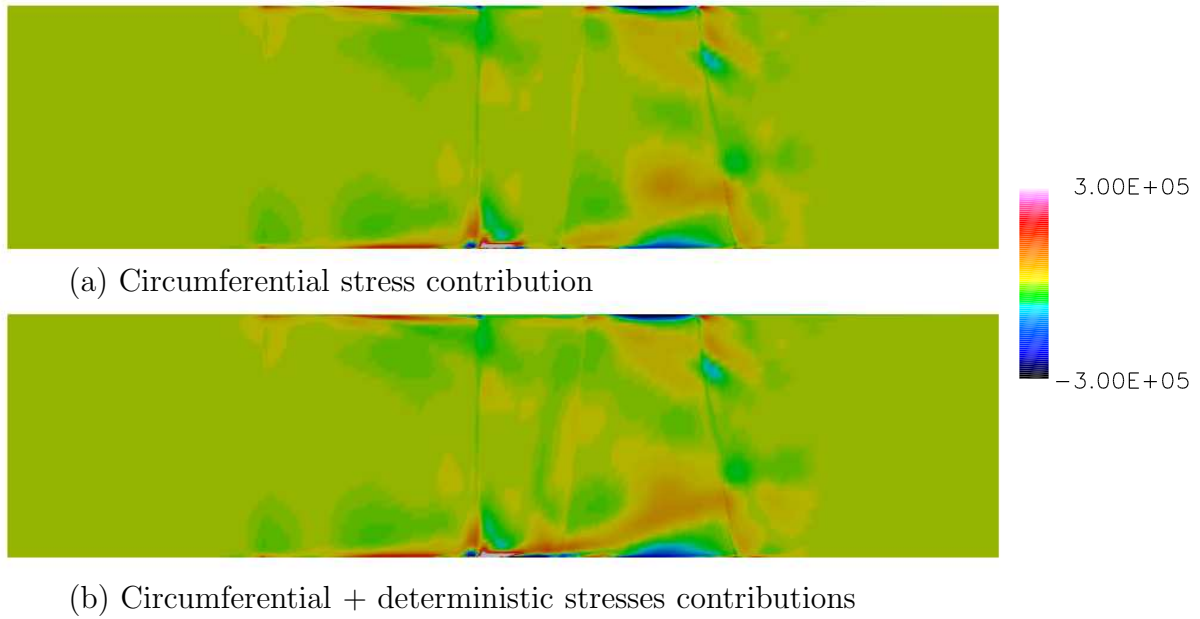
(a) Circumferential stress contribution



(b) Circumferential + deterministic stresses contributions

Figure D.6: Radial-circumferential stresses contributions to the circumferential momentum balance $\left( \dfrac{\partial \overline{\rho V_r' V_\theta'}}{\partial r} \right)$
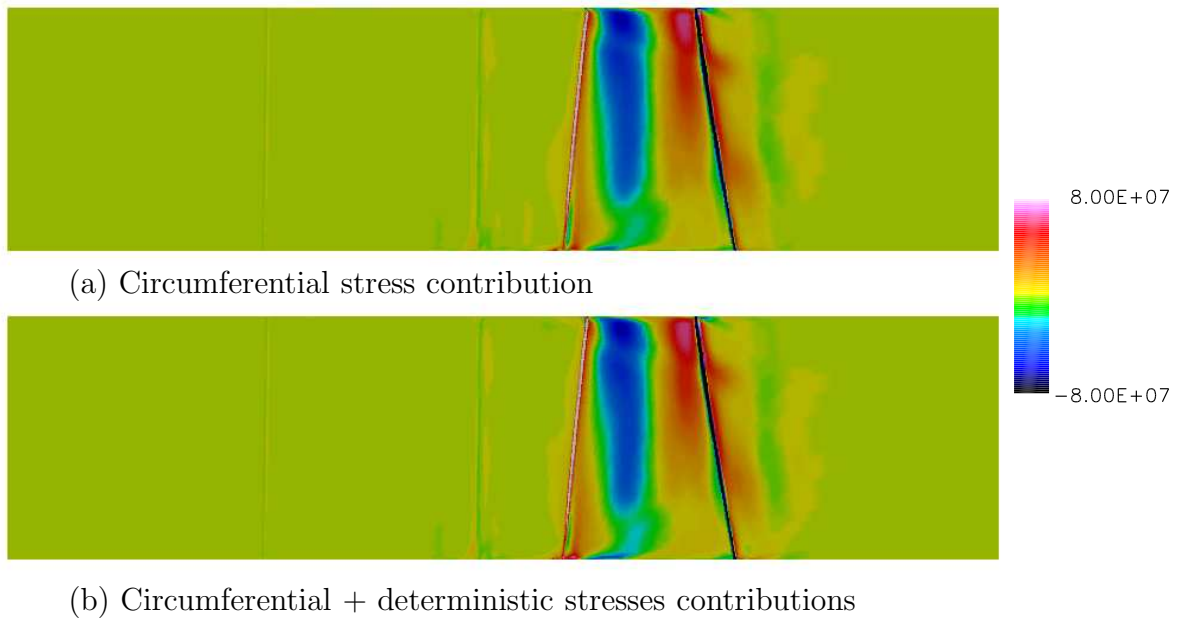


(a) Circumferential stress contribution



(b) Circumferential + deterministic stresses contributions

Figure D.7: Axial-enthalpy stresses contributions to the energy balance $\left( \dfrac{\partial \overline{\rho V_x' H'}}{\partial x} \right)$

(a) Circumferential stress contribution



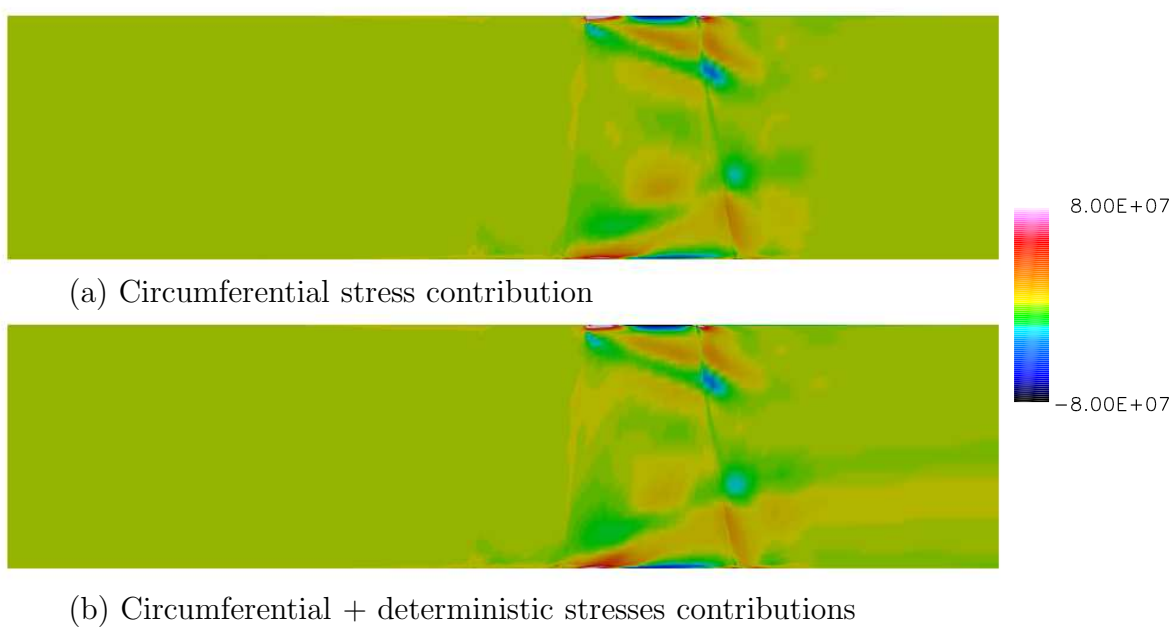(b) Circumferential + deterministic stresses contributions

Figure D.8: Radial-enthalpy stresses contributions to the energy balance $\left(\frac{\partial \overline{\rho V_r' H'}}{\partial r}\right)$